

**CARBON NANOTUBES**  
**MODIFICATION AND APPLICATION**

LIM SAN HUA  
(B.Sc. NUS, Singapore)

A THESIS SUBMITTED  
FOR THE DEGREE OF PHILOSOPHY OF PHYSICS  
DEPARTMENT OF PHYSICS  
NATIONAL UNIVERSITY OF SINGAPORE

2007

**ABSTRACT**

Theoretical studies of single-walled carbon nanotubes (SWNT) were based on density functional theory (DFT) using Dmol<sup>3</sup> and CASTEP codes available from Accelrys Inc. The structural, electronic and optical properties of ultra-small 4Å single-walled nanotubes were investigated for (3,3), (4,2) and (5,0) nanotubes. Ab initio calculations were also performed for various nitrogen-containing SWNTs. Structural deformations, electronic band structures, density of states, and ionization potential energies are calculated and compared among the different types of nitrogenated SWNTs. The electronic properties and chemical reactivity of bamboo-shaped SWNTs were studied for (10,0) and (12,0) nanotubes. DFT calculation also showed that the pentagon defects of the bamboo-shape possess high chemical reactivity, which is related to the presence of localized resonant states. The Universal forcefield was applied to model H<sub>2</sub> physisorption of carbon nanotube bundles. The Metropolis Monte Carlo simulations were also conducted to estimate the H<sub>2</sub> uptakes of SWNT bundles at 300K and 80K.

Single-walled and multi-walled carbon nanotube powders were synthesized via decomposition of methane over cobalt-molybdenum catalysts. A multi-step purification process was carried out to remove the impurities. Inorganic fullerenes such as TiO<sub>2</sub>-derived nanotubes and BN nanotubes were also synthesized using a hydrothermal and a catalyzed mechano-chemical process respectively.

Highly nitrogen-doped (CN<sub>x</sub>) multi-walled carbon nanotubes have been synthesized by pyrolysis of acetonitrile over cobalt-molybdenum catalysts. Raman, XPS-UPS and x-ray absorption techniques were employed to elucidate the changes in the electronic structures of carbon nanotubes caused by the nitrogen dopants. The enrichment of  $\pi$  electron in CN<sub>x</sub> carbon nanotube enhances its ultrafast saturable absorption, which suggests that CN<sub>x</sub> nanotubes can be used as saturable absorber devices.

The ever increasing demand for energy and depleting fossil fuel supply have triggered a grand challenge to look for technically viable and socially acceptable alternative energy sources. Hydrogen as an alternative energy has stand out among the proposed renewable and sustainable energy sources, because it is relatively safe, easy to produce, and non-polluting when coupled with fuel cell technology. The synthesis and application of advanced nano-materials offer new promises for addressing the H<sub>2</sub> energy challenge. Various carbon nanotubes, boron nitride nanotubes and TiO<sub>2</sub> nanotubes were tested for hydrogen storage. The hydrogen storage properties of these nano-materials were studied using pressure-composition (*P-C*) isotherms, temperature-programmed desorption (TPD), FTIR and N<sub>2</sub> adsorption isotherms at 77K (pore structure analysis).

Palladium nanoparticles were electrodeposited onto Nafion-solublized MWNT forming a novel Pd-Nafion-MWNT hybrid. In addition, a quick and easy pre-treatment was proposed to functionalize CNT with oxygen-containing functional groups using critic acid. Gold nanoparticles were beaded onto the sidewall of these critic acid-modified CNTs, which were subsequently attached with thiolated oligonucleotides. Electrochemical glucose biosensor and genosensor based on nanoparticle-CNT hybrids were fabricated with good working performance.

## ACKNOWLEDGEMENTS

I would like to express my deepest gratitude to my supervisors, Prof. Lin Jianyi and Prof. Ji Wei for their patience and guidance during my PhD candidature. I am also indebted to the assistance that I have received from the research fellows and technicians of Surface Science Laboratory.

I also like to show my appreciation to my fellow graduate students, Poh Chee Kok, Pan Hui and Sun Han who have helped me in one way or another.

Furthermore I would like to express my thanks to the research fellows of the Applied Catalysis at Institute of Chemical and Engineering Sciences (ICES). And also my Program Manager, Dr. P.K. Wong, and Team Leader, Dr. Armando Borgna, for their kindness and supports.

There are still many people who I have yet to thank, for help cannot be measured as big or small.



**TABLE OF CONTENTS**

<b>Chapter 1. Introduction</b> .....	1
1.1. Motivation.....	1
1.2. Objectives.....	2
1.3. Methodology.....	3
1.4. Thesis outline.....	4
References.....	5
<b>Chapter 2. Literature Background</b> .....	6
2.1. Fundamentals of single-walled carbon nanotubes.....	6
2.2. Potential applications carbon nanotubes.....	11
2.2.1. CNT-based electronic devices.....	11
2.2.2. Spinning of CNT thread.....	14
2.2.3. CNT-polymer composite.....	15
2.2.4. Field emission sources.....	16
2.2.5. CNT-modified AFM tips.....	18
2.2.6. Electrochemical applications.....	19
2.2.7. Energy storage.....	19
References.....	21
<b>Chapter 3. Theoretical studies of carbon nanotubes</b> .....	24
3.1 First-principles study of ultra-small 4Å single-walled carbon nanotubes.....	25
3.1.1. Computational methods.....	26
3.1.2. Structural Relaxation: Bond lengths & angles.....	28

3.1.3. Electronic properties: Band structures and density of states.....	30
3.1.4. Optical properties of 4Å carbon nanotubes.....	31
3.1.5. Effects of Stone-Wales defects on 4Å nanotubes.....	34
3.1.6. Conclusions.....	38
3.2. First-principles study of nitrogenated single-walled carbon nanotubes.....	39
3.2.1. Computation Methods.....	40
3.2.2. Atomic deformation, bond lengths, molecular orbital and energetics.....	42
3.2.3. Spin restricted electronic properties.....	52
3.2.4. Ionization potential energies.....	58
3.2.5. Spin-unrestricted electronic properties of singly N-chemisorbed SWNTs.....	58
3.2.6. Structural stability and coalescence of two neighboring chemisorbed N adatom...61	
3.2.7. Conclusions.....	69
3.3. First-principles study of carbon nanotubes with bamboo-shape and pentagon-pentagon fusion defects.....	70
3.3.1. Computation methods.....	71
3.3.2 Density of States and Fukui functions.....	73
3.3.3. Conclusions.....	80
3.4. Molecular simulations of carbon nanotube-H <sub>2</sub> interactions.....	81
3.4.1. Computational Methods.....	85
3.4.2. Hydrogen-graphene sheet interactions.....	87
3.4.3. Hydrogen-carbon nanotube interactions.....	90
3.4.4. Conclusions.....	98
References.....	99
<b>Chapter 4. Synthesis and characterizations of carbon nanotubes.....</b>	<b>104</b>
4.1. Synthesis and characterizations of carbon nanotubes.....	105

4.1.1. Decomposition of CH <sub>4</sub> over Co-Mo catalyst.....	105
4.1.2. Purification of CNT.....	108
4.1.3. Characterizations of carbon nanotube.....	110
4.1.4 Formation mechanism of carbon nanotube.....	125
References.....	127
<b>Chapter 5. Growth of vertically aligned carbon nanotubes.....</b>	<b>129</b>
5.1. Plasma-enhanced chemical vapor deposition.....	130
5.1.1. Growth procedure and patterning of VACNT.....	131
5.1.2. “Standard” conditions for VACNT growth.....	132
5.1.3. Effects of temperature.....	134
5.1.4. Optimized growth of VACNTs at 450°C.....	137
5.1.5. Effects of H <sub>2</sub> :C <sub>2</sub> H <sub>4</sub> flow ratio and pressure.....	139
5.1.6. Effects of other gas diluents.....	141
5.1.7. Deposition of 1nm Fe catalyst.....	142
5.1.8. Effects of metallic underlayers and electrical measurements.....	143
5.1.9. Conclusions.....	146
References.....	147
<b>Chapter 6. Nitrogen-doped carbon nanotubes.....</b>	<b>148</b>
6.1 Synthesis and characterizations of nitrogen-doped carbon nanotubes.....	149
6.1.1. Synthesis of CN <sub>x</sub> nanotube.....	150
6.1.2. Characterizations of CN <sub>x</sub> nanotubes.....	151
6.1.3. CN <sub>x</sub> nanotube with improved ultrafast saturable absorption.....	158
6.1.4. Conclusion.....	160
References.....	161

<b>Chapter 7. Pore structure modification and hydrogen storage</b> .....	163
7.1. Hydrogen storage of nanostructured materials.....	164
7.1.1. Introduction.....	164
7.1.2. Modes of H <sub>2</sub> storage.....	166
7.1.3. Techniques of measuring H <sub>2</sub> uptake.....	168
7.2. H <sub>2</sub> storage of carbon nanotubes with modified pores.....	171
7.2.1. Sample preparations and H <sub>2</sub> storage measurement procedures.....	171
7.2.2. Nitrogen adsorption isotherms at 77K.....	173
7.2.3. Hydrogen adsorption isotherms.....	177
7.2.4. Conclusions.....	182
7.3. Room temperature H <sub>2</sub> uptakes of TiO <sub>2</sub> nanotubes.....	183
7.3.1. Nitrogen adsorption isotherms at 77K.....	184
7.3.2. Hydrogen adsorption isotherms.....	186
7.3.3. TPD and FTIR studies of H <sub>2</sub> -soaked TiO <sub>2</sub> nanotubes.....	188
7.3.4. Conclusions.....	190
7.4. Room temperature H <sub>2</sub> uptakes of BN nanotubes.....	191
7.4.1. Nitrogen adsorption isotherms.....	191
7.4.2. Hydrogen adsorption isotherms.....	193
7.4.3. TPD of H <sub>2</sub> -soaked BN nanotubes.....	195
7.4.4. Conclusion.....	196
7.5. Insights into H <sub>2</sub> physisorption – concluding remark.....	197
References.....	200
Appendix A7.1.....	203
Appendix A7.2.Synthesis and characterizations of boron nitride nanotubes.....	205
Appendix A7.3. Synthesis and characterizations of TiO <sub>2</sub> -derived nanotubes.....	212

<b>Chapter 8. Carbon nanotube-nanoparticle hybrids</b> .....	227
8.1. Bio-electrochemistry of carbon nanotube.....	228
8.1.1. Introduction.....	228
8.1.2. Concepts of electrochemical biosensing.....	230
8.2. A glucose biosensor based on co-electrodeposition of palladium nanoparticles and glucose oxidase onto Nafion-solubilized carbon nanotube electrode.....	233
8.2.1. Experimental procedures.....	234
8.2.2. Solubilization of MWNT via wrapping of Nafion polymer.....	235
8.2.3. Electron micrographs of MWNT-nanoparticle hybrids.....	235
8.2.4. XRD patterns and FTIR spectroscopy.....	237
8.2.5. XPS analysis.....	239
8.2.6. Glucose quantification of GOx-Pd-MWNT-Nafion composite.....	240
8.2.7. Conclusions.....	246
8.3. Electrochemical genosensor based on gold nanoparticle-carbon nanotube hybrid.....	247
8.3.1. Experimental procedures.....	248
8.3.2. Electron micrographs of gold nanoparticle-MWNT hybrid.....	251
8.3.3. XRD patterns and UV-vis spectroscopy.....	252
8.3.4. XPS analysis.....	253
8.3.5. Electrochemical impedance spectroscopy (EIS).....	253
8.3.6. Cyclic voltammetry – guanine oxidation.....	255
8.3.7. a.c. voltammetry (ACV) – guanine oxidation.....	257
8.3.8. Conclusions.....	259
References.....	260
<b>Chapter 9. Functionalization of carbon nanotubes</b> .....	262
9.1. –OH functionalized carbon nanotubes.....	263

9.1.1. Experimental procedures.....264

9.1.2. Electron microscope analysis.....266

9.1.3. X-ray photoelectron spectroscopy core level analysis.....267

9.1.4. Optical spectroscopic characterizations.....267

9.1.5. UPS valence band analysis.....269

9.1.6. Optical limiting (OL) properties of SWNToh.....271

9.1.7. Conclusions.....272

9.2 Gravitation-dependent, thermally-induced self-diffraction of octadecylamine (ODA) modified carbon nanotubes solution.....273

9.2.1. Experimental procedures.....273

9.2.2. Gravitational dependent, thermally induced self-diffraction.....275

9.2.3. Conclusions.....280

References.....281

**Chapter 10. Conclusions and future work.....283**

## LIST OF FIGURES

- Figure 2.1.** (a) Definition of chiral vector,  $C_h$ , in a hexagonal lattice of carbon atoms by unit vectors  $\hat{a}_1$  and  $\hat{a}_2$ , and chiral angle  $\theta$  with respect to the zigzag axis (i.e.  $\theta=0$ ). (b) Possible vectors specified by pairs of integers (n,m) for general CNTs. A solid point represents metallic nanotube and an open circle represents semiconductor nanotubes. The condition for the metallic nanotube is:  $2n+m=3q$  (q: integer), or  $(n-m)/3$  is integer.....7
- Figure 2.2.** Typical density of states (DOS) for 3D, 2D, 1D and 0D entities.....8
- Figure 2.3.** Electronic density of states column (a) armchair nanotubes, (b) zigzag nanotubes, and (c) chiral nanotubes calculated by tight binding theory<sup>30</sup>.....9
- Figure 2.4.** (Left panel) Early fabrication of CNTFET devices<sup>18</sup>. (Right panel) A 5-stage complementary metal-oxide semiconducting (CMOS)-type ring oscillator built on a single 18 $\mu$ m-long SWNT<sup>35</sup>.....12
- Figure 2.5.** (Left panel) A schematic view of a suspended SWNT crossbar array with support structures<sup>21</sup>. SWNT can be switched OFF / ON by charging it with electrostatic forces. (Right panel) Experimental switching of crossed SWNTs device<sup>21</sup> between OFF and ON states with a resistance ratio  $\sim 10$ .....13
- Figure 2.6.** (Left panel) Conventional “face-up” structure of a transistor chip wire-bonded to the circuit board and heat dissipation is simply due to contact. (Right panel) A “flip-chip” design adopted by Fujitsu, which incorporates CNT bumps to connect the transistor chip and the circuit board<sup>36</sup>.....13
- Figure 2.7.** (Left panel) Schematic setup of the winding geometry CVD chamber used by Li et al.<sup>39</sup> for spinning CNT thread. (Right panel) The CNT thread is composed of intertwined carbon nanotubes.....15
- Figure 2.8.** (Left panel) Comparison of strength and failure strain for various CNT-composite fibers and 3000 materials types in the Cambridge Materials Selector database<sup>43</sup>. (Right panel) A textile supercapacitor composed of 2 orthogonally directed CNT fibers. This CNT fiber supercapacitor provides a capacitance (5Fg<sup>-1</sup>) and energy storage density (0.6Whkg<sup>-1</sup>) that are comparable to commercial supercapacitor<sup>43</sup>.....16
- Figure 2.9.** (Left panel) Randomly aligned CNT commercially available from Xintek Nanotechnology Innovations<sup>46</sup>. The inset shows bright and uniform emission sites by the CNT mats. (Right panel) Array of individual vertically aligned carbon nanofibers fabricated as a microwave diode<sup>47</sup>.....17
- Figure 2.10.** A CNT-modified AFM tips commercially available from nanoScience Instruments<sup>49</sup>.....18
- Figure 3.1.** Stick-and-ball models of ultra-small 4Å nanotubes: (a) armchair (3,3), (b) zigzag (5,0) and (c) chiral (4,2).  $a$ ,  $b$  and  $c$  represent the bond lengths of the carbon network while  $\alpha$ ,  $\beta$ , and  $\gamma$  are the bond angles.....28

**Figure 3.2.** (*Left panel*) Electronic band structures and (*Right panel*) density of states of (3,3), (5,0) and (4,2) nanotubes. Calculations were conducted within GGA-PBE parametrization using Dmol<sup>3</sup> code. Solid lines and dotted lines represent the computed results of the geometrically relaxed and cylindrically folded (unrelaxed) nanotubes respectively.....31

**Figure 3.3.** (*Left panel*) Imaginary part ( $\epsilon_2$ ) of the dielectric function for the tubes (3,3) (dotted lines), (5,0) (dashed lines) and (4,2) (solid lines) for light polarized parallel and perpendicular to the tube axes.  $\epsilon_2$  are calculated with CASTEP code. (*Right panel*) Optical absorption spectra of 4Å nanotubes embedded in zeolites. Taken from ref [17].....32

**Figure 3.4.** (a) A  $\pi/2$  rotation of C1-C2 bond in the hexagonal network to yield a Stone-Wales defect. Geometry optimizations of nanotubes with SW-defect: (b) (5,5) nanotube, (c) (3,3) nanotube, and (d) (5,0) nanotube. The bond lengths of the 5775 defects are given in Å.....35

**Figure 3.5.** (*Left panel*) Density of states (DOS) and (*Right panel*) scanning tunneling microscopic (STM) images of (a) (5,5), (b) (3,3) and (c) (5,0) nanotubes with Stone-Wales defects. Properties of (5,5), (3,3) and (5,0) nanotubes with SW-defects were calculated within CASTEP code. Solid line and dotted lines denote the DOS of the Stone-Wales and pristine states respectively.....36

**Figure 3.6.** (a) Geometrically optimized structures, highest occupied molecular orbital (HOMO) and bond lengths (in Å) of a pure zigzag (10,0) nanotube; (b) Direct substitution of two nitrogen atoms into the carbon framework without the formation of vacancies. Here the two N substitution atoms in C<sub>78</sub>N<sub>2</sub> are in the opposite positions, (c) N substitution into the carbon framework with the formation of vacancy: pyridine-like doping (C<sub>72</sub>N<sub>6</sub>) with two vacancies formed in opposite positions, (d) Chemisorption of a N adatom in “parallel” position, (e) Chemisorption of a N adatom in “perpendicular” position, (f) –NH<sub>2</sub> functionalization. Grey ball denotes C atom, blue ball denotes N atom, and white ball denotes H atom. A fragment of the supercell is taken out to elucidate the bond lengths at the vicinity of the N-impurities.....43-44

**Figure 3.7.** (a) Geometrically optimized structures, highest occupied molecular orbital (HOMO) and bond lengths (in Å) of a pure armchair (5,5) nanotube; (b) Direct substitution of two nitrogen atoms into the carbon framework without the formation of vacancies. Here the two N substitution atoms in C<sub>58</sub>N<sub>2</sub> are in the opposite positions, (c) N substitution into the carbon framework with the formation of vacancy: pyridine-like doping (C<sub>52</sub>N<sub>6</sub>) with two vacancies formed in opposite positions, (d) Chemisorption of a N adatom in “parallel” position, (e) Chemisorption of a N adatom in “perpendicular” position, (f) –NH<sub>2</sub> functionalization. Grey ball denotes C atom, blue ball denotes N atom, and white ball denotes H atom. A fragment of the supercell is taken out to elucidate the bond lengths at the vicinity of the N-impurities.....45-46

**Figure 3.8.** Band structures of (10,0) and (5,5) nanotubes: (a,g) pure, (b,h) N-substitution, (c,i) pyridine-like doping, (d,j) chemisorption at “parallel” position, (e,k) chemisorption at “perpendicular” position, (f,l) –NH<sub>2</sub> functionalization. (a-f) and (g-l) for (10,0) and (5,5) nanotubes respectively. The Fermi level is represented by the dotted horizontal lines.....51

**Figure 3.9.** Total density of states (TDOS) of (a) pristine (10,0) nanotube, (b-d) nitrogen-substitution, (e,f) pyridine-like doping, (g,h) chemisorption of N adatoms, and (i) –NH<sub>2</sub> functionalization. Projected DOS of nitrogen impurities and TDOS of undoped (10,0) nanotube with vacancy are indicated as red line and blue lines respectively. The Fermi level is at 0eV. A 120atoms/cell supercell is used to compute case (b) substitution.....54



**Figure 3.10.** Total density of states (TDOS) of (a) pristine (5,5) nanotube, (b) nitrogen-substitution, (c,d) pyridine-like doping, (e,f) chemisorption of N adatoms, and (g)  $-\text{NH}_2$  functionalization. Projected DOS of nitrogen impurities and TDOS of undoped (5,5) nanotube with vacancy are indicated as red line and blue lines respectively. The Fermi level is at 0eV.....57

**Figure 3.11.** Spin-polarized band structures of singly N-chemisorbed SWNTs in (a,c) “parallel” and (b,d) “perpendicular” positions. Majority spin and minority spin electrons are denoted by solid and dotted lines respectively.....59

**Figure 3.12.** Spin-polarized local density of states of a single N adatom chemisorbed on (10,0) and (5,5) nanotubes. The pink isosurface of the spin density is set at the value of  $0.05e/\text{\AA}^3$ . The grey and blue spheres represent C and N atoms respectively.....59

**Figure 3.13.** Possible configurations of two neighboring N adatoms chemisorbed on a graphene sheet.  $Z_1$  and  $Z_2$  directions represent the tubular axes of zigzag (10,0) and armchair (5,5) nanotubes respectively.....60

**Figure 3.14.** Energy versus path coordinate during transition state search. The path coordinate “0” represents the “reactant” (SWNT with two chemisorbed N adatoms), while path coordinate “1” represents the “products” (SWNT + a free  $\text{N}_2$  molecule). Case (a), (b,c) and (d,e) are the TS search and energy diagrams for a graphene sheet, (10,0) and (5,5) nanotubes respectively. *Energy diagrams are not drawn to scale*.....66-68

**Figure 3.15.** Relaxed geometries of bamboo-shaped (a) (10,0) nanotube, and (b) (12,0) nanotube with pentagon defects.....73

**Figure 3.16.** Localized density of states (LDOS) of bamboo-shaped (10,0) nanotube (a) and armchair (12,0) nanotube (b). A-to-M and N-to-V are the label of the carbon rows in the (10,0) tube (see Fig. 3.15a) and in (12,0) (see Fig. 3.15b) respectively. The Fermi level is located at 0eV. The LDOS has been shifted vertically for clarity of presentation.....74

**Figure 3.17.** Fukui functions (FF) for radical attack computed for (a) pristine (10,0), (b) bamboo-shaped (10,0), (c) pristine (12,0) and (d) bamboo-shaped (12,0) nanotubes. Isodensity surface is set from zero (blue color) to 0.008 (red color) a.u./ $\text{\AA}^2$ . The red region denotes high reactivity, while blue region denotes low reactivity.....76

**Figure 3.18.** (a) Relaxed structure, bond lengths and (b) localized density of states of (5,5) nanotube with a pentagon-pentagon fusion ring. The Fermi level is located at 0eV. The LDOS has been shifted vertically for clarity of presentation.....78

**Figure 3.19.** Fukui functions (FF) for radical attack computed for a (5,5) nanotube with a pentagon-pentagon fusion ring. Isodensity surface is set from zero (blue color) to 0.008 (red color) a.u./ $\text{\AA}^2$ . The red region denotes high reactivity, while blue region denotes low reactivity..79

**Figure 3.20.** (a) Schematic packing of an idealized SWNT (10,10) bundle showing 4 possible binding sites and energies for  $\text{H}_2$  calculated by Monte Carlo method<sup>72</sup>. (b) Herringbone and concentric MWNTs with exposed graphitic edges as potential sites for  $\text{H}_2$  chemisorption<sup>66</sup>. (c) DFT calculations<sup>75</sup> of  $\text{H}_2$ -SWNT bundle interactions.....83

**Figure 3.21.** Configurations of  $\text{H}_2$  adsorbed on a flat graphene sheet. The  $\text{H}_2$  molecular axis is parallel to the graphene sheet at adsorption site A (center of hexagon ring) and site B (carbon-

carbon bond). The  $H_2$  molecular axis is perpendicular to the graphene sheet at adsorption site *C* (center of hexagon ring), site *D* (carbon-carbon bond) and site *E* (top of a carbon atom). These sites are also defined for  $H_2$  adsorbing on the outside surface of SWNT.....87

**Figure 3.22.** (a) Potential energy curves of a flat graphene sheet- $H_2$  interaction calculated by Universal forcefield. The adsorption sites are *A* (-■-), *B* (-■-), *C* (-▼-), *D* (-◆-), and *E* (-▽-) as defined in Fig 3.21. (b) Potential energy curves of a flat graphene sheet- $H_2$  interaction calculated by different forcefields: COMPASS (-■-), Universal (-■-), cvff (-▲-), pcff (-▶-), and Dreiding (-○-). The adsorption site *A* was used only.....88

**Figure 3.23.** Potential energy curves of curved graphene sheets with curvature similar to (10,10) (square symbols) and (30,30) (triangle symbols) nanotubes. Solid and open symbols denote concave and convex side of the curved graphene sheets. Inset shows the curved graphene sheets with (10,10)-like and (30,30)-like curvature.....89

**Figure 3.24.** (a) Adsorption energy of a  $H_2$  molecule on the external surface of a single (5,5) nanotube. The surface adsorption sites are *A* (■; solid line= $H_2$  parallel to tube axis, dotted line= $H_2$  perpendicular to tube axis), *B* (■), *C* (■), *D* (■), and *E* (■) as defined in Fig 3.21. (b) Adsorption energy of  $H_2$  molecule on a (5,5) tube, (8,0) tube, (6,4) tube, (8,8) tube and a DWNT (3,3)@(8,8). Surface adsorption of site *A* is considered only.....91

**Figure 3.25.** (a) Cross-sectional view of relaxed (5,5) and (10,10) bundles which possesses several adsorption sites for  $H_2$  molecule at the surface (*S*), pore (*P*), groove (*G*), and interstitial channels (*IC*). The interstitial channel spacing is defined as the diameter of a circle (dotted) that can be fitted in the IC.....92

**Figure 3.26.** Potential energy curves of SWNT bundle- $H_2$  interactions at the (5,5) outside surface (site *A*, ●), pore (●= $H_2$  parallel to tube axis, ○= $H_2$  perpendicular to tube axis), and groove (●). Adsorption energy curve of  $H_2$  in the interstitial channels of (10,10) bundle is denoted by (○)...93

**Figure 3.27.** Van der Waals surfaces of (a)  $H_2$  adsorbed inside the pore a (5,5) tube, (b)  $H_2$  adsorbed on the outside surface of a (5,5) tube, (c)  $H_2$  adsorbed on the groove of a (5,5) bundle, (d)  $H_2$  intercalated into the interstitial channels of a (10,10) bundle. (e)  $H_2$  intercalated into the interstitial sites of a (5,5) bundle. The interaction distance is at the local minimum of the potential energy curve, except for (e).....94

**Figure 3.28.** Simulated Pressure-composition-isotherms of uncapped (5,5) and (10,10) bundle- $H_2$  interactions at 300K (open symbol) and 80K (closed symbol).....96

**Figure 3.29.** Density field for  $H_2$  in uncapped (5,5), (7,7), (9,9), (10,10) and (11,11) nanotube bundles. The red output field represents a density distribution of  $H_2$  molecules in the SWNT bundles under conditions of 1bar and 80K.  $\phi$  and  $\varphi$  denote the SWNT's diameter and interstitial channel spacing respectively. Unit length is Å.....96

**Figure 4.1.** Schematic setup of thermal CVD used for the synthesis of carbon nanotube.....106

**Figure 4.2.** Purification process of as-synthesized CNT powder.....108

**Figure 4.3.** Scanning electron micrographs of (a) as-synthesized and (b) purified SWNT. (c) Transmission electron micrograph of a purified SWNT bundle. (d) High resolution TEM micrographs of purified SWNT.....109

<b>Figure 4.4.</b> (a) Scanning electron micrograph and (b) transmission electron micrograph of purified MWNT.....	110
<b>Figure 4.5.</b> (a) TGA and (b) differentiated TG (DTG) of as-synthesized SWNT (black line), step 4 purified SWNT (blue line), and step 5 purified SWNT (red line). Temperature ramp rate = 10°C/min in 10% O <sub>2</sub> /Ar.....	111
<b>Figure 4.6.</b> (a) TGA and (b) differentiated TG (DTG) of as-synthesized MWNT (black line), step 4 purified MWNT (blue line), and step 5 purified MWNT (red line). Temperature ramp rate = 10°C/min in 10% O <sub>2</sub> /Ar.....	111
<b>Figure 4.7.</b> Schematic diagram depicting the atomic vibrations for (a) the radial breathing mode (RBM) and (b) tangential (G-band) modes of SWNT.....	113
<b>Figure 4.8.</b> A revised Kataura plot <sup>17</sup> of E <sub>g</sub> vs d <sub>t</sub> . The two lowest interband transitions are denoted by E <sup>S</sup> <sub>11</sub> (d <sub>t</sub> ), E <sup>S</sup> <sub>22</sub> (d <sub>t</sub> ), E <sup>M±</sup> <sub>11</sub> (d <sub>t</sub> ), where 11 is the first vHS, 22 is the second vHS, S for semiconducting (red) tubes, M for metallic (blue) tubes, and ± is the split into high (+) and (-) low energy transitions in metallic tubes.....	115
<b>Figure 4.9.</b> RBMs of SWNTs using resonance Raman laser excitation wavelengths at (a) 785nm, (b) 633nm, and (c) 514nm. The corresponding Kataura plot is displayed next to the observed RBMs with a transition window of ±0.1eV. <i>Red and blue deconvolutions for semiconducting and metallic tubes respectively. Chirality of SWNT is indicated beside the observed ω<sub>RBM</sub>.</i> .....	116
<b>Figure 4.10.</b> Deconvolved tangential G-band of the purified SWNT with three laser excitation wavelengths (a) 785nm, (b) 633nm and (c) 514nm.....	119
<b>Figure 4.11.</b> (a) Normalized XPS C1s core level and (b) loss energy spectra of purified SWNT and MWNT. <i>Loss energy spectra were shifted for clarity of presentation.</i> .....	123
<b>Figure 4.12.</b> Valence band (VB) spectra of purified SWNT and MWNT using (a) 40.8eV and (b) 60eV photon energies.....	125
<b>Figure 4.13.</b> Secondary electron tail threshold of SWNT (solid line), MWNT (dashed line) and gold (dot-dash line) using He I source (21.2eV). <i>Inset: Expanded view of the secondary electron tail threshold. Gold film was used as an internal reference.</i> .....	125
<b>Figure 5.1.</b> (Left panel) A radio-frequency plasma-enhanced chemical vapor deposition system. (Right panel) A schematic diagram of the main components of PE-CVD system. <i>Diagram not drawn to scale.</i> .....	131
<b>Figure 5.2.</b> (a-c) SEM and (d,e) TEM images of VACNTs synthesized at “standard” conditions .....	133
<b>Figure 5.3.</b> The temperature of sample stage (■■■) and silicon wafer (ΔΔΔ) with respect to the temperature of the graphite heater. ....	135
<b>Figure 5.4.</b> SEM images of CNTs synthesized at (a, b) 600°C, (c, d) 450°C, (e, f) 400°C and (g) 380°C using a 4nm-thick Fe catalyst. All the Fe catalysts are pre-treated at 600°C, 1Torr and 100W H <sub>2</sub> plasma power for 10min.....	136

**Figure 5.5.** (a) SEM images (top views) of VACNTs synthesized at 450°C and 1Torr using a 4nm-thick Fe catalyst which is pre-treated at different H<sub>2</sub> plasma power and duration. (b) Raman spectra of VACNTs synthesized at 50W, 100W and 150W plasma.....138

**Figure 5.6.** SEM images (top views) of VACNTs synthesized at 450°C with optimized pretreatment of the 4nm Fe catalysts: (a) 50W, 10min; (b) 50W, 30min; (c) 25W, 30min; and (d) 25W, 60min.....139

**Figure 5.7.** SEM images of VACNTs synthesized at higher flow rate of H<sub>2</sub>:C<sub>2</sub>H<sub>4</sub> =40sccm:80sccm.....140

**Figure 5.8.** SEM images of VACNTs synthesized at (a) 0.3 Torr and (b) 5 Torr of pressures .....140

**Figure 5.9.** (a) XPS N<sub>1s</sub> peak and (b) SEM images of VACNTs synthesized at “standard” conditions with an additional 10sccm of N<sub>2</sub>.....142

**Figure 5.10.** TEM images of VACNT synthesized by (a) simultaneous heating and H<sub>2</sub>-plasma treating, and (b) heated then followed by H<sub>2</sub>-plasma. (c) SEM images and (d) Raman spectrum of the VACNTs synthesized using simultaneous H<sub>2</sub> plasma etching and heating. Catalyst is 1nm Fe. ....143

**Figure 5.11.** SEM images of VACNT synthesized at “standard” conditions with 20nm Fe catalyst deposited on (a) 60nmTa/Si, (b) 50nmTi/60nmTa/Si, (c) 60nmTa/500nmCu/Si, (d) 120nmTa/500nmCu/Si, (e) 50nmTi/120nmTa/Cu underlayers.....144

**Figure 5.12.** (*Left panel*) Schematic setup of the two-terminal I-V measurements. (*Right panel*) Typical I-V measurements of VACNT samples.....145

**Figure 6.1.** Typical TEM images of bamboo-shaped nitrogen-doped carbon nanotubes and a diameter-distribution bar chart.....151

**Figure 6.2.** First-order Raman spectra of CN<sub>x</sub> nanotubes and pristine MWNT.....153

**Figure 6.3.** (a) XPS C1s core level spectra for pristine MWNT (dotted line) and CN<sub>x</sub> nanotube (solid line) with 12at% N-dopant. *Inset:* Energy loss due to π→π\* transition. (b-c) Deconvolved C1s and N1s core-level spectra for CN<sub>x</sub>NT, x ≈ 12at%.....153

**Figure 6.4.** (a) UPS He II (40.8eV) valence band spectra of pristine MWNT and CN<sub>x</sub> nanotube. (b) Secondary electron tail threshold spectra of pristine MWNT and CN<sub>x</sub> nanotube using photon energy = 60eV. *Inset:* Expanded view of the secondary electron tail threshold and top valence band regions.....155

**Figure 6.5.** XANES C1s K-edge absorption spectra of pristine MWNTs (dotted lines) and CN<sub>x</sub> nanotubes (solid lines). *Inset:* An expanded view of the graphitic C1s → π\* resonance.....157

**Figure 6.6.** Degenerate 130-fs-time-resolved pump-probe measurements of (a) pristine MWNT and (b) CN<sub>x</sub> nanotube performed at 780 nm with increasing irradiance. All the solid lines are two-

exponential fitting curves with  $\tau_1=130$  fs and  $\tau_2=1$  ps. (c) A plot of maximum  $\Delta T/T$  against irradiance for MWNT (○○○) and  $CN_xNT$  (●●●).....159

**Figure 7.1.** Current  $H_2$  storage technologies compared to DOE target and petroleum performance<sup>2</sup>. *The upper right box indicates future  $H_2$  storage technological breakthrough*.....165

**Figure 7.2.** An overview of  $H_2$  technology as an alternative energy source.....165

**Figure 7.3.** (a)  $N_2$  adsorption isotherms at 77K, (b) DR plots and (c) HK plots of *p*-SWNT, *act*-SWNT, *p*-MWNT and  $CN_xNT$ .....174

**Figure 7.4.** BJH mesopore size distribution of (a) single-walled and (b) multi-walled carbon nanotube samples.....176

**Figure 7.5.** Hydrogen adsorption isotherms at room temperature (open symbols) and 77K (filled symbols) for (a) *act*-SWNT and *p*-SWNT and (b)  $CN_xNT$  and *p*-MWNT samples. Isotherms at 300K and 77K are fitted with Henry's Law and Langmuir model respectively.....178

**Figure 7.6.** Variation of isosteric heat of adsorption with the amount of  $H_2$  adsorbed.....179

**Figure 7.7.** Variation of chemical potential of  $H_2$  ( $\mu$ ) with pressure and temperature. Legends are divided into 5 color bands (from  $-0.1$  eV to  $-0.4$  eV).....179

**Figure 7.8.** (a)  $N_2$  adsorption isotherms at 77K, (b) BJH pore size distribution of  $TiO_2$  nanotube and bulk anatase, (c) effective pore size distribution by HK method, and (d) DR plot.....185

**Figure 7.9.** (a) *P-C* isotherms of  $TiO_2$  nanotubes and bulk  $TiO_2$  at room temperature. (b) *P-C* isotherms of  $TiO_2$  nanotubes at 24°C, 70°C and 120°C.....186

**Figure 7.10.** (a)  $H_2$  desorption and (b)  $H_2O$  desorption process during TPD of hydrogenated  $TiO_2$  nanotubes at indicated ramp rate, using argon as carrier. (c) FTIR spectra of  $TiO_2$  nanotubes before and after  $H_2$  sorption. (d) Kissinger's plot of  $H_2$  desorption of  $TiO_2$  nanotubes.....189

**Figure 7.11.** (a)  $N_2$  adsorption isotherms at 77K and (b) BJH pore size distribution of BN nanotube. (c) Effective pore size distribution by HK method, and (d) DR plot.....192

**Figure 7.12.** *P-C* isotherms of BN nanotubes at 24°C (black curves), 180°C (blue curves) and 250°C (red curves). *Inset: P-C isotherm of bulk BN powder at room temperature*.....194

**Figure 7.13.**  $H_2$  desorption process during TPD of hydrogenated BN nanotubes at indicated ramp rate, using argon as carrier. *Inset: Kissinger's plot*.....196

**Figure 8.1.** A schematic set-up of (a) the electrochemical unit used for biosensing tests, and (b) a chemically modified electrode.....229

**Figure 8.2** TEM images of electrodeposited (i) Pd-GOx on MWNT, (ii) Pd nanoparticles on MWNT without GOx and (iii) Pd-GOx on Nafion-solubilized MWNT. (iv) SEM images of Nafion-solubilized MWNT cast onto a Si substrate.....236

- Figure 8.3.** (a) XRD patterns and (b) FTIR spectra of (i) electrodeposited Pd nanoparticle-MWNT hybrid (with GOx for IR spectrum) and (ii) pristine MWNT. (Asterisk\* denotes interfering IR signal of CO<sub>2</sub>).....238
- Figure 8.4.** XPS spectra of Pd-MWNT composite (a) survey scan, (b) *C1s*, (c) *O1s*, and (d) Pd3*d*. .....239
- Figure 8.5.** (a) Influence of the composition of PdCl<sub>2</sub> and GOx on the biosensor performance towards 5mM glucose at an applied +0.3V. For a fixed 1000U/mg of GOx, the results are shown as (■). For a fixed 1mM PdCl<sub>2</sub>, the results are shown as (○). (b) Cyclic voltammograms of Pd-GOx-Nafion MWNT before (dotted line) and after (solid line) adding 0.25mM of H<sub>2</sub>O<sub>2</sub> at a sweep rate of 25mVs<sup>-1</sup>.....241
- Figure 8.6.** Hydrodynamics voltammograms of Pd-MWNT (Δ) and Pd-GOx-Nafion MWNT (●) electrodes in 15mM glucose.....242
- Figure 8.7.** Calibration curve of the optimized Pd-GOx-Nafion MWNT bioelectrode. *Inset:* A comparative chronoamperometric response of Pd-GOx-Nafion MWNT and Pd-GOx GCE bioelectrodes upon successive addition of 5mM glucose at +0.3V.....243
- Figure 8.8.** (a) Effects of interfering signals of 0.5mM uric acid (UA) and ascorbic acid (AA) on the performance of Pd-GOx-MWNT and Pd-GOx-Nafion MWNT bioelectrodes at +0.3V in 0.1M phosphate buffer pH 7; stirring rate: 300rpm. (b) Long term storage stability of the (i) Pd(1mM)-GOx MWNT, (ii) Pd(1.5mM)-GOx-Nafion MWNT and (iii) Pd(1mM)-GOx-Nafion MWNT bioelectrodes toward the sensing of 5mM glucose during a storage period of 50 days. Dotted lines are drawn for visual aid only.....245
- Figure 8.9.** Schematic illustration of self-assembly of thiolated oligonucleotides onto Au-MWNT hybrid. The use of MCH assists the erection of *ss*DNA and facilitates hybridization of complementary oligonucleotides, which is detected via mediator Ru(bpy)<sub>3</sub><sup>2+</sup>. (*ss* denotes single stranded).....250
- Figure 8.10.** TEM images of gold nanoparticle-MWNT hybrids.....251
- Figure 8.11.** (a) XRD patterns of (i) Au nanoparticle-MWNT and (ii) pristine MWNT. (b) UV-vis absorption spectrum of MWNT bound with gold nanoparticles.....252
- Figure 8.12.** (a) XPS core-level *C1s* of citric acid functionalized-MWNT and (b) core-level Au4*f* of gold nanoparticle-MWNT hybrid.....253
- Figure 8.13.** Nyquist diagram (*Z*<sub>im</sub> vs *Z*<sub>re</sub>) for EIS measurements of Au-MWNT μ-electrode in the presence of 10mM [Fe(CN)<sub>6</sub>]<sup>3-/4-</sup> (1:1-mixture): (a) modified with MCH and without any attached oligonucleotides, (b) modified with oligonucleotide probes (**1**) and (c, d, e) duplexed with complementary oligonucleotides (**2**), 1.5μM, for 30, 90, 120mins respectively. The frequency range from 10mHz to 20kHz at an applied constant bias potential of +0.17V, with amplitude of alternating voltage at 10mV in 10mM PBS buffer, pH 7.0.....254
- Figure 8.14.** Cyclic voltammograms of Ru(bpy)<sub>3</sub><sup>2+</sup> (30μM) in 50mM phosphate buffer at pH 7 with 700mM NaCl at 25mVs<sup>-1</sup>: When Au-MWNT μ-electrode is modified with (a) MCH only,

(b) complementary *ss*-oligonucleotide (**2'**), (c) 2 mismatched *ss*-oligonucleotide (**3'**) and (d) single mismatched *ss*-oligonucleotide (**4'**). .....256

**Figure 8.15.** AC voltammetry measurements for Au-MWNT  $\mu$ -electrode (a) functionalized with probe oligonucleotides (**1**), (b) hybridized with complementary oligonucleotides (**2**), (c) with 2-mismatched target oligonucleotides (**3**) and (d) with 1-mismatched target oligonucleotides (**4**). ACVs are conducted with a sinusoidal wave of 5Hz and 10mV amplitude. *Inset*: Repeated ACV measurements for each oligonucleotide whereby the  $\mu$ -electrode is always loaded with fresh Au-MWNT powder.....258

**Figure 9.1.** SEM images of (a) purified SWNT, (b) milled SWNT without KOH, and (c) functionalized SWNToh which was cast from a methanol suspension and bundles of tubes can be seen protruding from the clusters.....265

**Figure 9.2.** (a) Deconvolved core-level XPS *C1s* spectrum of SWNToh. *Inset*: Normalized core-level *C1s* spectra of pristine SWNT and SWNToh. (b) The *C1s* photoelectron energy-loss spectra for SWNT (solid line) and SWNToh (dotted line). *Energy-loss spectra have been normalized to C1s main peak and relocated with the loss energy of the main peaks all being zero*.....266

**Figure 9.3.** (a) FTIR of SWNToh functionalized with hydroxyl groups. (b) UV-vis-NIR spectra of pristine SWNT (solid line) and SWNToh (dotted line). (c) Raman scattering spectra of pristine SWNT (solid line) and SWNToh (dotted line). *Inset*: RBM signals of pristine SWNT. *The spectra have been scaled so that the strongest  $\omega^+_G$  peaks have the same intensity to elucidate the upshift of  $\omega^+_G$  peaks*.....267

**Figure 9.4.** (a) UPS He II (40.8eV) valence band spectra of pristine SWNT (solid line) and SWNToh (dotted line). (b) UPS He I (21.2eV) secondary electron tail threshold and the Fermi level for pristine SWNT (solid line) and SWNToh (dotted line).....269

**Figure 9.5.** Optical limiting responses to 7ns, 532nm optical pulses of pristine SWNT (ooo) and SWNToh (▲▲▲) in aqueous medium.....272

**Figure 9.6.** (a) Raman spectrum and (b) TEM images of ODA-MWNT sample.....275

**Figure 9.7.** Gravitation-dependant, thermally-induced self-diffraction in carbon nanotubes solutions. (a) and (b) Schematic diagrams of two experimental set-ups. (c) and (d) Diffraction patterns recorded at 532nm with the set-ups shown in (a) and (b) respectively. (e) and (f) Diffraction patterns observed at 780nm with setups shown in (a) and (b) respectively. The input laser power used were  $\sim 100$ mW.....276

**Figure 9.8.** Far-field distribution of the transmitted irradiance measured at 780nm at different laser powers. The transmittance of the CNT solution is 85.2%. The half angle is defined as the ratio of the  $x'$ -coordinate on the observation screen to the distance of the  $z$ . The opened symbols denote experimental data. The results of left and right panels correspond to experimental setup I and II respectively. The solid lines of the left and right panels are the numerical simulations using Eqs [9.1 & 9.2] and Eqs [9.3 & 9.4] respectively.....277

**Figure 9.9.** Far-field distribution of the transmitted irradiance recorded at 780nm and in incident power of 9mW with different CNT solution concentrations. The opened symbols denote experimental data and the solid lines are the numerical simulations using Eqs [9.1 & 9.2].....278

**LIST OF TABLES**

<b>Table 2.1.</b> Fundamental properties of carbon nanotubes as reported in literature [29].....	11
<b>Table 2.2.</b> Comparison of threshold electric field values for different materials at 10mA/cm <sup>2</sup> current density <sup>44, 45</sup> .....	17
<b>Table 3.1.</b> Geometrical parameters for the ideally rolled graphene sheet and for the relaxed configuration using different nonlocal functionals. The parameters are defined as in Fig 3.1. All length units are in angstrom.....	29
<b>Table 3.2.</b> Deformation ( $\delta$ ), IP values and magnetic moment ( $\mu_B$ ) of nitrogenated SWNTs.....	47
<b>Table 3.3.</b> Formation energies of N-substituted and pyridine-like doped SWNTs.....	47
<b>Table 3.4.</b> Adsorption energies of chemisorbed N adatoms and $-NH_2$ on SWNTs.....	48
<b>Table 3.5.</b> Relaxed zigzag (10,0) SWNTs with two chemisorbed N adatoms.....	62
<b>Table 3.6.</b> Relaxed armchair (5,5) SWNTs with two chemisorbed N adatoms.....	63
<b>Table 3.7.</b> Comparison of adsorption energy <sup>†</sup> (meV) for a H <sub>2</sub> molecule physisorbed on a graphene sheet and various carbon nanotubes. Adsorption sites A, B, C, D, E, and groove, pore, IC are defined as in Fig 3.21 and Fig 3.25 respectively.....	97
<b>Table 4.1.</b> Composition of catalysts used for the synthesis of CNT.....	107
<b>Table 4.2.</b> Detailed lineshape analysis of the tangential G-band of the purified SWNT (0.83nm < d <sub>t</sub> < 1.24nm). The peak positions ( $\omega$ ) and FWHM ( $\Gamma$ ) are listed for the Lorentzian lineshapes, and (1/q) value is given for the BWF lineshapes.....	120
<b>Table 7.1.</b> Adsorptive parameters of modified and pristine carbon nanotube samples.....	173
<b>Table 7.2.</b> Adsorptive parameters of bulk TiO <sub>2</sub> and titania nanotubes.....	183
<b>Table 7.3.</b> Adsorptive parameters of BN nanotubes and bulk BN.....	191
<b>Table 7.4.</b> A comparison of H <sub>2</sub> uptake by various nanostructured materials.....	199



**LIST OF PUBLICATIONS**

1. S.H. Lim, J. Wei, J. Lin, *Electrochemical genosensing properties of gold nanoparticle-carbon nanotube hybrid*. Chem. Phys. Lett. 400, 578 (2004).
2. S.H. Lim, J. Wei, J. Lin, Q. Li, J.K. You, *A glucose biosensor based on electrodeposition of palladium nanoparticles and glucose oxidase onto Nafion-solubilized carbon nanotube electrode*. Biosens. & Bioelectrons. 20, 2341 (2005).
3. S.H. Lim, J. Luo, Z. Zhong, W. Ji, J. Lin, *Room-temperature hydrogen uptake by TiO<sub>2</sub> nanotubes*. Inorg. Chem. 44, 4124 (2005)
4. S.H. Lim, H.I. Elim, X.Y. Gao, A.T.S. Wee, W. Ji, J.Y. Lee, J. Lin, *Electronic and optical properties of nitrogen-doped multiwalled carbon nanotubes*. Phys. Rev. B. 73, 045402 (2006).  
This article was also published in the January 16, 2006 issue 2 of the Virtual Journal of Nanoscale Science & Technology ([www.vjnano.org](http://www.vjnano.org)).  
This article was also published in the February, 2006 issue 2 of the Virtual Journal of Ultrafast Science ([www.vjultrafast.org](http://www.vjultrafast.org)).
5. S.H. Lim, J. Luo, Ji. J. J. Lin, *Synthesis of boron nitride nanotubes and its hydrogen uptake*. Catal. Today 120, 346 (2007)
6. S.H. Lim, J. Luo, W. Ji, J. Lin, *Chemically modified carbon nanotubes with improved H<sub>2</sub> storage*. (in preparation).
7. S.H. Lim, W. Ji, J. Lin, *Controlling the synthetic pathways of TiO<sub>2</sub>-derived nanostructured materials*. J. Nanosci. Nanotech. 7, 1 (2007).
8. S.H. Lim, R. Li, W. Ji, J. Lin, *Effects of nitrogenation on single-walled carbon nanotubes within density functional theory*. Phys. Rev. B. 76, 195406 (2007).
9. S.H. Lim, W. Ji, J. Lin, *First-principles study of carbon nanotubes with bamboo-shape and pentagon-pentagon fusion defects*. J. Nanosci. Nanotech. 8, 1 (2007).
10. S.H. Lim, J.Y. Lin, Y.W. Zhu, C.H. Sow, W. Ji, *Synthesis, characterizations, and field emission studies of crystalline Na<sub>2</sub>V<sub>6</sub>O<sub>16</sub> nanobelt paper*. J. Appl. Phy. 100, 016106 (2006).
11. H. Pan, Zhu Y.W. Z.H. Ni, H. Sun, C. Poh, S.H. Lim, C. Sow, Z.X. Shen, Y.P. Feng, J.Y. Lin, *Optical and field emission properties of zinc oxide nanostructures*. J. Nanosci. Nanotech. 5, 1683 (2005).
12. V.G. Pol, S.V. Pol, A. Gedanken, S.H. Lim, Z. Zhong, J. Lin, *Thermal decomposition of commercial silicone oil to produce high yield high surface area SiC nanorods*. J. Phys. Chem. B. 110, 11237 (2006).
13. W. Ji, W. Chen, S.H. Lim, J. Lin, Z. Guo, *Gravitation-dependent, thermally-induced self-diffraction in carbon nanotube solutions*. Optics Express, 14, 8958 (2006).

## Chapter 1. Introduction

### 1.1. Motivation

The study of one-dimensional carbon nanotube (CNT) is greatly motivated by its unique properties that make them an interesting and potentially useful material. Carbon nanotubes have a wide range of potential applications, which include energy and data storage, chemical sensors, novel electronic devices, and reinforcing agents (see Chapter 2, page 11). A comprehensive study of carbon nanotube syntheses and characterizations become important steps in order for its applications to become viable. Designing CNT-based materials and devices often requires the control of properties of carbon nanotubes. In particular, modification of carbon nanotubes is desirable so that its properties can be tuned specifically for an application. Strategies to modify the properties of carbon nanotubes include sidewall covalent chemistry, substitutional doping with nonmetals (e.g. boron and nitrogen atoms), transition metal doping, alkali metal / halogen intercalation, adsorption of organic molecules, encapsulation of fullerenes and clusters, and topological defects of the carbon network<sup>1</sup>. For examples, pristine carbon nanotubes are hydrophobic and it does not disperse in organic solvents and water but sidewall functionalization of CNT renders it soluble in organic solvents and water. CNT solutions can be made into transparent thin film electrodes with electrical conductivity comparable to indium tin oxide (ITO) film electrodes<sup>2</sup>. The work function of carbon nanotube is reduced upon alkali-metal intercalations and this is beneficial to field emission. Indeed Wadhawan et al.<sup>3</sup> reported that the turn-on field for the field emission of Cs-intercalated CNT bundles is reduced by a factor of 2.1-2.8 while the emission current is enhanced by 6 orders of magnitude. As illustrated by these examples, the study of modified carbon nanotubes is an important step toward its application.

Hence, with these motivations, the modifications and applications of carbon nanotubes were conducted in this thesis.

## **1.2. Objectives**

In the present thesis pristine carbon nanotubes including single-walled CNT (SWNT) and multiwalled CNT (MWNT) were synthesized and studied in details. More importantly, modifications of CNTs have been conducted to understand and compare their properties with pristine carbon nanotubes to explore the possible applications. These include:

- a) Nitrogen doping to modify the electronic and optical properties of carbon nanotubes. The application of nitrogen-doped carbon nanotube as ultrafast saturable absorber is explored.
- b) Potassium hydroxide activation to modify the pore structures of carbon nanotubes. The application of KOH-activated CNTs and N-doped CNTs for hydrogen storage is studied. Two nanostructured inorganic fullerenes: TiO<sub>2</sub> and BN nanotubes have also been synthesized and investigated. They have shown better H<sub>2</sub> storage than carbon nanotubes.
- c) Decoration of carbon nanotubes with metallic nanoparticles and enzymes, for the application of these CNT/metal hybrids as biosensors.
- d) Functionalization of carbon nanotubes to modify their chemical properties. The functionalized CNTs become soluble in organic solvents or water. An interesting phenomenon of self-diffraction was observed for the CNTs dissolved in toluene.
- e) Growth of vertically aligned CNTs for microelectronic interconnect application

Besides experimental study of carbon nanotubes' modification and application, modeling of modified single-walled carbon nanotubes was also carried out using *ab initio* methods. These theoretical studies are focused on the simulation of fundamental properties of the SWNTs, including the electronic density of states and band structures, optical spectra, defect structures, and H<sub>2</sub> storage etc. They include:

- a) A first-principles study of ultra-small (diameter  $\sim 4\text{\AA}$ ) single-walled carbon nanotubes within DFT framework. The study of these  $4\text{\AA}$  nanotubes was chosen because its properties are markedly different from larger diameter nanotubes (diameter  $\sim 10\text{\AA}$  and above). The effects of Stone-Wales defects on the electronic properties of  $4\text{\AA}$  carbon nanotubes are also investigated.
- b) A first-principles study of various nitrogenated single-walled carbon nanotubes. This theoretical study of nitrogenated SWNTs is to complement the experimental studies and provide atomistic insights into the effect of nitrogen dopants on the electronic, magnetic, optical and field-emission properties of SWNT.
- c) A first-principles study of bamboo-shaped SWNTs to understand their electronic properties and chemical reactivity.
- d) A Universal forcefield (UFF) study of the  $\text{H}_2$ -SWNT interactions, which involves a Lennard-Jones potential to account for van der Waals interactions. Monte Carlo simulations are used to estimate the weight percentage of the  $\text{H}_2$  uptakes by SWNT bundles.

### **1.3. Methodology**

Single-walled and multi-walled carbon nanotubes were synthesized via decomposition of  $\text{CH}_4$  over cobalt-molybdenum catalysts. The as-synthesized carbon nanotubes were purified using a 5-step purification process. Vertically aligned carbon nanotubes (both MWNT and SWNT) were synthesized on patterned Fe catalysts on silicon substrates, using plasma-enhanced chemical vapor deposition method.  $\text{TiO}_2$ -derived nanotubes and BN nanotubes were synthesized using a hydrothermal and catalyzed mechano-chemical method respectively. These nano-materials were characterized using a wide range of methods: electron microscopes, photoelectron spectroscopy, Raman and Fourier-transform Infrared spectroscopies, x-ray absorption spectroscopy, x-ray diffraction, thermal-gravimetric analysis, and nitrogen adsorption isotherm at 77K.

*Ab initio* calculations of SWNTs were conducted using various modules available in the commercial software, Materials Studio (Accelrys Inc). Specifically, density functional theory (DFT) calculations were performed with DMol<sup>3</sup> and CASTEP modules. The Forcite module and Universal forcefield were used for molecular mechanics calculations. Monte Carlo simulations were carried with Sorption modules and Universal forcefield.

#### **1.4. Thesis outline**

Chapter 1 presents the motivation, scope, objectives and methodologies of the thesis. The properties and potential applications of SWNTs which have been reported in literature were briefly reviewed in Chapter 2, the literature background. The results of my theoretical studies of single-walled carbon nanotubes are collected in Chapter 3. Chapter 4 describes the synthesis, characterizations and formation mechanism of pristine carbon nanotubes using chemical vapor deposition. Chapter 5 studies the growth of vertically aligned carbon nanotubes (VACNTs), using plasma-enhanced chemical vapor deposition, and their potential application as microelectronic interconnect. Chapter 6 investigates experimentally the modification of CNT by nitrogen-dopants carbon nanotubes and how this affects its electronic and optical properties. The pore structure modification of carbon nanotubes and its hydrogen storage are described in Chapter 7. The kinetics and mechanism of H<sub>2</sub> adsorption on modified carbon nanotubes, TiO<sub>2</sub> and BN nanotubes are also presented in this chapter. Chapter 8 is devoted to the studies of the CNT / nano metal / enzymes hybrid and its application as biosensors. Chapter 9 focuses on hydroxyl (-OH) and octadecylamine (CH<sub>3</sub>(CH<sub>2</sub>)<sub>17</sub>NH<sub>2</sub>, -ODA) functionalized carbon nanotubes. Chapter 10 gives the conclusion of the thesis.

### **References**

- [1] J.J. Zhao, R.H. Xie, J. Nanosci. Nanotech. 3, 459 (2003).
- [2] Z. Wu, Z. Chen, X. Du, J.M. Logan, J. Sippel, M. Nikolou, K. Kamaras, J.R. Reynolds, D.B. Tanner, A.F. Hebard, A.G. Rinzler, Science 305, 1273 (2004).
- [3] A. Wadhawan, R.E. Stallcup, J.M. Perez, Appl. Phys. Lett. 78, 108 (2001).

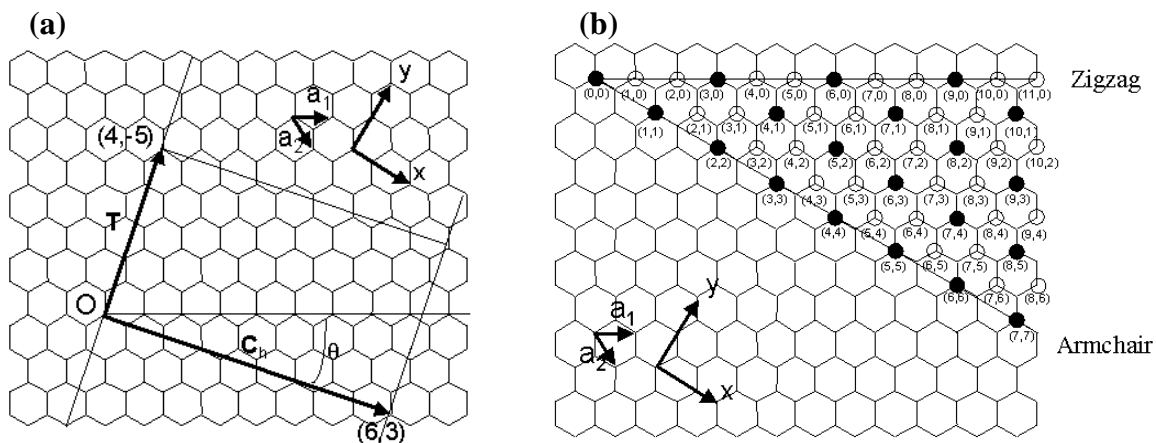
## Chapter 2. Literature Background

### **2.1. Fundamentals of single-walled carbon nanotubes**

Since S. Iijima<sup>1</sup> reported the observation of multi-walled carbon nanotubes (MWNT) in arc discharge soot, tremendous amounts of research had focused on the synthetic methods, characterizations, formation mechanism, chemical modifications and potential applications<sup>2-6</sup>. The synthesis of single-walled carbon nanotube (SWNT) was demonstrated via a laser ablation technique<sup>7</sup>. Thus the molecular SWNT is considered as a new advanced form of carbon and a sister material of C<sub>60</sub>. Carbon nanotube has also been considered as a distinct form of carbon allotrope such as graphite and diamond. This is followed by the emergence of other fascinating nanostructured carbon such as nanoscrolls<sup>8</sup>, nanohorns<sup>9</sup>, nanowalls<sup>10</sup>, nanoballs<sup>11</sup> and nanographite ribbons<sup>12</sup>.

A single-walled carbon nanotube can be visualized as a cylindrically folded and seamless graphene sheet. High-resolution transmission electron microscopy (TEM) and scanning tunneling microscopy<sup>1,13</sup> (STM) provide direct experimental evidence that the nanotubes are seamless cylinders derived from a honeycomb lattice of carbon. The unusual properties of SWNTs arise from the strong covalent C-C bonds, a unique one-dimensional structure and nanometer-size. These properties include a high axial Young's modulus, high thermal conductivity, the presence of hollow structures that can be used as nanosized test tubes and ultrafiltration membranes, and electronic conductivities that vary from metallic to semiconducting. Metallic SWNTs are model systems for studying rich quantum phenomena such as ballistic transport<sup>14</sup>, single-electron charging<sup>15</sup>, Luttinger liquid<sup>16</sup>, weak localization and quantum interference<sup>17</sup>. Semiconducting SWNTs have been employed to fabricate nanotube-based electronics such as transistors and logic<sup>18-20</sup>, memory and sensory devices<sup>21-23</sup>.

The structure of a SWNT is suitably explained by the vectors  $C_h$  and  $T$  in Figure 2.1. The circumference of any SWNT is expressed in terms of the chiral vector  $C_h = n\hat{a}_1 + m\hat{a}_2$ , which connects two crystallographically equivalent sites on the 2D graphene sheet (see Figure 2.1a). The pair of integers  $(n,m)$  uniquely specify the chiral vector for the construction of SWNT. Figure 2.1a shows the chiral angle  $\theta$  between the chiral vector  $C_h$  and the ‘zigzag’ direction ( $\theta = 0$ ), and the unit vectors  $\hat{a}_1$  and  $\hat{a}_2$  of the graphitic carbon honeycomb.



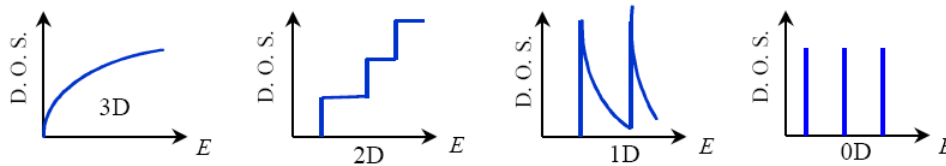
**Figure 2.1.** (a) Definition of chiral vector,  $C_h$ , in a hexagonal lattice of carbon atoms by unit vectors  $\hat{a}_1$  and  $\hat{a}_2$ , and chiral angle  $\theta$  with respect to the zigzag axis (i.e.  $\theta=0$ ). (b) Possible vectors specified by pairs of integers  $(n,m)$  for general CNTs. A solid point represents metallic nanotube and an open circle represents semiconductor nanotubes. The condition for the metallic nanotube is:  $2n+m=3q$  ( $q$ : integer), or  $(n-m)/3$  is integer.

Figure 2.1b illustrates three distinct types of nanotubular structures that can be constructed by rolling up the graphene sheet into a cylinder. The zigzag and armchair nanotubes correspond to chiral angles of  $\theta=0$  and  $30^\circ$  respectively. For  $0<\theta<30^\circ$ , the nanotubes are called chiral nanotubes. The translation vector  $T$  is obtained from the intersection with the first lattice point of the honeycomb lattice. The unit cell of the 1D lattice is the rectangle defined by the vectors  $C_h$  and  $T$ .



Multi-walled carbon nanotubes contain several coaxial cylinders, each cylinder being a single-walled carbon nanotube. The interlayer spacing of MWNTs is  $\sim 0.34\text{nm}$ , which is very close to that of graphite. Both experimental<sup>8a</sup> and theoretical considerations<sup>8b</sup> have also supported a scroll structure as an alternative structure of MWNT. The indexing of SWNTs has been extended to other tubular structures such as  $\text{BC}_3$ ,  $\text{BC}_2\text{N}$ ,  $\text{CN}$ ,  $\text{C}_3\text{N}_4$  and  $\text{Si}$  nanotubes<sup>24-27</sup>. The nomenclature is similar to that of carbon nanotubes.

Figure 2.2 shows the electronics density of states for a 3D (e.g. bulk graphite (semi-metallic)), 2D (e.g. graphene sheet), 1D (e.g. nanotube / nanowire) and 0D (e.g.  $\text{C}_{60}$  / quantum dots) entities. Figure 2.2 clearly demonstrates that the electronic properties of nanostructured materials are fundamentally different from its bulk counterparts, which are mainly due to the reduced dimensionality. The unique electronic properties of nanostructured materials can be exploited to fabricate novel electronic devices<sup>28</sup>.



**Figure 2.2.** Typical density of states (DOS) for 3D, 2D, 1D and 0D entities.

M. S. Dresselhaus and co-workers<sup>29</sup> have employed a simple tight binding calculation to elucidate the electronic properties of SWNTs with different chiralities and diameters. Figure 2.3 shows the calculated density of states (DOS) for various zigzag, armchair and chiral nanotubes by the tight binding methods<sup>30</sup>. For pedagogic purposes, I have selected a few examples to illustrate the geometry-dependent properties of SWNTs.

In general the electronic structures of SWNTs possess spike-like electronic density of states (known as von Hove Singularities). This strongly implies that optical transitions between

these spike-like states are very likely to occur (at least for the first and second von Hove Singularities). Indeed, optical absorption<sup>31</sup> (from  $\sim 1400\text{nm}$ - $400\text{nm}$ ), resonance Raman scatterings<sup>32</sup>, and photoluminescence spectroscopy<sup>33</sup> (for semiconducting tubes) of SWNTs have been studied and ascribed to the transition between these von Hove Singularities.

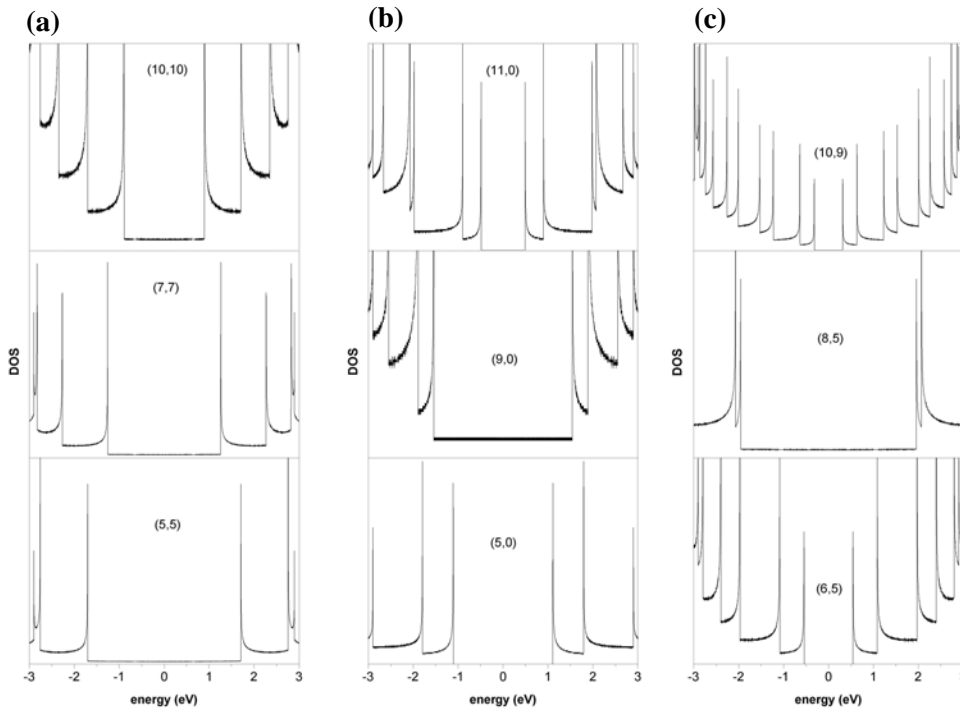


**Figure 2.3.** Electronic density of states column (a) armchair nanotubes, (b) zigzag nanotubes, and (c) chiral nanotubes calculated by tight binding theory<sup>30</sup>.

For armchair ( $m,m$ ) nanotubes, tight binding calculations reveal that the electronic density of states (DOS) at the Fermi level is finite, which is due to the crossing of two 1D energy bands at degenerate points of the 2D graphite energy band structure. An expanded view of (10,10) nanotube shows that the DOS is finite at the Fermi level (Figure 2.3 column (a), top most panel), and therefore the electronic properties of armchair nanotubes are expected to be metallic.

On the basis of Figure 2.3b, in contrast, zigzag ( $m,0$ ) nanotubes ( $m$  is not divisible 3) have empty DOS at the Fermi level, and these nanotubes (e.g. (5,0) and (11,0)) are semi-conducting in

nature. While for zigzag  $(n,0)$  nanotubes ( $n$  is divisible by 3) the DOS at the Fermi level is finite and therefore this types of zigzag nanotubes (e.g.  $(9,0)$ ) are metallic in nature.

For chiral nanotubes  $(m,n)$  ( $m \neq n$  and  $(m-n)$  is not divisible by 3) the DOS at the Fermi level is empty and therefore these nanotubes (e.g.  $(6,5)$  and  $(10,9)$ ) are semiconducting. For chiral nanotubes  $(m,n)$  ( $m \neq n$  and  $(m-n)$  is divisible by 3) the DOS at the Fermi level is finite and therefore these nanotubes (e.g.  $(8,5)$ ) are metallic. Upon closer inspection, the first and second von Hove Singularities of  $(8,5)$  nanotube are very close together, compared to the DOS of  $(9,0)$  and  $(10,10)$  nanotubes. Detailed Raman experiments have shown that for these metallic chiral nanotubes the characteristic radial breathing mode (RBM) split into a slightly higher and lower frequency (see Chapter 4, Figure 4.8, Page 113 and ref [32]). Thus SWNT provide a real physical system for the study of effects of reduced dimensionality.

Within tight binding scheme, it was found that armchair nanotubes  $(m,m)$  and zigzag  $(n,m)$  with  $n-m$  being a multiple of 3 are metallic. This relation is known as the 1/3 rule. The band gap of the remaining 2/3 semiconducting nanotubes is inversely proportional to the diameter of the nanotube. In other words, the smaller diameter nanotubes possess a larger band gap (compared to the band gaps of  $(5,0)$  and  $(11,0)$  nanotubes, Fig 2.3b). The simple tight binding scheme, which considers  $2p\pi$ -electrons only, works reasonably well for nanotubes with an average diameter of  $10\text{\AA}$  or greater, and the effect of  $\sigma$ - $\pi$  hybridization is not taken into consideration. Recent first-principles studies<sup>34</sup> on ultra-small  $4\text{\AA}$  SWNTs (such as  $(4,2)$ ,  $(5,0)$ , and  $(3,3)$  nanotubes) showed that  $(5,0)$  is metallic instead of semiconducting as predicted by the tight binding scheme. The metallicity of  $(5,0)$  tubes is attributed to the  $\sigma^*$  and  $\pi^*$  mixing induced by the large curvature of the tube. Additionally,  $(4,2)$  tube possesses a small indirect band gap of  $\sim 0.2\text{eV}$ , instead of the expected large direct band gap. Since the effects of  $\sigma$ -electrons are normally ignored for tight binding calculations, and therefore the theory fail to predict accurately the electronic properties of small radii nanotubes.

## **2.2. Potential applications of carbon nanotubes**

### *Fundamental properties of carbon nanotubes*

Table 2.1 summarizes the fundamental properties of carbon nanotubes which are relevant to technological applications. The outstanding electrical and thermal properties of carbon nanotubes immediately imply that CNTs are ideal candidates for future electronic devices and heat dissipaters. For example, the current density of CNT bundles is  $\sim 10^7 \text{ A/cm}^2$  which is superior to that of a copper wire of  $\sim 10^5 \text{ A/cm}^2$ . The excellent mechanical properties and lightweight of carbon makes CNTs ideal candidates for reinforcement of various materials. Section 2.2 reviews major technological advances brought about by the studies and applications of carbon nanotubes.

**Table 2.1.** Fundamental properties of carbon nanotubes as reported in literature [29].

<b><u>Optical gap</u></b>	
For (n, m); n-m is divisible by 3 [Metallic]	0eV
For (n, m); n-m is not divisible by 3 [Semi-Conducting]	$\sim 0.5\text{eV}$
<b><u>Electrical transport</u></b>	
Conductance quantization	$n \times (12.9\text{k}\Omega)^{-1}$
Resistivity	$10^{-4}\Omega\text{cm}$
Maximum current density	$10^{13}\text{A/m}^2$
<b><u>Thermal transport</u></b>	
Thermal conductivity (298K)	$\sim 2000\text{W/mK}$
Phonon mean free path	$\sim 100\text{nm}$
Relaxation time	10ps
<b><u>Elastic behavior</u></b>	
Young's modulus (SWNT)	$\sim 1\text{TPa}$
Young's modulus (MWNT)	1.28TPa
Maximum tensile strength	30GPa

### **2.2.1. CNT-based electronic devices**

Future transistors involve the development of molecular electronics whereby the active components is composed of a single or a few molecules. The unique properties of single-walled carbon nanotubes are most suitable for the development of nano-transistors, particularly field-effect transistors. In addition CNTs do not have interface states and can be integrated with high  $\epsilon$ -



At each cross point in the array, the suspended SWNT can be in either the separated OFF mode or the ON mode in contact with the lower perpendicular SWNT. Voltage pulses can be used to manipulate the suspended SWNT to activate the ON / OFF mode.

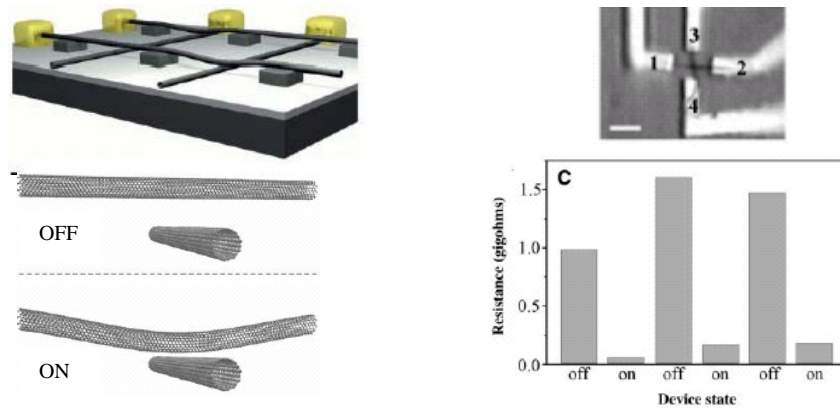


**Figure 2.5.** (Left panel) A schematic view of a suspended SWNT crossbar array with support structures<sup>21</sup>. SWNT can be switched OFF / ON by charging it with electrostatic forces. (Right panel) Experimental switching of crossed SWNTs device<sup>21</sup> between OFF and ON states with a resistance ratio  $\sim 10$ .

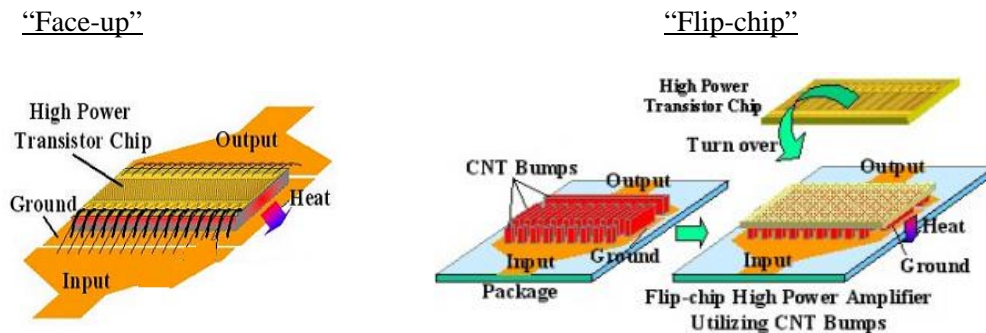


**Figure 2.6.** (Left panel) Conventional “face-up” structure of a transistor chip wire-bonded to the circuit board and heat dissipation is simply due to contact. (Right panel) A “flip-chip” design adopted by Fujitsu, which incorporates CNT bumps to connect the transistor chip and the circuit board<sup>36</sup>.

As the volume of information transmission continues to increase, higher power and higher frequencies in amplifiers used in mobile communication systems are much sought after. Heat dissipation for high power transistors, which is an output source for high-performance amplifier and generates high amount of heat, is a vital issue for performance. A “flip-chip”

structure, which connects the inverted transistor electrode and the package electrode with short metallic bumps (made of gold or other metals) offers improved heat dissipation than the conventional “face-up structure” (see Fig 2.6). However, the use of high power amplification, the metallic bumps are still inadequate in dissipating high level of heat generated by high-power transistors. Fujitsu Limited and Fujitsu Laboratories Ltd<sup>36</sup> have succeeded in the development of carbon nanotube-based heatsinks for semiconductor chips (see Fig 2.6). Taking advantage of the excellent thermal conductivity of CNT (~2000W/mK), such CNT heatsink is capable of achieving high-frequency high power amplification and heat dissipation simultaneously, which is vital for the realization of high-performance amplifiers with high frequency and power for next-generation mobile communication systems.

### **2.2.2. Spinning of CNT thread**

High quality and large quantity of carbon nanotubes can be synthesized quite easily using chemical vapor deposition (CVD) methods. However the lengths of the CNTs are usually tens of micrometers. Recently vertically aligned CNT with height of millimeters have been synthesized using plasma-enhanced CVD in the presence of very low concentration of oxygen-containing impurities such as H<sub>2</sub>O and O<sub>2</sub><sup>37</sup>. The role of these oxygen-containing impurities has been hypothesized to sustain the activity of the catalysts by etching away amorphous carbon, so that very long synthesis times are possible.

Zhu et al.<sup>38</sup> applied a floating catalyst CVD technique (ferroene + thiophene + *n*-hexane) to synthesize CNT and the resulting product contains centimeter-long CNT. Li et al.<sup>39</sup> has also synthesized centimeter-long CNT using a unique winding geometry CVD chamber (see Fig 2.7), whereby the CNT thread is collected from the hot reaction zone using a rotating collector during the synthesis. The feedstock, a mixture of ferroene, thiophene and ethanol, is sprayed into the reaction zone. The winding geometry CVD offers the possibility of continuous spinning of

ultralong CNT thread, which can be optimally spun up to a few meters in length, and it has great potential applications.

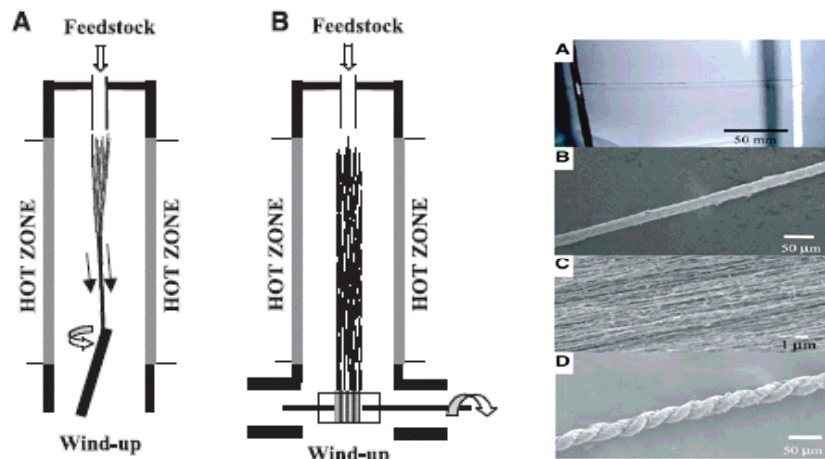


**Figure 2.7.** (Left panel) Schematic setup of the winding geometry CVD chamber used by Li et al.<sup>39</sup> for spinning CNT thread. (Right panel) The CNT thread is composed of intertwined carbon nanotubes.

The National Aeronautics and Space Administration (NASA) of the United States has awarded Rice university US\$11 million contract to utilize carbon nanotube as electric power cable<sup>40</sup>. For an idealized CNT fiber assumed to consist of  $10^{14}$  CNT/cm<sup>2</sup>, the maximum current density of the CNT fiber is estimated to deliver  $100 \times 10^6$  A/cm<sup>2</sup>, with 5% tube-tube efficiency conduction, which is 100 times of the best low-temperature superconductors<sup>41</sup>. In addition, CNT fiber has negligible eddy current and is lightweight. Current power losses in transmission lines are about ~7%. If the power loss is cut by 1%, this will translate to an annual energy saving of  $4 \times 10^{10}$  KWh or an equivalent of 24 million barrels of oil per year. Thus the synthesis and utilization of ultralong CNT threads have tremendous technological impact.

### 2.2.3. Carbon nanotube-polymer composites

Qian et al.<sup>42</sup> have shown that an addition of 1wt% CNT resulted in a 25% increase in the tensile strength of polystyrene-based composite film. Dalton et al.<sup>43</sup> have successfully synthesized



100m long super-tough CNT composite (polyvinyl alcohol) fibers using an improved coagulation-based CNT spinning method, and also used these fibers to fabricate supercapacitors in the form of textiles (see Fig 2.8). The CNT composite fibers are  $\sim 50\mu\text{m}$  in diameter and compose of 60wt% of SWNTs with a tensile strength of 1.8Gpa, which matches that of spider silk. A comparison of the strength and failure strain for CNT composite fibers and 3000 materials in the database of Cambridge Materials Selector, indicates that the performance of CNT composite fibers are very promising and exceeds some the known materials in the database. Thus carbon nanotubes are very useful additives to strengthen the mechanical properties of polymers.

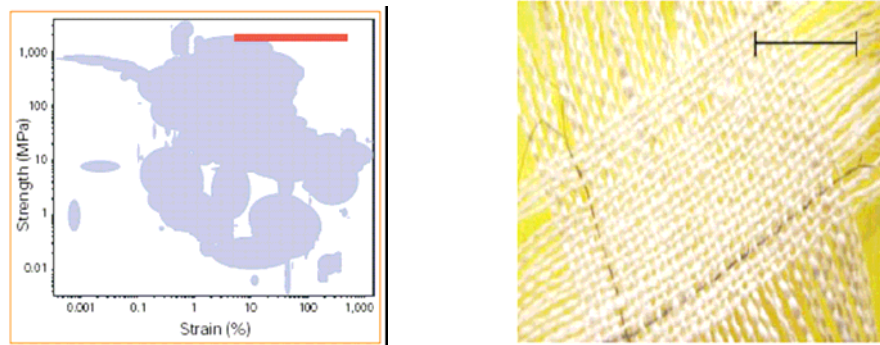


**Figure 2.8.** (Left panel) Comparison of strength and failure strain for various CNT-composite fibers and 3000 materials types in the Cambridge Materials Selector database<sup>43</sup>. (Right panel) A textile supercapacitor composed of 2 orthogonally directed CNT fibers. This CNT fiber supercapacitor provides a capacitance ( $5\text{Fg}^{-1}$ ) and energy storage density ( $0.6\text{Whkg}^{-1}$ ) that are comparable to commercial supercapacitor<sup>43</sup>.

#### 2.2.4. Field emission sources

In the field of vacuum microelectronics, field emission (FE) is an attractive alternative to thermionic emission for electron sources. Field emission is a quantum effect. Under the influence of a sufficiently high electric field, electrons near the Fermi level can overcome the barrier energy to escape to the vacuum level. The emission current from a surface is determined by the well-known Fowler-Nordheim equation:

$$I = \frac{A\gamma\beta^2V^2}{\phi d^2} \exp\left(\frac{-Bd\phi^{3/2}}{\beta V}\right) \equiv A'V^2 \exp(-B'/V) \quad [2.1]$$

where  $I$  is the current,  $V$  the applied voltage,  $d$  the spacing,  $\phi$  the work function,  $\gamma$  the effective emission area,  $\beta$  the enhancement factor,  $A$  and  $B$  are constants.

**Table 2.2.** Comparison of threshold electric field values for different materials at  $10\text{mA}/\text{cm}^2$  current density<sup>44, 45</sup>.

Materials	Threshold electrical field (V/ $\mu\text{m}$ )
Mo tips	50-100
Si tips	50-100
<i>p</i> -type semiconductor diamond	130
Undoped, defective CVD diamond	30-120
Amorphous diamond	20-40
Cs-coated diamond	20-30
Graphite powder (<1mm size)	17
Nanostructured diamond ( $\text{H}_2$ plasma treated)	3-5 (unstable > $30\text{mA}/\text{cm}^2$ )
Random SWNT film	1-3 (stable at $1\text{A}/\text{cm}^2$ )

Electron field emission materials have been widely studied for applications such as flat panel displays, electron guns in electron microscopes and microwave amplifiers. A current density of  $1\text{-}10\text{mA}/\text{cm}^2$  and  $>500\text{mA}/\text{cm}^2$  are required for displays and microwave amplifiers respectively. Table 2.2 shows the threshold electric field values for  $10\text{mA}/\text{cm}^2$  current density for different materials. Factors such as nanometer-size diameter, structural integrity, high electrical conductivity, chemical stability and lower threshold electric field make carbon nanotubes good electron emitters.

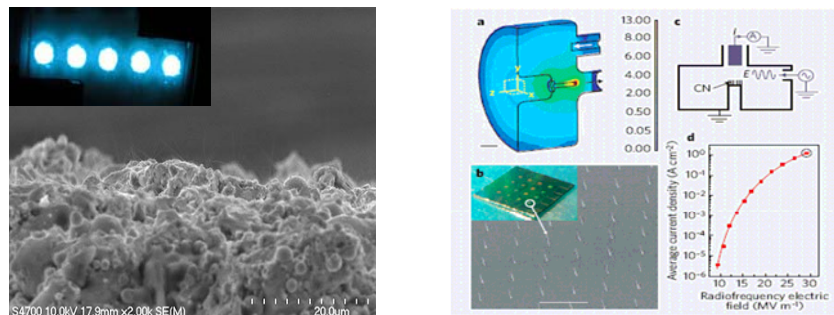


**Figure 2.9.** (Left panel) Randomly aligned CNT commercially available from Xintek Nanotechnology Innovations<sup>46</sup>. The inset shows bright and uniform emission sites by the CNT mats. (Right panel) Array of individual vertically aligned carbon nanofibers fabricated as a microwave diode<sup>47</sup>.

Figure 2.9 (left panel) shows commercially available carbon nanotube field emitters from Xintek Nanotechnology Innovations<sup>46</sup>. These CNTs are randomly aligned, and exhibited low onset electric field ( $\sim 1\text{V}/\mu\text{m}$ ) and stable electron emission ( $\sim 18\text{hours}$  at  $3\text{mA}/\text{cm}^2$ ). The oscillatory electric field component of an electromagnetic radiation has recently been demonstrated to cause electron emission from array of individual vertically aligned carbon nanofibers<sup>47</sup>. Teo et al.<sup>47</sup> has constructed a CNT-based microwave diode, whereby the field emission is driven by gigahertz (GHz) frequencies (see Fig 2.9 right panel). The performance of such carbon nanotube cathode is comparable to present-day microwave transmission devices.

### **2.2.5. CNT-modified AFM tips**

An ideal AFM tip should have a high aspect ratio with  $0^\circ$  cone angle, smallest possible radius curvature and a well-defined reproducible molecular structure. In addition, it should be mechanically and chemically robust and stable in different working environments. Hence, carbon nanotube is the most promising candidate probe for AFM imaging. A carbon nanotube modified AFM probe can be fabricated using CVD techniques<sup>48</sup>. Using carbon nanotube probes, biological structures have been investigated in the fields of amyloid-beta protein aggregation and chromatin remodeling<sup>48</sup>. Furthermore, the unique tip-group chemistry of CNT has been applied for chemical force microscopy and allowed single-molecule measurements<sup>48</sup>. Figure 2.10 shows a CNT-modified AFM tip commercially available from nanoScience Instruments<sup>49</sup>.

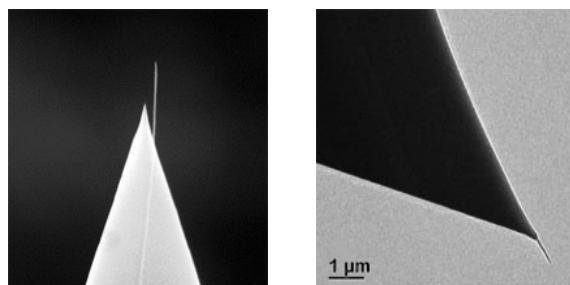


**Figure 2.10.** A CNT-modified AFM tip commercially available from nanoScience Instruments<sup>49</sup>.

### **2.2.6. Electrochemical applications**

Carbon is a widely used and preferred material for many electrochemical systems due to its rich surface chemistry, polymorphic structures, abundance (it is cheaper than metals) and good inertness in harsh acidic / alkaline media. Glassy carbon, carbon paste (crystalline graphite powder mixed with mineral oil and packed smoothly into a cavity), pyrolytic graphite, carbon felts and fibers are commonly used as laboratory electrodes. Carbon is also used as a support for electrocatalysts. Pt nanoparticles supported on carbon black are commonly used for fuel cell applications. Carbon materials are also employed as electrodes or as additive to enhance the electrical conductivity of electrodes in batteries. The electrochemistry of novel carbon materials such as nanostructured B-doped diamond, C<sub>60</sub>, and carbon nanotubes has also been widely studied. The use of CNT-based electrodes is particularly attractive, mainly due to the excellent electrical properties, faster electron transfer rate and suitable fabrication techniques (see Chapter 8, page 227 for the application of nanoparticle-CNT bioelectrodes).

### **2.2.7. Energy storage**

The unique tubular and bundle assembly of carbon nanotubes have been considered as very beneficial properties for energy storage. Specifically, the electrochemical lithium intercalations<sup>50</sup> and hydrogen storage<sup>51</sup> of carbon nanotubes are two important aspect of energy storage. For lithium or hydrogen storage, storage capacity can be augmented via the inter-shell van der Waals spaces, inter-tube channels and inner cavity of carbon nanotube, which has been proposed to be accessible for Li intercalation or H<sub>2</sub> storage. Although carbon nanotubes as Li-ion battery shows higher capacity and high-rate performance than graphite, the presence of voltage hysteresis and occasional irreversible Li storage are still undesirable. The field of hydrogen storage of carbon nanotubes still remains active but controversial. A wide discrepancy has been reported for the H<sub>2</sub> storage of carbon nanotube, reported values range from 65wt% to 0.1wt% storage<sup>51</sup>. Initial optimism about the high H<sub>2</sub> storage of carbon nanotubes is probably due to poor

characterization of carbon nanotubes and lack of understanding fundamental gas-solid interactions of carbon nanotubes and hydrogen molecules (see Chapter 3.4 for theoretical and chapter 7 for experimental studies of H<sub>2</sub> storage of carbon nanotubes).

## References

- [1] S. Iijima, *Nature (London)* 354, 56 (1991).
- [2] J.E. Fischer, *Acc. Chem. Res.* 35, 1079 (2002).
- [3] O. Zhou, H. Shimoda, B. Gao, S. Oh, L. Fleming, G. Yue, *Acc. Chem. Res.* 35, 1045 (2002).
- [4] S. Nyogi, M.A. Hamon, H. Hu, B. Zhao, P. Bhowmik, R. Sen, M.E. Itkis, R.C. Haddon, *Acc. Chem. Res.* 35, 1105 (2002).
- [5] R. Andrews, D. Jacques, D. Qian, T. Rantell, *Acc. Chem. Res.* 35, 1008 (2002).
- [6] H. Dai, *Acc. Chem. Res.* 35, 1035 (2002).
- [7] A. Thess, R. Lee, P. Nikolaev, H.J. Dai, P. Petit, C.H. Xu, Y. H. Lee, S.G. Kim, A.G. Rinzler, D.T. Colbert, G.E. Scuseria, D. Tomanek, J.E. Fischer, R.E. Smalley, *Science* 273, 483 (1996).
- [8] (a) L.M. Viculis, J.J. Mack, R.B. Kaner, *Science* 299, 1361 (2003); H. Shioyam, T. Akita, *Carbon* 41, 179 (2003). (b) H. Pan, Y. Feng, J. Lin, *Phys. Rev. B* 72, 085415 (2005).
- [9] S. Iijima, M. Yudasaka, R. Yamada, S. Bandow, K. Suenaga, F. Kokai, K. Takahashi, *Chem. Phys. Lett.* 309, 165 (1999).
- [10] Y.H. Wu, P.W. Qiao, T.C. Chong, Z.X. Shen, *Adv. Mater.* 14, 64 (2002).
- [11] S. Bandow and Y. Saito, *Jpn. J. Appl. Phys.* 32, 1677 (1993).
- [12] Y. Li, S. Xie, W. Zhou, D. Tang, X. Zou, Z. Liu, G. Wang, *Carbon* 39, 615 (2001).
- [13] T.W. Odom, J. Huang, P. Kim, C.M. Lieber, *Nature (London)* 39, 62 (1998).
- [14] C.T. White, T.N. Todorov, *Nature (London)* 393, 240 (1998).
- [15] M. T. Woodside, P. L. McEuen, *Science* 296, 1098 (2002).
- [16] M. Bockrath, D.H. Cobden, J. Lu, A.G. Rinzler, R.E. Smalley, L. Balents, P.L. McEuen, *Nature* 397, 598 (1999).
- [17] M. Ouyang, J. Huang, C.M. Lieber, *Phys. Rev. Lett.* 88, 066804 (2002).
- [18] R. Martel, T. Schmidt, H.R. Shea, T. Hertel, Ph. Avouris, *Appl. Phys. Lett.* 73, 2447 (1998).
- [19] S. Tan, S. Verschueren, C. Dekker, *Nature* 393, 49 (1998).
- [20] A. Bachtold, P. Hadley, T. Nakanishi, C. Dekker, *Science* 294, 1317 (2001).
- [21] T. Rueckes, K. Kim, E. Joselevich, G.Y. Tseng, C. Cheung, C.M. Lieber, *Science* 289, 94 (2000).
- [22] S. Ghosh, A.K. Sood, N. Kumar, *Science* 299, 1042 (2003).
- [23] J. Kong, N.R. Franklin, C. Zhou, M.G. Chapline, S. Peng, K. Cho, H. Dai, *Science* 287, 622 (2000).
- [24] Y. Miyamoto, A. Rubio, S.G. Louie, M.L. Cohen, *Phys. Rev. B* 50, 18360 (1994).
- [25] Y. Miyamoto, A. Rubio, M.L. Cohen, S.G. Louie, *Phys. Rev. B* 50, 4976 (1994).
- [26] Y. Miyamoto, M.L. Cohen, S.G. Louie, *Solid State Commun.* 102, 605 (1997).

- [27] X.B. Yang, J. Ni, Phys. Rev. B 72, 195426 (2005).
- [28] F. Leonard, J. Tersoff, Phys. Rev. Lett. 83, 5174 (1999).
- [29] R. Saito, M. Fujita, G. Dresselhaus, M.S. Dresselhaus, Appl. Phys. Lett. 60, 2204 (1992); R. Saito, G. Dresselhaus, M.S. Dresselhaus, Physical Properties of Carbon nanotubes (Imperial College Press, London, 1998); M.S. Dresselhaus, G. Dresselhaus, P. Avouris (Eds), Carbon Nanotubes: Synthesis, Structures, Properties, and Applications (Topics in Applied Physics Volume 80, Springer 2001).
- [30] Free online simulation; <http://msl.stanford.edu/>; <http://www.photon.t.u-tokyo.ac.jp/~maruyama/kataura/kataura.html#DOS>
- [31] S. Maruyama, Y. Miyauchi, Y. Murakami, S. Chiashi, New. J. Phys. 5, 149.1 (2003).
- [32] M.S. Dresselhaus, P.C. Eklund, Adv. Phys. 49, 705 (2000).
- [33] M.J. O'Connell, S.M. Bachilo, C.B. Huffman, V.C. Moore, M.S. Strano, E.H. Haroz, K.L. Rialon, P.J. Boul, W.H. Noon, C. Kittrell, J. Ma, R.H. Hauge, R.B. Weisman, R.E. Smalley, Science 297, 593 (2002).
- [34] H.J. Liu, C.T. Chan, Phys. Rev. B 66, 115415 (2002); M. Machon, S. Reich, C. Thomsen, D. Sanchez-Portal, P. Ordejon, Phys. Rev. B 66, 155410 (2002); K. Iyakutti, A. Bodapati, X. Peng, P. Keblinski, S.K. Nayak, Phys. Rev. B 73, 035413 (2006).
- [35] Z. Chen, J. Appenzeller, Y. Lin, J. Sippel-Oakley, A. G. Rinzler, J. Tang, S. J. Wind, P. M. Solomon, Ph. Avouris, Science 311, 1735 (2006).
- [36] <http://www.fujitsu.com/global/news/pr/archives/month/2005/20051205-01.html>
- [37] K. Hata, D.N. Futaba, K. Mizuno, T. Namai, M. Yumura, S. Iijima, Science 306, 1362 (2004); G. Zhang, D. Mann, L. Zhang, A. Javey, Y. Li, E. Yenilmez, Q. Wang, J.P. McVittie, Y. Nishi, J. Gibbons, H.J. Dai, PNAS 102, 16141 (2005).
- [38] H.W. Zhu, C.L. Xu, D.H. Wu, B.Q. Wei, R. Vajtai, P.M. Ajayan, Science 296, 884 (2002).
- [39] Y.L. Li, I.A. Kinloch, A.H. Windle, Science 304, 276 (2004).
- [40] <http://www.nasa.gov/centers/johnson/news/releases/J05-018.html>
- [41] Nanoscience Research for Energy Needs: Report of the National Nanotechnology Initiative Grand Challenge Workshop, March 16-18, 2004, Page 10.
- [42] D. Qian, E.C. Dickey, R. Andrews, T. Rantell, Appl. Phys. Lett. 76, 2868 (2000).
- [43] A.B. Dalton, S. Collins, E. Munoz, J.M. Razal, V.H. Ebron, J. P. Ferraris, J.N. Coleman, B.G. Kim, R.H. Baughman, Nature 423, 703 (2003).
- [44] W. Zhu, G. Kochanski, S. Jin, Science 282, 1471 (1998).

[45] C. Bower, O. Zhou, W. Zhu, A.G. Ramirez, G.P. Kochanski, S. Jin, Amorphous and nanostructured Carbon. J.P. Sullivan, J.R. Robertson, B.F. Coll, T.B. Allen, O. Zhou (Eds) Mater. Res. Soc. Symp. Proc. 593, 215 (2000).

[46] [www.xintek.com](http://www.xintek.com)

[47] K.B.K. Teo, E. Minoux, L. Hudanski, F. Peauger, J-P. Schnell, L. Gangloff, P. Legagneux, D. Dieumegard, G.A.J. Amaratunga, W. I. Milne, Nature 437, 968 (2005).

[48] J.H. Hafner, C.-L. Cheung, A.T. Woolley, C.M. Lieber, Prog. Biophys & Mol. Biol. 77, 73 (2001).

[49] [http://www.nanoscience.com/products/carbon\\_nanotube\\_probes\\_plus.html](http://www.nanoscience.com/products/carbon_nanotube_probes_plus.html)

[50] B. Gao, A. Kelinhammes, X.P. Tang, C. Bower, Y. Wu, O. Zhou, Chem. Phys. Lett. 307, 153 (1999).

[51] M. Hirscher, M. Becher, J. Nanosci. Nanotech. 3, 3 (2003).



## Chapter 3. Theoretical studies of carbon nanotubes

### *Summary*

The theoretical studies of carbon nanotubes were divided into the following sections: (3.1) First-principles study of ultra-small 4Å single-walled carbon nanotubes. (3.2) First-principles study of nitrogenated single-walled carbon nanotubes. (3.3) First-principles study of carbon nanotubes with bamboo-shape and pentagon-pentagon fusion defects. (3.4) Molecular simulations of carbon nanotube-H<sub>2</sub> interactions. Density functional theory (DFT) calculations were performed with Dmol<sup>3</sup> and CASTEP codes, while molecular mechanics (MM) and Metropolis Monte Carlo calculations were carried out using Universal forcefield-based Forcite and Sorption modules, respectively, available from Materials Studio.

### **3.1. First-principles study of ultra-small 4Å single-walled carbon nanotubes.**

#### *Introduction*

The classifications of single-walled carbon nanotubes as metal or semi-conductors were given on the basis of how the underlying graphitic band structure is “folded” (zone-folding scheme) when one applies the nanotube’s azimuthal periodic boundary conditions. Early theoretical work<sup>1</sup> showed that (n,m) nanotubes with n-m being a multiple of 3 are metallic. This relation is known as the 1/3 rule. The band gap of the remaining 2/3 semiconducting nanotubes is inversely proportional to the diameter of the nanotube. The hybridization of the graphitic  $\sigma$ ,  $\pi$ ,  $\pi^*$ , and  $\sigma^*$  states due to nanotube’s curvature was not fully appreciated, and the electronic states near the Fermi level were described mainly as  $\pi$  and  $\pi^*$  states within the zone folding scheme. Recently, the synthesis of single-walled carbon nanotubes within the channels of zeolite<sup>2</sup> ( $\text{AlPO}_4$ <sup>-5</sup> crystal with inner diameters of 7.3Å) constraints the nanotube diameter distribution to around 4Å, and three nanotube chiralities are identified: namely (3,3), (5,0) and (4,2) nanotubes. These ultra-small 4Å nanotubes are anticipated to possess properties which are markedly different from larger diameters (tens of angstrom) nanotubes. Below the temperature of 20K, these ultra-small 4Å nanotubes are reported to exhibit superconductivity behavior<sup>3</sup>. The extremely small radii of these nanotubes strongly suggest that simple zone-folding scheme, which ignores curvature effects and hybridization effects of  $\sigma$  and  $\pi$ , is inadequate to predict its electronic properties. Therefore, in this section 3.1 density-functional calculations are carried out to study the structural, electronic properties and optical properties of these ultra-small nanotubes. Currently there is a lack of report on these 4Å nanotubes with Stone-Wales defects, and therefore it would be interesting to study its electronic properties within DFT calculations.

### **3.1.1. Computational methods**

All geometrical optimizations and subsequent single-point energy calculations of (3,3), (5,0) and (4,2) nanotubes were carried out using the Dmol<sup>3</sup> code<sup>4</sup>. The generalized gradient approximation (GGA) proposed by Perdew, Burke and Ernzerhof (PBE)<sup>5</sup> is used for the exchange-correlation energy. Although it is reported that PBE functional provides reasonable bond lengths in molecular systems and good lattice constants in bulk solids<sup>6</sup>, the geometrical optimizations of the nanotubes have also been carried out with other nonlocal functionals (e.g. Perdew-Wang (PW91)<sup>7</sup>, Becke exchange plus Perdew correlation (BP)<sup>8</sup>, and Becke exchange plus Lee-Yang-Parr correlation (BLYP)<sup>9</sup>) available in the Dmol<sup>3</sup> code (see Table 3.1). Geometry optimizations are performed with the Broyden-Fletcher-Goldfarb-Shanno (BFGS) algorithm with convergence criterion of  $10^{-3}$  a.u. on gradient and displacement, and  $10^{-5}$  a.u. on the total energy and electron density. The core treatment is performed with DFT semi-local pseudopotentials (DSPP), and the electronic wave functions are expanded in a double-numeric polarized (DNP) basis set truncated at a real space cutoff of  $3.7\text{\AA}$ . Integrations in  $k$  space were performed over 16  $k$  points for (3,3) and (5,0) nanotubes and 3  $k$  points for (4,2) nanotube in the  $k_z$  direction. The unit cells of (3,3), (5,0) and (4,2) nanotubes contain 12, 20 and 56 carbon atoms respectively. A hexagonal lattice was used to simulate the single-walled nanotubes, with a wall-to-wall distance of at least  $8\text{\AA}$ , sufficient to avoid in-plane interactions between nanotubes in adjacent unit cells. The electronic properties of the fully relaxed  $4\text{\AA}$  nanotubes were compared with cylindrically folded (unrelaxed) nanotubes, which were generated by Materials Studios v4.0 software.

The optical properties, density of states (DOS) and simulated scanning tunneling microscopic (STM) images of SWNTs were also studied using the CASTEP code (Cambridge serial total energy package)<sup>10</sup>, which is a plane-wave basis DFT pseudopotential method. The ionic potentials are described by the ultrasoft nonlocal pseudopotential proposed by Vanderbilt<sup>11</sup> with energy cutoff of 310eV and the total energy was converged to  $1\times 10^{-5}$  eV/atom. The tunneling current is defined to first order as followed:

$$I = \frac{2\pi e}{\hbar} \sum_{\mu\nu} f(E_\mu)[1 - f(E_\nu + eV)] |M_{\mu\nu}|^2 \delta(E_\mu - E_\nu) \quad [3.1]$$

where  $f(E_\mu)$  is the Fermi function,  $V$  is the applied bias voltage,  $M_{\mu\nu}$  is the tunneling matrix element between states  $\Psi_\mu$  of the probe and  $\Psi_\nu$  of the surface, and  $E_\mu$  is the energy of the state  $\Psi_\mu$  in the absence of tunneling. The tunneling matrix element  $M_{\mu\nu}$  is given by

$$M_{\mu\nu} = \frac{\hbar^2}{2m} \int (\psi_\mu^* \nabla \psi_\nu - \psi_\nu^* \nabla \psi_\mu) d\vec{S} \quad [3.2]$$

where the integral is over any surface lying entirely within the vacuum (barrier) region separating two sides. The Tersoff-Hamann model, which neglects the actual geometry of the STM tip, is further used to simplify equation [3.1] for the tunneling current:

$$I \approx \sum_{\nu} |\psi(r_t)| \delta(E_\mu - E_\nu) = \rho(r_t, E_{Fermi}) \quad [3.3]$$

Therefore the tunneling current is simply proportional to the local density of states at  $E_{Fermi}$  and the position of the tip. The Tersoff-Hamann approximation reproduces the important features of most experimental STM images and it has been shown to be a very good estimate<sup>12</sup>.

The structural and electronic properties of Stone-Wales (SW) defects (i.e. a pentagon-heptagon pair defects, or simply 5775 defects formed by a bond rotation of  $\pi/2$ ) in ultra-small 4Å nanotubes are also investigated. The armchair (3,3) and zigzag (5,0) tubes with SW-defects were described using supercell lengths of 12.25Å (60atoms/supercell) and 12.74Å (60atoms/supercell) respectively. A carbon nanotube (n,m) with a Stone-Wales defect is denoted with a “SW-“ prefix.

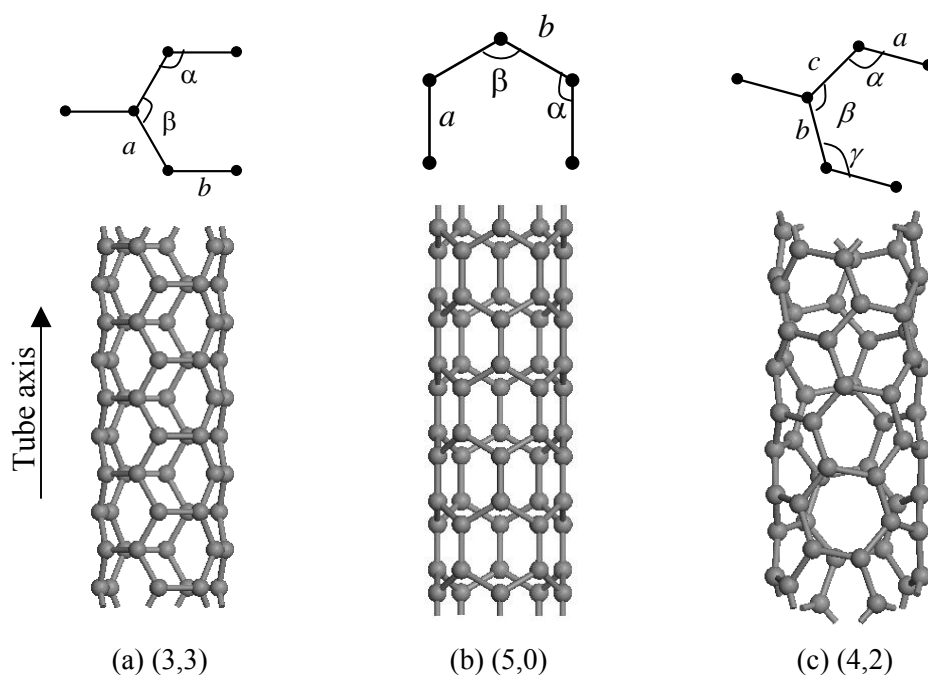


**Figure 3.1.** Stick-and-ball models of ultra-small 4Å nanotubes: (a) armchair (3,3), (b) zigzag (5,0) and (c) chiral (4,2).  $a$ ,  $b$  and  $c$  represent the bond lengths of the carbon network while  $\alpha$ ,  $\beta$ , and  $\gamma$  are the bond angles.

### 3.1.2. Structural Relaxation: Bond lengths & angles

Figure 3.1 shows the schematic atomic arrangement (stick-and-ball models) of the 4Å nanotubes. The fully relaxed structural parameters for these nanotubes are summarized in Table 3.1. The geometry optimizations of 4Å nanotubes using the PBE functional agree well with other nonlocal functionals, and therefore the following discussions are based on the results of PBE functional. In general, the radii of these relaxed ultra-small nanotubes are slightly larger (~3-4%) than the radii of the cylindrically folded nanotubes. The changes in the translational vectors (lattice constant) along the relaxed tubes axis are marginal with respect to the cylindrically folded nanotubes. After relaxation of the 4Å NTs, carbon bond  $a$  for (3,3) and (5,0) tubes, and bonds  $b$  and  $c$  for (4,2) tube (see Fig 3.1 and Table 3.1, which make the smallest angles with the tube axis) are changed the least with respect to the ideal tubes. The strained carbon bonds (bond  $b$  for (3,3)

and (5,0) tubes, and bond  $a$  for (4,2) tube) wrapping around the tube circumference are more affected by the curvature and elongated up to  $\sim 4\%$ . This is due to the curvature effect that weakens the C-C bonds wrapping around the tube circumference. The alternation of bond angles is similar to that of bond lengths. The relaxed bond angles deviate  $\sim 0.5\text{-}1.8\%$  from the ideal bond angles. The difference in bond angles is largest for the (5,0) tube and least for the (3,3) tube.

**Table 3.1.** Geometrical parameters for the ideally rolled graphene sheet and for the relaxed configuration using different nonlocal functionals. The parameters are defined as in Fig 3.1. All length units are in angstrom.

		Radius	Lattice Constant	$a$	$b$	$c$	$\alpha$	$\beta$	$\gamma$
Armchair (3,3)	Ideal	2.03	2.45	1.413	1.386	-	115.6	120.3	-
	PBE	2.09	2.45	1.426	1.445	-	116.4	118.4	-
	PW91	2.09	2.45	1.426	1.445	-	116.3	118.5	-
	BLYP	2.11	2.46	1.429	1.452	-	116.4	118.1	-
	BP	2.10	2.46	1.427	1.446	-	116.4	118.4	-
	<i>Ref 13</i>	2.10	2.47	1.433	1.438	-	116.2	118.7	-
	<i>Ref 14</i>	2.10	2.46	1.430	1.440	-	-	-	-
Zigzag (5,0)	Ideal	1.95	4.25	1.415	1.398	-	120.4	110.2	-
	PBE	2.03	4.25	1.403	1.454	-	119.7	111.4	-
	PW91	2.03	4.25	1.404	1.452	-	119.7	111.2	-
	BLYP	2.04	4.26	1.403	1.459	-	119.5	112.0	-
	BP	2.04	4.25	1.402	1.453	-	119.7	111.3	-
	<i>Ref 13</i>	2.04	4.27	1.412	1.450	-	119.8	111.2	-
	<i>Ref 14</i>	2.04	4.25	1.400	1.450	-	-	-	-
Chiral (4,2)	Ideal	2.07	11.30	1.389	1.415	1.410	113.3	120.4	118.1
	PBE	2.13	11.28	1.440	1.415	1.441	114.3	118.4	118.8
	PW91	2.13	11.28	1.440	1.415	1.440	114.2	118.5	118.8
	BLYP	2.14	11.28	1.448	1.417	1.444	114.5	118.2	118.7
	BP	2.14	11.27	1.441	1.416	1.441	114.3	118.4	118.8
	<i>Ref 13</i>	2.14	11.28	1.440	1.421	1.443	114.1	118.7	118.7
	<i>Ref 14</i>	2.14	11.27	1.440	1.420	1.440	-	-	-

### **3.1.3. Electronic properties: Band structures and density of states**

Figure 3.2 shows the band structures and density of states (DOS) of the 4Å nanotubes. The electronic properties of both fully relaxed and cylindrically folded (unrelaxed) 4Å nanotubes are calculated using GGA-PBE functional. Zone-folding scheme predicts that (5,0) tubes to be semiconducting with a large energy gap. However an energy band (labeled as  $\lambda$  in Fig 3.2) crosses the Fermi level and makes (5,0) metallic. The metallicity of (5,0) is due to the large tubular curvature which causes the  $\sigma^*$  band to hybridize with the  $\pi^*$  band. Blasé et al.<sup>15</sup> has reported that as the diameters of zigzag nanotubes are reduced to as small as (6,0) nanotube (4.68Å), the degree of hybridization of the carbon  $\pi$  and  $\sigma$  orbitals becomes more pronounced as the tube curvature increases. Hence the effect of curvature which is neglected in the simple zone-folding scheme becomes crucial in the study of very small diameter (~4-5Å) nanotubes. Furthermore (5,0) nanotube has a fairly large DOS (0.36states/eV/atom) at the Fermi level, which suggests that (5,0) might be a potential candidate for one-dimensional superconducting fluctuation<sup>14</sup>.

Figure 3.2 shows that armchair (3,3) nanotube is metallic and the two bands crossing the Fermi level exhibit very little dispersion near the center zone. As shown in Figure 3.2 (right panel), the DOS of (3,3) at the Fermi level is about 0.06states/eV/atom. Yang et al.<sup>16</sup> suggested that alkali-doped (3,3) nanotube might possess very high DOS at the Fermi level if the Fermi level is shifted to the sharp van Hove singularity at ~1.3eV (see Fig 3.2 right panel, label as  $\psi$ ). These alkali-doped (3,3) tubes are anticipated to possess improved conductance and even superconductivity<sup>14,16</sup>. Our calculation shows that a chiral (4,2) nanotube is semiconducting with a small indirect energy gap of 0.2eV, while zone-folding scheme predicts a direct and wide energy gap of 1.8eV. The valence band maximum is located about 1/5  $\Gamma$  X away from the  $\Gamma$  point, while the conduction minimum is located at the X point.

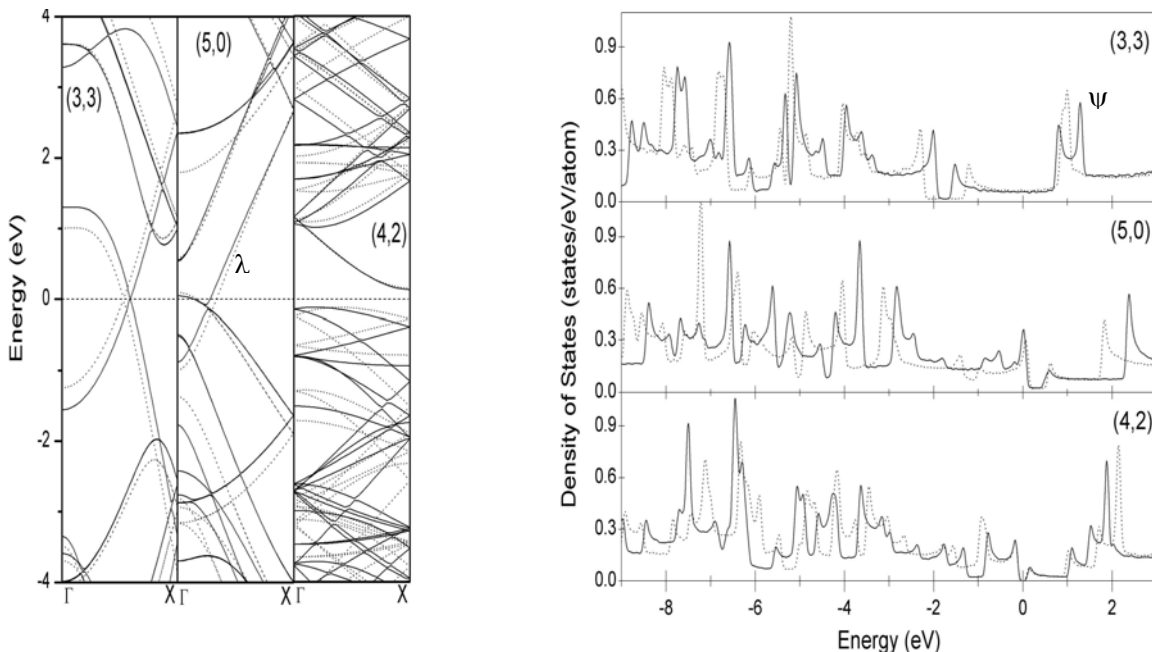


**Figure 3.2.** (Left panel) Electronic band structures and (Right panel) density of states of (3,3), (5,0) and (4,2) nanotubes. Calculations were conducted within GGA-PBE parametrization using Dmol<sup>3</sup> code. Solid lines and dotted lines represent the computed results of the geometrically relaxed and cylindrically folded (unrelaxed) nanotubes respectively.

Figure 3.2 also shows that the DOS (compare the first van Hove singularities of Fig 3.2 with Fig 2.3 at page 9), valence and conduction bands of these ultra-small 4Å nanotubes are asymmetric with respect to the Fermi level, while those obtained by zone-folding or simple tight-binding model are typically symmetrical. The band structures and DOS of the unrelaxed cylindrical 4Å tubes are also displayed in Figure 3.2 (dotted lines). Although there are noticeable differences between the electronic structures of the unrelaxed and relaxed tubes at higher energy regions, the differences in the vicinity of the Fermi level are marginal. The metallic behavior of (5,0) tube and the small indirect gap of (4,2) tube are also observed for the unrelaxed nanotubes. However the geometry optimizations of the 4Å nanotubes, which have been carried out with 4 different nonlocal functionals, unanimously indicated that the geometry of the 4Å nanotubes deviates from the cylindrical configuration and thus the electronic properties are best described by the relaxed tubes.



### 3.1.4. Optical properties of 4Å carbon nanotubes

Figure 3.3 shows the computed optical properties of the 4Å nanotubes using the CASTEP code, along with the experimental optical adsorption spectra taken from ref [17]. The imaginary part of the dielectric constant ( $\epsilon_2$ ) was calculated from

$$\epsilon_2(q \rightarrow O_n, \hbar\omega) = \frac{2e^2\pi}{\Omega\epsilon_0} \sum_{k,v,c} |\langle \Psi_k^c | \hat{u} \cdot r | \Psi_k^v \rangle|^2 \times \delta(E_k^c - E_k^v - E), \quad [3.4]$$

where  $\hat{u}$  is the vector defining the polarization of the incident electric field. This expression is similar to the Fermi's Golden rule for time-dependent perturbations, and can be considered as the real transitions between occupied and unoccupied electronic states.

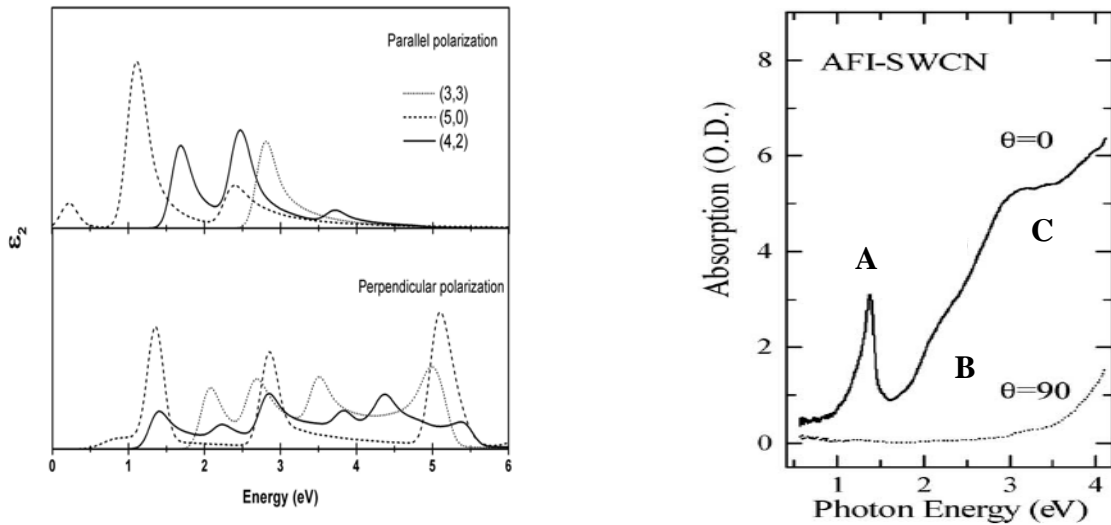


**Figure 3.3.** (Left panel) Imaginary part ( $\epsilon_2$ ) of the dielectric function for the tubes (3,3) (dotted lines), (5,0) (dashed lines) and (4,2) (solid lines) for light polarized parallel and perpendicular to the tube axes.  $\epsilon_2$  are calculated with CASTEP code. (Right panel) Optical absorption spectra of 4Å nanotubes embedded in zeolites. Taken from ref [17].

However the computation of optical properties using CASTEP code has several limitations. The level of approximation used in CASTEP ignores any local field effects that might

arise when the electric field experienced at a particular location in the system is screened by the polarizability of the system itself. In the absence of local field effects, excitonic effects are not treated in the present CASTEP formalism. Recent theoretical and experimental<sup>18</sup> studies show that excitonic effects are important to the optical properties of carbon nanotubes. Nonetheless, within the limitations of CASTEP code, the computed optical properties of 4Å nanotubes can serve as useful approximations to understand the experimental optical absorption spectra.

Due to the anisotropy of the carbon nanotubes, the response of the dielectric function of the 4Å nanotubes is greatly dependent on the polarization of the incident light. As shown in Figure 3.3, in the parallel light polarization, the dominant absorption is within the 1-3.5eV regions, while in the perpendicular light polarization the absorption is extended to 5.5eV. The right panel of Figure 3.3 shows the experimentally polarized absorption spectra of 4Å nanotubes arrayed within one-dimensional channels of a zeolite crystal taken from ref [17]. Experimentally, there are 3 main absorption peaks for these 4Å nanotubes in the parallel light polarization (label as A, B and C). Li et al.<sup>17</sup> observed a homogeneous decrease in the absorption intensity as the polarization angle is increased. This is attributed to the screening of the electric field perpendicular to the nanotube axis and it is also known as the depolarization effect<sup>19</sup>, which hinder the comparison of theoretical and experimental optical properties in the perpendicular light polarization. Therefore, the results are compared for the parallel light polarization.

On the basis of Figure 3.3, the most dominant absorption peak of the (3,3) and (5,0) nanotubes are computed to be at ~2.8eV and 1.1eV. The (4,2) nanotube has two strong absorption peaks at ~1.7eV and 2.5eV respectively. Therefore the peak A is assigned as the optical absorption of (5,0) nanotube. The broad shoulder labeled as B in the absorption spectra is probably due to 2.4eV peak of (5,0), and 1.7eV and 2.5eV peak of (4,2). The peak C is identified as the 2.8eV peak of (3,3) nanotubes. Thus, within the approximation level of CASTEP code, the computed optical properties of the 4Å nanotubes give a reasonable agreement with the experimentally measured optical absorption spectra.

### **3.1.5. Effects of Stone-Wales defects on 4Å nanotubes**

Topological defects such as pentagon and heptagon rings, kinks or bents, junctions and impurities may be present in as-synthesized carbon nanotubes. These defects may significantly change the physical, chemical and mechanical properties of carbon nanotubes. The Stone-Wales (SW) defect is one of the most important defects in the CNT structures because it is proposed that SW-defects play a crucial role in the growth and subsequent annealing down to yield a structurally ordered ground state of the carbon nanotubes<sup>20</sup>. As shown in Figure 3.4a, a SW-defect is formed by a  $\pi/2$  rotation of a C-C bond in the hexagonal network and resulted in a pentagon-heptagon pair (or 5775 ring pair)<sup>21</sup>. The SW-defect could migrate along the structure and create dislocation centers in curved regions, which eventually lead to a closed nanostructure. The DOS of 4Å SW-nanotubes is computed for (3,3) and (5,0) tubes, and the DOS of a (5,5) SW-nanotube (diameter ~6.8Å) has also been computed and compared with the 4Å SW-nanotubes.

Figure 3.4 also shows the relaxed structures of (5,5), (3,3) and (5,0) nanotubes with SW-defects. The formation energy of a SW-defect ( $E_{SW}$ ) is determined as:  $E_{SW} = E[SW-tube] - E[pristine tube]$ . The  $E_{SW}$  for (5,5), (3,3) and (5,0) nanotubes are ~3.1eV, 3.4eV and 2.9eV respectively. The C1-C2 bonds (~1.29-1.40Å, see Fig 3.4b-d) of SW-nanotubes are shorter than the C-C bonds of pristine tubes, an indication of a rather localized C=C double bond. The local carbon skeletal of the 5775 defects of armchair nanotubes move toward the tubular center and it is nearly planar, while the C1-C2 bond of SW-(5,0) tube are moved slightly outwards. For defect-free carbon nanotubes, the curvature-induced pyramidalization angles (PA) of the carbon atoms are ~5.7°, 9.8° and 10.5° for (5,5), (3,3) and (5,0) tubes respectively. However, the pyramidalization angles of C1 / C2 atoms of the 5775 defects are reduced to ~3.93°, 4.9°, and 6.8° for (5,5), (3,3) and (5,0) tubes respectively. Hence the reduction of a local curvature at the 5775-defect is anticipated to significantly affect the electronic properties of carbon nanotubes, especially the 4Å nanotubes.

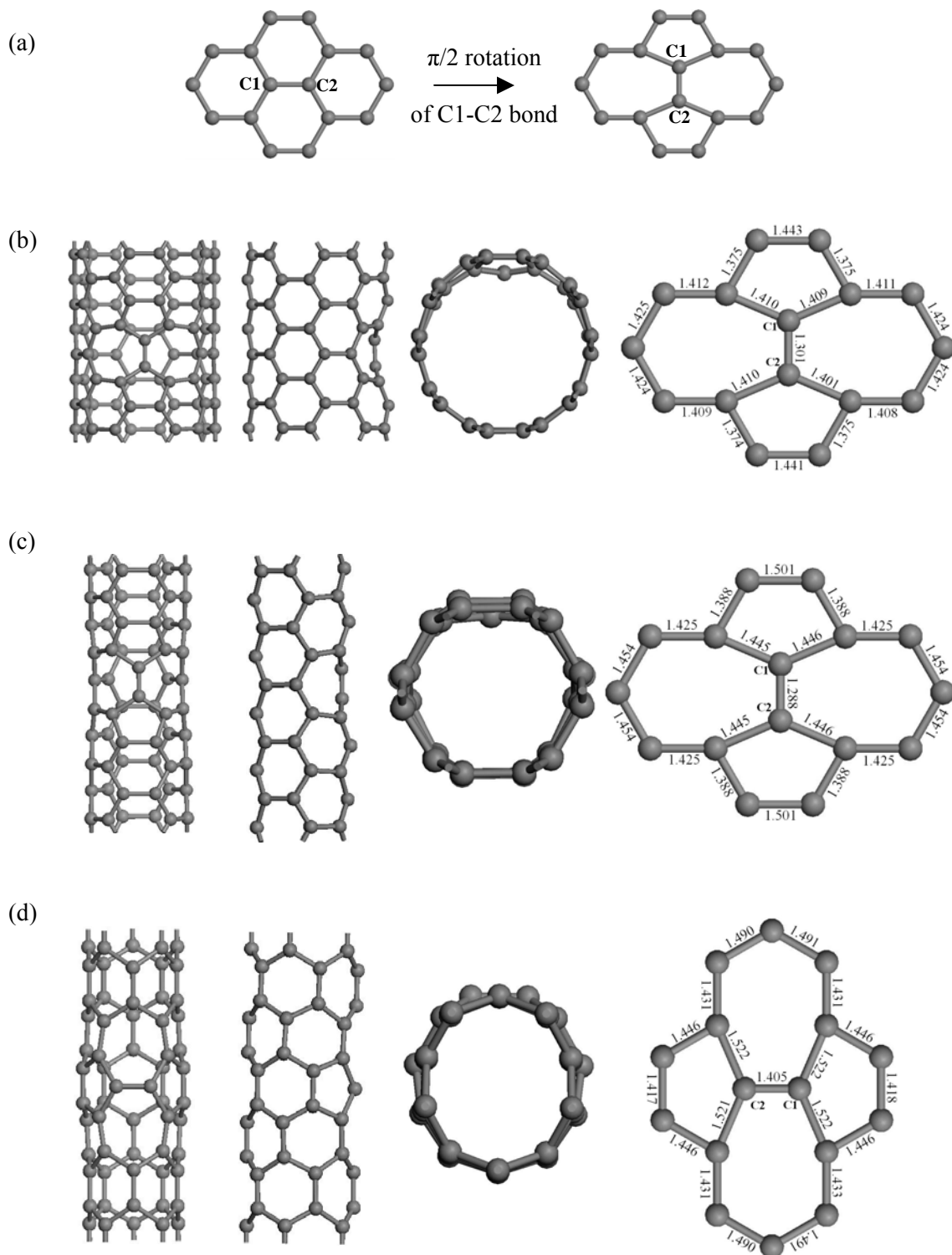


**Figure 3.4.** (a) A  $\pi/2$  rotation of C1-C2 bond in the hexagonal network to yield a Stone-Wales defect. Geometry optimizations of nanotubes with SW-defect: (b) (5,5) nanotube, (c) (3,3) nanotube, and (d) (5,0) nanotube. The bond lengths of the 5775 defects are given in Å.

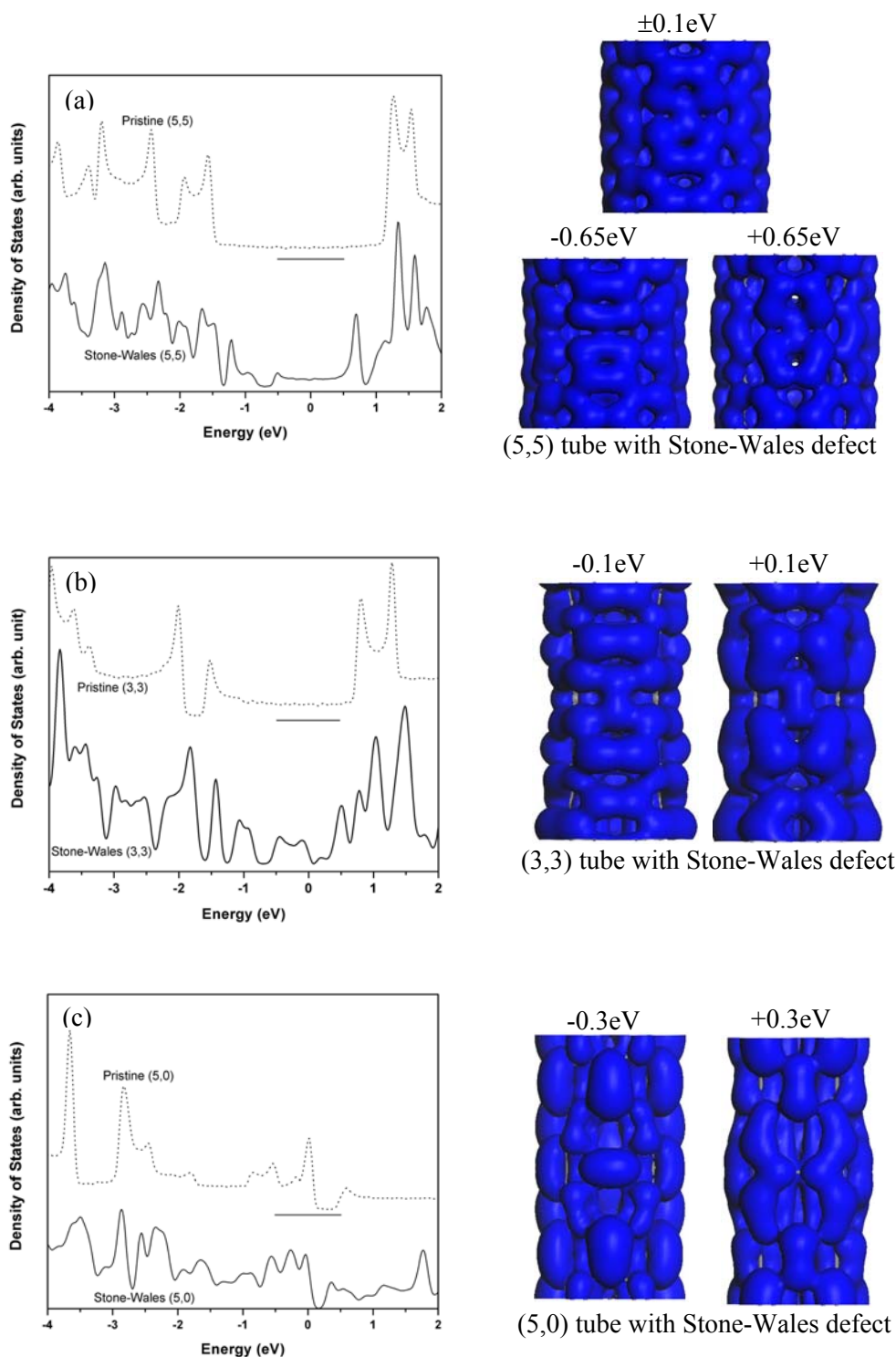


**Figure 3.5.** (Left panel) Density of states (DOS) and (Right panel) scanning tunneling microscopic (STM) images of (a) (5,5), (b) (3,3) and (c) (5,0) nanotubes with Stone-Wales defects. Properties of (5,5), (3,3) and (5,0) nanotubes with SW-defects were calculated within CASTEP code. Solid line and dotted lines denote the DOS of the Stone-Wales and pristine states respectively.

Figure 3.5 shows the DOS and STM images of the (5,5), (3,3) and (5,0) nanotubes with Stone-Wales defects. A pristine (5,5) nanotube possesses a relatively wide DOS plateau from about  $-1.5\text{eV}$  to  $1\text{eV}$ . In the presence of a 5775 ring, two localized peaks appear at about  $-0.5\text{eV}$  and  $0.7\text{eV}$ . The SW-defect induces these two quasibound states, which are located chiefly at the defect. The right panel of Fig 3.5a shows the STM simulations at different applied bias potential of  $\pm 0.1\text{eV}$  and  $\pm 0.65\text{eV}$  for the SW-(5,5) nanotube. The STM image of SW-(5,5) at bias  $\pm 0.1\text{eV}$  exhibits a localized image of a 5775 defect, and the STM image of the occupied states ( $-0.1\text{eV}$ ) is similar to the STM image of unoccupied states ( $+0.1\text{eV}$ ). However, at bias  $\pm 0.65\text{eV}$ , the STM image of SW-(5,5) is dependent on the polarity of the bias. This is because at bias  $\pm 0.65\text{eV}$  the STM simulation is probing close the quasibound states of the 5577 defect.

Likewise the DOS of the pristine (3,3) nanotube has a plateau (from about  $-0.9\text{eV}$  to  $0.7\text{eV}$ ) in the vicinity of the Fermi level. However, the DOS of SW-(3,3) nanotube is drastically changed (see Fig 3.5b). The DOS plateau of the pristine (3,3) is replaced by several quasibound states when a Stone-Wales defect is introduced into its carbon structure. The two quasibound states of SW-(3,3), which are closest to the Fermi level, are located at  $-0.1\text{eV}$  and  $0.18\text{eV}$ . As shown in Figure 3.5b, the simulated STM images of SW-(3,3) is also dependent on the applied bias voltage of  $\pm 0.1\text{eV}$ . For SW-(5,0) nanotube, a small gap is opened at  $0.17\text{eV}$  and two quasibound states, which are closest to the Fermi level, are located at about  $-0.26\text{eV}$  and  $0.36\text{eV}$ . Similarly, the STM images of SW-(5,0) at bias  $\pm 0.3\text{eV}$  shows a clear protrusion at the pentagon sites and it is dependent on the polarity of the applied bias. Our calculations show that Stone-Wales can be experimentally identified by STM measurements. However, this could be a herculean task because the SW-defect has to be properly oriented with respect to the STM tip.

### **3.1.6. Conclusions**

DFT calculations of the geometry, electronic band structure, density of states, and optical properties of (3,3), (5,0) and (4,2) SWNTs have been performed. Significant deviations from the ideal cylindrical structures are noted for the fully relaxed 4Å nanotubes. (5,0) nanotube is found to be metallic, which is previously predicted to be semiconducting by zone folding approximation, and the metallicity is due to the strong curvature of the nanotubes. (4,2) nanotube is predicted to possess an indirect small band gap of 0.2eV instead of having a large gap of 1.8eV. 4Å nanotubes exhibit strong anisotropy of the optical responses as exemplified by the calculated complex dielectric function of the nanotubes. Within the approximation level of CASTEP code, the calculated complex dielectric function of the 4Å nanotubes has been used to interpret experimental optical absorption of the nanotubes.

### **3.2. First-principles study of nitrogenated single-walled carbon nanotubes**

#### *Introduction*

Single-walled carbon nanotubes (SWNTs) can be metallic or semi-conducting, depending greatly on their tubular diameter and chirality. Thus it is difficult to synthesize SWNTs with uniform chirality and electronic properties. To overcome this difficulty, dopants and defects can be introduced to alter the electronic properties of SWNTs. The creation of new energy levels in the band gap with associated electronic states is an important step to make electronic devices.

The intercalation of alkali metals and halogens into SWNT bundles has been utilized to modify the electronic properties<sup>22</sup>. B and/or N atoms are also good choice of dopants because they have roughly the same atomic radius as C atoms, and possess one electron less/more than C respectively. Nitrogen doping is particularly attractive because the extra electrons from the nitrogen dopants are expected to make semiconducting nanotubes metallic. Various approaches have been made to incorporate nitrogen atoms into carbon nanotubes, including magnetron sputtering,<sup>23</sup> pyrolysis of nitrogen-rich organic chemicals,<sup>24</sup> and arc-discharge in nitrogen atmosphere.<sup>25</sup> However, most of the syntheses yield nitrogen-doped multi-walled carbon nanotubes (MWNT) with bamboo-shaped morphology. Recently, Villalpando-Paez et. al.<sup>26</sup> reported the synthesis of nitrogen-doped SWNT bundles via an aerosol-assisted chemical vapor deposition (CVD) method, but the doping concentration is unknown. It has been suggested that the nitrogen dopants are substituted into the carbon network with and without vacancy formation. On the other hand, nitrogenation of pristine carbon nanotubes (CNT) has also been conducted using ammonia / nitrogen glow-discharge,<sup>27,28</sup> ball milling in ammonia atmosphere<sup>29</sup> and N ion implantation<sup>30</sup> methods. These methods exohedrally nitrogenate the sidewalls of CNT with  $-NH_2$  functional groups and chemisorbed N adatoms. In addition, the presence of nitrogen impurities in  $\pi$ -conjugated systems<sup>31,32</sup> can alter its magnetic properties. Ma et al.<sup>32</sup> showed that a magnetic moment of  $0.6\mu_B$  is localized at an N adatom chemisorbed on a graphite surface.



In this section 3.2, a theoretical investigation of nitrogenated carbon nanotubes was carried out to study its atomic deformation, electronic structures, molecular orbital, ionization potential (IP) energies, spin polarization, and structural stability of chemisorption process.

### **3.2.1. Computation Methods**

The electronic properties of nitrogenated SWNTs were studied using first-principles density functional theory (DFT), DMol<sup>3</sup> code, available from Accelrys Inc.<sup>4</sup> Each electronic wave function is expanded in a localized atom-centered basis set with each basis function defined numerically on a dense radial grid. For supercell geometries, spin-restricted calculations were carried out with a double numeric polarized (DNP) basis set available and the atomic cutoff set at 4.5Å, along with gradient-corrected Perdew-Burke-Ernzerhof (PBE) functional.<sup>5</sup> Scalar relativistic effects<sup>33</sup> were included via a local pseudopotential for all-electron calculations. Five and eight Monkhorst-Pack *k*-points<sup>34</sup> were used for the Brillouin zone integration along the axes of (10,0) and (5,5) nanotubes respectively. Geometry optimizations were performed with the Broyden-Fletcher-Goldfarb-Shanno (BFGS) algorithm with convergence criterion of 10<sup>-3</sup> a.u. on gradient and displacement, and 10<sup>-5</sup> a.u. on the total energy and electron density. A hexagonal lattice was used to simulate the single-walled nanotubes, with a wall-to-wall distance of at least 10Å, sufficient to avoid in-plane interactions between nanotubes in adjacent unit cells. The Fermi levels of the spin-restricted band structures and density of states (DOS) of (10,0) nanotubes were reset at the 0eV position. For Dmol<sup>3</sup> code, the molecular orbital of periodic systems was computed using only the  $\Gamma$ -point. The isodensity surfaces of highest occupied molecular orbital (HOMO) of Figure 3.6 and 3.7 were fixed at 0.02e/a.u.<sup>3</sup>. A smearing of 0.003 a.u. was applied for all DOS graphs.

Calculations were performed with supercells of zigzag (10,0) (see Fig. 3.6a) and armchair (5,5) SWNTs (see Fig. 3.7a). The supercell length of the zigzag and armchair nanotubes are  $a=8.52\text{\AA}$  (80atoms/cell) and  $a=7.38\text{\AA}$  (60atoms/cell) respectively, unless otherwise stated. Four types of nitrogenated carbon nanotubes were considered: (i) Direct substitution of nitrogen dopants into the carbon framework without a formation of vacancy (see Figs. 3.6b and 3.7b). Doping density varies from 0.83–5at%. (ii) Substitution of nitrogen dopants with vacancy formation, by removing a central C atom among three hexagons and replacing the three surrounding C atoms with 3 N atoms (see Figs. 3.6c and 3.7c). This pyridine-like structure was proposed by Czerw et al.<sup>35</sup>, and this type of N-doping is hereinafter termed as pyridine-like doping. Doping density varies from 3.8-7.6at%. (iii) Exohedral chemisorption of nitrogen adatoms. The chemisorbed N adatoms can be in “parallel” or “perpendicular” positions. The N adatom that bridges over the C-C bond is in a “parallel” position, while the N adatom bridges over a broken C-C bond is in a “perpendicular” position. In Figure 3.6d, for a zigzag nanotube, the N adatom chemisorbed over the C1-C2 bond is in parallel position, while “perpendicular” position refers to the N adatom bridging the C2-C3 bond which is broken (compare Figs. 3.6d and 3.6e). For an armchair nanotube, the “parallel” position refers to the N adatoms above the C4-C5 bond (see Fig. 3.7d), while the “perpendicular” position is bridged over the C5-C6 bond (in Fig. 3.7e C5-C6 bond is broken), (iv) sidewall covalent  $-\text{NH}_2$  functionalization (see Figs. 3.6f and 3.7f). Hence the atomic deformation, bond lengths, molecular orbital and energetic of nitrogenated SWNTs were presented in section 3.2.2. Spin restricted electronic properties of nitrogenated SWNTs were presented in section 3.2.3.

The ionization potential (IP) values have been determined for the nitrogenated nanotubes and the results were presented in section 3.2.4. The IP is defined as the energy difference between a positively charged system (+1) and the originally neutral system (0). A constant electric field of  $1\text{eV/\AA}$  is applied parallel to the tube axis, whereby field emission is assumed to occur at this order of magnitude.

Spin unrestricted (polarized) calculations were also performed for the nitrogenated SWNTs. However spin polarization was significant only for the case of N adatom chemisorption. The spin polarized band structures, local DOS and magnetism of singly N-chemisorbed SWNTs were presented in section 3.2.5.

The structural stability and coalescence of two N adatoms chemisorbed on SWNTs into a  $N_2$  molecule were presented in section 3.2.6. The transition state energies of the coalescence processes were investigated using a generalized synchronous transition (GST) method.<sup>36</sup> This method involved a linear synchronous transit (LST) maximization, followed by repeated conjugated gradient (CG) minimizations, and then quadratic synchronous transit (QST) maximizations and repeated CG minimizations until a transition state had been located (see ref [36] for details). The geometry optimization convergence threshold of the RMS forces was set at 0.005 Ha/Å. The “reactants” and “products” correspond to N-chemisorbed carbon structures and carbon structures with a  $N_2$  molecule respectively. The “reactants” and “products” are geometrically optimized before the full LST/QST search (see Table 3.5 and 3.6 for the relaxed “reactants”). The coalescence process was carried out for periodic systems of a graphene sheet and selected nanotubes.

### **3.2.2. Atomic deformation, bond lengths, molecular orbital and energetics**

Figures 3.6 and 3.7 show the relaxed geometries of (10,0) and (5,5) nanotubes along with the distribution of the highest-occupied molecular orbital (HOMO). Generally, it is noted that the cylindrically pristine nanotube is deformed to an ellipsoidal shape upon doping. A deformation factor ( $\delta$ ) is defined as the ratio of the major axis to the minor axis of the nanotubes. The  $\delta$  values for the various types of nitrogenation are listed in Table 3.2, together with the computed IP values.

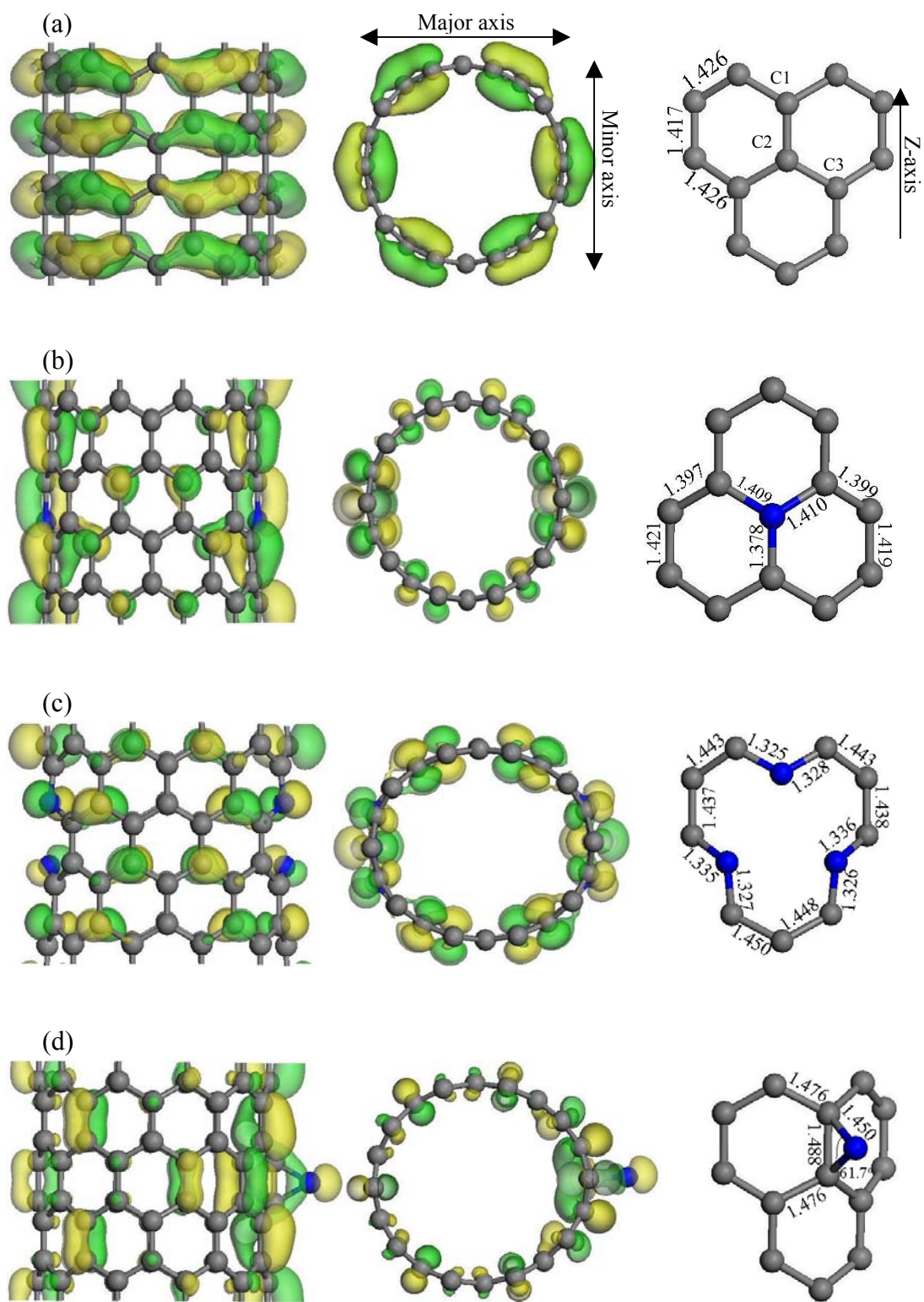
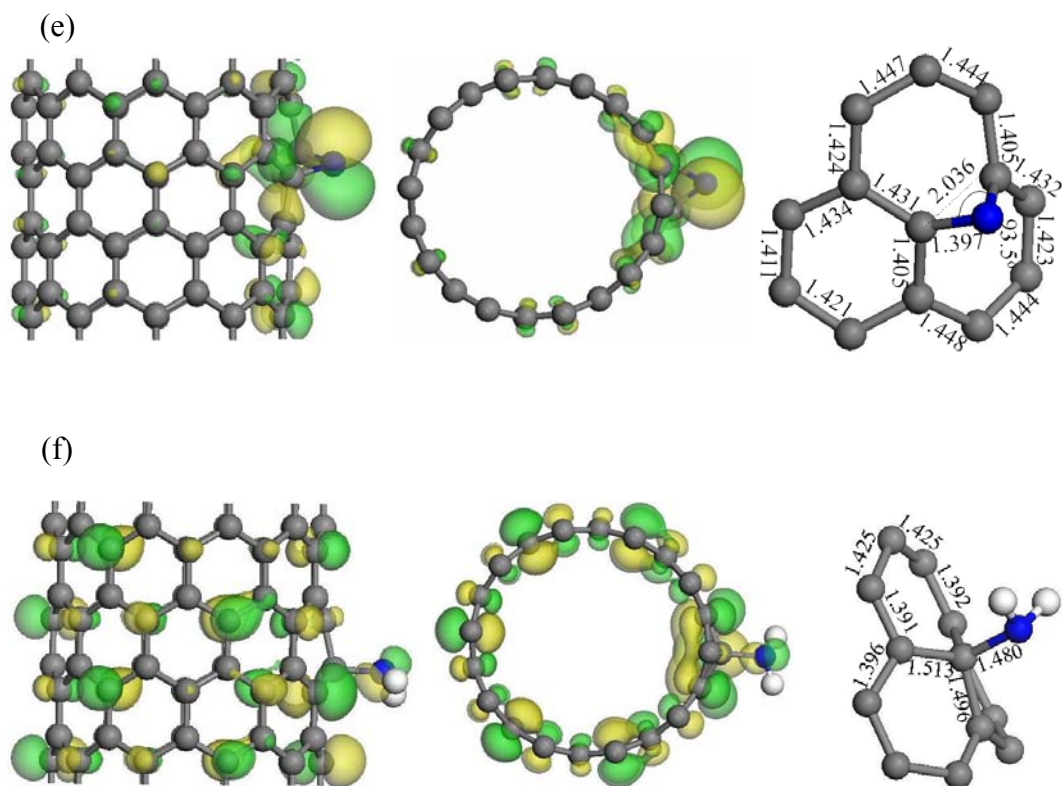
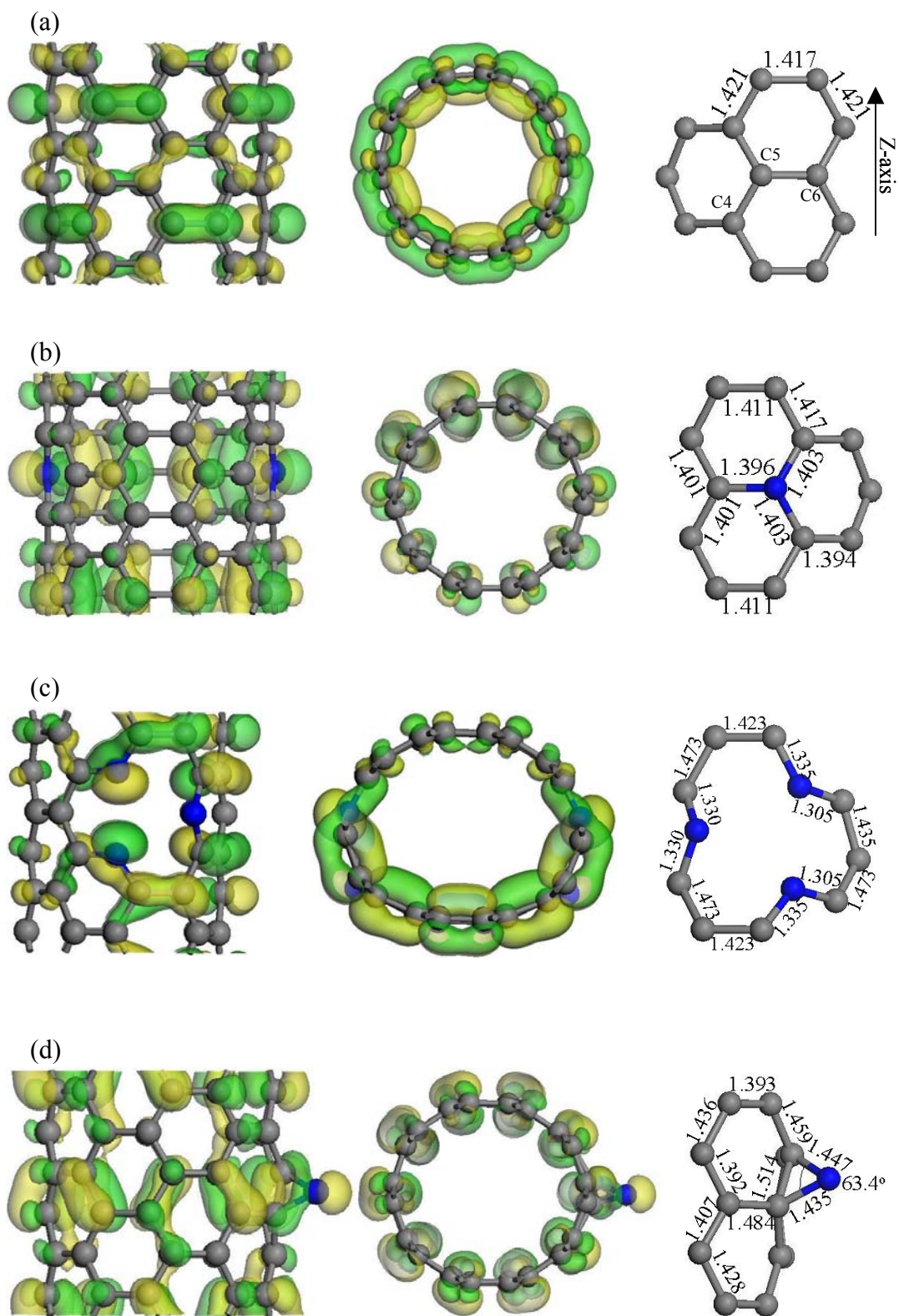


Figure 3.6. (Continues next page)



**Figure 3.6.** (a) Geometrically optimized structures, highest occupied molecular orbital (HOMO) and bond lengths (in Å) of a pure zigzag (10,0) nanotube; (b) Direct substitution of two nitrogen atoms into the carbon framework without the formation of vacancies. Here the two N substitution atoms in  $C_{78}N_2$  are in the opposite positions, (c) N substitution into the carbon framework with the formation of vacancy: pyridine-like doping ( $C_{72}N_6$ ) with two vacancies formed in opposite positions, (d) Chemisorption of a N adatom in “parallel” position, (e) Chemisorption of a N adatom in “perpendicular” position, (f)  $-NH_2$  functionalization. Grey ball denotes C atom, blue ball denotes N atom, and white ball denotes H atom. A fragment of the supercell is taken out to elucidate the bond lengths at the vicinity of the N-impurities.





**Figure 3.7.** (Continues next page)

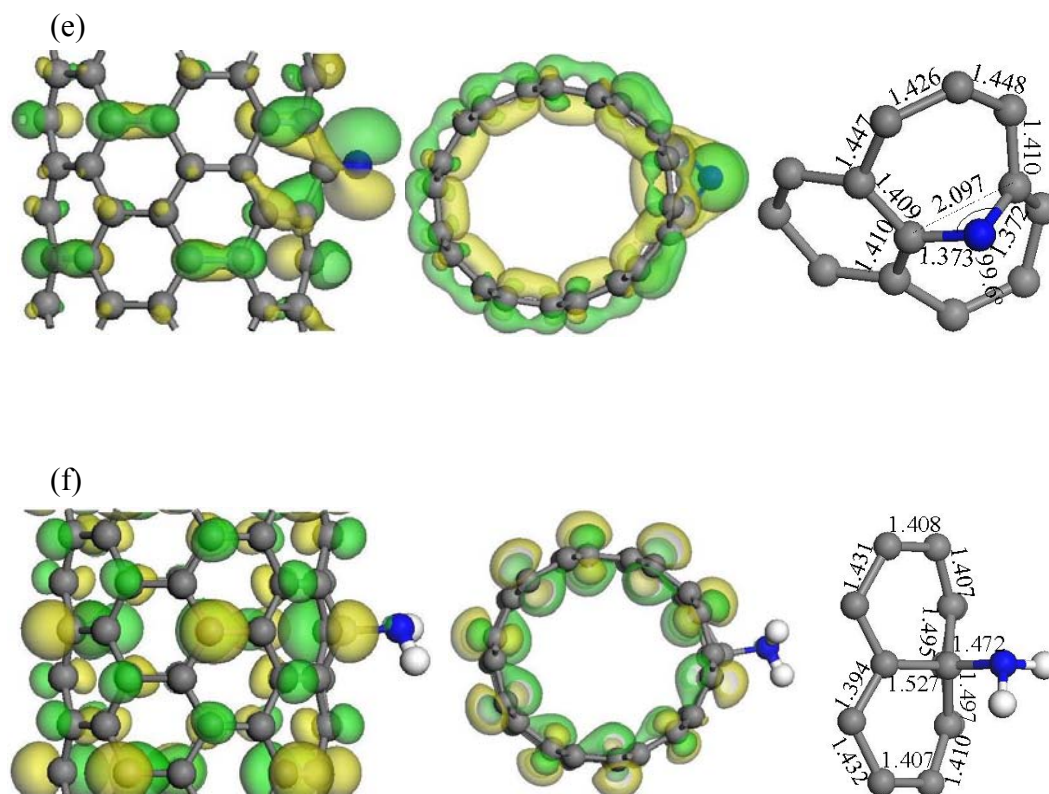


**Figure 3.7.** (a) Geometrically optimized structures, highest occupied molecular orbital (HOMO) and bond lengths (in Å) of a pure armchair (5,5) nanotube; (b) Direct substitution of two nitrogen atoms into the carbon framework without the formation of vacancies. Here the two N substitution atoms in C<sub>58</sub>N<sub>2</sub> are in the opposite positions, (c) N substitution into the carbon framework with the formation of vacancy: pyridine-like doping (C<sub>52</sub>N<sub>6</sub>) with two vacancies formed in opposite positions, (d) Chemisorption of a N adatom in “parallel” position, (e) Chemisorption of a N adatom in “perpendicular” position, (f) –NH<sub>2</sub> functionalization. Grey ball denotes C atom, blue ball denotes N atom, and white ball denotes H atom. A fragment of the supercell is taken out to elucidate the bond lengths at the vicinity of the N-impurities.

**Table 3.2.** Deformation ( $\delta$ ), IP values and magnetic moment ( $\mu_B$ ) of nitrogenated SWNTs.

	<b>Types of nitrogenation</b>	$\delta$	IP (eV/Å)	Magnetic moment, $\mu_B$
Zigzag (10,0) nanotubes	Pure	1.0	6.19	-
	Substitution, C78N2	1.12	4.69	-
	Pyridine-like doping, C72N6	1.13	4.85	-
	“Parallel” chemisorption	1.07	4.77	0.72
	“Perpendicular” chemisorption	1.15	5.25	0.58
	-NH <sub>2</sub> functionalized	1.18	4.63	-
Armchair (5,5) nanotubes	Pure	1.0	5.91	-
	Substitution, C58N2	1.05	4.55	-
	Pyridine-like doping, C52N6	1.28	4.79	-
	“Parallel” chemisorption	1.08	4.60	0.61
	“Perpendicular” chemisorption	1.07	5.08	0.53
	-NH <sub>2</sub> functionalized	1.17	4.50	-

**Table 3.3.** Formation energies of N-substituted and pyridine-like doped SWNTs

	<b>Types of nitrogenation</b>	$E_f$ (eV) <sup>‡</sup>
(10,0) nanotubes	Substitution, C79N1	1.78
	Substitution, C78N2	3.62
	Pyridine-like doping, C76N3	6.46
	Pyridine-like doping, C72N6	11.20
(5,5) nanotubes	Substitution, C59N1	1.71
	Substitution, C58N2	3.55
	Pyridine-like doping, C56N3	5.61
	Pyridine-like doping, C52N6	10.57

<sup>‡</sup>Formation energy of (10,0)NT, C76N3, is calculated as followed:  $C80 + 3N \rightarrow C76N3 + (1/80)C80$ , i.e.,  $E_f = E[C76N3] + 1/80E[C80] - E[C80] - 3E[N]$ . Similar energy calculations are performed for the other cases.



**Table 3.4.** Adsorption energies of chemisorbed N adatoms and  $-NH_2$  on SWNTs

	<b>Types of nitrogenation</b>	<b><math>E_a</math>(eV)<sup>†</sup></b>
(10,0) nanotubes	“Parallel” chemisorption, C80N1	1.77
	“Perpendicular” chemisorption, C80N1	2.40
	$-NH_2$ functionalization	2.34
(5,5) nanotubes	“Parallel” chemisorption, C60N1	1.49
	“Perpendicular” chemisorption, C60N1	2.75
	$-NH_2$ functionalization	2.21

<sup>†</sup>Adsorption energy is calculated as followed:  $E_a = E(\text{CNT} + \text{impurity}) - E(\text{CNT}) - E(\text{impurity})$

It is noted that both (10,0) and (5,5) tubes have almost the same order of deformation factor  $\delta$  for “parallel” chemisorption and  $-NH_2$  functionalization. For pyridine-like doping, a (5,5) nanotube ( $\delta \approx 1.28$ ) suffers a larger deformation than a (10,0) nanotubes ( $\delta \approx 1.13$ ) which could be due to the smaller diameter of (5,5) nanotube. On the other hand, direct substitution and “perpendicular” chemisorption cause more deformation in (10,0) nanotubes than (5,5) nanotubes. Noteworthy, the sidewall of (5,5) nanotubes with chemisorbed N adatom is buckled while (10,0) nanotubes are not so susceptible to buckling (compared Fig 3.6d,e and Fig 3.7d,e).

The bond lengths of the relaxed nanotubes in the vicinity of the nitrogen impurities are also displayed in Figure 3.6 and 3.7. The C-N bond lengths of direct nitrogen substitution are determined to be  $\sim 1.40$ - $1.38 \text{ \AA}$  for the doped nanotubes both in Fig. 3.6 and Fig. 3.7. Due to the missing central C atom, the C-N bond lengths of pyridine-like doping are determined to be  $\sim 1.30$ - $1.35 \text{ \AA}$ , depending on the orientation, as compared to  $1.42$ - $1.47 \text{ \AA}$  for the C-C bonds (see Figs 3.6c and 3.7c). For the chemisorbed N dopants, the C-N bond lengths of (5,5) tubes are about  $1.45 \text{ \AA}$  (vs.  $1.51 \text{ \AA}$  C-C bond) in the “parallel” positions and  $1.37 \text{ \AA}$  (vs.  $2.10 \text{ \AA}$ , C-C separation in this case) in “perpendicular” position. These bond length values are more locally distorted than (10,0)

nanotubes (compare Figs 3.7d,e and 3.6d,e). Covalent  $-NH_2$  functionalization results a C-N bond length of  $\sim 1.47$ - $1.48\text{\AA}$ , while the surrounding C-C bonds are elongated to  $\sim 1.50\text{\AA}$ . Thus it can be surmised that nitrogen impurities in CNTs produce their own local strains and results in the respective deformation. The relaxed structures of nitrogenated SWNTs correlate well with experimental observations of compartmentalized and defective nitrogen-doped CNTs.<sup>24,37</sup>

The effects of dissimilar nitrogenation on armchair and zigzag nanotubes are also reflected by the differences in the HOMO distribution. For instance, the HOMO of a nitrogen substituted (10,0) nanotube is polarized at two opposite nitrogen dopants, while this is not the case for a nitrogen substituted (5,5) nanotube (see Fig 3.6b and 3.7b). Pyridine-like doping causes the HOMO of doped (5,5) NT to be more concentrated at one side of the ellipsoidal ring (see Figs 3.6c and 3.7c). Another marked difference between doped (5,5) and (10,0) NTs is for the case of chemisorption of N adatoms at the “perpendicular” positions. The HOMO of a (10,0) nanotube is concentrated at the vicinity of the “perpendicularly” chemisorbed N adatom, while the HOMO of a (5,5) nanotube is roughly still distributed throughout the tube (compare Fig 3.6e and 3.7e).

The formation energies ( $E_f$ ) and absorption energies ( $E_a$ ) of the nitrogenated SWNTs were given in Table 3.3 and Table 3.4 respectively. The energy cost to  $sp^2$ -substitute a C atom with an N atom in (10,0) and (5,5) nanotubes are 1.78 and 1.71eV respectively. On the other hand, it costs 6.46 and 5.61eV to form pyridine-like doping in (10,0) and (5,5) nanotubes respectively. The adsorption energies of exohedral N adatoms on SWNTs are dependent on the orientation of the C-N bridges relative to the tubular axes. The “parallel” chemisorption of SWNTs has lower absorption energy than the “perpendicular” chemisorption, which is understandable since the C-N bond lengths in the “parallel” positions are shorter than those in the “perpendicular” positions (1.45 vs.  $1.37\text{\AA}$  in (5,5) nanotube, and 1.45 vs.  $1.39\text{\AA}$  in (10,0) nanotube). The adsorption energy of  $-NH_2$  on the outer surface of SWNTs is about 2.3eV, which is comparable to the absorption energy of “perpendicular” N adatom chemisorption. The synthesis of N-doped carbon nanotubes is usually carried out at 700-900°C using nitrogen-rich

precursors for CVD processes.<sup>24,38,39</sup> Spectroscopic studies and peak analysis revealed that C-N bonding of N-doped carbon nanotubes involved  $sp^2$ ,  $sp^3$ -typed and intercalated  $N_2$  as well, which might be attributed to  $sp^2$ -substitution of C atom with an N atom, pyridine-like doping and molecular  $N_2$  respectively. The relatively high synthesis temperature and use of catalysts might provide sufficient energies to form pyridine-like defects in N-doped carbon nanotubes, though the formation energies of pyridine-like defects is higher than  $sp^2$ -substitution. Furthermore, the decomposition of nitrogen-rich precursors might generate N adatoms which chemisorbed on the graphitic layers of carbon nanotubes and subsequently coalesce to form intercalated  $N_2$  molecules (see section 3.2.6). Pristine carbon nanotubes can also be modified with nitrogen impurities using N ion irradiation,  $N_2$  /  $NH_3$  plasma treatment. Khare et al.<sup>27,28</sup> showed that the  $-NH_2$  functional group is mostly attached to carbon nanotube after  $N_2$  /  $NH_3$  plasma treatment, whereby the absorption energy of  $\sim 2eV$  is supplied by the plasma. Atomistic simulations study<sup>30</sup> of N ion implantation into carbon nanotubes showed that up to 40% of the N ion irradiation results in  $sp^2$ -substitution of the nanotube C network, and annealing the N-bombarded nanotubes further increases the  $sp^2$  N dopants. Thus the synthetic conditions, nitrogen plasma treatment and N ion implantation can be utilized to favorably control the types of N-impurities in carbon nanotubes. This in turn implied that the electronic properties of carbon nanotubes can be experimentally tuned according to the types of N impurities introduced, and this is important for nanotube-based electronic devices. The electronic properties of different nitrogenated SWNTs are presented in section 3.2.3.

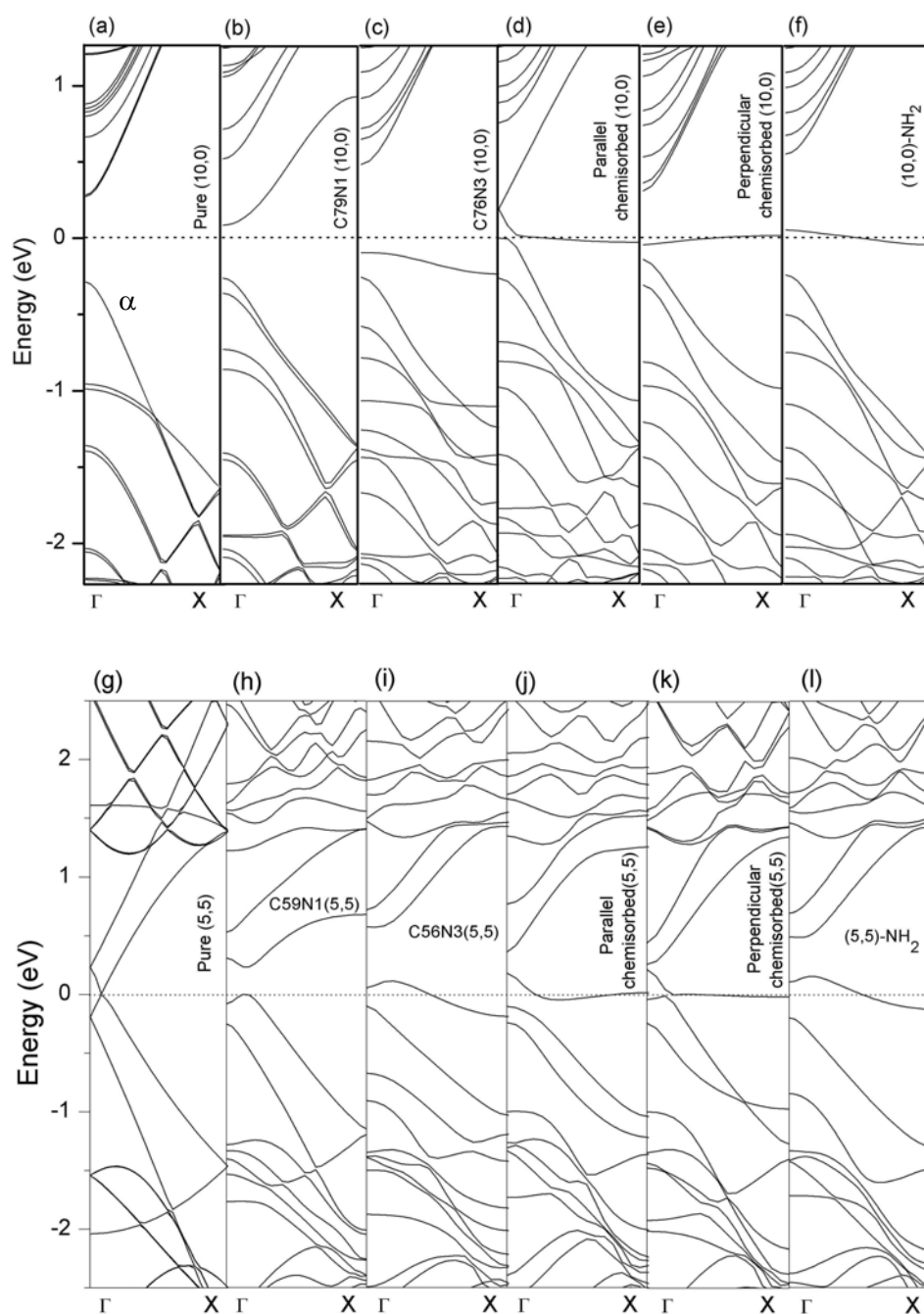


**Figure 3.8.** Band structures of (10,0) and (5,5) nanotubes: (a,g) pure, (b,h) N-substitution, (c,i) pyridine-like doping, (d,j) chemisorption at “parallel” position, (e,k) chemisorption at “perpendicular” position, (f,l)  $\text{-NH}_2$  functionalization. (a-f) and (g-l) for (10,0) and (5,5) nanotubes respectively. The Fermi level is represented by the dotted horizontal lines.

### **3.2.3. Spin restricted electronic properties**

Figures 3.8a-f compare the electronic band structures of pure and nitrogenated (10,0) nanotubes in the vicinity of the Fermi level. A pure zigzag (10,0) SWNT has a  $D_{10h}$  symmetry, and most of the energy levels are doubly degenerate due to the rotational point group  $C_n$ . Figure 3.8a shows the band structure of a pure (10,0) nanotube, which is very similar to that in Ref [40]. The topmost valence band and bottom conduction band correspond to the big  $\pi$ -bonding and  $\pi^*$ -antibonding states along the ring of the tube respectively. Upon nitrogenation, the degeneracies of the energy bands of (10,0) nanotubes are removed. That is, the presence of nitrogen impurities causes the  $\alpha$  band to split. The splitting of the band is most prominent for “parallel” chemisorption (Fig. 3.8d). A new band develops just below the Fermi level for pyridine-like doping (*p*-type, Fig. 3.8c), while a new band develops in the middle of the Fermi level for  $-\text{NH}_2$  functionalization (Fig. 3.8f, still regarded as *p*-type doping due to the presence a small gap between the new energy band and valence band). Direct nitrogen substitution creates a new band just above the Fermi level (i.e. below the lowest conduction bands), which exemplifies an *n*-type doping. Band structure study reveals a significant difference between “parallel” and “perpendicular” chemisorption. A new energy band cuts across the Fermi level for “parallel” chemisorption and makes the doped (10,0) nanotube metallic. On the other hand, a new energy band is developed at the Fermi level narrowing of the gap between the new band and the conduction band for the “perpendicular” chemisorption (considered as *n*-type).

Band structures of Figure 3.8 are consistent with J. Zhao et al.<sup>41</sup> who have investigated the band structures of SWNTs with covalent sidewall functionalization (e.g. COOH, OH, F, H, CH<sub>3</sub>) and pointed out the marked difference between covalent functionalization and substitutional doping. As in the case of semiconducting (10,0) nanotubes, substitutional doping does not disturb the  $sp^2$  hybridization of the  $\pi$ -electrons and the N impurity states contributes mainly to the minimum of the conduction band, while tube-impurity covalent interaction creates an impurity

state in the top of the valence band due to  $sp^3$ -defect. As indicated in Figure 3.6b and Figure 3.6f, the C-C bond lengths of  $-NH_2$  functionalized nanotubes are elongated to  $\sim 1.50\text{\AA}$  ( $sp^3$ -defect), while the C-C bond lengths of nitrogen substitution is  $\sim 1.40\text{\AA}$  ( $sp^2$ ).

The electronic band structures of pure and doped (5,5) nanotubes are displayed in Figures 3.8g-l. The  $\pi-\pi^*$  band crossing of the pure (5,5) metallic tube is disturbed by the presence of N impurities. Small band gaps open up between the conduction and valence bands, which are attributed to the breaking of the armchair nanotube mirror symmetry due to the tube-impurity interaction. The opening of small gaps has also been reported for covalently functionalized and Cu-adsorbed metallic nanotubes.<sup>41,42</sup>

In Figure 3.9, we present the electronic density of states (DOS) of pristine and nitrogenated (10,0) nanotubes. At low concentration of dopants (0.83at%), direct substitution of nitrogen narrows the band gap and slightly shifts the Fermi level towards the conduction band. Projected DOS of the nitrogen dopant indicated that an impurity state is developed at  $\sim 0.5\text{eV}$  in the conduction bands (*n*-type doping, see Fig 3.9b), but complicated hybridization also occurs at the higher energy regions of the valence bands, along with the removal of the double degeneracies as indicated in the band structures. At higher level of doping (see Figure 3.9c,d), the band gap continues to narrow and eventually filled with impurity states at higher concentration of dopants. For instance, N-substituted (10,0) nanotubes of 2.5at% become metallic due to the finite states at the Fermi level (see Fig 3.9d).

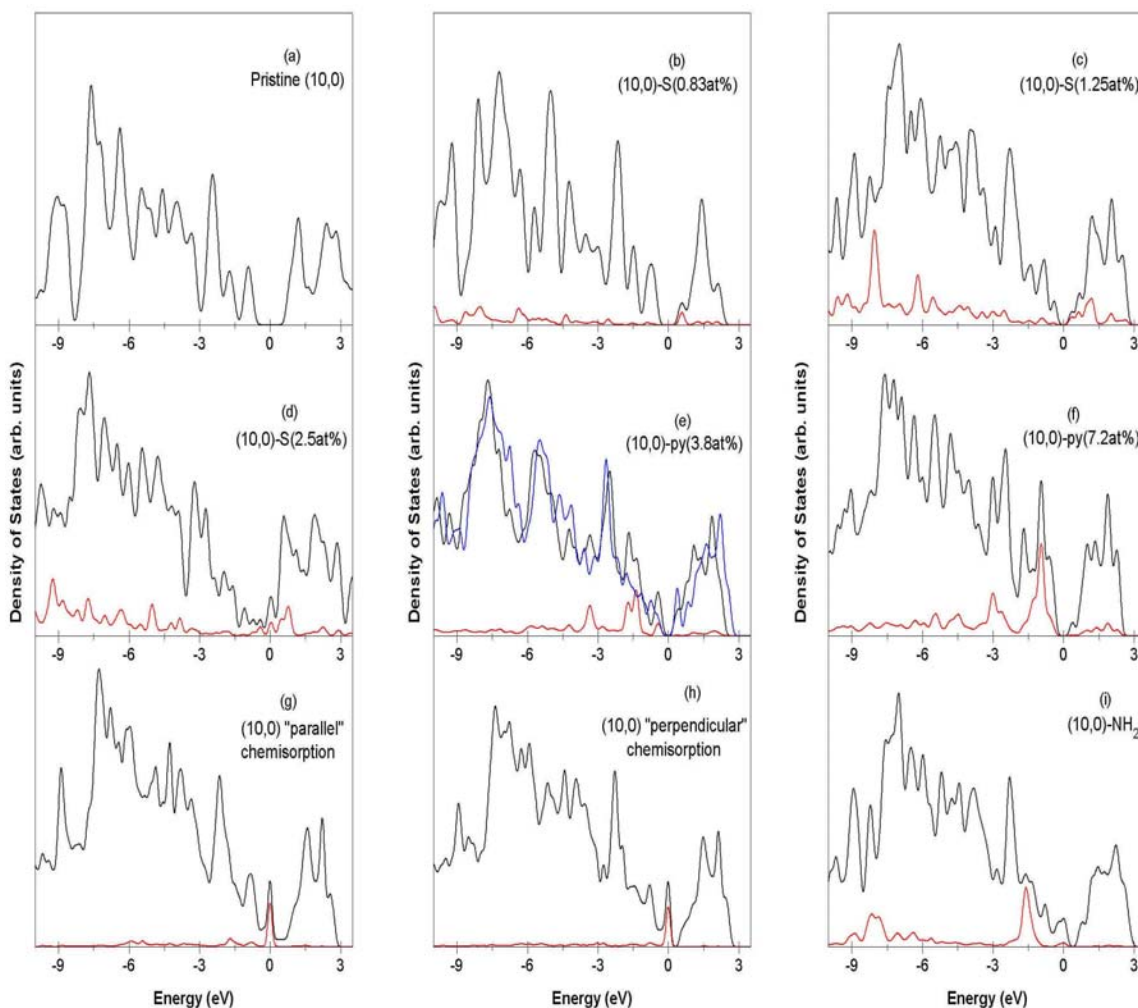


**Figure 3.9.** Total density of states (TDOS) of (a) pristine (10,0) nanotube, (b-d) nitrogen-substitution, (e,f) pyridine-like doping, (g,h) chemisorption of N adatoms, and (i)  $-\text{NH}_2$  functionalization. Projected DOS of nitrogen impurities and TDOS of undoped (10,0) nanotube with vacancy are indicated as red line and blue lines respectively. The Fermi level is at 0 eV. A 120 atoms/cell supercell is used to compute case (b) substitution.

Although pyridine-like doping has a relatively higher concentration of dopants (compared  $\sim 3.8\text{at}\%$ , Fig 3.9e, of pyridine-like doping vs.  $2.5\text{at}\%$ , Fig 3.9d, of N-substitution), the band gap remains though narrower. At even higher concentration of pyridine-like doping ( $7.2\text{at}\%$ , Fig 3.9f), the doped (10,0) nanotube still remains as a narrow gap semiconductor. This is in contrast to direct substitution ( $\sim 2.5\text{at}\%$ ) which can yield metallic nanotubes at higher impurity

concentrations. However our calculated DOS of (10,0) nanotube with pyridine-like doping does not agree to Czerw's calculation,<sup>35</sup> which was based on tight-binding method, and concluded that nanotubes with pyridine-like nitrogen doping behave as donor-type doping. Kang et al.<sup>43</sup> also calculated SWNTs with pyridine-like nitrogen doping and concluded that the resultant SWNTs possessed acceptor-like impurities due to the presence of lone pair states. Our calculated DOS of (10,0) tubes with pyridine-like nitrogen doping (Fig 3.9e) agree well to the results of Kang et al.<sup>43</sup> To understand the role of nitrogen impurities in the pyridine-like vacancy, we have also computed the DOS of a (10,0) tube with pyridine-like vacancy but without nitrogen dopants (see Fig 3.9e, blue line). The relaxed geometry of such a (10,0) tube with mono-vacancy shows a similar deformation and, interestingly, a reduction of band gap which matches quite closely to (10,0) tube with pyridine-like nitrogen doping. Therefore the effects of the nitrogen dopants in pyridine-like doping do not significantly modify the band gap, but noticeable increase (decrease) in the density of states at about -0.4eV, -1.5eV and -3.3eV (-4.4eV and -6.7eV) in the valence band. In other words, the pyridine-like doping causes the zigzag nanotube to become a narrow gap semiconductor, and the projected DOS of the N-dopants show that the impurity states are located ~0.4eV below the Fermi level (Kang et al.<sup>25</sup> obtained impurity states at ~0.5eV below the Fermi level) and thus can be regarded as acceptor-like impurities.

The exohedral chemisorption of a single N adatom onto a (10,0) nanotube significantly alters the band gap. As shown in Figure 3.9h, the projected DOS of the exohedrally “perpendicular” chemisorbed N adatom indicates that it is behaving as *n*-type dopant, which is in contrast to endohedrally chemisorbed N adatom (*p*-type).<sup>44</sup> However, a closer inspection of chemisorption in the “parallel” position indicates that the (10,0) nanotubes shows metallic behavior which is consistent with band structure study (Fig 3.8d).

We also noted that the DOS profile of -NH<sub>2</sub> functionalization of a (10,0) nanotube is reminiscent of -OH functionalization.<sup>40</sup> The projected DOS of the -NH<sub>2</sub> moiety shows that a weak impurity state is located at the Fermi level, and a stronger impurity state is located at



~1.2eV below the Fermi level (Fig 3.9i). It is considered that a -NH<sub>2</sub> moiety behaves as an acceptor impurity. J. Zhao et al.<sup>41</sup> showed that regardless of the types of covalent sidewall functionalization of SWNTs, sp<sup>3</sup> hybridization between the functional group and nanotube induces an impurities state near the Fermi level.

The electronic density of states of pure and nitrogenated armchair (5,5) nanotubes are displayed in Figure 3.10. The DOS of pure (5,5) tubes exhibit a finite DOS at the Fermi level, which renders it metallic. Figure 3.10b shows that nitrogen substitution develops an impurity state below the conduction bands (~0.6eV above the Fermi level), and a small valley is noted near to the Fermi level. The presence of small valleys in the vicinity of the Fermi level is also observed for other nitrogenated (5,5) tubes, and this is mainly due to the broken mirror symmetry of the  $\pi$ — $\pi^*$  band crossing as discussed in the band structure studies. For the case of (5,5) tube with pyridine-like doping (Fig 3.10c,d), a peak at the Fermi level is observed. However the projected DOS of the nitrogen impurities shows that the impurity states are mainly located below the Fermi level ~1.3eV, and the impurity states at Fermi level are very weak for ~5at% doping level. Likewise, we have also computed the DOS of (5,5) tubes with pyridine-vacancy without N-impurities, and its DOS also shows a sharp peak at the Fermi level (see Fig 3.10c, blue line). Thus the observed DOS peak at the Fermi level of the pyridine-like nitrogenated (5,5) tube is due the vacancy and not the nitrogen dopants. The DOS of pyridine-like nitrogenated (5,5) tubes is quite similar to (5,5) tubes with mono-vacancy (without N-impurities), except for a marked decrease (slight increase) at about -3.5eV and 0.7eV (-0.8eV and -1.3eV). The DOS of chemisorption of nitrogen adatoms and -NH<sub>2</sub> functionalization of (5,5) nanotubes is quite similar to the case of doped (10,0) nanotubes.

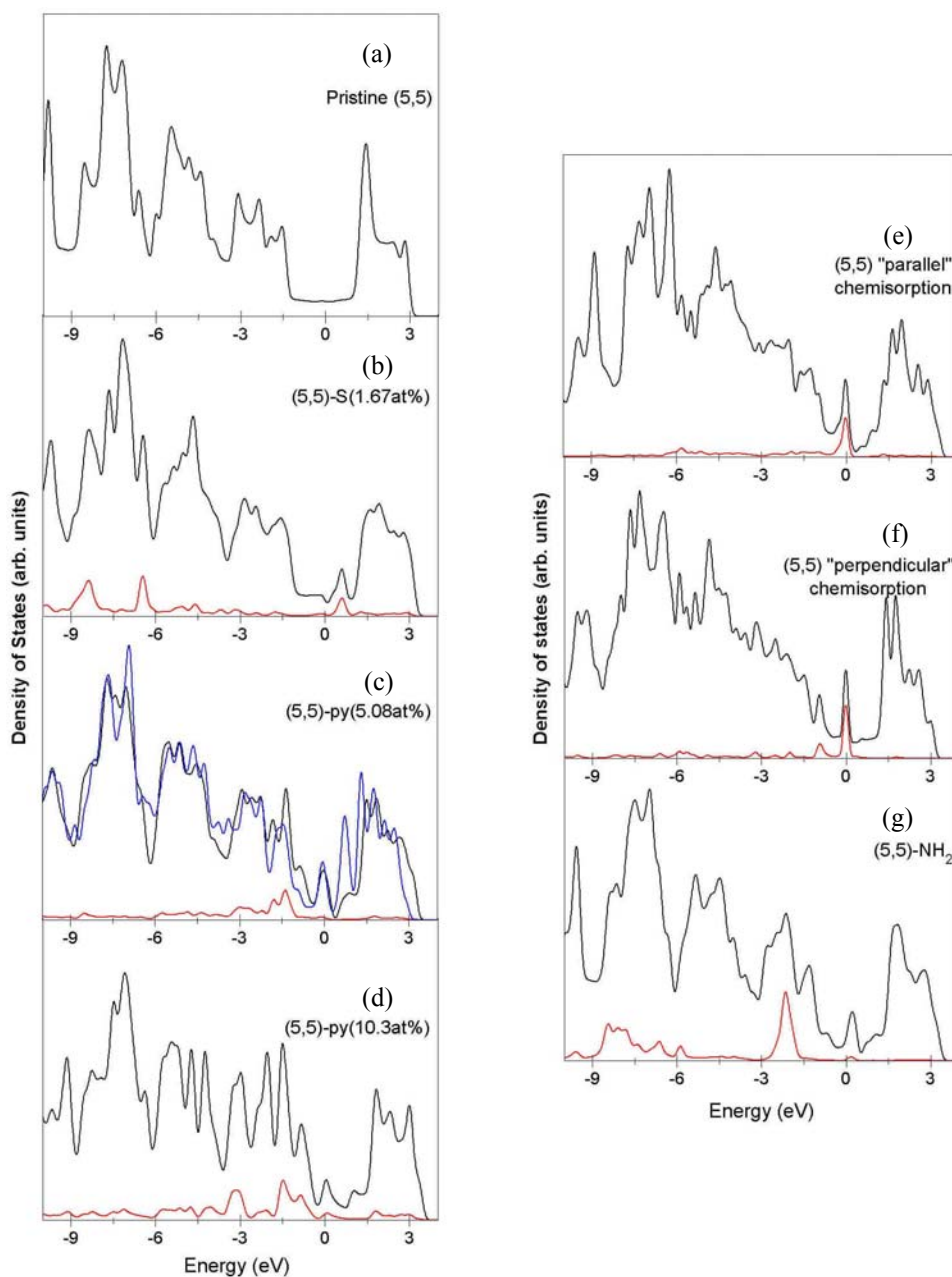


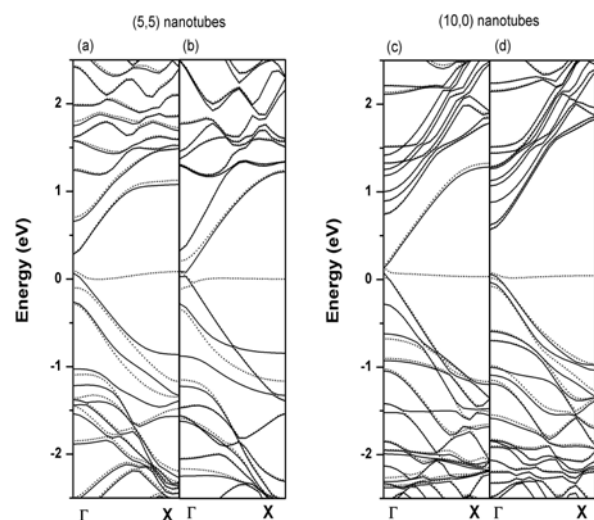
**Figure 3.10.** Total density of states (TDOS) of (a) pristine (5,5) nanotube, (b) nitrogen-substitution, (c,d) pyridine-like doping, (e,f) chemisorption of N adatoms, and (g)  $-\text{NH}_2$  functionalization. Projected DOS of nitrogen impurities and TDOS of undoped (5,5) nanotube with vacancy are indicated as red line and blue lines respectively. The Fermi level is at 0eV.

#### **3.2.4. Ionization potential energies**

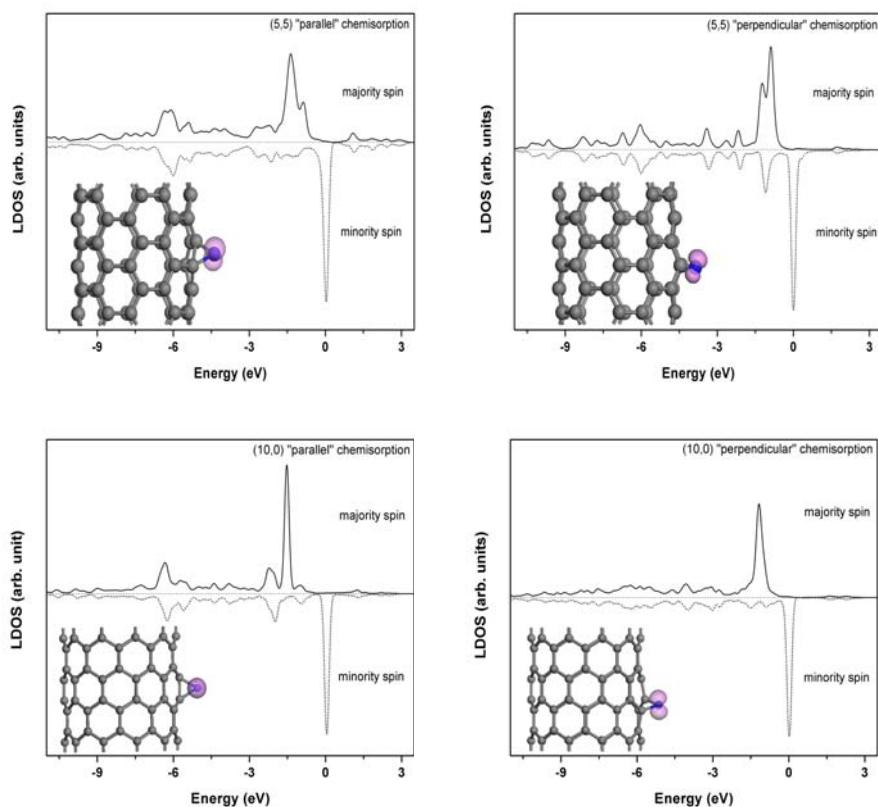
Although most theoretical calculations of field emission (FE) properties of carbon nanotubes are performed with finite clusters, the aim of using supercell geometries in this paper is to compare qualitatively the FE properties among the nitrogenated nanotubes. The IP values of the nitrogenated SWNTs are displayed in Table 3.2. The IP value of a pure (10,0) nanotube is calculated to be  $6.19\text{eV}/\text{\AA}$ , which is slightly lower than the IP value of  $6.4\text{eV}/\text{\AA}$  for a closed capped (5,5) nanotube reported by Maita et al.<sup>45</sup> The IP values of nitrogenated (10,0) nanotubes in increasing order are  $4.63\text{eV}$  ( $-\text{NH}_2$  functionalization),  $4.69\text{eV}$  (substitution),  $4.77\text{eV}$  (“parallel” chemisorption),  $4.85\text{eV}$  (pyridine-like doping) and  $5.25\text{eV}$  (“perpendicular” chemisorption). A similar trend of IP values is also noted for nitrogenated (5,5) nanotubes, but the IP values are lower than the nitrogenated (10,0) NTs. Therefore,  $-\text{NH}_2$  functionalization and nitrogen substitution might be advantageous to the field emission properties of carbon nanotubes. Our results indicate that the field emission properties of pristine carbon nanotubes can be experimentally improved using  $\text{N}_2$  /  $\text{NH}_3$  plasma treatment and N ion implantation to modify carbon nanotubes with  $\text{NH}_2$  moiety and  $sp^2$ -substitution respectively.

#### **3.2.5. Spin-unrestricted electronic properties of singly N-chemisorbed SWNTs**

We have also evaluated the electronic properties of the nitrogenated SWNTs using spin unrestricted calculations. The spin unrestricted (polarized) band structures and DOS of the nitrogenated SWNTs are very similar to the spin restricted calculations, except for nitrogen chemisorptions. Hence the spin polarized band structures and local DOS of the singly N-chemisorbed SWNTs are displayed as Figure 3.11 and Figure 3.12 respectively.

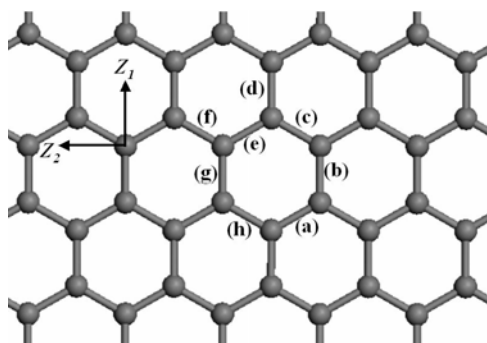


**Figure 3.11.** Spin-polarized band structures of singly N-chemisorbed SWNTs in (a,c) “parallel” and (b,d) “perpendicular” positions. Majority spin and minority spin electrons are denoted by solid and dotted lines respectively.



**Figure 3.12.** Spin-polarized local density of states of a single N adatom chemisorbed on (10,0) and (5,5) nanotubes. The pink isosurface of the spin density is set at the value of  $0.05e/\text{\AA}^3$ . The grey and blue spheres represent C and N atoms respectively.

It is noted that the minority spin band structures are quite similar to the spin restricted band structures, while the majority spin band structures are different. On the basis of Figure 3.11, majority spin LDOS peaks are located at about 0.9–1.5eV below the Fermi level, while minority spin LDOS peaks are located at the Fermi level. Furthermore the distribution of the spin polarization (insets of Fig 3.11), which comes from the  $p$  orbital of the N adatoms, is perpendicular to the C-N-C plane. This resembles the case of a N adatom chemisorbed on a graphene sheet whereby the spin distribution is also perpendicular to the C-N-C plane.<sup>32</sup> The magnetic moment ( $\mu_B$ ) of the chemisorbed (10,0) and (5,5) nanotubes are also tabulated in Table 3.2. The magnitude of the magnetic moment depends on the positions of the chemisorbed N adatoms, the chiralities and diameters of the SWNTs. A “parallel” chemisorption has a larger magnetic moment than a “perpendicular” chemisorption. Also, the magnitudes of the magnetic moment of a semiconducting (10,0) nanotube are larger than a metallic (5,5) nanotube. Ma et al.<sup>32</sup> reported that the magnitude of the magnetic moment of nitrogenated graphite is related to the coupling of the N adatom’s  $p$  orbital with the carbon  $\pi$  orbital. That is, a larger coupling of the  $p$ - $\pi$  orbital yields a smaller magnetic moment. The broken C-C bond in the “perpendicular” chemisorption may have given rise to a stronger coupling between the N adatom’s  $p$  orbital and the carbon  $\pi$  orbital, and therefore “perpendicular” chemisorption has a smaller  $\mu_B$  than “parallel” chemisorption. Likewise the more delocalized  $\pi$  orbital of a metallic (5,5) nanotube couples more strongly to the N adatom’s  $p$  orbital than a semiconducting (10,0) nanotube. Therefore N-chemisorbed (5,5) nanotube has a smaller magnitude of magnetic moment than (10,0) nanotube.

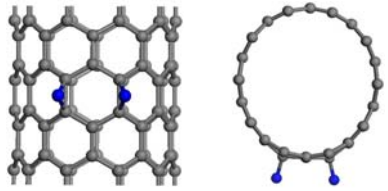
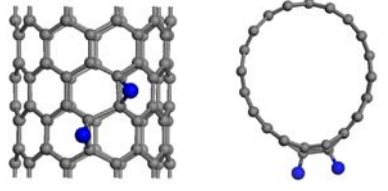
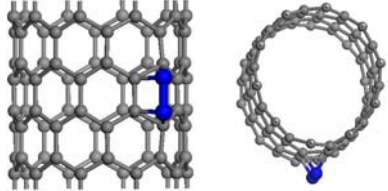
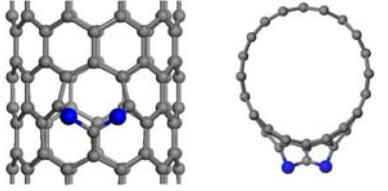
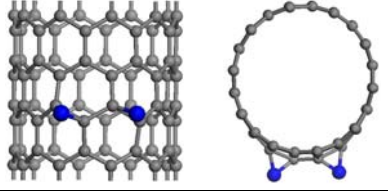
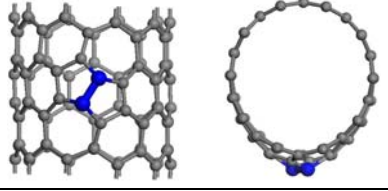
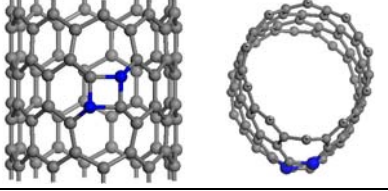


**Figure 3.13.** Possible configurations of two neighboring N adatoms chemisorbed on a graphene sheet.  $Z_1$  and  $Z_2$  directions represent the tubular axes of zigzag (10,0) and armchair (5,5) nanotubes respectively.

### 3.2.6. Structural stability and coalescence of two neighboring chemisorbed N adatoms

In the case of high density nitrogen chemisorption, the stability of the defects with respect to recombination into  $N_2$  molecules is an important issue to study. For example, intercalation of  $N_2$  molecules between the graphitic layers of nanotubes has been experimentally observed.<sup>38,39</sup> Thus in this section, we examine the structural stability of two neighboring N adatoms chemisorbed on SWNT surfaces and the coalescence process into a  $N_2$  molecule. We assume that the two N adatoms on a graphitic surface must be sufficiently close to each other before they coalesce to form a  $N_2$  molecule. In Figure 3.13, various positions for holding two neighboring N adatoms on a graphene sheet are considered and labeled from (a) to (h).  $Z_1$  and  $Z_2$  vectors in the figure represent the tubular axes of (10,0) and (5,5) nanotubes respectively. The structures with two neighboring N adatoms at the assumed positions are allowed to relax fully. The relaxed structures of SWNTs with two N adatoms are schematically presented in Table 3.5 and Table 3.6, together with the calculated bond lengths (or atom-to-atom separation distance), bond angles, and total energies.

**Table 3.5.** Relaxed zigzag (10,0) SWNTs with two chemisorbed N adatoms.

	Relaxed configurations	Remarks <sup>†</sup>
“Parallel” chemisorption		<u>(g)-(b) position</u> (N...N) = 3.182Å (C-C) = 1.513Å (C-N) = 1.460Å ∠CNC = 62.381° E <sub>T</sub> = -3155.478503Ha
		<u>(g)-(d) position</u> (N...N) = 3.200Å (C-C) = 1.481Å (C-N) = 1.480 / 1.392Å ∠CNC = 61.996° E <sub>T</sub> = -3155.4925991Ha
“Perpendicular” Chemisorption		<u>(c)-(a) position</u> (N-N) = 1.566Å (C-C) = 1.575Å (C-N) = 1.492 / 1.546Å ∠CNC = 62.425° E <sub>T</sub> = -3155.5578901Ha
		<u>(c)-(e) position</u> (N...N) = 2.252Å (C...C) = 2.164Å (C-N) = 1.374 / 1.395Å ∠CNC = 102.884° E <sub>T</sub> = -3155.5446995Ha
		<u>(c)-(f) position</u> (N...N) = 3.554Å (C-C) = 1.611Å (C-N) = 1.414 / 1.459Å ∠CNC = 68.171° E <sub>T</sub> = -3155.4927862Ha
		<u>(c)-(h) position</u> (N-N) = 1.491Å (C...C) = 2.408Å (C-N) = 1.383 / 1.429Å ∠CNC = 117.708° E <sub>T</sub> = -3155.6035269Ha
		<u>(f)-(h) position</u> (N...N) = 1.998Å (C...C) = n.a. (C-N) = 1.390/ 1.408Å ∠CNC = n.a. E <sub>T</sub> = -3155.6149498Ha

<sup>†</sup>(X...X) and (Y-Y) denote atom-to-atom separation length and bond length respectively. E<sub>T</sub> is the total energy of the system in unit of Hartree. ∠CNC denotes the average bond angle. Positions of N adatoms and carbon-carbon lengths are labeled according to Fig 3.13.

**Table 3.6.** Relaxed armchair (5,5) SWNTs with two chemisorbed N adatoms.

	Relaxed configurations	Remarks <sup>†</sup>
“Perpendicular” chemisorption		<u>(g)-(b) position</u> (N-N) = 1.537Å (C...C) = 2.309Å (C-N) = 1.440Å ∠CNC = 106.630° E <sub>T</sub> = -2394.0002572Ha
		<u>(g)-(d) position</u> (N...N) = 3.524Å (C...C) = 2.137Å (C-N) = 1.391 / 1.350Å ∠CNC = 102.377° E <sub>T</sub> = -2393.8851250Ha
“Parallel” Chemisorption		<u>(c)-(a) position</u> (N...N) = 3.251Å (C-C) = 1.518 / 1.519Å (C-N) = 1.441 / 1.468Å ∠CNC = 62.977° E <sub>T</sub> = -2392.8118746Ha
		<u>(c)-(e) position</u> (N-N) = 1.109 (free N <sub>2</sub> ) (C...C) = n.a. (C-N) = n.a. ∠CNC = n.a. E <sub>T</sub> = -2394.0731784Ha
		<u>(c)-(f) position</u> (N...N) = 2.903Å (C-C) = 1.515Å (C-N) = 1.436 / 1.471Å ∠CNC = 62.809° E <sub>T</sub> = -2393.8028447Ha
		<u>(c)-(h) position</u> (N...N) = 3.128Å (C-C) = 1.566Å (C-N) = 1.437 / 1.458Å ∠CNC = 65.525° E <sub>T</sub> = -2393.7949533Ha
		<u>(f)-(h) position</u> (N...N) = 3.444Å (C-C) = 1.506Å (C-N) = 1.435 / 1.479Å ∠CNC = 62.256° E <sub>T</sub> = -2393.8252540Ha

<sup>†</sup>(X...X) and (Y-Y) denote atom-to-atom separation length and bond length respectively. E<sub>T</sub> is the total energy of the system in unit of Hartree. ∠CNC denotes the average bond angle. Positions of N adatoms and carbon-carbon lengths are labeled according to Fig 3.13.



Most of the relaxed structures in Tables 3.5 and 3.6 are very similar to their counterparts of single N adatom chemisorption, except that the number of N adatoms increases from one to two. That is, the bridged C-C bonds are also broken for “perpendicular” chemisorption (see (c)-(e) position of (10,0) tube and (g)-(d) position of (5,5) tube), with the exception of “perpendicular” (c)-(f) position of (10,0) nanotube whereby the bridged C-C bonds are prevented from being broken due to the “squeezing” of the C-C at position (e). The relaxation of the “parallel” chemisorptions of two N adatoms can also be anticipated from the results of single chemisorption (see (g)-(b), and (g)-(d) positions of (10,0) tubes, and (c)-(a),(c)-(f), (c)-(h) & (f)-(h) positions of (5,5) tubes).

However, some of the structures in Tables 3.5 and 3.6 are unexpected and dissimilar to the above listed ones. Their structures are more complex and richer in defects, as expatiated below. In the first case of this series, the (5,5) (c)-(e) (“parallel” chemisorption) in Table 3.6, the relaxed structures yield a pristine (5,5) nanotube and a N<sub>2</sub> molecule. In comparison with other “parallel” positions of (5,5) nanotube, the N adatoms in the (c)-(e) position can be considered as unstable and, upon relaxation, can form N<sub>2</sub> molecule. For the two N adatoms chemisorbed at the (c)-(e) positions in a (10,0) nanotube (“perpendicular” chemisorption), however, the relaxed structures yield a (10,0) nanotube chemisorbed with two N adatoms and two broken C-C bonds. Geometry optimization revealed that the nitrogen-nitrogen repulsion had caused the two chemisorbed N adatoms of (5,5) nanotube at (c)-(e) position to elongate their C-N bonds, and transform the C-N bridges to become C-N single bonds. The two C-N single bonds are able to rotate and form an intermediate N-N bond before breaking the C-N bonds and escaping as a free N<sub>2</sub> molecule. However for chemisorbed two N adatoms on (10,0) at (c)-(e) positions (“perpendicular”), the broken C-C bond kept the N-to-N atoms farther apart, not forming a free N<sub>2</sub>. In the second cases of the series, the formation of N-N bond is possible at some of the “perpendicular” positions (see (c)-(a) and (c)-(h) positions for (10,0) tube, and (g)-(b) position for (5,5) tube), which is due to the breaking or elongating of bridged C-C bonds and allowing the two

N adatoms to come closer together to form a N-N bond. Consequently, pentagon-heptagon pair defects are formed on these SWNTs if the bridged C-C bonds are broken. These N-N bond lengths are  $\sim 1.49\text{-}1.56\text{\AA}$ , which is longer than the bond length of a free  $\text{N}_2$  molecule ( $1.11\text{\AA}$ ), but close to the N-N bond lengths of boron nitride nanotubes with pentagon-heptagon defects.<sup>46</sup> In the third case of the series, the “perpendicular” (f)-(h) positions of (10,0) tube consists of fourfold and sevenfold ring defects, and the total energy is the lowest among the positions considered (see Table 3.5). Besides breaking the C-C bonds at position (f) and (h) (see Figure 3.13), the C-C bond at position (g) is torn apart due to the formation of a weak N-N bond which is subsequently broken as well. The relaxed C-N bond is  $\sim 1.40\text{\AA}$ , which is close to the C-N bond length observed in  $\text{sp}^2$  substitution. Bettinger et al.<sup>47</sup> has investigated a 4774 defect (fourfold and sevenfold ring defects) in carbon nanotube, but a 5775 defect (fivefold and sevenfold ring defects, or simply Stone-Wales defect) is more stable. Although the relaxed “perpendicular” position (f)-(h) of (10,0) nanotube does not resemble the 4774 defect, our results suggest that the presence of N impurities can give rise to a single fourfold and two sevenfold ring defects in semiconducting carbon nanotubes. Furthermore the relaxed structures of the N dopants are no longer protruding out the SWNT surface and substantially different from other cases of chemisorption.

On the basis of geometry optimization of the SWNTs with two neighboring N adatoms, we have demonstrated the important effects of the relative adsorption positions of N adatoms and the nanotube chiralities on the tube structural stability and the resultant defects.

We have applied the GST method<sup>36</sup>, as implemented in DMol<sup>3</sup> code, to search the transition state of the coalescence process of two chemisorbed N adatoms. We tested the method for the case of a graphene sheet with two chemisorbed N adatoms. As shown in Figure 3.14a, the transition state consists of one N adatom bridging over the C-C bond while the other forming a single bond with the graphene sheet. Furthermore, the two chemisorbed N adatoms had severely distorted the graphene sheet. The N $\cdots$ N separation of this transition state is  $2.0\text{\AA}$  and the reaction energy barrier is  $0.80\text{eV}$ , which is in good agreement with a previous report.<sup>32</sup>

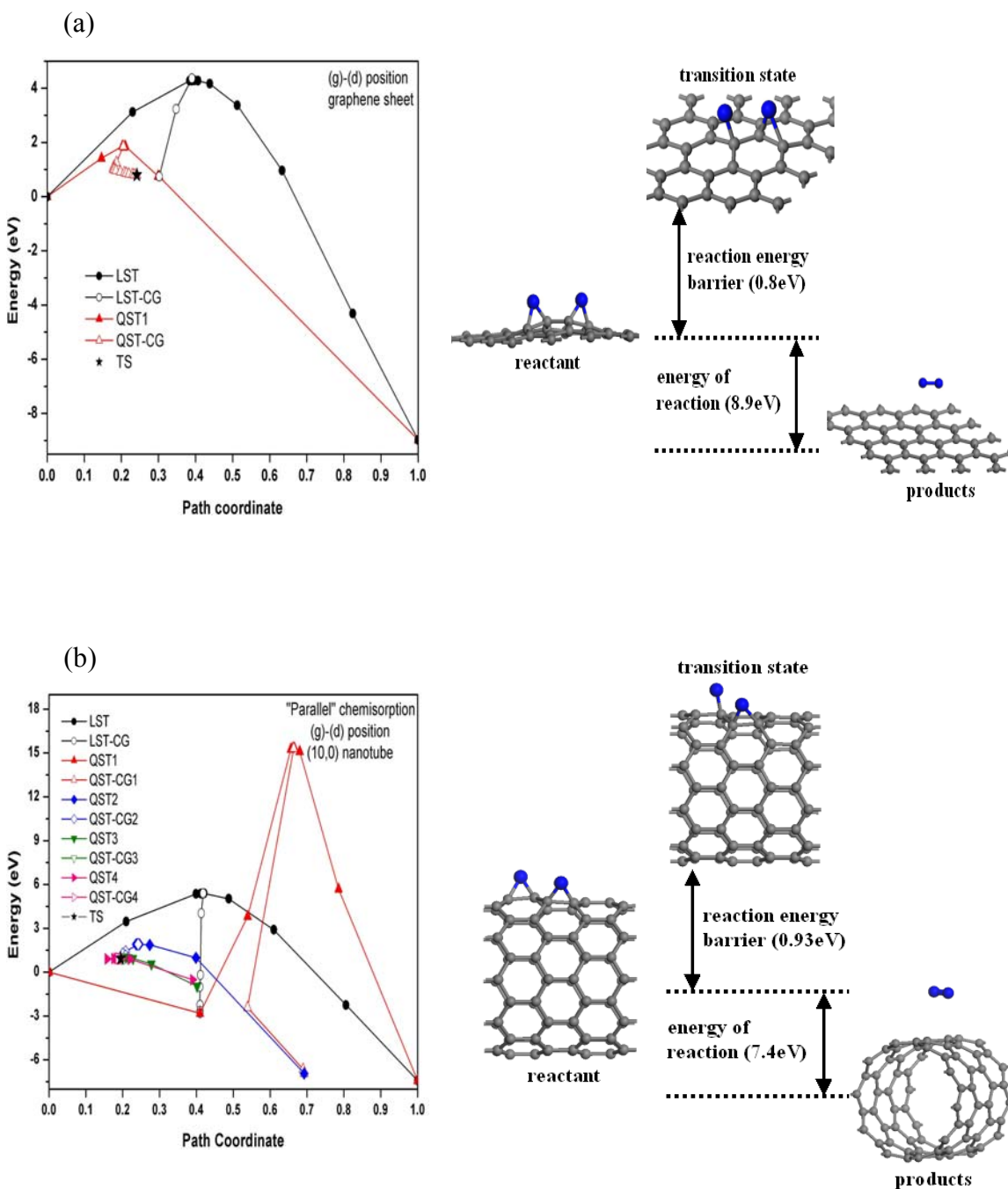


Figure 3.14. (Continues next page)

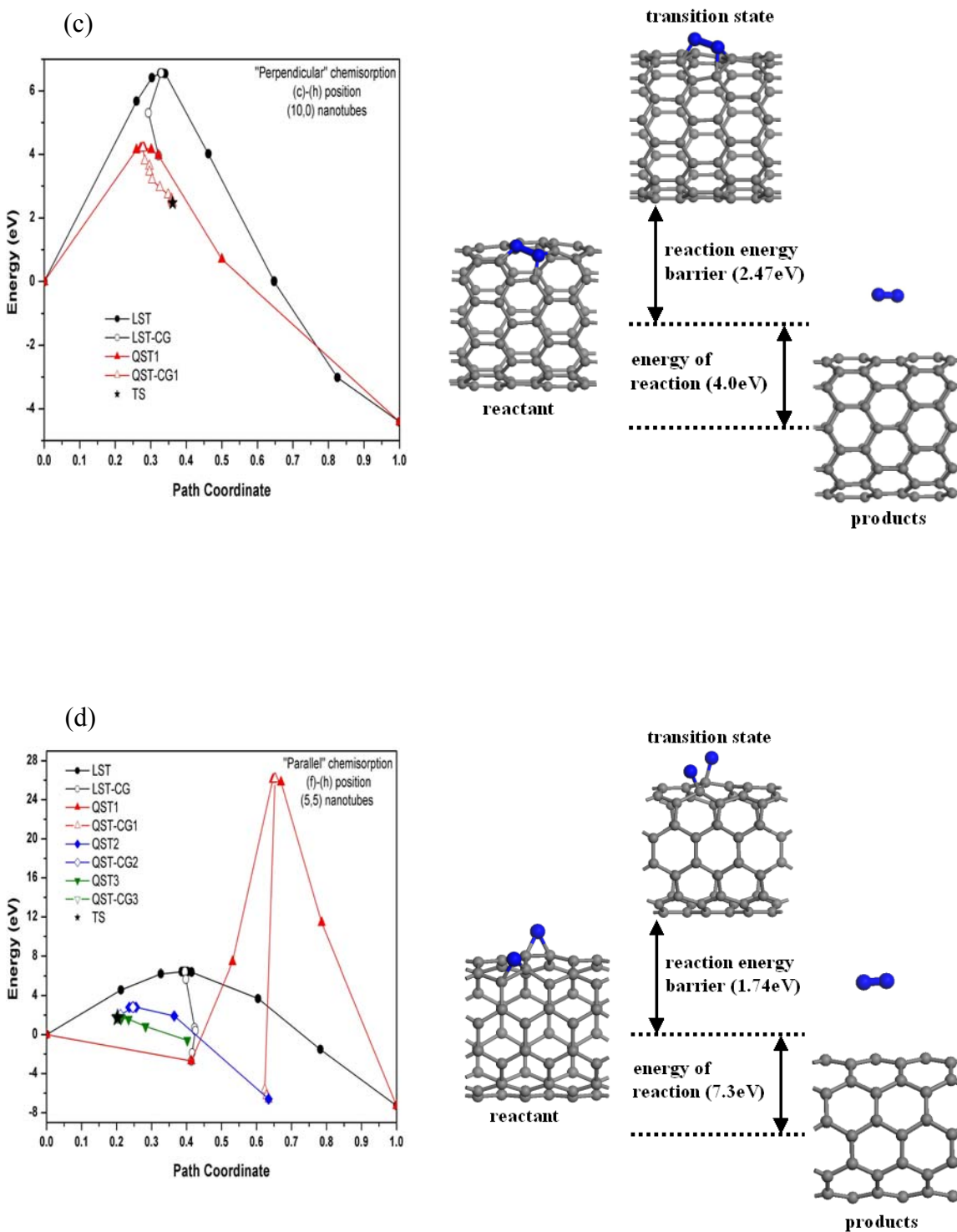
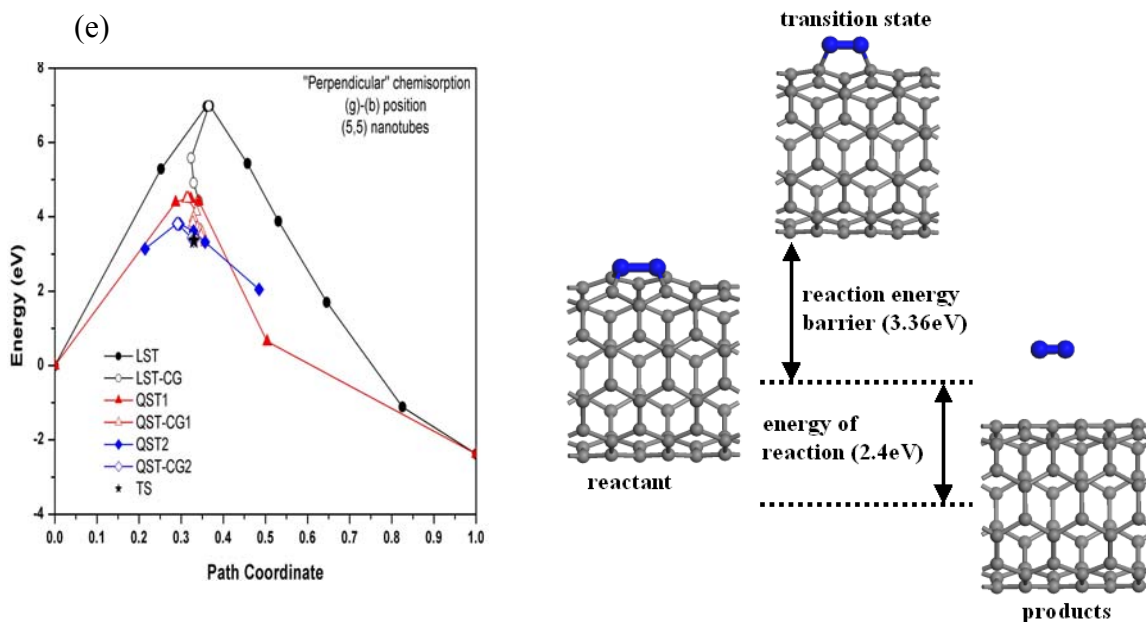


Figure 3.14. (Continues next page)



**Figure 3.14.** Energy versus path coordinate during transition state search. The path coordinate “0” represents the “reactant” (SWNT with two chemisorbed N adatoms), while path coordinate “1” represents the “products” (SWNT + a free  $N_2$  molecule). Case (a), (b,c) and (d,e) are the TS search and energy diagrams for a graphene sheet, (10,0) and (5,5) nanotubes respectively. *Energy diagrams are not drawn to scale.*

Therefore we had conducted the LST/QST search for selected nitrogenated SWNTs using the same procedure. For (10,0) nanotubes, chemisorption at positions (g)-(d) and (c)-(h) were chosen because it had the lowest total energies. However (c)-(h) positions of (10,0) is preferred over (f)-(h) positions because it still retained the C-N brigdelike bonds. Similarly, (f)-(h) and (g)-(b) positions were chosen for nitrogenated (5,5) nanotubes since these positions have the lowest total energies. The coalescence processes of two N adatoms chemisorbed on SWNTs into a free  $N_2$  molecule are presented in Figure 3.14b-e. It is noted that the reaction energies barrier of SWNTs are higher than the graphene sheet. The coalescence of N adatoms with “perpendicular” chemisorption is less complex than the “parallel” chemisorption (involving fewer numbers of LST/QST search). The reaction energy barrier (energy of reaction) of “perpendicular” chemisorption is much higher (lower) than the “parallel” chemisorption. This implied that it is

more difficult to coalesce two chemisorbed N adatoms into  $N_2$  molecule in the “perpendicular” positions than the “parallel” positions. The reaction energy barrier of (10,0) nanotube is  $\sim 0.8\text{eV}$  lower than (5,5) nanotube, which might be due to the larger curvature of (10,0) nanotube and stronger C-N bonding of (5,5) nanotube. It can be surmised that the intercalation of  $N_2$  molecules in nanotube interlayer are most likely due to the coalescence of N adatoms chemisorbed in “parallel” configurations.

### **3.2.7. Conclusions**

The structural and electronic properties of nitrogenated (5,5) and (10,0) have been studied using first-principles methods. The effects of different types of nitrogenation have been elucidated from the band structures, density of states (DOS), and molecular orbital. Our calculations indicate that the substitutional nitrogenation,  $-NH_2$  functionalization as well as chemisorption will convert semiconducting (10,0) nanotubes ( $\sim 0.7\text{ eV}$  band gap) into metallic; while pyridine-like nitrogenation can only shorten the band gap, converting the (10,0) tube to narrow gap ( $< 0.2\text{ eV}$ ) semiconductors. For metallic (5,5) nanotubes the N-doping is shown to significantly enhance the state density at the vicinity of Fermi level, which can enhance its chemical activity. Comparing among the calculated ionization potentials of the various nitrogenated nanotubes indicates that covalent sidewall  $-NH_2$  functionalization is as effective as direct substitutional doping in lowering the IP values which are beneficial for field emission. The magnetic moment of chemisorbed N adatom ranges from  $0.5\text{--}0.7\mu_B$  and depends on the nanotube chirality and diameter, and the orientation of the chemisorbed N adatom as well. Our study also indicates that structural relaxation of SWNTs with two chemisorbed N adatoms in certain “perpendicular” configurations may result in the formation of N-N bond, mainly due to the breaking or elongating of the bridged C-C bonds. The coalescence of two neighboring N adatoms into a  $N_2$  molecule needs to overcome an energy barrier in the range between  $0.9$  and  $3.4\text{eV}$ , depending on the N-chemisorption configuration and tubular diameter.

### **3.3. First-principles study of carbon nanotubes with bamboo-shape and pentagon-pentagon fusion defects**

#### *Introduction*

Single-walled carbon nanotubes (SWNTs) are seamlessly rolled-up graphene sheets. They can be metallic or semi-conducting, depending on their tubular diameter and chirality.<sup>1</sup> The geometry-dependent properties of SWNT strongly implies that structural changes including the introduction of defects, dopants, twists and deformations to the carbon bond network will alter the electronic properties. Carroll et al.<sup>48</sup> and De Vita et al.<sup>49</sup> have conducted scanning tunnelling spectroscopy studies and tight binding calculations to correlate the electronic properties of SWNT and the topology of the carbon bond network at the tip. The relative position of pentagons in the SWNT tips in the curved tips was found to be responsible for the observation of localized resonant states. Recently Okada et al.<sup>50</sup> reported that carbon nanotubes with topological line defects (pentagon-octagon rings) possessed a small but finite ferromagnetic moment. The nature of the ferromagnetic spin ordering was associated with edge-localized states of graphite flakes. Maiti et al.<sup>51</sup> also showed that the bandgap of nanotubes could be modulated under an atomic deformation. This opens up a possibility of changing the conductance of SWNTs with mechanical strain.

Another interesting topological defect of carbon nanotube (CNT) is the formation of compartments along the tube axis. Compartmentalized CNTs have been observed in pure, nitrogen-doped and boron-doped states.<sup>52-58</sup> These compartmentalized CNTs are also termed bamboo-shaped (BS) nanotubes or carbon nanobells. Theoretical calculation<sup>59</sup> indicates that the dopants of CNTs produce their own local strains and result in atomic-scale deformations, and consequently these doped CNTs tend to adopt a bamboo-shaped morphology. Scanning tunnel microscopy of Sun et al.<sup>60</sup> revealed humps along the sidewalls of nitrogen-doped BS-nanotubes, which are attributed to the presence of an acceptor state. Pure CNTs with bamboo-shapes have

also been synthesized, and the morphologies are particularly affected by the choice of catalysts.<sup>52</sup> Moreover, BS-nanotubes show better electrochemical properties than normal concentric-type nanotubes.<sup>52</sup> These findings demonstrate an interesting interplay between the electronic properties of carbon nanotubes and the structure of carbon bond network.

In this section 3.3, I report the first-principles study of single-walled carbon nanotubes with bamboo-shape and pentagon-pentagon 5-5 fusion ring. Previous semi-empirical (PM3) study of bamboo-shaped nanotubes shows such structures are stable.<sup>61</sup> However, a density functional theory (DFT) study of bamboo-shaped nanotubes will provide better insights into its electronic properties. The variation of local density of electronic states (LDOS) is investigated along the BS-nanotubes axes and chemical reactivity of the topological defects is also studied using frontier orbital theory of Fukui, which was further developed by Parr and Yang.<sup>62</sup> From the calculation, the strong resonance of LDOS and chemical activity are both found to correlate to topological defects of the bamboo-shaped structure.

### **3.3.1. Computation methods**

The self-consistent field (SCF) electronic structure calculations are performed based on density functional theory (DFT) with localized basis (Dmol<sup>3</sup> available from Accelrys).<sup>4</sup> A double numerical basis including d-polarization function (DND) is used for the relativistic all-electron SCF calculations. The density functional is treated by the local density approximation (LDA) with exchange-correlation parametrized by Perdew and Wang.<sup>63</sup> Geometry optimisations are performed with the Broyden-Fletcher-Goldfarb-Shanno (BFGS) algorithm with convergence criterion of  $10^{-3}$  au on gradient and displacement, and  $10^{-5}$  au on the total energy and electron density. The Harris functional<sup>64</sup> is used to speed up the geometrical relaxation of the (10,0) bamboo-shaped nanotube only, and subsequent single-point energy calculations are carried out without the use of Harris functional. Polatoglou et al.<sup>65</sup> had applied the LDA-Harris functional to study *sp*- and *d*-bonded metals (Be, Al, V, and Fe), covalently bonded Si and ionic NaCl solids,



and the calculated cohesive energies, lattice constant and bulk moduli compared well with those derived from conventional fully self-consistent calculations. Noteworthy, experimentally observed bamboo-shaped carbon nanotube are multi-walled carbon nanotubes, and presently there is no report of bamboo-shaped single-walled carbon nanotube. Thus the use of Harris functional to model the structure of hypothetical bamboo-shaped (10,0) SWNT is assumed to give a reasonable structural approximation. In addition, DFT calculations of (5,5) nanotube with heptagon-pentagon pair defect (consists of a pentagon-pentagon 5-5 fusion ring, see Figure 3.18) have been carried out to elucidate the role of pentagon defects. We denote this particular heptagon-pentagon pair defect with 5-5 fusion ring simply as 7557 defect. Five  $k$  points along the direction of the tube axis were chosen according to the Monkhorst-Pack scheme<sup>34</sup> for the sampling of  $k$  points in the Brillouin zone. Good convergence was obtained with these parameters. A hexagonal lattice was used to simulate the single-walled nanotubes, with a wall-to-wall distance of at least 10Å, sufficient to avoid in-plane interactions between nanotubes in adjacent unit cells. The unit lengths of bamboo-shaped (10,0), (12,0) and (5,5) are 12.68Å, 8.46Å and 9.76Å respectively. The Fukui function is determined for a radical attack,  $f^0(\mathbf{r})$ , which represents the average of the Fukui functions for electrophilic,  $f(\mathbf{r})$ , and nucleophilic attacks  $f^+(\mathbf{r})$ . The Fukui function measures the sensitivity of the charge density,  $\rho(\mathbf{r})$ , with respect to the loss of electrons (electrophilic attack,  $f(\mathbf{r})$ ), or gain of electrons (nucleophilic attack,  $f^+(\mathbf{r})$ ) via the expressions:

$$f^+(\mathbf{r}) = \frac{1}{\Delta N} [\rho_{N+\Delta}(r) - \rho_N(r)] \quad [3.5]$$

$$f(\mathbf{r}) = \frac{1}{\Delta N} [\rho_N(r) - \rho_{N-\Delta}(r)] \quad [3.6]$$

The Fukui functions are computed using finite difference approximation and the self-consistent charge densities for neutral molecule, cation and anion. A value of  $\Delta N=0.1$  is used in the computation in order to achieve faster SCF convergence.

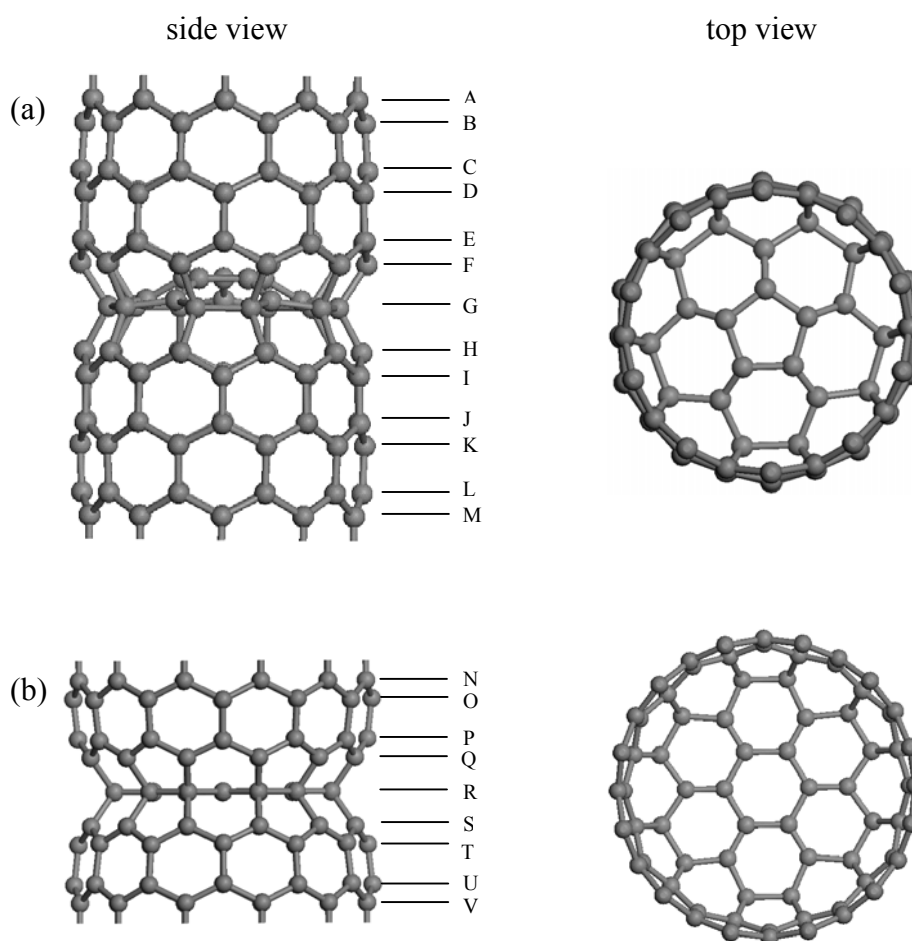


**Figure 3.15.** Relaxed geometries of bamboo-shaped (a) (10,0) nanotube, and (b) (12,0) nanotube with pentagon defects.

### 3.3.2 Density of States and Fukui functions

The relaxed geometries of the bamboo-shaped (10,0) and (12,0) nanotubes are displayed in Figure 3.15. The BS-(10,0) nanotube was constructed from a pure zigzag (10,0) nanotube by removing the G row of carbon atoms, and joining a compartment to the F and H rows of carbon atoms (see Fig 3.15a). The compartment of BS-(10,0) is made up of 5 hexagons joined to a

central pentagon, and it is curved toward one ends of the tube. This compartment of BS-(10,0) is similar to the tip of  $C_{70}$ . Similarly, the BS-(12,0) nanotube was constructed by joining a coronene molecule with two pure zigzag (12,0) nanotubes (see Fig 3.15b). The C-C bond lengths of the relaxed BS-(10,0) and BS-(12,0) nanotubes have a range of 1.38-1.49Å and 1.37-1.51Å respectively, which indicate a mixture of  $sp^2$  and  $sp^3$  bonds.

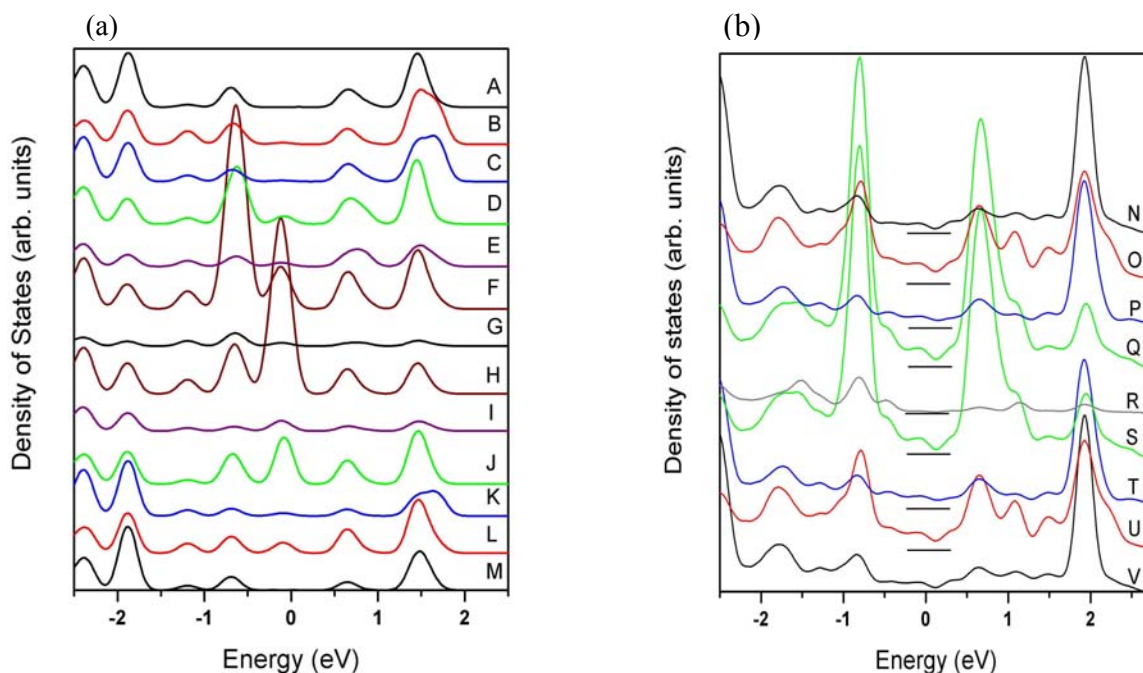


**Figure 3.16.** Localized density of states (LDOS) of bamboo-shaped (10,0) nanotube (a) and armchair (12,0) nanotube (b). A-to-M and N-to-V are the label of the carbon rows in the (10,0) tube (see Fig. 3.15a) and in (12,0) (see Fig. 3.15b) respectively. The Fermi level is located at 0eV. The LDOS has been shifted vertically for clarity of presentation.

Figure 3.16a shows the LDOS of bamboo-shaped (10,0) nanotube within LDA calculations. For the carbon atoms at positions A and M, the LDOS of BS-(10,0) nanotube is similar to that of pure cylindrical (10,0) nanotube. Moving from A to E (or from position M to I), a new peak begins to develop at  $\sim 0.1$ eV below the Fermi level of the BS-(10,0) nanotube. However, for F carbon atoms, the LDOS peaks located at -0.65eV and -0.1eV are intensified

drastically. Likewise, a strong resonance of LDOS peaks at  $-0.1\text{eV}$  and  $-0.65\text{eV}$  occurs at H carbon atoms. For G carbon atoms at the partition in the BS-(10,0) nanotube, the localized density is rather low. The conduction band becomes almost depleted and only weak states are discernible in the valence band. Thus the LDOS of BS-(10,0) along the tube axis exhibits a strong resonance at F and H, the positions adjacent to the partition of the BS-tube and a relatively weaker resonance at D and J. The LDOS peak at  $-0.65\text{eV}$  is observed for all carbon positions while the resonance state at  $-0.1\text{eV}$  is observed mainly at the locations near the partition (G) of the bamboo structure and hence can be regarded as a defect acceptor state. The local increase in the density of states of BS-(10,0) suggests the high chemical reactivity, particularly, at the vicinity positions, F and H.

Ab initio study indicates that pristine (12,0) nanotube is metallic due to the finite state density at the Fermi level. However, the LDOS of BS-(12,0) nanotubes in Fig. 3.16b exhibit a small valley (pseudogap) at  $\sim 0.1\text{eV}$  above the Fermi level. The opening of a pseudogap has also been reported for doped metallic carbon nanotubes, e.g. adsorbed Cu atoms,<sup>42</sup> surface functionalization and substitution,<sup>41</sup> which is attributed to the broken symmetry of  $\pi-\pi^*$  band. In Figure 3.16b the LDOSs of BS-(12,0) show a mirror-image behaviour with respect to the partition R. Moving from N to O (likewise from V to U) an increment of the LDOS intensity at the Fermi level is noted and the peaks at about  $0.6\text{eV}$ ,  $1.1\text{eV}$ , and  $-0.8\text{eV}$  rise. However, moving from O to P (likewise from U to T) the LDOS becomes similar to that at N (V) position. For position Q carbon atoms, which involve the pentagon-hexagon ring, a large enhancement of LDOS is observed at about  $0.7\text{eV}$  and  $-0.8\text{eV}$ , and the pseudogap deepened as well. For position R, carbon atoms at the partition of the bamboo-shaped (12,0) nanotube, the LDOS at the Fermi level and the conduction band are almost depleted, and only some weak states are observed at the valence level. This observation is similar to the LDOS of bamboo-shaped (10,0) nanotube as discussed previously. Thus the LDOS of BS-(12,0) nanotube exhibits a strong resonance at position Q and S, and a moderate resonance at position O and U.

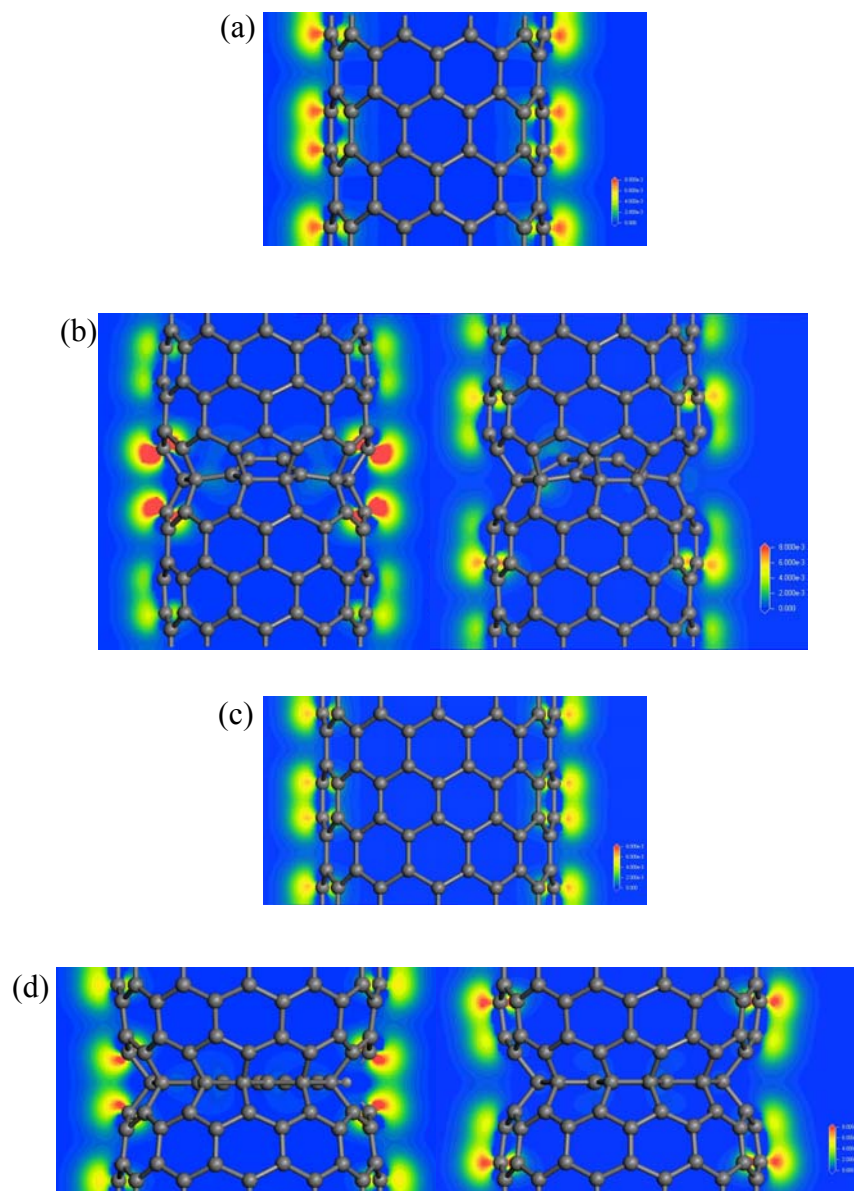


**Figure 3.17.** Fukui functions (FF) for radical attack computed for (a) pristine (10,0), (b) bamboo-shaped (10,0), (c) pristine (12,0) and (d) bamboo-shaped (12,0) nanotubes. Isodensity surface is set from zero (blue color) to 0.008 (red color) a.u./Å<sup>2</sup>. The red region denotes high reactivity, while blue region denotes low reactivity

Figure 3.17 compares the Fukui function,  $f^0(r)$ , of pristine and bamboo-shaped nanotubes for radical attack. A uniform distribution of  $f^0(r)$  field is noted both for pristine (10,0) and (12,0) carbon nanotubes, which means that pristine carbon nanotubes do not have any preferred site for chemical attacks. However the red  $f^0(r)$  field in Fig. 3.17a indicates that (10,0) nanotube is more reactive than (12,0) whose blue  $f^0(r)$  field in Fig. 3.17c denotes low reactivity. This could be due to the semiconducting and smaller diameter of (10,0) compared to (12,0) nanotube. Clearly, the  $f^0(r)$  field of BS-(10,0) and BS-(12,0) is non-uniform and strongly polarized around the F and H carbon atoms in (10,0) and O and Q in (12,0) (see Figs. 3.17b and 3.17d). A slightly higher reactivity is also noted around the D and J carbon atoms in (10,0), though not as reactive as the F and H carbon atoms. Thus the topological defects of bamboo-shaped structure have generated preferred sites for chemical attacks. Interestingly, the reactivity of the bamboo-shaped nanotubes (i.e. Fukui function,  $f^0(r)$ ) is closely related to the calculated LDOS. Generally, high  $f^0(r)$  regions of the BS-nanotubes coincide with the sharp resonant states. This finding qualitatively agrees well with literature that the tip of carbon nanotube possesses resonant state and it is most likely to be susceptible to chemical attacks.<sup>48,49</sup>

To understand the roles of pentagon defects of bamboo-shaped nanotubes better, the electronic properties and Fukui function of a (5,5) nanotube with a heptagon-pentagon pair defect (7557 defect), which consists of a pentagon-pentagon 5-5 fusion ring, are investigated. This particular 7557 defect is different from the Stone-Wales defect (5775 defect) which has a heptagon-heptagon 7-7 fusion ring. The purpose of choosing this particular 7557 defect with a 5-5 fusion ring is to elucidate the electronic and chemical reactivity of pentagon defects. The fully relaxed structure and bond lengths of the 7557 defect are shown in Figure 3.18. Particularly, the C1-C2 bond length of the 5-5 fusion ring is 1.59Å (sp<sup>3</sup> bond) which is longer than the normal C-C bond length (~1.42Å) of graphite.

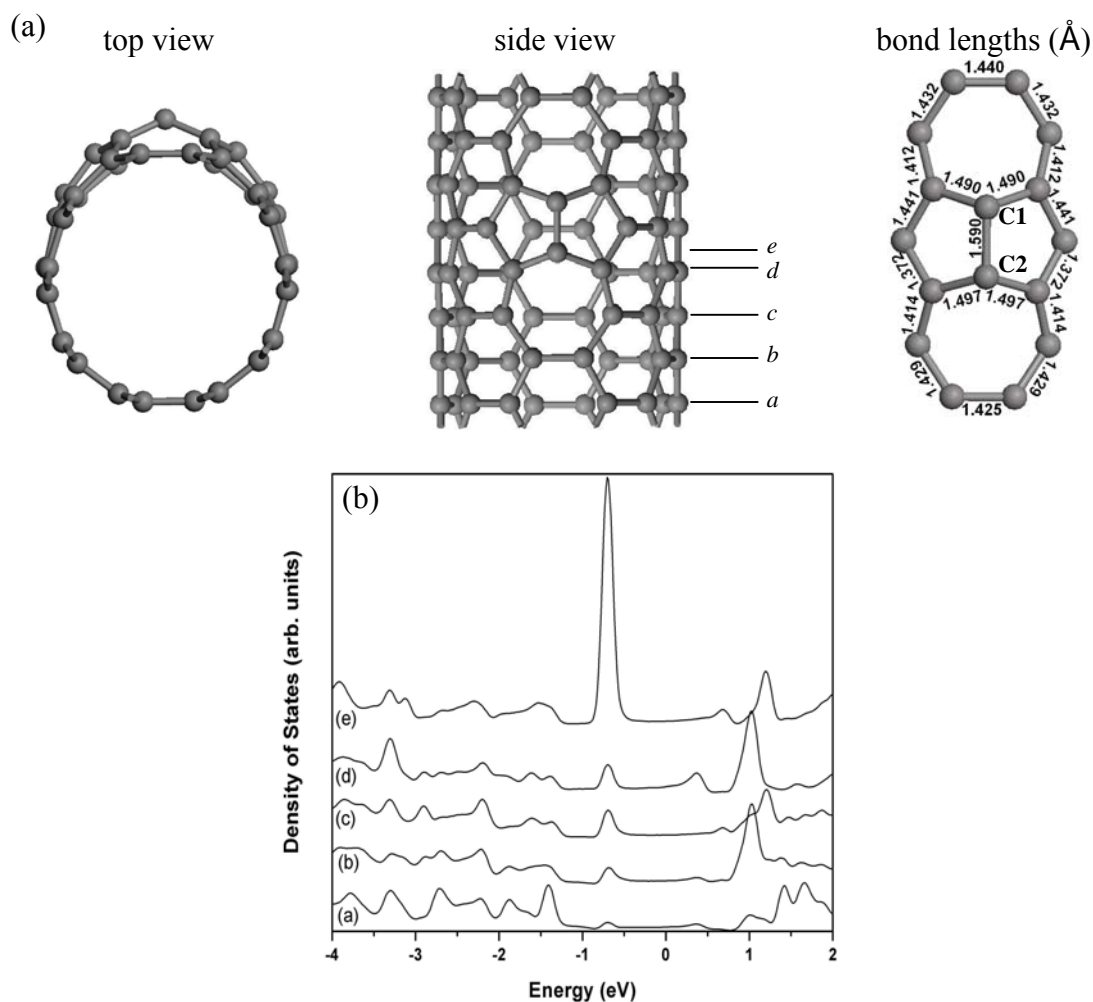


**Figure 3.18.** (a) Relaxed structure, bond lengths and (b) localized density of states of (5,5) nanotube with a pentagon-pentagon fusion ring. The Fermi level is located at 0eV. The LDOS has been shifted vertically for clarity of presentation.

Figure 3.18b shows the LDOS of the (5,5) nanotube with a 7557 defect. A sharp resonant peak at -0.68eV is noted at carbon “e”. Therefore the sharp resonance at -0.68eV in (5,5) nanotube with 7557 defect is attributed to the presence of the pentagon-pentagon fusion ring. Figure 3.19 shows the Fukui function of (5,5) nanotube with 7557 defect. A very high chemical reactivity is concentrated at the 5-5 fusion ring, while a much weaker chemical reactivity is noted at the heptagon rings and the defect-free regions. Similarly the observation of high chemical

reactivity at the 5-5 fusion ring is strongly correlated the sharp resonant states. The presence of a 5-5 fusion ring distorts the  $sp^2$  carbon network into  $sp^3$  (bond length of C1-C2 1.59Å), and consequently an electron localized on the  $sp^3$  orbital tends to be more reactive. Therefore, on the basis of the DFT calculations of SWNTs with bamboo-shape and 5-5 fusion ring, it can be surmised that the observation of sharp resonance and high chemical reactivity comes from the pentagonal defects.

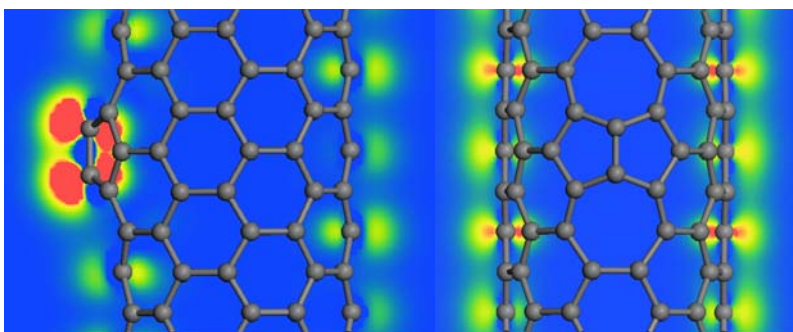


**Figure 3.19.** Fukui functions (FF) for radical attack computed for a (5,5) nanotube with a pentagon-pentagon fusion ring. Isodensity surface is set from zero (blue color) to 0.008 (red color) a.u./Å<sup>2</sup>. The red region denotes high reactivity, while blue region denotes low reactivity.

The electronic properties of SWNTs with bamboo-shape and 5-5 fusion ring are reminiscent of the electronic properties of bent SWNTs or SWNTs with semiconducting-metal junctions.<sup>66,67</sup> For example, Lambin et al.<sup>66</sup> had studied the structural and electronic properties of bent carbon nanotubes which possessed a pair of diametrically opposed pentagon and heptagon defects. These bent carbon nanotubes can be constructed by joining a zigzag (n,0) nanotube and an armchair (m,m) nanotube with similar diameters. The presence of such odd-membered rings (particularly pentagon rings) destroyed the electron-hole symmetry of the DOS within the vicinity of the defects, and the distribution of the unoccupied states was more affected than that of the



occupied states. When moving from the pentagon defect along the axis of an armchair nanotube, the local density of states was noted to oscillate around the value of the DOS plateau of the nanotube. The Fermi wavelength, which is three times the lattice constant of an armchair nanotube, controls the period of the LDOS oscillation. The oscillations of the DOS indicate the presence of standing waves generated by metallic Bloch states with wave vectors close to the Fermi  $k_F$ , and the stationary Bloch wave takes place over a large distance in front of the interface and its period is triple that of the isolated nanotube.<sup>68,69</sup> A similar situation is also observed for the bamboo-shaped SWNTs.

### **3.3.3. Conclusions**

The electronic and chemical properties of single-walled carbon nanotubes with topological defects have been investigated using DFT calculations. Our results indicate that resonance of local density of states occurs at topological defects of the bamboo-shape and pentagon-pentagon defects, and the chemical reactivity is correlated to these resonant states. The increased chemical reactivity of bamboo-shaped carbon nanotubes strongly suggests that these unique tubes might be more suitable for electrochemical biosensors and gas sensors. In addition, it provides qualitative insights into the electronic and chemical properties of experimentally observed bamboo-shaped multi-walled carbon nanotubes.

### **3.4. Molecular simulations of carbon nanotube-H<sub>2</sub> interactions.**

#### *Introduction*

The advent of single-walled carbon nanotubes has rekindled the interests of storing hydrogen in carbon materials. Dillon et al.<sup>70</sup> first reported the hydrogen storage behavior of unpurified SWNT using thermal desorption spectroscopy (TDS) technique. In her experiments, she soaked the SWNT (and mesoporous activated carbon as comparison) sample in 300torr of H<sub>2</sub> pressure at 133K and then cooled the sample to 90K. The H<sub>2</sub> desorption of the H<sub>2</sub>-loaded SWNT was monitored as the sample was heated from 90K to 500K under high vacuum TDS. It was noted that only the TDS of SWNT sample exhibited an additional H<sub>2</sub> desorption signal at 288K. Both activated carbon and unpurified SWNT samples exhibited H<sub>2</sub> desorption signals at ~120K, which is the expected H<sub>2</sub> desorption of H<sub>2</sub>-carbon system. The significance of the H<sub>2</sub> desorption signal at 288K strongly suggests that H<sub>2</sub>-loaded SWNTs are capable of retaining H<sub>2</sub> close to room temperature before desorption occurs. Since the H<sub>2</sub> desorption peak at 288K was not observed for activated carbon (without SWNT), Dillon et al.<sup>70</sup> ascribed the observed H<sub>2</sub>-desorption signal at 288K to the unique condensation of H<sub>2</sub> inside SWNTs under conditions that did not occur in a mesoporous activated carbon. The desorption activation energy of H<sub>2</sub>-loaded SWNT at 288K was estimated to be 19.6kJ/mol (~202meV). However the condensation of H<sub>2</sub> inside SWNT bundle was very unlikely because the experiments were conducted at temperatures higher than the critical temperature of H<sub>2</sub> (33.2K). Furthermore, Dillon et. al.<sup>70</sup> projected that purified SWNTs had a high H<sub>2</sub> storage of ~5-10wt% (the H<sub>2</sub>-desorption signal of the unpurified SWNT sample at 288K accounted for ~0.01wt% storage in her report).

However, experimental studies on the hydrogen storage of carbon nanotubes are often inconclusive and even contradictory. Initial reports on the H<sub>2</sub> storage of carbon nanotubes gave high uptakes of ~4.2-8wt%.<sup>71</sup> However, these results did not survive a round robin test conducted by other research groups (see review papers by Hirscher and co-workers<sup>71</sup>). Recent investigations

have reported a much lower H<sub>2</sub> storage, ie  $\leq 1\text{wt}\%$  at room temperature and moderate pressure conditions. Arguably, the reasons for the wide discrepancy were the lack of systematic characterization methods for nanosized materials and different quality of the samples used<sup>71</sup>.

It is well known that activated carbon and fiber possess nano-sized pores or slits (micropore size  $\sim 2\text{nm}-0.36\text{nm}$ ). How does the H<sub>2</sub> storage mechanism of SWNT bundles and MWNT be different from activated carbons? What are the strategies to optimize the H<sub>2</sub> storage capacity of carbon nanotubes? Modeling of H<sub>2</sub>-CNT interactions will give insights into its H<sub>2</sub> storage mechanism and optimization.

Figure 3.20a shows an idealized model of hexagonally packed ‘ropes’ of (10,10) SWNT ( $\Phi_d \sim 1.37\text{nm}$ ) and the spacing of the interstitial channel is assumed to be  $\sim 0.32\text{nm}$ . Monte Carlo simulations<sup>72</sup> of physisorption of H<sub>2</sub> in bundles of open-capped SWNTs suggest 4 possible adsorption sites (and binding energies): (i) external surface of the bundles (63meV), (ii) groove of the bundle (89meV), (iii) inside of the nanotubes (49meV) and (iv) interstitial channels of the bundles (119meV), which are generally higher than the binding energy on activated carbon<sup>73,74</sup> ( $\sim 40\text{-}50\text{meV}$ ). The higher binding energy of H<sub>2</sub> on the interstitial channels of the SWNT bundles has been suggested for storing H<sub>2</sub> at room temperature.

J. Zhao et. al.<sup>75</sup> employed a density functional theory (DFT, see Figure 3.20c) to evaluate the binding energy of H<sub>2</sub> onto a bundle of (10,10) SWNT for (i) outside surface (94meV), (ii) groove (114meV), (iii) inside tubes (111meV), and interstitial channels (174meV). On the basis of DFT calculations, storing H<sub>2</sub> via interstitial channels of SWNTs is also more favorable than the hollow cavities, which is consistent with Monte Carlo methods. The differences in the absolute values of binding energies of H<sub>2</sub>-SWNT interaction suggest a limitation of theoretical calculations which serve only as a guide.

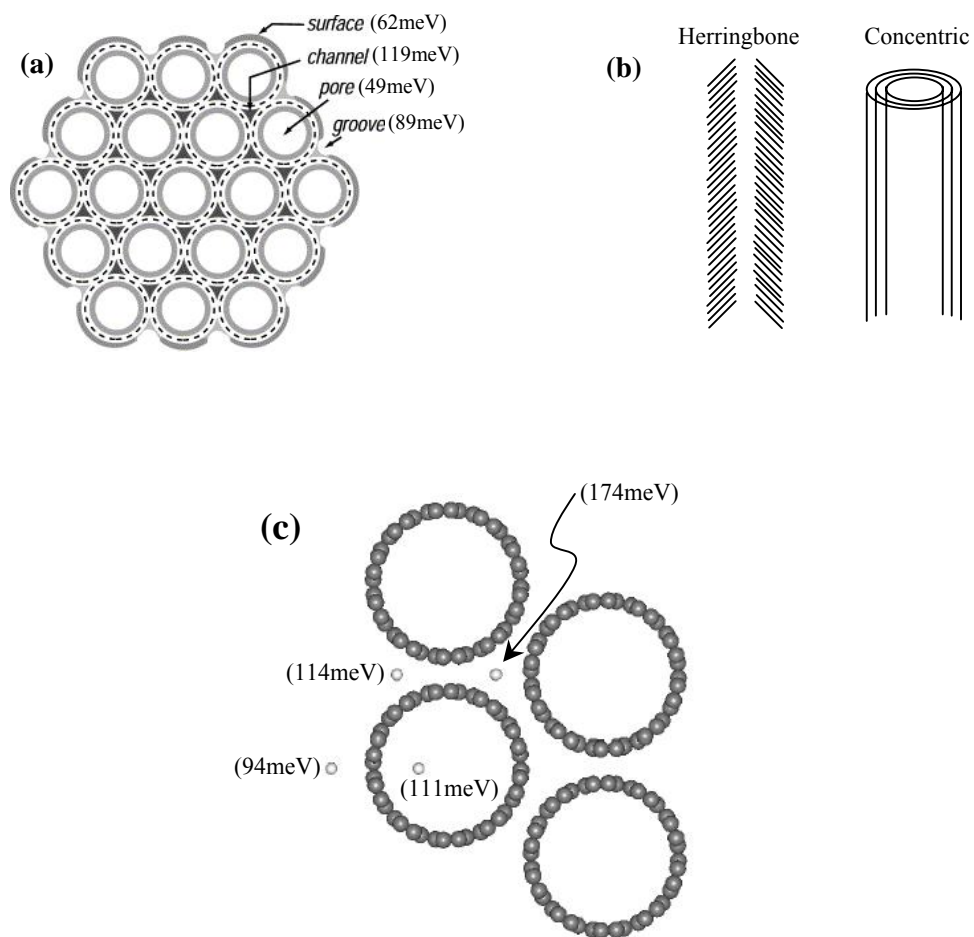


**Figure 3.20.** (a) Schematic packing of an idealized SWNT (10,10) bundle showing 4 possible binding sites and energies for H<sub>2</sub> calculated by Monte Carlo method<sup>72</sup>. (b) Herringbone and concentric MWNTs with exposed graphitic edges as potential sites for H<sub>2</sub> chemisorption<sup>66</sup>. (c) DFT calculations<sup>75</sup> of H<sub>2</sub>-SWNT bundle interactions.

Multi-walled carbon nanotubes can adopt either herringbone structures or concentric layers (see Figure 3.20b). The exposed graphitic edges (interlayer distance  $\sim 0.34$  nm) are proposed to be potential chemisorption sites for carbon-hydrogen (C-H) bond formation<sup>76</sup>. Moreover the internal cavity of carbon nanotubes has been demonstrated store fluid via capillary effects. Chamber et al.<sup>77</sup> claimed a 60wt% H<sub>2</sub> uptake was achieved by carbon nanofibers and proposed that the H<sub>2</sub> molecules (kinetic diameter,  $\sim 0.29$  nm) can intercalate into the slightly larger interlayer spacing of carbon nanofiber ( $\sim 0.34$  nm, herringbone structure). However, this extremely

high H<sub>2</sub> uptake could not be confirmed by other research groups and it is suggested that intercalation of H<sub>2</sub> into the graphitic interlayer spacing is most unlikely to happen<sup>78</sup>. On the other hand, wedging the interlayer spacing of graphitic materials with appropriate intercalatants<sup>78</sup> has been suggested to be a good strategy to enhance the overall H<sub>2</sub> storage. Nonetheless, on the basis of theoretical considerations, SWNT bundles and MWNTs give rise to new and interesting concepts of gas storage properties.

Although there are numerous reports on the simulation of H<sub>2</sub> storage of carbon nanotubes, there are still several shortcomings and gray areas in the reports. *Ab initio* density functional theory (DFT) calculations have been widely employed to study the physisorption of H<sub>2</sub> on carbon nanotubes. However, *ab initio* DFT methods, which are based on the local electronic density, gradient and kinetic energy density, are inadequate to describe the interaction energy at a distance where the electronic overlap is very weak. In other words, DFT methods are not appropriate to study a physisorption process whereby the nature of interactions is mainly van der Waal (vdW) forces. Sometimes the local density approximation (LDA)<sup>79</sup> might provide a good estimate for the interaction energy of a physisorption process, but it is argued that the results are unphysical and largely fortuitous due to favorable error cancellations.<sup>80</sup> On the other hand, *ab initio* DFT calculations are suitable for chemisorption of hydrogen, which involves bond breaking and formation. Recently, Du et al.<sup>81</sup> reported a van der Waals-corrected DFT study of hydrogen-nanotube interactions and the results give a good estimate for the physisorption process. Another gray area of H<sub>2</sub>-nanotube simulations is the geometry of SWNT bundles. The SWNT bundles are always presumed to be hexagonally assembled (as in Fig 3.20c) with a tube-to-tube distance of ~0.32nm. The interstitial channels are assumed to be accessible to H<sub>2</sub> molecules and often it is not clear whether the insertion of H<sub>2</sub> molecules will upset the packing of the SWNT bundles. In most calculations a H<sub>2</sub> molecule is artificially inserted in the interstitial channels and then the adsorption energy is evaluated. Recent simulations<sup>78,82</sup>, which specifically consider the interstitial channels as potential H<sub>2</sub> storage sites, take into the account of the re-organization of the SWNT

bundles and reveal that the tube-to-tube distance has to be wedged to a much larger distance in order to store an appreciate amount of H<sub>2</sub> in SWNT bundles.

In this section 3.4, the interactions of H<sub>2</sub> and carbon nanostructures (graphene sheets and nanotubes) are studied using molecular mechanics (MM) and molecular dynamics (MD). The Universal forcefield (UFF)<sup>83</sup> is used to parameterize the van der Waals interactions between the H<sub>2</sub> molecule and carbon surfaces. The results of UFF-based calculations are mostly consistent with recent simulations, except that the interstitial channels of smaller diameter SWNT bundles are determined to be unfavorable for H<sub>2</sub> adsorption. The pressure-composition-isotherms (PCI) of H<sub>2</sub>-nanotube bundles are carried out to estimate the H<sub>2</sub> weight percent storage.

#### **3.4.1. Computational Methods**

The H<sub>2</sub> uptake of CNT is a physisorptive process and the interactions are due to van der Waals forces. The Forcite module available in Material Studio is employed to model gas-solid H<sub>2</sub>-carbon interactions. Forcite is collection of molecular mechanics (MM) tools that allow one to investigate large systems with thousands of atoms. The key approximation of MM is the use of a classical forcefield to represent the potential energy surface where the atomic nuclei move on. Five forcefields are available in Forcite: (i) COMPASS (Condensed-phase Optimized Molecular Potentials for Atomistic Simulation Studies), (ii) Dreiding, (iii) Universal, (iv) cvff (Consistent Valence ForceField), and (v) pcff (Polymer Consistent ForceField). The choice of a forcefield is crucial for reliable MM simulations, and the Universal forcefield (UFF) is tested to yield the best estimate, as compared to the other four forcefields, for H<sub>2</sub>-carbon interactions (see below). The conjugate gradient algorithm is used for the Forcite geometry optimization and the convergence tolerance is set at “Ultra-fine” quality.

The potential energy of an arbitrary geometry for a molecule is expressed as a sum of bonded (valence) interactions and nonbonded interactions:

$$E = \underbrace{E_R + E_\theta + E_\phi + E_\omega}_{\text{valence}} + \underbrace{E_{\text{vdw}} + E_{\text{el}}}_{\text{nonbonded}} \quad [3.7]$$

The valence interactions include bond stretching ( $E_R$ ) and angular distortions [bond angle bending ( $E_\theta$ ), dihedral angle torsion ( $E_\phi$ ), and inversion ( $E_\omega$ )]. The nonbonded interactions consist of van der Waals ( $E_{\text{vdw}}$ ) and electrostatic ( $E_{\text{el}}$ ) terms. The van der Waals interactions are described by the Lennard-Jones potential. It is noted that for the study of hydrogen-carbon systems the van der Waals term is important and the rest of the terms are spectator terms.

The interactions of  $\text{H}_2$ -graphene and  $\text{H}_2$ -nanotube are simulated with cluster models. All the dangling bonds of the clusters are saturated with H-bond and made as large as possible to avoid any interactions from the C-H bonds. The lengths of individual carbon nanotubes and SWNT bundles are at least 5-10 times its diameters and the center portion of the nanotube / SWNT bundle is used for the evaluation of the potential energy curves. The adsorption energy ( $E_a$ ) of a  $\text{H}_2$  molecule is defined as:

$$E_a = E[\text{adsorbent} + \text{H}_2] - E[\text{adsorbent}] - E[\text{H}_2 \text{ molecule}] \quad [3.8]$$

The negative value of  $E_a$  corresponds to energy gain upon adsorption.

In addition, the pressure-composition-isotherms (PCI) of uncapped SWNT bundle- $\text{H}_2$  interactions are obtained using the Sorption module available in Materials Studio. The PCI consists of a series of fixed pressure simulations at a set temperature. In each fixed pressure simulation, the configurations are sampled from a grand canonical ensemble. The Metropolis Monte Carlo method<sup>84</sup> is applied for the simulations in which trial configurations are generated without bias. In this method, the  $\text{H}_2$  molecule (sorbate) is treated as a rigid body, and only rigid body translations and reorientations are incorporated. The Metropolis sampling scheme is also used to map the  $\text{H}_2$  density profile of SWNT bundles. The interaction energies are parameterized using the Universal forcefield. The SWNT bundles are composed of armchair nanotubes and the periodic lengths of the supercells are set at 4 times its unit cell.

### 3.4.2. Hydrogen-graphene sheet interactions

Figure 3.21 shows a fragment of a flat graphene sheet and five possible adsorption sites of  $H_2$  molecules. Static calculations of potential energy have been carried out to investigate the interaction of the  $H_2$  molecules with the graphene sheet. The axis of the  $H_2$  molecule is parallel to the graphene sheet at site A (center of hexagon ring) and site B (mid-point of the C-C bond), while the axis of  $H_2$  is perpendicular to the graphene sheet at site C (center of hexagon ring), site D (mid-point of the C-C bond) and site E (top of a C atom). These sites are also defined for  $H_2$  adsorbing on the outside surface of a SWNT.

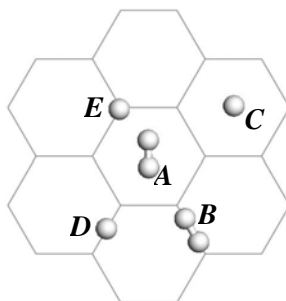


**Figure 3.21.** Configurations of  $H_2$  adsorbed on a flat graphene sheet. The  $H_2$  molecular axis is parallel to the graphene sheet at adsorption site A (center of hexagon ring) and site B (carbon-carbon bond). The  $H_2$  molecular axis is perpendicular to the graphene sheet at adsorption site C (center of hexagon ring), site D (carbon-carbon bond) and site E (top of a carbon atom). These sites are also defined for  $H_2$  adsorbing on the outside surface of SWNT.

Figure 3.22a shows the potential energy curves for flat graphene sheet- $H_2$  interactions at different adsorption sites calculated within the Universal forcefield. The adsorption energies of  $H_2$  on a graphene sheet vary from 52-69meV, dependent on the orientation and location of the  $H_2$  molecule. The strongest adsorption is at site A. The diffusion barrier of a  $H_2$  molecule on a graphene sheet is very weak  $\sim 17$ meV. The magnitude of the adsorption energy for a graphene- $H_2$  interaction is well within a physisorption process (50-500meV), and the present UFF-based estimate ( $E_a=69$ meV,  $d=2.92\text{\AA}$ ) is in good agreement with the recent van der Waals-corrected



DFT calculation<sup>81</sup> ( $E_a=60\text{meV}$ ,  $d=2.92\text{\AA}$ ) and experimental estimate<sup>73,74</sup> ( $E_a=42\text{meV}$ ,  $d=2.87\text{\AA}$ ). The UFF-based estimate of  $E_a$  is higher than the experimental value because experimentally a monolayer of  $\text{H}_2$  is adsorbed on the graphitic surface, while a single  $\text{H}_2$  molecule is adsorbed on the graphene sheet in the simulation. Furthermore the experimental value of  $E_a$  is expected to be larger at very low  $\text{H}_2$  coverage.

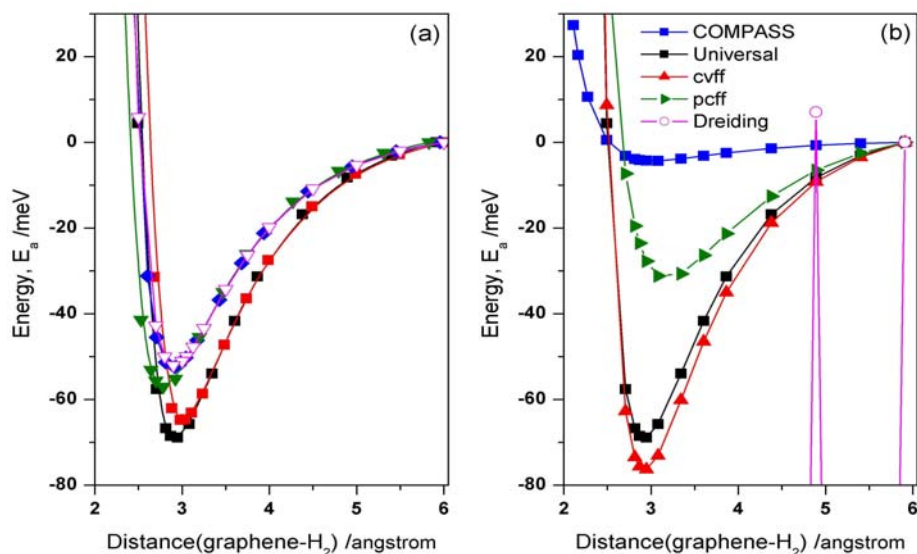


**Figure 3.22.** (a) Potential energy curves of a flat graphene sheet- $\text{H}_2$  interaction calculated by Universal forcefield. The adsorption sites are A (-■-), B (-■-), C (-▼-), D (-◆-), and E (-▽-) as defined in Fig 3.21. (b) Potential energy curves of a flat graphene sheet- $\text{H}_2$  interaction calculated by different forcefields: COMPASS (-■-), Universal (-■-), cvff (-▲-), pcff (-▶-), and Dreiding (-○-). The adsorption site A was used only.

The reliability of the Universal forcefield is tested against other available forcefield types. Figure 3.22b compares the graphene- $\text{H}_2$  interactions for adsorption site A using different forcefields. It is noted that potential energy curves obtained by COMPASS, which is an *ab initio* forcefield and the parameters were derived from *ab initio*-based data, are almost repulsive and have a very weak attractive range ( $>-4\text{meV}$ ). This is similar to DFT calculations using the generalized gradient approximation (GGA) reported in literature. The potential energy curve

obtained by the Drieding forcefield (data are beyond the display range, and only 2 points can be seen) fails to produce any local minima and some points blow up unexpectedly. The  $E_a$  value obtained by pccf is  $\sim 30$  meV which is lower than experimental  $E_a$  value. On the other hand, cvff yields an  $E_a$  value of 76 meV which is slightly larger than the  $E_a$  value determined by UFF. Thus COMPASS, pccf and Drieding forcefields are not suitable for the calculations of graphene- $H_2$  interactions. The potential energy curve based on cvff is similar to that of Universal forcefield and both forcefields are deemed suitable for the calculations (there is not hard rule to determine which forcefield really give the “accurate”  $E_a$  value due to the nature of the present calculations). However, the application of Universal forcefield is still preferred over cvff because cvff is parameterized mainly for amino acids, water and a variety of functional groups. UFF has a full coverage of the periodic table and it is used for organic molecules, main-group inorganics and metal complexes. It is also suitable for organometallic systems and other systems for which other forcefields do not have parameters. More importantly, the UFF-based geometry optimizations of carbon nanotubes are close to the results of DFT-based geometry optimizations.

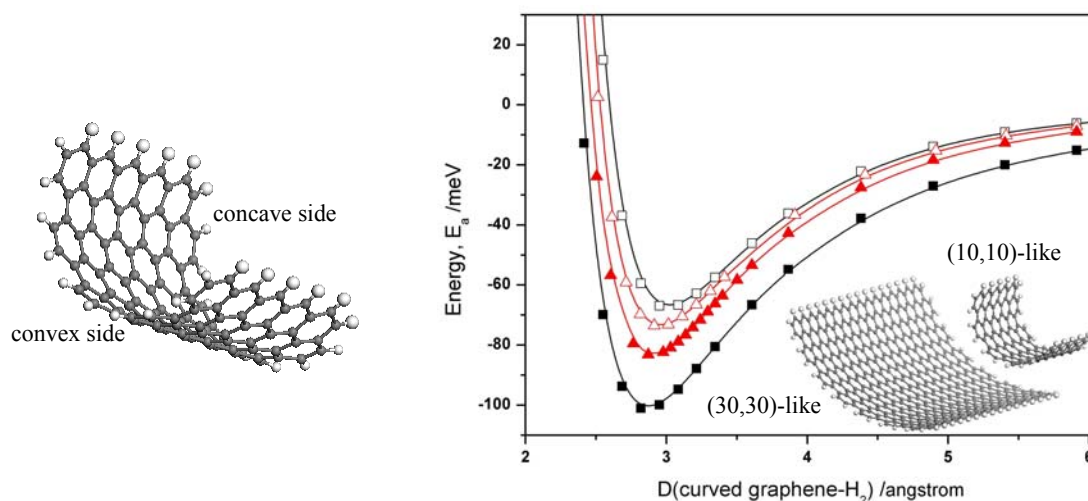


**Figure 3.23.** Potential energy curves of curved graphene sheets with curvature similar to (10,10) (square symbols) and (30,30) (triangle symbols) nanotubes. Solid and open symbols denote concave and convex side of the curved graphene sheets. Inset shows the curved graphene sheets with (10,10)-like and (30,30)-like curvature.

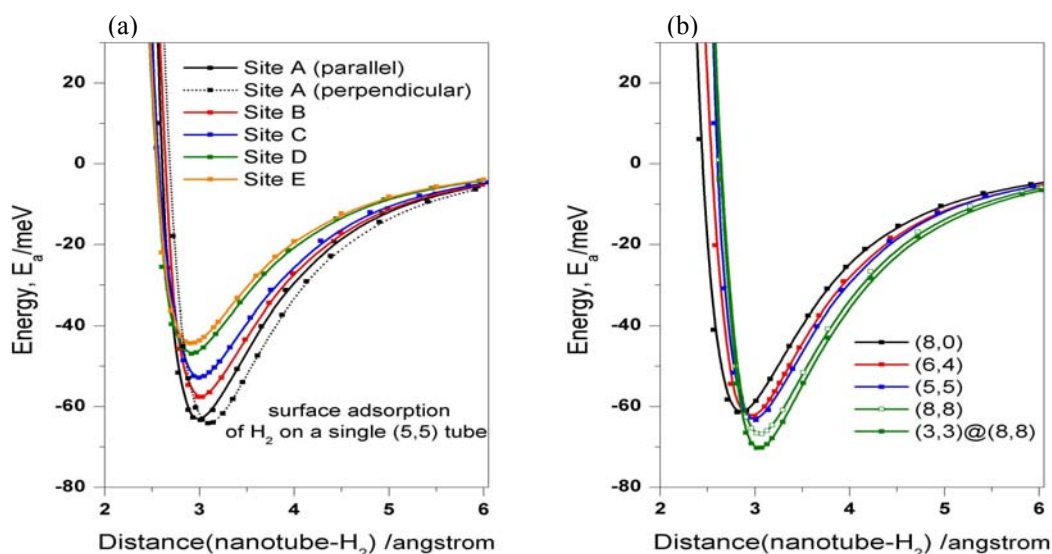
The calculated physisorption energy of a flat graphene- $H_2$  interaction indicates that it is too weak for practical application to hydrogen storage because of the unstable physisorbed state at room temperature (see below on molecular dynamics simulations). On the other hand, it is found that curved structures of graphene significantly enhance the physisorption energy of a  $H_2$  molecule. The potential energy curves of  $H_2$  molecules on curved graphene sheets are shown in Figure 3.23. The curvatures of the curved graphene are similar to (10,10) and (30,30) carbon nanotubes (simply called the curved graphene as (10,10)-like and (30,30)-like sheets). The adsorption energies are determined to be different for the two sides of the curved graphene. The concave side of the curved graphene sheet has a higher  $E_a$  value than the convex side. Particularly, the adsorption energy of a (10,10)-like graphene sheet is increased to about 100meV at the concave side, while the  $E_a$  value at the convex side is about 66meV. Hence the results of Figure 3.23 indicate that single-walled carbon nanotubes, particularly the inner hollow of the tube, might yield higher  $H_2$  adsorption energies.

### **3.4.3. Hydrogen-carbon nanotube interactions**

Figure 3.24a shows the adsorption energy of a  $H_2$  molecule on the outer surface of a single (5,5) nanotube. The configurations of the  $H_2$  molecule adsorbing on the external surface of a (5,5) nanotube is defined as given in Fig 3.21, except that at the site A where the axis of the  $H_2$  molecule at the center of the hexagon ring can be either perpendicular or parallel to the nanotube axis. The highest adsorption energy of a  $H_2$  molecule is  $\sim 65$ meV at Site A, while the lowest adsorption energy is  $\sim 45$ meV at site E. The adsorption energies of  $H_2$  at site A are almost the same whether the hydrogen axis is parallel or perpendicular to the tube axis.

The effects of nanotube chiralities and double-walled layers on the adsorption energy of  $H_2$  are presented in Figure 3.24b. The (8,0), (6,4) and (5,5) nanotubes have similar tubular diameter ( $\sim 6.3$ - $6.8\text{\AA}$ ), and the adsorption energies of hydrogen molecule on these tubes are almost the same and independent of chirality. The  $E_a$  of a double-walled carbon nanotube

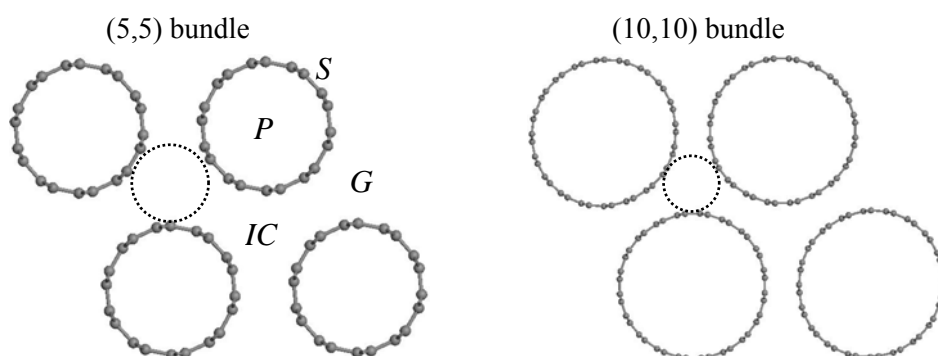
(DWNT) (3,3)@(8,8), which has the same outer diameter as a (8,8) nanotube, is 71 meV while the  $E_a$  of (8,8) nanotube is 66 meV. Although the increment of  $E_a$  value is not substantial, the beneficial effects of having an inner tube in DWNT are clear. In addition, Miyamoto et al.<sup>85</sup> showed that DWNTs stored  $H_2$  more efficiently than SWNTs due to the unique packing of DWNTs.



**Figure 3.24.** (a) Adsorption energy of a  $H_2$  molecule on the external surface of a single (5,5) nanotube. The surface adsorption sites are A ( $\blacksquare$ ; solid line= $H_2$  parallel to tube axis, dotted line= $H_2$  perpendicular to tube axis), B ( $\blacksquare$ ), C ( $\blacksquare$ ), D ( $\blacksquare$ ), and E ( $\blacksquare$ ) as defined in Fig 3.21. (b) Adsorption energy of  $H_2$  molecule on a (5,5) tube, (8,0) tube, (6,4) tube, (8,8) tube and a DWNT (3,3)@(8,8). Surface adsorption of site A is considered only.

Structural properties of uncapped (5,5) and (10,10) bundles are displayed in Figure 3.25. UFF-based geometry optimizations show that the final geometries of the SWNT bundles (consist of 4 single tubes) are always hexagonally packed regardless of the initial packing. The UFF-based geometry optimizations are consistent with DFT-based geometry optimizations. It should be noted that the exact definition of the IC spacing is hardly clear-cut in literature. As mentioned previously, Clement and Zhao et al.<sup>72,75</sup> stated that the interstitial channel spacing of (10,10)

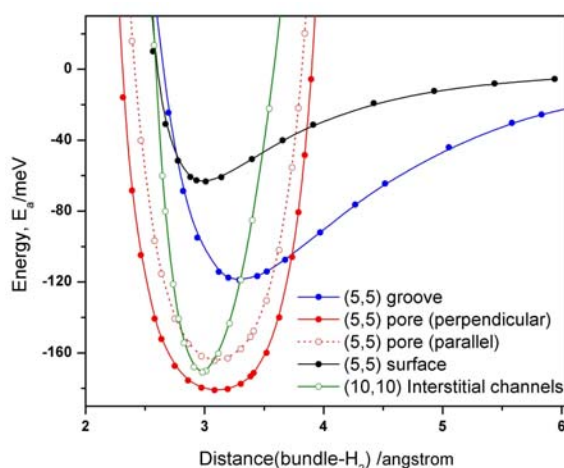
bundle is  $\sim 3.2\text{\AA}$  without further quantification. Thus, as shown in Fig 3.25, the geometrical meaning of the interstitial channels spacing is indicated by the dotted circle. The closest tube-to-tube distance in the relaxed SWNT bundles are  $\sim 3.2\text{\AA}$  regardless of the diameters, which is very close to the experimental estimate<sup>86</sup> of  $3.15\text{\AA}$  (see Fig 3.29 for more relaxed SWNT bundles). The interstitial channel spacing of SWNT bundle is defined as the diameter of a circle that can be fitted into the IC. The interstitial channel spacing of (5,5) and (10,10) bundles are  $4.17\text{\AA}$  and  $5.01\text{\AA}$  respectively. The interstitial channel spacing of (5,5) bundle is not unfavorable for  $\text{H}_2$  adsorption (see below).



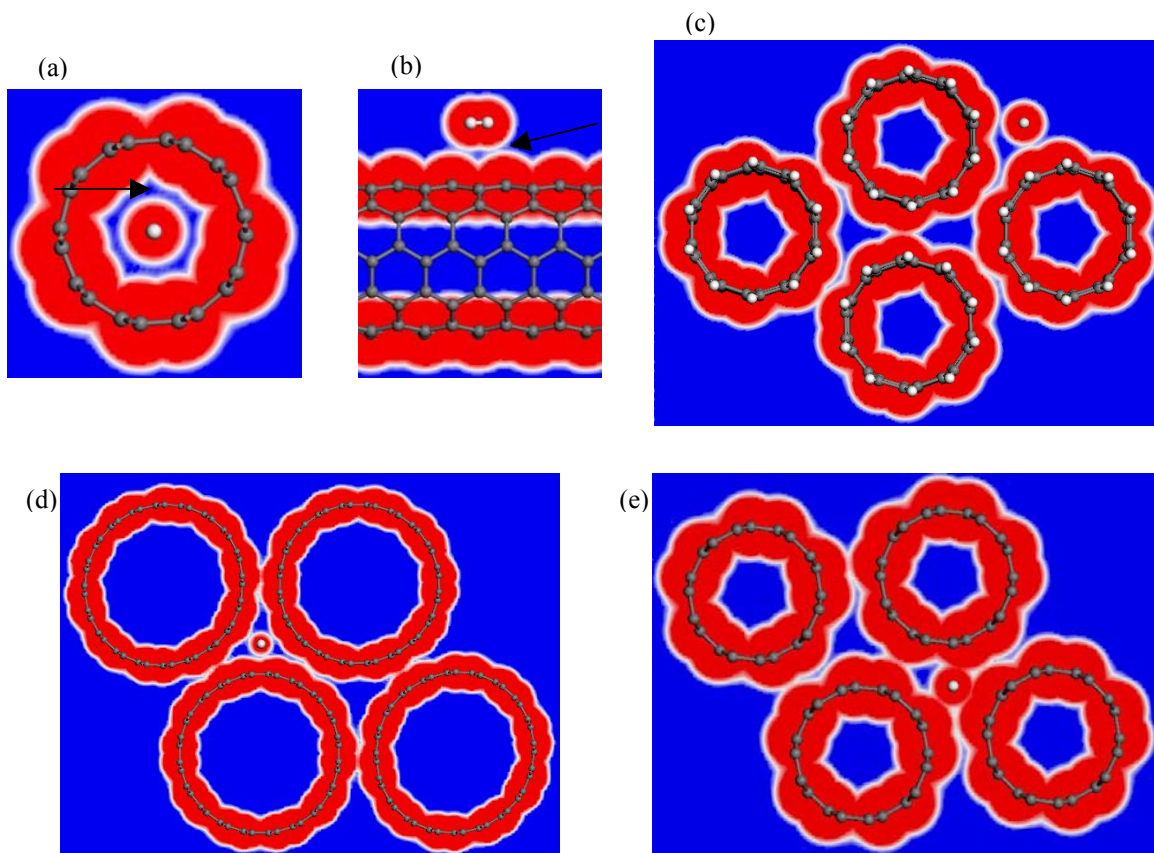
**Figure 3.25.** (a) Cross-sectional view of relaxed (5,5) and (10,10) bundles which possess several adsorption sites for  $\text{H}_2$  molecule at the surface (*S*), pore (*P*), groove (*G*), and interstitial channels (*IC*). The interstitial channel spacing is defined as the diameter of a circle (dotted) that can be fitted in the IC.

The potential energy curves of  $\text{H}_2$ -(5,5) bundle interactions are shown in Figure 3.26. The axis of the  $\text{H}_2$  molecule is set to be parallel to the bundle axis, unless otherwise stated. The adsorption energy of  $\text{H}_2$  on external surface of a (5,5) bundle is  $\sim 65\text{meV}$  at site A, which is identical to the  $E_a$  value of a single (5,5) tube. The adsorption energy of  $\text{H}_2$  at the groove of the (5,5) bundle is  $\sim 120\text{meV}$  which is significantly higher than the surface  $E_a$ . For uncapped SWNT bundle, the adsorption energy of the pore is determined to be  $\sim 180\text{meV}$  ( $170\text{meV}$ ) for  $\text{H}_2$  axis

parallel (perpendicular) to the tube axis. The distance of  $H_2$  inside the pore is measured from the center of  $H_2$  to the circumference of the tube. The potential energy curve  $H_2$  molecule inside the pore of a (5,5) tube shows a narrow potential well of  $\sim 1\text{\AA}$  width. However, positive adsorption energy of  $H_2$  (repulsive) is always determined when the  $H_2$  is inserted into the interstitial channels of (5,5) bundle. Even after a full geometry optimization, the  $E_a$  of  $H_2$  at the interstitial channels is still positive. In other words, the intercalation of  $H_2$  into the interstitial channels of a relaxed (5,5) bundle is energetically unfavorable. As a result, the adsorption energy of  $H_2$  at interstitial channels of (10,10) bundle, which has a larger IC spacing, is determined to be  $\sim 170\text{meV}$ . Thus an uncapped (5,5) bundle has only 3 useful adsorption sites, chiefly the outer surfaces, grooves and pores. It is surmised that for a capped SWNT bundle, the groove would be a favorable adsorption site and a reduction of the bundle size (i.e. creating more grooves) might enhance the amount of  $H_2$  uptake. To understand why the interstitial channels of (10,10) bundle are favorable for adsorbing  $H_2$  while the interstitial channels of (5,5) bundle are not, the Connolly surfaces<sup>87</sup> of the  $H_2$  and nanotubes are investigated.



**Figure 3.26.** Potential energy curves of SWNT bundle- $H_2$  interactions at the (5,5) outside surface (site A, ●), pore (●= $H_2$  parallel to tube axis, ○= $H_2$  perpendicular to tube axis), and groove (●). Adsorption energy curve of  $H_2$  in the interstitial channels of (10,10) bundle is denoted by (○).



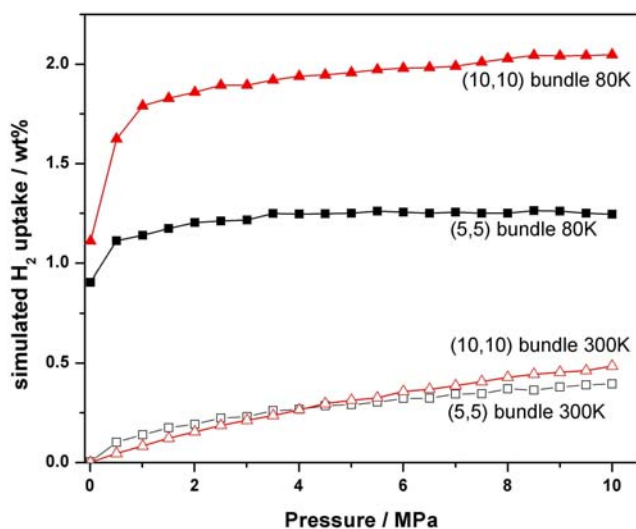
**Figure 3.27.** Van der Waals surfaces of (a)  $\text{H}_2$  adsorbed inside the pore a (5,5) tube, (b)  $\text{H}_2$  adsorbed on the outside surface of a (5,5) tube, (c)  $\text{H}_2$  adsorbed on the groove of a (5,5) bundle, (d)  $\text{H}_2$  intercalated into the interstitial channels of a (10,10) bundle. (e)  $\text{H}_2$  intercalated into the interstitial sites of a (5,5) bundle. The interaction distance is at the local minimum of the potential energy curve, except for (e).

Figure 3.27 shows the Connolly surfaces of  $\text{H}_2$  and carbon nanotubes, which is set equivalent to the van der Waals (vdW) surfaces (Connolly probe radius of zero). The red region is defined as the vdW surface, the white border is defined as the accessible region and the blue region is the “external” surface. At the local minima of the potential energy curves of the  $\text{H}_2$ -nanotube interactions, the accessible regions (white border) of  $\text{H}_2$  and carbon nanotubes are very close to each other and overlapping of the white border can be observed (arrows of Fig 3.27),

which is attributed to vdW binding. The overlapping of the white border can also be observed in SWNT bundles, and this is the vdW forces that assembles the nanotubes into bundles. Furthermore, the vdW surfaces of a (10,10) bundle show that its interstitial channel spacing is large enough to accommodate H<sub>2</sub> molecules. In contrast, the vdW surfaces of (5,5) bundle show that its interstitial channel spacing is too small to accommodate H<sub>2</sub> molecules. Repulsion between H<sub>2</sub> and the (5,5) bundle at the interstitial channels is indicated by the overlapping of the red region (vdW surface). It is confirmed that overlapping of the red region (vdW surface) is a sign of repulsion by plotting the vdW surface at location of the potential energy curve where it is positive.

The H<sub>2</sub> uptakes (weight percent, wt%) of uncapped (5,5) and (10,10) bundles are obtained from the simulated pressure-composition-isotherms (PCI) as shown in Figure 3.28. The simulated PCIs are conducted for (5,5) and (10,10) bundles, which consist of four nanotubes packed hexagonally, and the H<sub>2</sub> uptakes are investigated as a function of pressure (from 0.01-10MPa). An appreciate amount of H<sub>2</sub> (~1-2wt%) is stored at 80K, while a diluted amount ( $\leq 0.5$ wt%) of H<sub>2</sub> is stored in the SWNT bundles at 300K. Furthermore, the H<sub>2</sub> uptakes of SWNT bundles reach saturation at ~1MPa and 80K (langmuir-type behaviour). The H<sub>2</sub> uptakes of SWNT bundles are almost a linear function of pressure at 300K (Henry-type behaviour). The simulated H<sub>2</sub> uptakes of SWNT bundles are in good agreement with experimental results (see section 7.2, page 171). At 300K, the H<sub>2</sub> uptake of (10,10) bundle is almost the same as the uptake of (5,5) bundle over the pressure ranges. At 80K, the H<sub>2</sub> uptake of (10,10) bundle (~2wt%) is higher than a (5,5) bundle (~1.25wt%), which can be attributed to the availability of the interstitial channels and its larger pore size.





**Figure 3.28.** Simulated Pressure-composition-isotherms of uncapped (5,5) and (10,10) bundle-H<sub>2</sub> interactions at 300K (open symbol) and 80K (closed symbol).

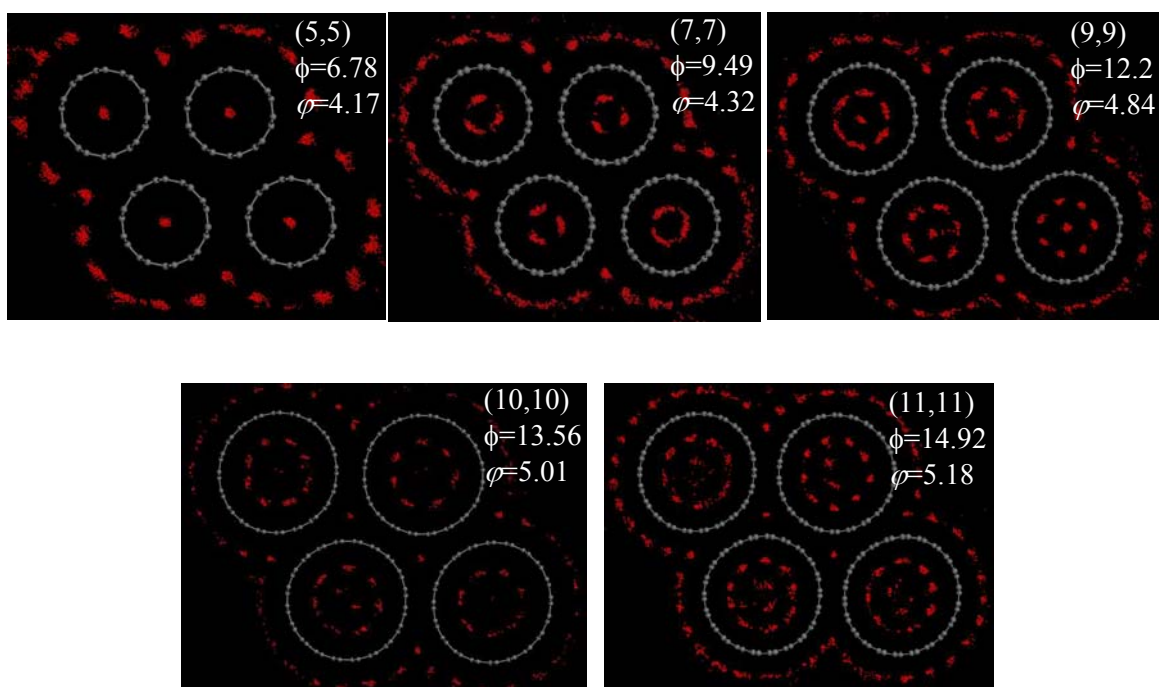


**Figure 3.29.** Density field for H<sub>2</sub> in uncapped (5,5), (7,7), (9,9), (10,10) and (11,11) nanotube bundles. The red output field represents a density distribution of H<sub>2</sub> molecules in the SWNT bundles under conditions of 1bar and 80K.  $\phi$  and  $\varphi$  denote the SWNT's diameter and interstitial channel spacing respectively. Unit length is Å.

Figure 3.29 shows that density field for H<sub>2</sub> (red spots) in uncapped (5,5), (7,7), (9,9), (10,10) and (11,11) nanotube bundles simulated at 1bar and 80K. The simulation shows that the SWNT bundles' surface, groove and pore are possible adsorption sites for H<sub>2</sub>. For outside surface adsorption, the density field of H<sub>2</sub> is concentrated above the hexagonal ring of SWNT and this is consistent with static calculations. The pore of the SWNT can accommodate more H<sub>2</sub> molecules as the diameter increases. The adsorption of H<sub>2</sub> in the interstitial channels occurs only for (10,10) and (11,11) bundles. The Metropolis sampling scheme reveals that a minimum IC spacing of ~5Å is needed to accommodate the H<sub>2</sub> molecules. The results of the Metropolis sampling scheme are consistent with static calculations and van der Waals surface plot.

**Table 3.7.** Comparison of adsorption energy<sup>†</sup> (meV) for a H<sub>2</sub> molecule physisorbed on a graphene sheet and various carbon nanotubes. Adsorption sites A, B, C, D, E, and groove, pore, IC are defined as in Fig 3.21 and Fig 3.25 respectively.

	A	B	C	D	E	Groove	Pore	IC
Graphene sheet	68.5	64.4	56.5	52.6	52	-	-	-
Single (5,5) tube	63.0	57.5	52.3	46.6	44.3	-	180.1	-
(5,5) bundle	63.8	-	-	-	-	117.8	180.1	170.3 <sup>‡</sup>
Single (6,4) tube	61.9	-	-	-	-	-	-	-
Single (8,0) tube	61.4	-	-	-	-	-	-	-
Single (8,8) tube	66.6	-	-	-	-	-	-	-
(3,3)@(8,8)	70.0	-	-	-	-	-	-	-
Ref 75 (LDA) (10,10) bundle	94	-	-	-	-	114	111	174
Ref 72 (Monte Carlo) (10,10) bundle	62	-	-	-	-	89	49	174
Ref 81 (LDA + vdW) Single (8,8) tube	60	-	-	-	-	-	80	76

<sup>†</sup>maximum adsorption energy only

<sup>‡</sup>(10,10) bundle

#### **3.4.4. Conclusions**

Table 3.7 summarizes the adsorption energy of H<sub>2</sub> on a graphene sheet, nanotube and nanotube bundle. Molecular mechanics and Monte Carlo simulations have been performed to study H<sub>2</sub> physisorption of SWNTs. The Universal forcefield gives an excellent estimate H<sub>2</sub> physisorption of graphene and carbon nanotubes. Additionally, UFF-based geometry optimization of SWNT bundles is very close to the experimental observed lattice constant. Static calculations show that the adsorption energy is slightly lower (higher) than a flat graphene sheet for a H<sub>2</sub> physisorbed outside (inside) a (5,5) nanotube due to curvature effect. Assembly of SWNTs in bundle array gives rise to additional stronger adsorption sites such as groove (~118meV) and interstitial channels (~170meV). Although SWNT bundle possesses higher H<sub>2</sub> adsorption energy, it does not automatically mean that the H<sub>2</sub> storage capacity will be enhanced. For H<sub>2</sub>-graphite interactions, the E<sub>a</sub> is ~40-50meV and the desorption temperature is ~80K. Therefore, the presence of H<sub>2</sub> adsorption sites with higher E<sub>a</sub> implies that higher desorption temperature can be observed. As demonstrated by Monte Carlo simulations, the H<sub>2</sub> uptakes of SWNT bundles are very low (~0.5wt% for (5,5) and (10,10) tubes) at 300K and the amount of H<sub>2</sub> stored can be enhanced to ~1-2wt% at low temperature of 80K. Other factors such as defects, micropores, mesopores, charge transfer and catalytic centers can also affect the H<sub>2</sub> storage capacity. The H<sub>2</sub> density field of SWNT bundles reveals that the interstitial channel spacing (as defined in present context) must be at least ~5Å so that H<sub>2</sub> molecules can be intercalated in it.

## References

- [1] R. Saito, M. Fujita, G. Dresselhaus, M.S. Dresselhaus, *Appl. Phys. Lett.* 60, 2204 (1992).
- [2] N. Wang, Z. K. Tang, G. D. Li, J. S. Chen, *Nature (London)* 408, 51 (2000).
- [3] Z. K. Tang, L. Zhang, N. Wang, X. X. Zhang, G. H. Wen, G. D. Li, J. N. Wang, C. T. Chan, P. Shen, *Science* 292, 2467 (2001).
- [4] B. Delley, *J. Chem. Phys.* 92, 508 (1990).
- [5] J. P. Perdew, K. Burke, and M. Ernzerhof, *Phys. Rev. Lett.* 77, 3865 (1996).
- [6] (a) J. Tao, J. P. Perdew, V. N. Staroverov, G. E. Scuseria, *Phys. Rev. Lett.* 91, 146401 (2003).  
(b) V. N. Staroverov, G. E. Scuseria, J. Tao, J. P. Perdew, *Phys. Rev. B* 69, 075102 (2004).
- [7] J. P. Perdew, J. A. Chevary, S. H. Vosko, K. A. Jackson, M. R. Pederson, D. J. Singh, C. Fiolhais, *Phys. Rev. B* 46, 6671 (1992).
- [8] A. D. Becke, *J. Chem. Phys.* 88, 2547 (1988).
- [9] C. T. Lee, W. T. Yang, R. G. Parr, *Phys. Rev. B.* 37, 785 (1988).
- [10] M. D. Segall, P. J. D. Lindan, M. J. Probert, C. J. Pickard, P. J. Hasnip, S. J. Clark, M. C. Payne, *J. Phys.: Condens. Matter* 14, 2717 (2002).
- [11] D. Vanderbilt, *Phys. Rev. B* 41, 7892 (1990).
- [12] F. Palmino, E. Ehret, L. Mansour, J.-C. Labrune, G. Lee, H. Kim, J.-M. Themlin. *Phys. Rev. B*, 67, 195413 (2003).
- [13] M. Machon, S. Reich, C. Thomsen, D. Sanchez-Portal, P. Ordejon, *Phys. Rev. B* 66, 155410 (2002).
- [14] H. J. Liu, C. T. Chan, *Phys. Rev. B* 66, 115416 (2002).
- [15] X. Blasé, L. X. Benedict, E. L. Shirley, S. G. Louie, *Phys. Rev. Lett.* 72, 1878 (1994).
- [16] J. L. Yang, H. J. Hui, C. T. Chan, *Phys. Rev. B* 64, 085420 (2001).
- [17] (a) N. Nagasawa, H. Sugiyama, N. Naka, I. Kudryashov, M. Watanabe, T. Hayashi, I. Bozovic, N. Bozovic, G. Li, Z. Li, Z. K. Tang, *J. Lumin.* 97, 161 (2002). (b) Z. M. Li, Z. K. Tang, H. J. Liu, N. Wang, C. T. Chan, R. Saito, S. Okada, G. D. Li, J. S. Chen, N. Nagasawa, S. Tsuda, *Phys. Rev. Lett.* 87, 127401-1 (2001).
- [18] (a) Z. Wang, H. Zhao, S. Mazumdar, *Phys. Rev. B* 74, 195406 (2006). (b) O. J. Korovyanko, C. X. Sheng, Z. V. Vardeny, A. B. Dalton, R. H. Baughman, *Phys. Rev. Lett.* 92, 017403-1 (2004).
- [19] L. X. Benedict, S. G. Louie, M. L. Cohen, *Phys. Rev. B* 52, 8541 (1995).
- [20] Y. Miyamoto, A. Rubio, S. Berber, M. Yoon, D. Tomanek, *Phys. Rev. B* 69, 121413 (2004).
- [21] A. J. Stone, D. J. Wales, *Chem. Phys. Lett.* 128, 501 (1986).

- [22] R. S. Lee, H. J. Kim, J. E. Fischer, A. Thess, and R. E. Smalley, *Nature (London)* 388, 255 (1997).
- [23] K. Suenage, M. P. Johansson, N. Hellgren, E. Broitman, L. R. Wallenberg, C. Colliex, J. Sundgren, and L. Hultman, *Chem. Phys. Lett.* 300, 695 (1999).
- [24] S.H. Lim, H. I. Elim, X. Y. Gao, A. T. S. Wee, W. Ji, J. Y. Lee, and J. Lin, *Phys. Rev. B* 73, 045402 (2006).
- [25] R. Droppa, Jr., C. T. M. Ribeiro, A. R. Zanatta, M. C. dos Santos, and F. Alvarez, *Phys. Rev. B* 69, 045405 (2004).
- [26] F. Villalpando-Paez, A. Zamudio, A. L. Elias, H. Son, E. B. Barros, S. G. Chou, Y. A. Kim, H. Muramatsu, T. Hayashi, J. Kong, H. Terrones, G. Dresselhaus, M. Endo, M. Terrones, and M. S. Dresselhaus, *Chem. Phys. Lett.* 424, 345 (2006).
- [27] B. N. Khare, P. Wilhite, R. C. Quinn, B. Chen, R. H. Schingler, B. Tran, H. Imanaka, C. R. So, C. W. Bauschlicher, Jr., and M. Meyyappan, *J. Phys. Chem. B* 108, 8166 (2004).
- [28] B. Khare, P. Wilhite, B. Tran, E. Teixeira, K. Fresquez, D. N. Mvondo, C. Bauschlicher, Jr., and M. Meyyappan, *J. Phys. Chem. B* 109, 23466 (2005).
- [29] Z. Konya, I. Vesselenyi, K. Niesz, A. Kukovecz, A. Demortier, A. Fonseca, J. Delhalle, Z. Mekhalif, J. B. Nagy, A. A. Koos, Z. Osvath, A. Kocsonya, L. P. Biro, and I. Kiricsi, *Chem. Phys. Lett.* 360, 429 (2002).
- [30] J. Kotakoski, A. V. Krasheninnikov, Y. Ma, A. S. Foster, K. Nordlund, and R. M. Nieminen, *Phys. Rev. B* 71, 205408 (2005).
- [31] I. Hagiri, N. Takahashi, and K. Takeda, *J. Phys. Chem. A* 108, 2290 (2004).
- [32] Y. Ma, A. S. Foster, A. V. Krasheninnikov, and R. M. Nieminen, *Phys. Rev. B* 72, 205416 (2005).
- [33] B. Delley, *J. Quant. Chem.* 69, 423 (1998).
- [34] H. J-Monkhorst, and J. D. Pack, *Phys. Rev. B* 13, 5188 (1976).
- [35] R. Czerw, M. Terrones, J.-C. Charlier, X. Blasé, B. Foley, R. Kamalakaran, N. Grobert, H. Terrones, D. Tekleab, P. M. Ajayan, W. Blau, M. Ruhle, and D. L. Carroll, *Nano Lett.* 1, 457 (2001).
- [36] N. Govind, M. Petersen, G. Fitzgerald, D. King-smith, and J. Andzelm, *Comput. Mater. Sci.* 28, 250 (2003).
- [37] C. Sun, H. Wang, M. Hayashi, L. Chen, and K. Chen, *J. Am. Chem. Soc.* 128, 8368 (2006).
- [38] H. C. Choi, S. Y. Bae, J. Park, K. Seo, C. Kim, B. Kim, H. J. Song, and H. J. Shin, *Appl. Phys. Lett.* 85, 5742 (2004).
- [39] M. Terrones, R. Kamalakaran, T. Seeger, and M. Ruhle, *Chem. Commun.* 23, 2335 (2000).

- [40] H. Pan, Y. P. Feng, and J. Y. Lin, *Phys. Rev. B* 70, 245425 (2004).
- [41] J. Zhao, H. Park, J. Han, and J. P. Lu, *J. Phys. Chem. B* 108, 4227 (2004).
- [42] K. Kong, S. Han, and J. Ihm, *Phys. Rev. B* 60, 6074 (1999).
- [43] H. S. Kang, and S. Jeong, *Phys. Rev. B* 70, 233411 (2004).
- [44] M. Zhao, Y. Xia, Y. Ma, M. Ying, X. Liu, and L. Mei, *Phys. Rev. B* 66, 155403 (2002).
- [45] A. Maita, J. Andzelm, N. Tanpipat, P. von Allmen, *Phys. Rev. Lett.* 87, 155502 (2001).
- [46] H. S. Kang, *J. Phys. Chem. B* 110, 4624 (2006).
- [47] H. F. Bettinger, T. Dumitrica, G. E. Scuseria, and B. I. Yakobson, *Phys. Rev. B* 65, 041406 (2002).
- [48] D. L. Carroll, P. Redlich, P. M. Ajayan, J. C. Charlier, X. Blasé, A. De Vita, and R. Car, *Phys. Rev. Lett.* 78 2811 (1997).
- [49] A. De Vita, J.-Ch. Charlier, X. Blasé and R. Car, *Appl. Phys. A* 68 283 (1999).
- [50] S. Okada, K. Nakada, K. Kuwabara, K. Daigoku, and T. Kawai, *Phys. Rev. B* 74 121412(R) (2006).
- [51] A. Maiti, A. Svizhenko, and M. P. Anantram, *Phys. Rev. Lett.* 88 126805-1 (2002).
- [52] S. Shanmugam, and A. Gedanken, *Electrochem. Commum.* 8 1099 (2006).
- [53] C. P. Ewels, M Gelrup, *J. Nanosci. Nanotech.* 5, 1345 (2005).
- [54] D. Golberg, Y. Bando, W. Han, K. Kurashima and T. Sato, *Chem. Phys. Lett.* 308, 337 (1999).
- [55] W. Han, Y. Bando, K. Kurashima and T. Sato, *Chem. Phys. Lett.* 299, 368 (1999).
- [56] M. Terrones, P. M. Ajayan, F. Banhart, X. Blase, D. L. Carroll, J. C. Charlier, R. Czerw, B. Foley, N. Grobert, R. Kamalakaran, P. Kohler-Redlich, M. Ruhle, T. Seeger and H. Terrones, *Appl. Phys. A* 74, 355 (2002).
- [57] R. Czerw, M. Terrones, J. C. Charlier, X. Blase, B. Foley, R. Kamalakaran, N. Grobert, H. Terrones, D. Tekleab, P. M. Ajayan, W. Blau, M. Ruhle and D. L. Carroll, *Nano Lett.* 1, 457 (2001).
- [58] E. Borowiak-Palen, T. Pichler, G. G. Fuentes, A. Graff, R. J. Kalenczuk, M. Knupfer and J. Fink, *Chem. Phys. Lett.* 378, 516 (2003).
- [59] Y. L. Mao, X. H. Yan, Y. Xiao, J. X. Cao, and J. Xiang, *Int. J. Mod. Phys. C* 1363, 16 (2005).
- [60] H. Sun, J. Jia, D. Zhong, Q. Shen, M. Sun, Q. Xue, and E. G. Wang, *Phys. Rev. B* 66 085423 (2002).
- [61] S. Erkoc, *Physica E* 31 62 (2006).

- [62] R.G. Parr, W. Yang, Density-Functional Theory of Atoms and Molecules, Oxford University Press: New York (1989).
- [63] J. P. Perdew, and Y. Wang, Phys. Rev. B 45 13244 (1992).
- [64] J. Harris, Phys. Rev. B 31 1770 (1985).
- [65] H.M. Polatoglou, M. Methfessel, Phys. Rev. B 37 10403 (1988).
- [66] P. Lambin, A. Fonseca, J. P. Vigneron, J. B. Nagy, and A. A. Lucas, Chem. Phys. Lett. 85, 245 (1995).
- [67] P. Lambin, and V. Meunier, Appl. Phys. A 263, 68 (1999).
- [68] J.W. Mintmire, B.I. Dunlap and C.T. White, Phys. Rev. Lett. 631, 68 (1992).
- [69] N. Hamada, S.I. Sawada and A. Oshiyama. Phys. Rev. Lett. 1579, 68 (1992).
- [70] A.C. Dillon, K.M. Jones, C.H. Bekkedahl, C.H. Kiang, D.S. Bethune, M.J. Heben, Nature 386, 377 (1997).
- [71] M. Hischer, M. Becher, J. Nanosci. Nanotech. 3, 3 (2003).
- [72] K.A. Williams, P.C. Eklund, Chem. Phys. Lett. 320, 352 (2000).
- [73] G. Vidali, G. Ihm, H. Y. Kim, M. W. Cole, Surf. Sci. Rep. 12 133 (1991).
- [74] S.H. Jhi, Y. K. Kwon, K. Bradley, J.C.P. Gabriel, Solid State Commun. 129, 769 (2004).
- [75] J. Zhao, A. Buldum, J. Han, J. P. Lu, Nanotechnology 13, 195 (2002).
- [76] (a) D.J. Browning, M.L. Gerrard, J.B. Lakeman, I.M. Mellor, R.J. Mortimer, M.C. Turpin, Nano Lett. 2, 201 (2002). (b) S.P. Chan, G. Chen, X.G. Gong, Z.F. Liu, Phys. Rev. Lett. 87, 205502 (2001).
- [77] A. Chambers, C. Park, R.T.K. Baker, N.M. Rodriguez, J. Phys. Chem. B 102, 4253 (1998).
- [78] W.Q. Deng, x. Xu, W.A. Goddard, Phys. Rev. Lett. 92, 66103-1 (2004).
- [79] J. S. Arellano, L. M. Molina, A. Rubio, M. J. Lopez, J. A. Alonso, J. Chem. Phys. 117, 2281 (2002).
- [80] H. Rydberg, N. Jacobson, P. Hyldgaard, S. Simak, B. I. Lundqvist, D. C. Langreth, Surf. Sci. 532, 606 (2003).
- [81] A. J. Du, S. C. Smith, Nanotechnology 16, 2118 (2005).
- [82] P. Guay, B. L. Stansfield, A. Rochefort, Carbon 42, 2187 (2004).
- [83] A. K. Rappe, C. J. Casewit, K. S. Colwell, W. A. Goddard, W. M. Skiff, J. Am. Chem. Soc. 114, 10024 (1992).
- [84] N. Metropolis, A. W. Rosenbluth, M. N. Rosenbluth, A. H. Teller, E. Teller, J. Chem. Phys. 21, 1087 (1953).
- [85] J. Miyamoto, Y. Hattori, D. Noguchi, H. Tanaka, T. Ohba, S. Utsumi, H. Kanoh, Y. A. Kim, H. Muramatsu, T. Hayashi, M. Endo, K. Kaneko, J. Am. Chem. Soc. 128, 12636 (2006).

[86] Y. Yoshia, J. Appl. Phys. 87, 3338 (2000).

[87] M. L. Connolly, Science 221, 709 (1983).



## **Chapter 4. Synthesis and Characterizations of carbon nanotubes.**

### *Summary*

Single-walled and multi-walled carbon nanotubes were synthesized via decomposition of methane over Co-Mo catalysts. A 5-step purification process was employed to purify the as-synthesized carbon nanotubes. The carbon nanotubes were characterized using electron microscopy, thermo-gravimetric analysis, Raman spectroscopy, x-ray and ultraviolet photoelectron spectroscopy.

## **4.1. Synthesis and characterizations of carbon nanotube**

### *Introduction*

Carbon nanotube (CNT) is one of the most promising molecular structures, which has been envisioned for a wide range of future technological innovations. However the full potential applications of CNT will be hard to achieve unless the synthesis of CNT can be well controlled and optimized. There are several established synthetic methods to produce CNT, which include arc discharge<sup>1</sup>, laser ablation<sup>2</sup>, and chemical vapor deposition (CVD). For CVD methods, hydrocarbons (e.g. CH<sub>4</sub>, C<sub>2</sub>H<sub>2</sub>, C<sub>2</sub>H<sub>4</sub>)<sup>3-5</sup>, alcohol vapor<sup>6</sup>, and carbon monoxide<sup>7</sup> have been used as the carbon source for the synthesis of CNT. Anodic aluminum oxide (AAO) template<sup>8</sup> and plasma-enhanced CVD<sup>9</sup> (PE-CVD) methods are also useful technique to fabricate neat arrays of CNT. Although arc discharge and laser ablation methods can produce high quality single-walled carbon nanotubes (SWNT), the available quantity can be limited. On the other hand, CVD may be a better choice for large-scale production of CNT. This method has already been implemented to scale up the production of multi-walled carbon nanotubes<sup>10</sup>. Rice University<sup>7</sup> has pioneered the SWNT synthesis via high-pressure disproportionation of carbon monoxide (HiPco) process, which is able to produce 10g/day of high-purity SWNT.

In this section 4.1, single-walled and multi-walled carbon nanotubes were synthesized via the CVD method. The as-synthesized CNT powder was purified using a multi-step purification process. Electron microscopy, thermogravimetric analysis, Raman spectroscopy and photoelectron spectroscopy were employed to characterize the purified CNT. The formation mechanism of CNT was also discussed.

### **4.1.1. Decomposition of CH<sub>4</sub> over Co-Mo catalyst**

Bulk quantities of carbon nanotube powder were synthesized by the CVD method. Methane (CH<sub>4</sub>) was chosen as the carbon source for the CNT growth because it is relatively safer and produces less amorphous carbon. The catalytic decomposition of CH<sub>4</sub> (purity >99.95%) was

carried out with bimetallic cobalt-molybdenum (Co-Mo) catalysts for the production of SWNT and MWNT. Figure 4.1 shows the schematic setup of the CVD system.

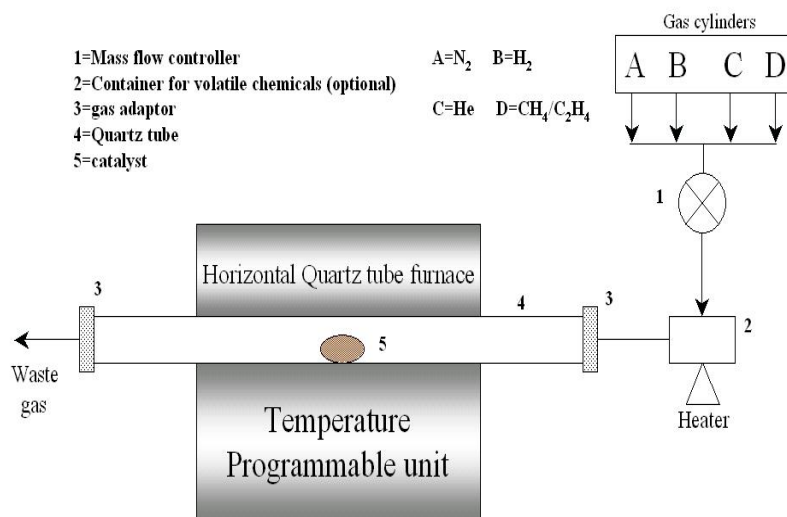


**Figure 4.1.** Schematic setup of thermal CVD used for the synthesis of carbon nanotube.

The mass flow controller controls two different gases flowing simultaneously into the tube furnace (e.g. CH<sub>4</sub> and H<sub>2</sub>). The CVD setup was appended with a glass vessel (labeled 2 in Fig 4.1) for the generation of other chemical vapors. For example, heating ammonium carbonate salts in the glass vessel, ammonia (with CO<sub>2</sub>) gas can be generated. Likewise, acetonitrile (CH<sub>3</sub>CN) vapor can be produced for the synthesis of nitrogen-doped carbon nanotubes (see Chapter 6, page 149).

The Co-Mo catalysts were dispersed over an oxide support. Magnesium oxide (MgO) support was preferred to other supports (Al<sub>2</sub>O<sub>3</sub>, SiO<sub>2</sub> and zeolites) because common acids can easily remove the MgO support. The role of the support was to prevent the agglomeration and sintering of the Co-Mo catalysts at high temperature. The sintering of the Co-Mo catalyst was undesirable, as it would decrease the activity of the catalyst and result in poor growth of carbon

nanotubes. The addition of molybdenum increases the yield of carbon nanotube and suppresses the formation of amorphous carbon<sup>11</sup>.

The catalysts were prepared by wet mechanical mixing and combustion technique, with citric acid as foaming and combustion additive. The use of citric acid as a fuel results in milder combustion and larger specific surface area of metal oxide support. From a catalytic viewpoint, a larger surface area of metal oxide support is desirable because the bimetallic Co-Mo is better dispersed and the interactions with CH<sub>4</sub> and H<sub>2</sub> molecules are improved.

The weighted amounts of catalyst ingredients (nitrate salts: Mg(NO<sub>3</sub>)<sub>2</sub>·6H<sub>2</sub>O, Co(NO<sub>3</sub>)<sub>2</sub>·6H<sub>2</sub>O, and molybdenum salts: (NH<sub>4</sub>)<sub>6</sub>Mo<sub>7</sub>O<sub>2</sub>·4H<sub>2</sub>O) in molar ratio denoted as Co<sub>α</sub>Mo<sub>β</sub>Mg<sub>1-α-β</sub>O were dissolved in 5ml of water, following by the addition of 4g citric acid. The resulting aqueous solution was gelled at ~60°C while constant stirring. It was then put directly into a furnace held at 550°C to be baked for at least 2 hour. A beige foamy product was obtained and grinded into fine powder. Table 4.1 gives the detailed composition of catalysts and the corresponding synthesized CNT.

**Table 4.1.** Composition of catalysts used for the synthesis of CNT.

No.	Types of carbon nanotube	Composition of catalyst
1	SWNT	<b>Co<sub>0.05</sub>Mo<sub>0.025</sub>Mg<sub>0.925</sub>O:</b> 10g Mg(NO <sub>3</sub> ) <sub>2</sub> ·6H <sub>2</sub> O + 0.222g Co(NO <sub>3</sub> ) <sub>2</sub> ·6H <sub>2</sub> O + 0.134g (NH <sub>4</sub> ) <sub>6</sub> Mo <sub>7</sub> O <sub>2</sub> ·4H <sub>2</sub> O
2	MWNT (10-30nm)	<b>Co<sub>0.1</sub>Mo<sub>0.1</sub>Mg<sub>0.8</sub>O:</b> 10g Mg(NO <sub>3</sub> ) <sub>2</sub> ·6H <sub>2</sub> O + 1.42g Co(NO <sub>3</sub> ) <sub>2</sub> ·6H <sub>2</sub> O + 0.862g (NH <sub>4</sub> ) <sub>6</sub> Mo <sub>7</sub> O <sub>2</sub> ·4H <sub>2</sub> O

The production of CNT was carried out in a horizontal quartz tube furnace (see Fig 4.1). Typically, ~0.2g of the supported Co-Mo catalyst was heated in a continuous flow of CH<sub>4</sub>-H<sub>2</sub> mixture (flow rate of H<sub>2</sub> and CH<sub>4</sub>, = 50:20sccm/min respectively) at ambient pressure. The

furnace temperature was heated up quickly from room temperature to 400°C and held for about ~30 minutes to purge away air and moisture, as the catalyst tends to adsorb considerable amount of moisture. The furnace was then heated at a rate of 5°C/min up to a maximum of 1000°C with no dwell time. Once the temperature reached 1000°C, the CH<sub>4</sub>-H<sub>2</sub> supply was cut off and the samples were cooled down naturally under nitrogen gas protection.

#### **4.1.2. Purification process of CNT**

The as-synthesized CNTs are often contaminated with residual catalysts and amorphous carbon. Therefore it is pertinent to remove these impurities so that the characterizations of CNT can be more accurate. In order to obtain high quality carbon nanotube, a multi-step purification process was carried out to remove the impurities. Figure 4.2 summarizes the purification process employed in this thesis.

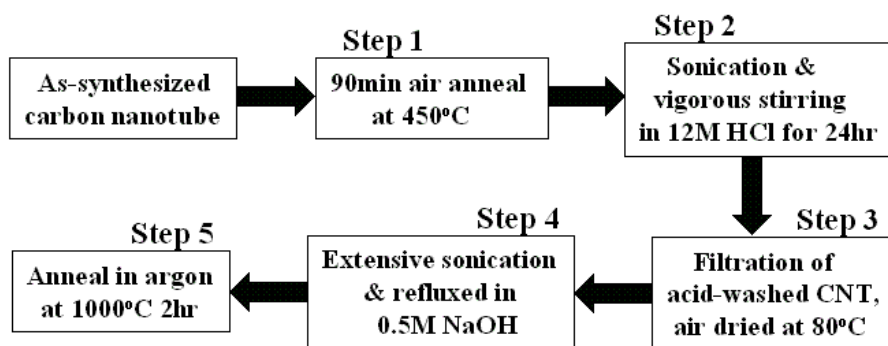


**Figure 4.2.** Purification process of as-synthesized CNT powder.

In step 1, the as-synthesized CNT powder was air-annealed at 450°C for 90min to remove the amorphous carbon. It is known with hindsight that the oxidative temperatures for amorphous carbon, SWNT and MWNT are about 330-400°C, 500-600°C and 700°C respectively (see below, Fig 4.5-4.6). Therefore air oxidation at 450°C is sufficient to burn off the amorphous carbon

without damaging the CNT. In step 2, the CNT was briefly sonicated and stirred vigorously in 12M HCl acid so that metal catalysts trapped inside the entanglement of CNTs can be removed effectively. This is followed by step 3 whereby the acid-washed CNT was filtered, rinsed with distilled water and air-dried at 80°C. Step 4 was proposed by M. Shiraishi et al.<sup>12</sup> as an additional step to rid the external surfaces of CNT from amorphous carbon. In step 5, the CNT was annealed at 1000°C for 2hr in argon / helium gas (purity  $\geq 99.9995\%$ ) to remove surface oxides that might be formed during the acid treatment and to improve its crystallinity<sup>13</sup>. Step 5 was crucial for careful spectroscopic investigations of pristine CNT samples.

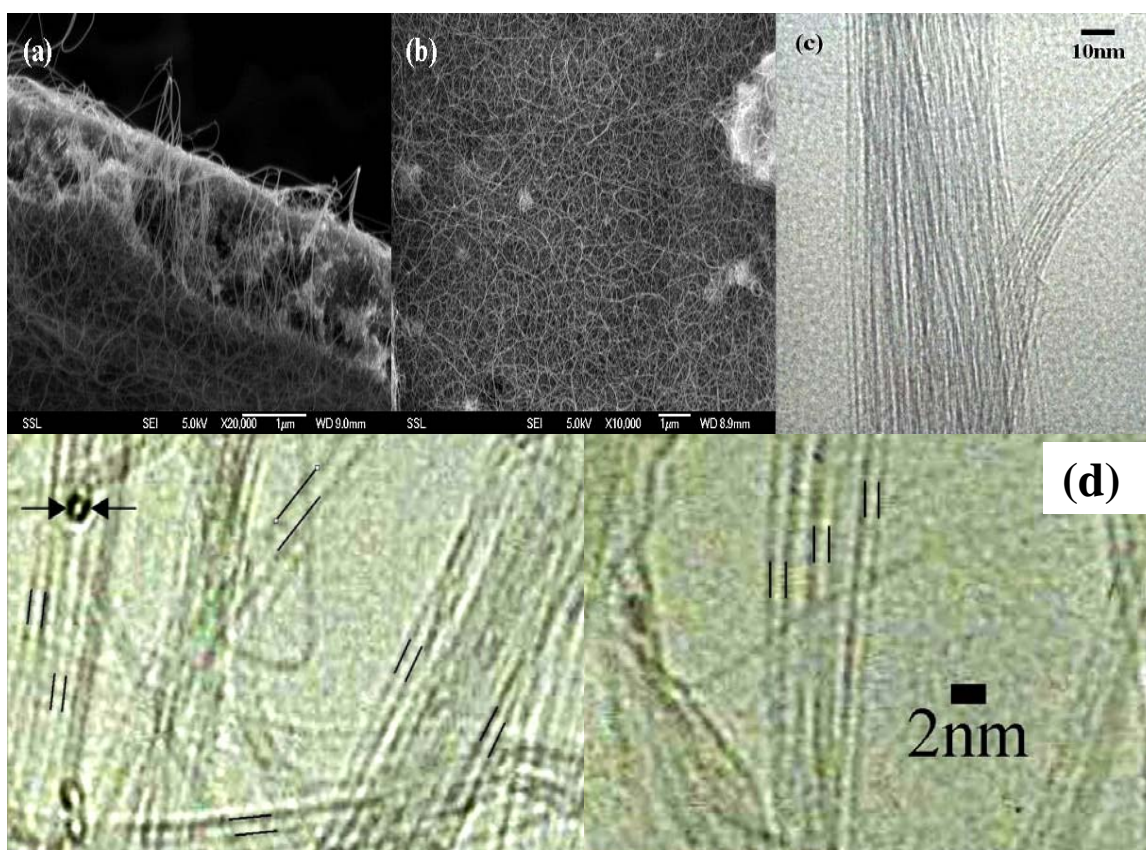


**Figure 4.3.** Scanning electron micrographs of (a) as-synthesized and (b) purified SWNT. (c) Transmission electron micrograph of a purified SWNT bundle. (d) High resolution TEM micrographs of purified SWNT.

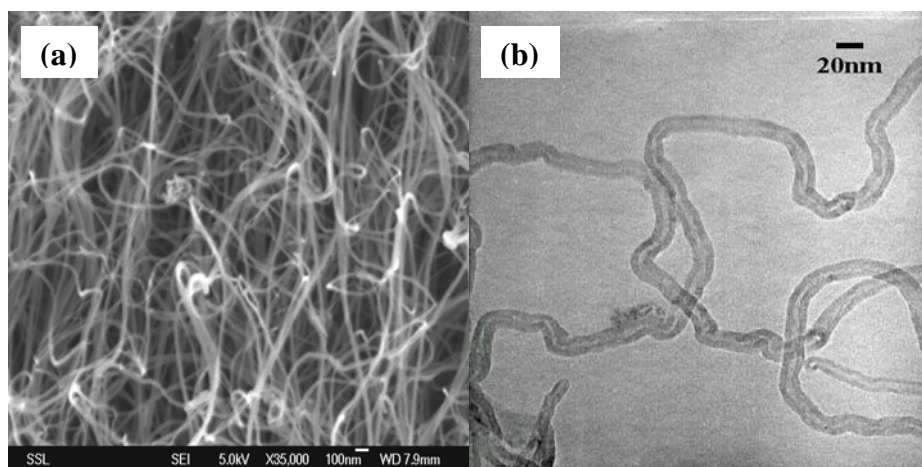


**Figure 4.4.** (a) Scanning electron micrograph and (b) transmission electron micrograph of purified MWNT.

### **4.1.3. Characterizations of carbon nanotube**

#### *Electron microscopy*

Figure 4.3 shows the electron microscopy images (TEM, JEOL JEM-2010J / Tecnai TF 20 S-twin and SEM, JEOL JSM-6700F) of the SWNT samples. For the as-synthesized SWNT, dense bundles of SWNT can be seen growing out of the Co-Mo cluster. Figure 4.3b-d show the SWNT after the 5-step purification process. The diameters of the purified SWNT bundles are estimated to be around 10-50nm, and length of tens of micrometer. The diameters of individual SWNTs were estimated to be from 0.9nm-1.3nm based on high-resolution TEM images (Fig 4.3d). Furthermore, the external surfaces of the purified SWNT bundles are very clean and do not have amorphous carbon. Figure 4.4a-b show the electron microscopy images of the MWNT after the 5-step purification process. The outer diameters of purified MWNTs are about 10-30nm, with length of tens of micrometer. Thermogravimetric analysis (TGA) was further employed to evaluate the purity of the carbon nanotube samples.

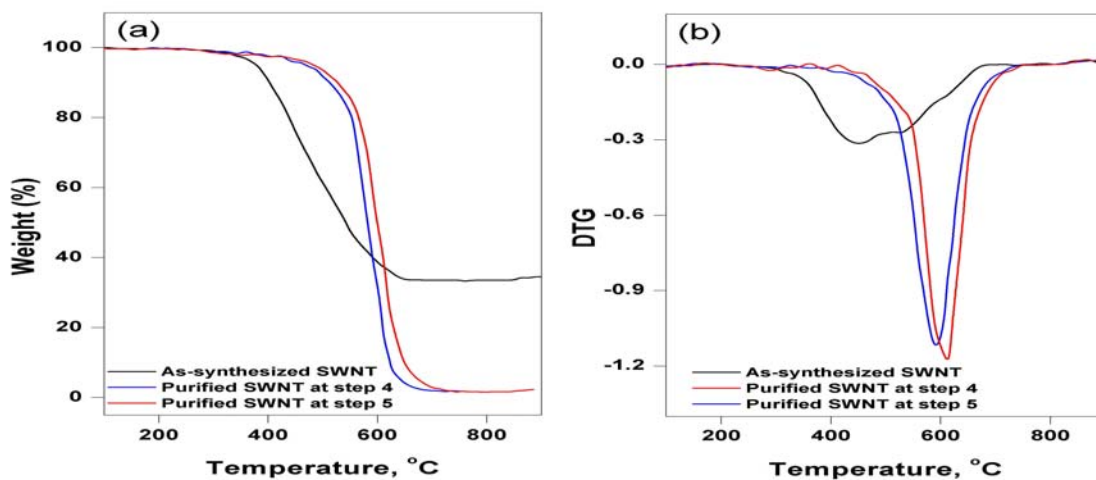


**Figure 4.5.** (a) TGA and (b) differentiated TG (DTG) of as-synthesized SWNT (black line), step 4 purified SWNT (blue line), and step 5 purified SWNT (red line). Temperature ramp rate =  $10^{\circ}\text{C}/\text{min}$  in 10%  $\text{O}_2/\text{Ar}$ .

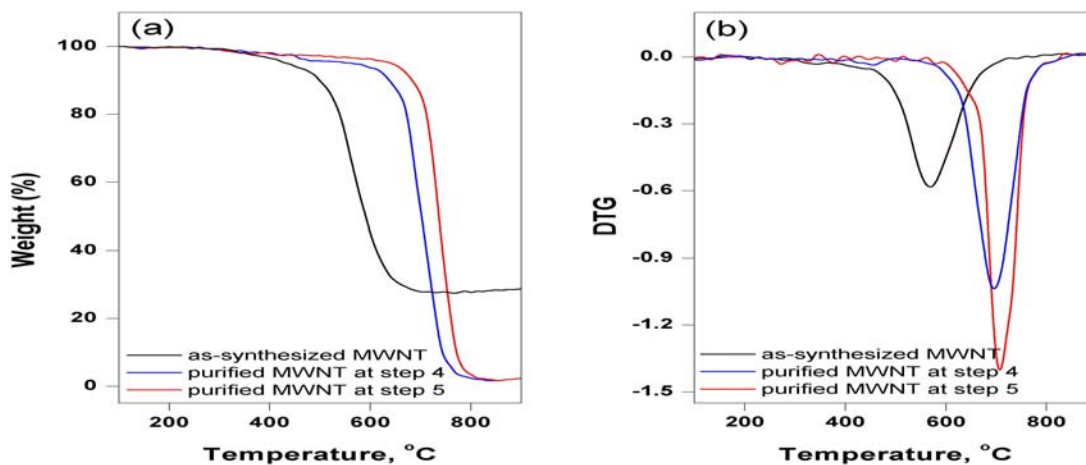


**Figure 4.6.** (a) TGA and (b) differentiated TG (DTG) of as-synthesized MWNT (black line), step 4 purified MWNT (blue line), and step 5 purified MWNT (red line). Temperature ramp rate =  $10^{\circ}\text{C}/\text{min}$  in 10%  $\text{O}_2/\text{Ar}$ .



*Thermogravimetric analysis (TGA)*

Thermogravimetric analysis (TGA and differentiated TG (DTG), PERKIN ELMER TGA7) is a useful tool to monitor the combustion of carbon nanotubes in air, which can be related to the purity and quality of the carbon nanotube. In a typical TGA run, ~20mg of the CNT samples were loaded into a ceramic cup and held at 100°C for 2hr to remove moisture. The temperature was increased at 10°C/min from 100°C to 950°C in 10%O<sub>2</sub>-90%argon carrier.

Figure 4.5 and Figure 4.6 show the TGA-DTG analysis of SWNT and MWNT samples respectively. In general, the burning temperatures of the as-synthesized CNTs were much lower than the purified and annealed CNTs. The as-synthesized SWNT had a broad oxidation temperature and it was estimated from DTG curve (Fig 4.5b) that there were 3 ignition points located at ~455°C, 522°C and 603°C. The ignition temperature at 455°C was attributed to the burning of amorphous carbon<sup>14</sup>, and the residual catalyst induced SWNT to be burned off at a lower temperature of ~522°C onwards. The presence of metallic particles is known to assist in burning off the amorphous carbon, but also reduces the overall oxidation temperatures of carbon nanotubes<sup>15</sup>.

The oxidation temperature of as-synthesized MWNT exhibited a clear ignition at ~569°C (Figure 4.6b). The absence of an ignition temperature at ~450°C for the as-synthesized MWNT might be due to the use of higher molybdenum ratio in the Co-Mo catalyst, which effectively suppresses amorphous carbon formation. The carbon content of the as-synthesized SWNT and MWNT are about 65% and 72% as estimated from the remaining metal oxides. After the 5-step purification process, the metal content was reduced to <3%. For convenience, high temperature annealing at 1000°C was performed in-situ with argon gas (purity >99.9995%) in the TG equipment. The temperature was raised at 5°C/min to 1000°C and the CNT samples were annealed for 2hr in argon atmosphere.

On the basis of the DTG curves, the oxidation temperatures of the SWNT and MWNT at step 4 purification were ~589°C and ~692°C respectively. After annealing at 1000°C in argon

(step 5 purification), the oxidative resistance temperatures of SWNT and MWNT were enhanced to  $\sim 614^{\circ}\text{C}$  and  $\sim 707^{\circ}\text{C}$  respectively. The improved oxidation resistance of CNT is ascribed to the high temperature annealing, which have been reported to improve the graphitic crystallinity and ‘heal’ defective wall structures<sup>13</sup>. Therefore TGA-DTG experiments demonstrate that the ignition temperature of the purified SWNT and MWNT are  $\sim 614^{\circ}\text{C}$  and  $707^{\circ}\text{C}$  respectively. This is higher than the burning temperature of  $\text{C}_{60}$  ( $425^{\circ}\text{C}$ ) but lower than highly graphitized carbon fibers (up to  $800^{\circ}\text{C}$ ).

#### *Raman spectroscopy*

A Raman scattering signal is usually weak and involves only the phonons, being independent of the electronic structures of the material and the laser excitation energy. However, if the laser excitation energy matches the energy of the optically allowed electronic transitions in the materials, then the Raman scattering efficiency is enhanced. This intensity enhancement process is called resonance Raman scattering, whereby a strong coupling between electrons and phonons occur. For one-dimensional systems, which possess spike-like density of electronic states (DOS) and available for optical transitions, resonance effects will be prominent. Therefore resonance Raman spectroscopy is a powerful tool to probe the nature of the electronic structures (semiconducting or metallic nature), diameter distributions, defects and charge-transfer effects of SWNT<sup>16-19</sup>. In addition, Raman spectroscopy is an established method to characterize carbon materials owing to its sensitivity to the amount of ordering, degree of  $\text{sp}^2$ - $\text{sp}^3$  bonding and domain size of samples.

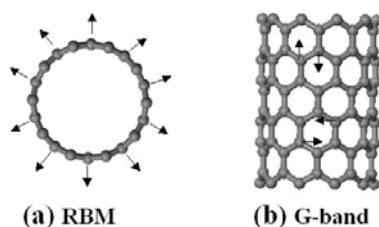


**Figure 4.7.** Schematic diagram depicting the atomic vibrations for (a) the radial breathing mode (RBM) and (b) tangential (G-band) modes of SWNT.

Figure 4.7 depicts two atomic vibrational modes of SWNT. The radial breathing mode (RBM) and tangential (G-band) mode are the signatures of SWNT Raman scattering, which can be observed at the lower wavenumbers ( $\sim 100\text{-}400\text{cm}^{-1}$ ) and higher wavenumbers ( $\sim 1600\text{cm}^{-1}$ ) respectively. A comparison G-band study of SWNT, highly oriental pyrolytic graphite (HOPG) and glassy carbon indicates that the G-band of SWNT similarly belongs to the  $E_{2g}$  G-band of the graphite sheet<sup>18</sup>. However the G-band of SWNT is predicted and observed to split into two bands due to two different tangential vibration modes (see Fig 4.7b): one upshifted  $G^+$ -band independent of the tube diameter and another downshifted  $G^-$ -band dependent of the tube diameter (resonance effects), which can further splitted into other components<sup>19</sup> (see page 119). However the RBM signals provide more useful and direct information on SWNT. The RBM is diameter-dependent and it has been shown to have the following experimental relationship<sup>18,19</sup>:

$$\omega_{\text{RBM}} = A/d_t + B \quad [4.1]$$

where  $\omega_{\text{RBM}}$  is the observed Raman RBM signal,  $A$  and  $B$  are parameters determined experimentally. For SWNT bundles, the parameters were fitted experimentally with  $A=234\text{nm}\cdot\text{cm}^{-1}$  and  $B=10\text{cm}^{-1}$ . The parameter  $B$  is an upshift due to tube-tube interaction. For isolated SWNT,  $A=248\text{ nm}\cdot\text{cm}^{-1}$  and  $B=0$ . Since the purified SWNT are assembly of bundles,  $\omega_{\text{RBM}} = 234 (\text{nm}\cdot\text{cm}^{-1}) /d_t (\text{nm}) + 10 (\text{cm}^{-1})$  is used in this thesis.

It has been pointed out that for  $d_t \ll 1\text{nm}$ , equation [4.1] exhibits deviation from the measured values due to nanotube lattice distortions leading to a chirality dependence of RBM frequencies. For  $d_t > 2\text{nm}$ , the intensity of the RBM is very weak and hardly observable<sup>18</sup>.

#### *Kataura Plot and Resonance conditions*

On the basis of tight-binding zone-folding method, H. Kataura et al.<sup>16</sup> demonstrated that the bandgap energy,  $E_g$ , between two von Hove Singularities (vHS) of a SWNT was related to its diameter,  $d_t$ , and chirality as well. The Kataura plot ( $E_g$  vs  $d_t$ ) is the formalism resulting in the

organization of metallic and semiconducting SWNTs based on the chirality vector. Hence if one employs resonance Raman spectroscopy and a Kataura plot to analyze the results, one should be able to experimentally determine the diameter, chirality, and electronic nature of the SWNT. However, this simplified theory has limited success in assigning real SWNT samples. For real sample, effects such as warping of the Brillion zone, changes in the circumferential bond length (especially  $d_t \ll 1\text{nm}$ ) due to curvature and inter-tube coupling effects (SWNT bundles) complicate the Raman spectra and such effects need to be taken into considerations.

Thus a revised Kataura plot<sup>17</sup> based on new experimentally mapping of  $E_g$  vs  $d_t$  was reported in literature. It is sufficient to consider only the two lowest interband transitions because higher order transitions generally have very weak intensity. This revised Kataura plot is displayed in Figure 4.8, and it is employed in this thesis for the chirality assignment of the purified SWNT; otherwise the assignment and interpretation of the Raman spectra of SWNT can be confusing and complicating.

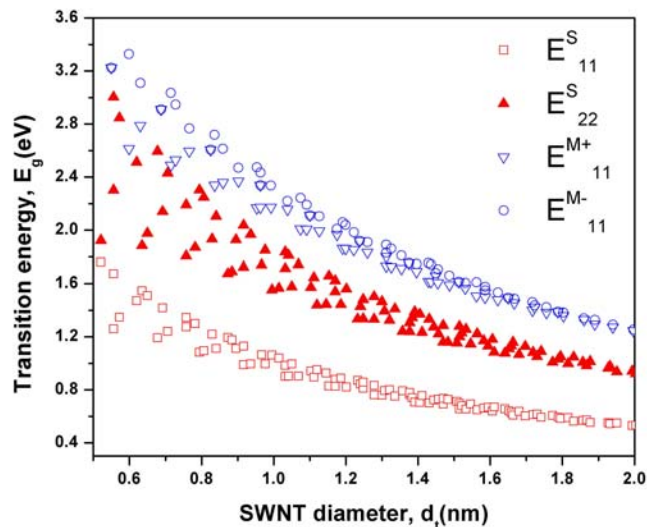


**Figure 4.8.** A revised Kataura plot<sup>17</sup> of  $E_g$  vs  $d_t$ . The two lowest interband transitions are denoted by  $E_{11}^S(d_t)$ ,  $E_{22}^S(d_t)$ ,  $E_{11}^{M\pm}(d_t)$ , where 11 is the first vHS, 22 is the second vHS, S for semiconducting (red) tubes, M for metallic (blue) tubes, and  $\pm$  is the split into high (+) and (-) low energy transitions in metallic tubes.

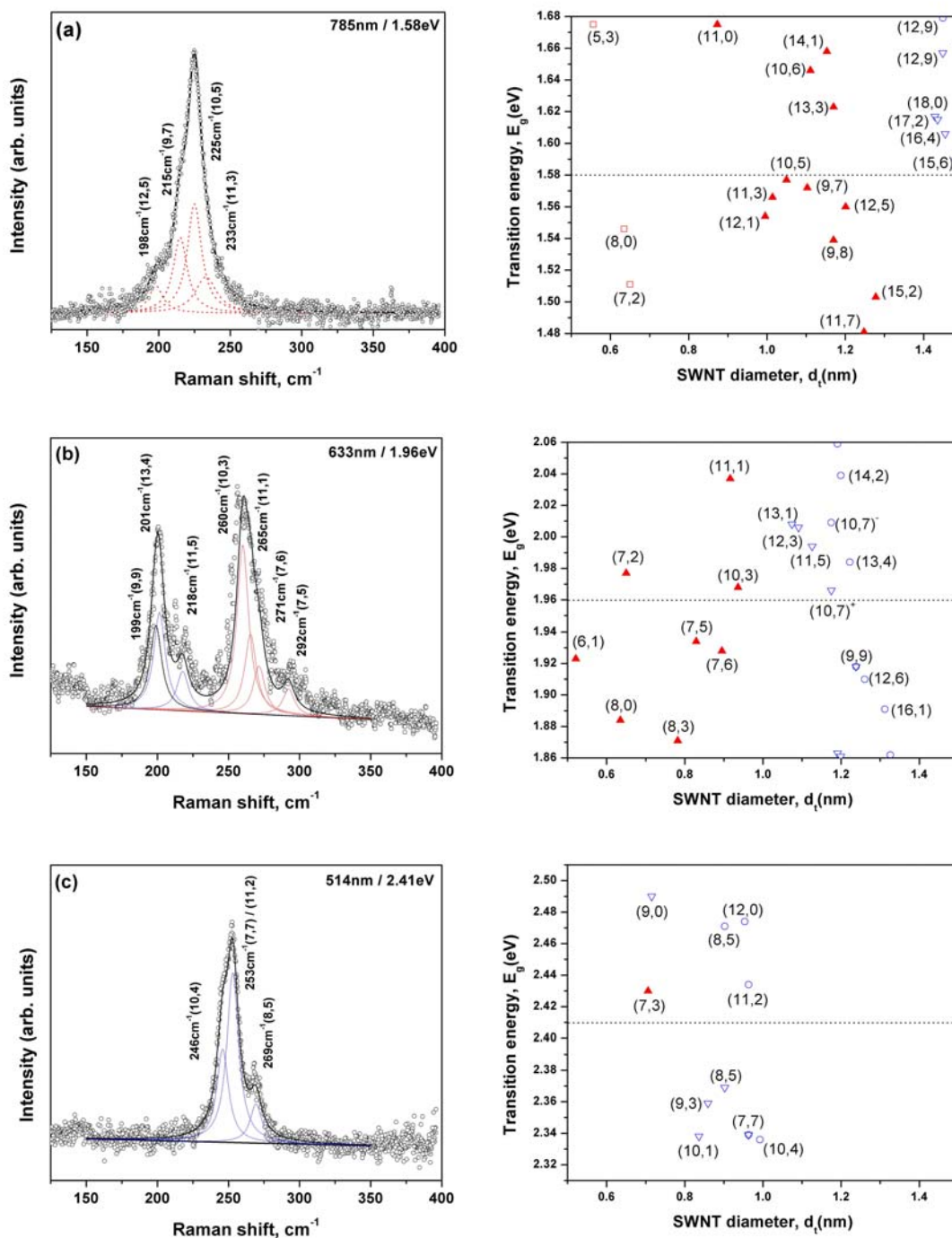


**Figure 4.9.** RBMs of SWNTs using resonance Raman laser excitation wavelengths at (a) 785nm, (b) 633nm, and (c) 514nm. The corresponding Kataura plot is displayed next to the observed RBMs with a transition window of  $\pm 0.1\text{eV}$ . *Red and blue deconvolutions for semiconducting and metallic tubes respectively. Chirality of SWNT is indicated beside the observed  $\omega_{\text{RBM}}$ .*

*Assigning chirality of the observed RBM frequencies.*

In this thesis, three laser excitation wavelengths (energies) of 785nm (1.58eV), 633nm (1.96eV) and 514nm (2.41eV) were employed to collect the RBM spectra of the purified SWNT. The transition within the resonance window of the excitation laser is observed to be  $\pm 100$ meV. For MWNT samples, which do not have resonance effect, it is sufficient to study its Raman spectra using only a single laser wavelength (namely, 514nm). The G-band of MWNT will be appropriately discussed in conjunction with the synthesis of nitrogen-doped carbon nanotubes (Chapter 6, page 149).

Figure 4.9 shows the RBM spectra of the purified SWNT recorded at 3 different Raman laser energies. The observed Raman shift represents the most frequently observed positions for different laser spots on the samples. A Lorentzian fitting was used to deconvolve the RBM signals. The chirality of the SWNT was assigned based on its determined diameter (equation 4.1 for SWNT bundle), which matches closest to those given on the Kataura plot. The analysis of the recorded RBMs was as followed:

For 785nm (1.58eV) excitation, three distinct types of RBM signals are possible as shown by the Kataura plot (Fig 4.9a). The  $E_{11}^S$ ,  $E_{22}^S$  and  $E_{11}^M$  vHS transitions of semiconducting and metallic nanotubes are allowed. The  $E_{11}^S$  vHS transitions belong to semiconducting SWNTs with small diameters ( $d_t \leq 0.6$ nm), while the  $E_{22}^S$  vHS transitions belong to semiconducting SWNTs with larger diameters  $\sim 0.9$ - $1.2$ nm. The  $E_{11}^M$  vHS transitions are due to metallic SWNTs with slightly larger diameters  $\sim 1.45$ nm. A comparison of the recorded and predicted RBM signals revealed that the recorded RBM signals were solely due to  $E_{22}^S$  vHS transitions of semiconducting SWNTs with diameters of  $\sim 0.92$ - $1.20$ nm. No  $E_{11}^S$  and  $E_{11}^M$  vHS transitions were recorded. This strongly implied that small diameter ( $d_t < 0.6$ nm) semiconducting SWNTs and large diameter ( $d_t \geq 1.4$ nm) metallic SWNTs were absent in the purified SWNT samples. The deconvolution and chirality assignments of SWNTs were displayed in Figure 4.9.

A similar analysis had been carried out for the recorded RBM signals of SWNTs with 633nm and 514nm laser excitations. For 633nm laser excitations, both  $E_{22}^S$  and  $E_{11}^M$  vHS transitions of SWNTs were observed simultaneously. The observed diameter distributions of the semiconducting SWNTs were ~0.83nm-0.94nm and metallic SWNTs were ~1.13nm-1.24nm at 633nm laser excitation. In contrast, only  $E_{11}^M$  vHS transitions of metallic SWNTs ( $0.9\text{nm} < d_t < 0.99\text{nm}$ ) was observed at 514nm laser excitation. This is consistent with the Kataura plot, which predicts a dominant  $E_{11}^M$  vHS transition of metallic nanotubes at 514nm laser excitation.

The overall diameter distribution of the purified SWNT was ~0.83nm-1.24nm as determined by resonance Raman spectroscopy. This diameter range agreed well with HRTEM estimation. However it should be emphasized that Raman spectroscopy can pick out SWNT RBMs in resonance with the laser energy, and the ratio of semiconducting-to-metallic nanotubes cannot be conclusively determined solely from a single laser excitation. As an illustration, it is not conclusive to state that there are more semiconducting nanotubes than metallic nanotubes from Figure 4.9b, and the absence of semiconducting (metallic) nanotubes from Figure 4.9c (Figure 4.9a). On the other hand, if the RBM spectrum collected at 633nm laser excitation shows a disappearance of semiconducting nanotubes after a chemical process to remove semiconducting tubes, then it is conclusive to state that the resulting sample is enriched with metallic nanotubes using only a single laser excitation.

On the basis of Figure 4.9, it can be seen that it is very difficult to synthesize SWNT with uniform tube diameter and even more challenging to have unique tube chirality. Suppose that the diameter of the fabricated SWNT is uniform,  $d_t \approx 1.37\text{nm}$ , but the chirality may be attributed to more than one type of nanotubes, namely metallic (10,10) tube and semiconducting (11,9) and (15,4) tubes. On the other hand, the synthesis of uniform small diameter ( $d_t \approx 0.43\text{nm}$ ) SWNT was met with some success using a zeolite template<sup>20</sup>. These very small diameter SWNTs possess interesting properties because of its much stronger tube-curvature effects.

*Tangential mode (G-band) of SWNT*

Figure 4.10 shows the G-bands of the purified SWNT recorded at 785nm, 633nm and 514nm laser excitations. The deconvolution of the G-band was performed with Lorentzian and Breit-Wigner Fano (BWF) fittings. The Lorentzian lineshape was used for semiconducting modes and metallic  $A^{LO}$  modes. The BWF fitting was used to fit the broadening of the G-band due to resonance metallic nanotubes ( $A^{TO}$  symmetry) at 633nm and 514nm laser excitations. The asymmetrical BWF lineshape is given by the following equation:

$$I(\omega) = I_o \frac{\left(1 + \frac{\omega - \omega_o}{q\Gamma}\right)^2}{1 + \left(\frac{\omega - \omega_o}{\Gamma}\right)^2} \quad [4.2]$$

where  $I_o$ ,  $\omega_o$ , and  $\Gamma$  are the intensity, renormalized discrete-mode frequency and broadening parameter respectively. The  $(1/q)$  parameter determines the departure of the BWF lineshape from a symmetric Lorentzian lineshape.

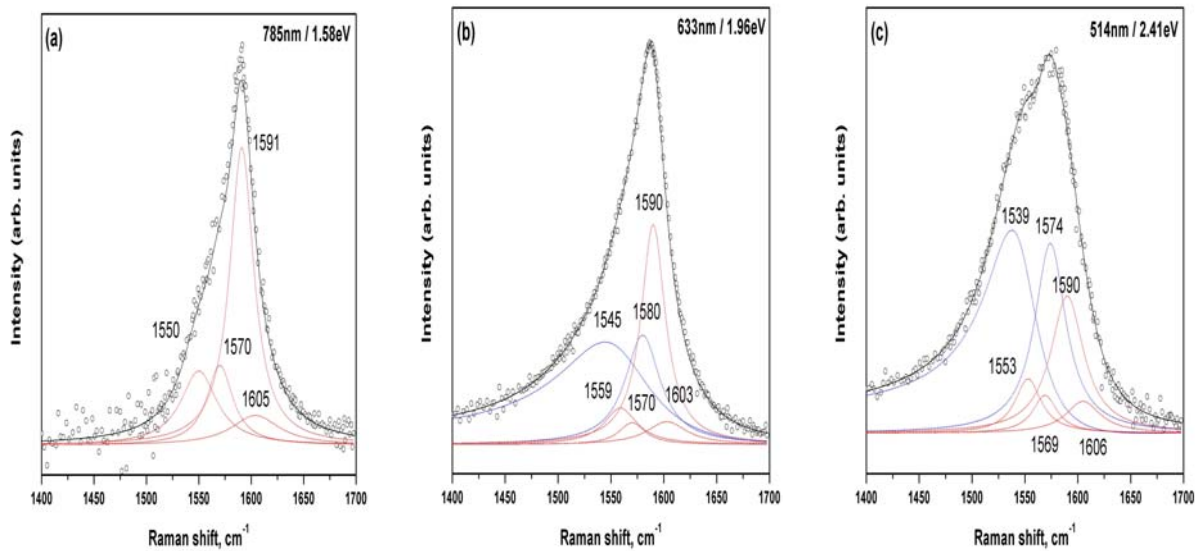


**Figure 4.10.** Deconvolved tangential G-band of the purified SWNT with three laser excitation wavelengths (a) 785nm, (b) 633nm and (c) 514nm.



**Table 4.2.** Detailed lineshape analysis of the tangential G-band of the purified SWNT ( $0.83\text{nm} < d_t < 1.24\text{nm}$ ). The peak positions ( $\omega$ ) and FWHM ( $\Gamma$ ) are listed for the Lorentzian lineshapes, and ( $1/q$ ) value is given for the BWF lineshapes.

	$\omega$ ( $\text{cm}^{-1}$ )	$\Gamma$ ( $\text{cm}^{-1}$ )	$1/q$
<b>785nm</b> (1.58eV)	1550 <sup>sc</sup>	21	-
	1570 <sup>sc</sup>	15	-
	1591 <sup>sc</sup>	14	-
	1605 <sup>sc</sup>	28	-
<b>633nm</b> (1.96eV)	1545 <sup>m</sup>	53	-0.20
	1559 <sup>sc</sup>	19	-
	1570 <sup>sc</sup>	15	-
	1580 <sup>m</sup>	20	-
	1590 <sup>sc</sup>	14	-
	1603 <sup>sc</sup>	23	-
<b>514nm</b> (2.41eV)	1539 <sup>m</sup>	32	-0.24
	1553 <sup>sc</sup>	15	-
	1569 <sup>sc</sup>	14	-
	1574 <sup>m</sup>	20	-
	1590 <sup>sc</sup>	19	-
	1606 <sup>sc</sup>	21	-

<sup>m</sup>Metallic nanotube  
<sup>sc</sup>Semiconducting nanotube

The fitting parameters of the tangential G-bands are displayed in Figure 4.10 and Table 4.2. For laser energy  $E_{\text{laser}}=1.58\text{eV}$  (785nm, Fig 4.10a), the G-band is deconvolved with four symmetrical Lorentzian lineshapes located at  $\sim 1550$ , 1570, 1591 and  $1605\text{cm}^{-1}$  for semiconducting species. This is consistent with RBM study (Fig 4.9a) at  $E_{\text{laser}}=1.58\text{eV}$ , whereby only semiconducting nanotubes are in resonance. For  $E_{\text{laser}}=1.96\text{eV}$  (633nm), the tangential G-band in Fig 4.10b is broadened at  $\sim 1545\text{cm}^{-1}$ , which is attributed to the Raman signal of metallic nanotubes. On the basis of RBM study (Fig 4.9b), it was already indicated that both semiconducting and metallic nanotubes were resonant at  $E_{\text{laser}}=1.96\text{eV}$ . The deconvolution of the G-band at  $E_{\text{laser}}=1.96\text{eV}$  was performed with five symmetrical Lorentzian lineshapes (four were attributed to the semiconducting nanotubes and one to metallic nanotubes) and one BWF lineshape for metallic nanotubes. In Fig 4.10c, the deconvolution of the G-band at  $E_{\text{laser}}=2.41\text{eV}$

(514nm) resonance requires the addition of semiconducting Lorentzian fittings, even though RBM study (Fig 4.9c) indicated that only metallic nanotubes were resonant at  $E_{\text{laser}}=2.41\text{eV}$ .

Group theory predicts that a typical chiral SWNT possesses 6 Raman-active modes within the G-band, which consists of two modes each with  $A_{1g}$ ,  $E_{1g}$  and  $E_{2g}$  symmetry<sup>18</sup>. The G-band of a pure semiconducting nanotube has been experimentally deconvoluted into 4 symmetrical Lorentzian components, which are located at  $\sim 1553$  ( $E_{2g}$ ),  $1569$  ( $A_{1g}$  and  $E_{1g}$ ),  $1592$  ( $A_{1g}$  and  $E_{1g}$ ) and  $1607$  ( $E_{2g}$ )  $\text{cm}^{-1}$ . Therefore the G-band at  $E_{\text{laser}}=1.58\text{eV}$  (Fig 4.10a) is consistent with literature. Likewise it is expected that a typical chiral metallic nanotube also possesses 6 active-Raman modes. However for a metallic nanotube only two components are needed to account for the G-band features ( $\sim 1540$  and  $\sim 1580\text{cm}^{-1}$  with split  $A_{1g}$  symmetry). The applications of Stokes and anti-Stokes Raman scattering supported these observations of metallic nanotubes<sup>18,19</sup>. For metallic nanotube, the G-band of anti-Stokes Raman scatterings required only two fitting components (one Lorentzian and one BWF lineshape), while the G-band of Stokes Raman scattering was made up of the same two components (as observed in anti-Stokes) and together with four additional semiconducting components at the same laser excitations. Duesberg et al.<sup>21</sup> confirmed that metallic SWNT exhibits an antenna effect, which is the preferential absorption and emission of light polarized parallel to the tube axis. The dominance of antenna effect in metallic SWNT consequently suppresses the  $E_{1g}$  and  $E_{2g}$  symmetry modes. Therefore, the experimental G-band of metallic SWNT can be fitted with only two components, which belong to  $A^{\text{LO}}$  and  $A^{\text{TO}}$  modes (LO and TO denote vibration parallel and perpendicular to the tubule axis respectively). The deviation of the BWF lineshape from a symmetrical Lorentzian lineshape was attributed to the coupling of a discrete phonon mode and an electronic continuum. Therefore the broadening of the G-band is observed for metallic nanotubes which possess finite DOS at the Fermi level, while semiconducting nanotubes have empty DOS at the Fermi level. The coupling of the discrete phonon mode with a phonon continuum is very unlikely because

both semiconducting and metallic nanotubes have similar multiphonon continua. Hence the fitting of a BWF lineshape was carried out for metallic nanotubes only.

In short, resonance Raman spectroscopy is an important and useful tool for the characterization of SWNT because the RBM spectra of SWNT provide valuable information about the diameter distributions, tube chirality and electronic properties. Although the G-band of SWNT also exhibits resonance effect, the assignment of tube chirality is not as straight forward as the RBM spectra.

#### *Photoelectron spectroscopy: XPS, UPS and work function studies*

The *C1s* core-level and energy loss features of the purified CNTs were studied with x-ray photoelectron spectroscopy (XPS, ESCA MK II using Mg  $K\alpha$  (1254.6eV) source under UHV better than  $3 \times 10^{-9}$  torr). The valence bands of the purified SWNT and MWNT were measured using ultraviolet photoelectron spectroscopy (UPS, He II 40.8eV) and also at the Singapore Synchrotron Light Source using photon energy of 60eV. The work functions ( $\Phi$ ) of the purified CNTs were studied using UPS He I (21.2eV) source, and determined from the secondary electron cutoff of the spectra using a gold reference ( $\Phi_{Au}=5.1\text{eV}$ ). The samples were biased at  $-10\text{V}$  during the work function measurements to accelerate the low energy secondary electrons. The carbon samples were pressed into thin pellets (pressurized at 10 tons and the pellet thickness was about a few hundred micrometers) and annealed at  $1000^\circ\text{C}$  under argon protection for at least 2 hours. This was to ensure that no air was trapped inside the pressed sheets. The pressed CNT sheets were attached to the XPS-UPS sample stub using a silver paste.

Figure 4.11a compares the normalized XPS *C1s* core-level of MWNT and SWNT. The *C1s* core-level of MWNT and SWNT was located at 284.3eV and 284.4eV respectively, which were downshifted from the *C1s* position of graphite (284.6eV) by  $\sim 0.2\text{-}0.3\text{eV}$ . The downshift of the nanotube *C1s* core-level could be due to the weaker C-C binding strained by the rolling-up of

the graphene sheet<sup>22</sup>. Figure 4.11b compares the *CI*s core-level loss energy of MWNT and SWNT. The energy loss features were composed of a  $\pi$ -plasmon ( $\pi \rightarrow \pi^*$  transition,  $\sim 6\text{eV}$ ) and a broad  $\sigma$ - $\pi$  plasmon ( $\sim 27\text{eV}$ ). Both SWNT and MWNT have similar  $\sigma$ - $\pi$  plasmons, but the lineshape of the  $\pi$ -plasmons are slightly difference. The MWNT exhibits some extra low-energy loss energy transitions at  $\sim 4.8\text{eV}$ , while SWNT has a sharper  $\pi$ -plasmon at  $\sim 6.2\text{eV}$ . The normalized  $\pi$ -plasmon intensity is also stronger in SWNT than MWNT, which indicates that SWNT possesses more  $\pi$ -electrons. This is consistent with valence band comparison study between SWNT and MWNT (vide infra).

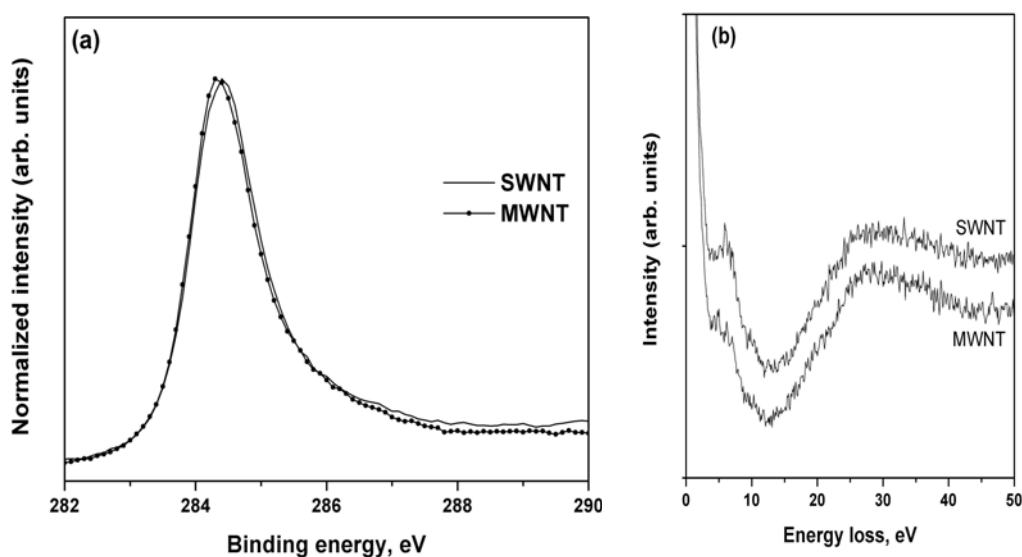


**Figure 4.11.** (a) Normalized XPS *CI*s core level and (b) loss energy spectra of purified SWNT and MWNT. *Loss energy spectra were shifted for clarity of presentation.*

As displayed in Figure 4.12, the valence band density of states (DOS) of CNTs are composed of  $2p-\pi$  electrons ( $\sim 3.2\text{eV}$ ) and  $2p-\sigma$  electrons ( $\sim 7.7\text{eV}$ ). The binding energy region between  $3-8\text{eV}$  is assigned to the overlapping of the  $2p-\pi$  and top of  $2p-\sigma$  electrons. Chen et al.<sup>22</sup> reported that the valence band DOS of MWNT closely resembles that of graphite, reflecting the similarity of their electronic structures. However, on the basis of Figure 4.12, the UPS spectra lineshape ( $40.8\text{eV}$  and  $60\text{eV}$  photon energies) of SWNT and MWNT are considerably different, although the main features of  $\pi$ - and  $\sigma$ -electrons are present. The  $\pi$ -electron intensity is more prominent in SWNT than MWNT. On the other hands, the spectra weight at  $\sim 6.5\text{eV}$  ( $2p-\pi$  overlaps with top of  $2p-\sigma$ ) and  $10.5\text{eV}$  ( $2p-\sigma$ ) is more pronounced in MWNT than SWNT. This strongly suggests differences in  $\pi$ - and  $\sigma$ -electrons between SWNT and MWNT. The DOS of MWNT can be approximated as a superposition of coaxial carbon shells with weak interlayer interaction, similar to the stacking of graphene sheets in graphite. However for SWNT bundle, theoretical calculations<sup>23,24</sup> have shown that the degree of the  $\sigma$ - $\pi$  hybridization depends on the tube curvature and tube-tube interaction can vastly affect its overall electronic properties. For example, the tube-tube interactions induce a pseudogap at the Fermi level of metallic zigzag nanotube bundle  $(n,0)$   $n=\text{multiple of three}$ .<sup>23,24</sup>

The work functions ( $\Phi$ ) of SWNT and MWNT were determined with respect to a gold standard ( $\Phi=5.1\text{eV}$ ). On the basis of Figure 4.13, the secondary electron tail thresholds of SWNT and MWNT were shifted toward higher binding energy by  $0.2\text{eV}$  and  $0.3\text{eV}$  respectively. In other words, the work function of SWNT bundle is higher than MWNT by  $0.1\text{eV}$ . Suzuki et al.<sup>25</sup> reported that  $\Phi_{\text{SWNT}}$  is larger than  $\Phi_{\text{graphite}}$  by  $0.1-0.2\text{eV}$ , while Chen<sup>22</sup> and Ago et al.<sup>26</sup> reported that the  $\Phi_{\text{MWNT}}$  is smaller than  $\Phi_{\text{graphite}}$  by  $\sim 0.1\text{eV}$ . Suzuki et al.<sup>27</sup> also measured the work function of individually suspended SWNT and reported that the observed work functions are weakly dependent on the chirality.

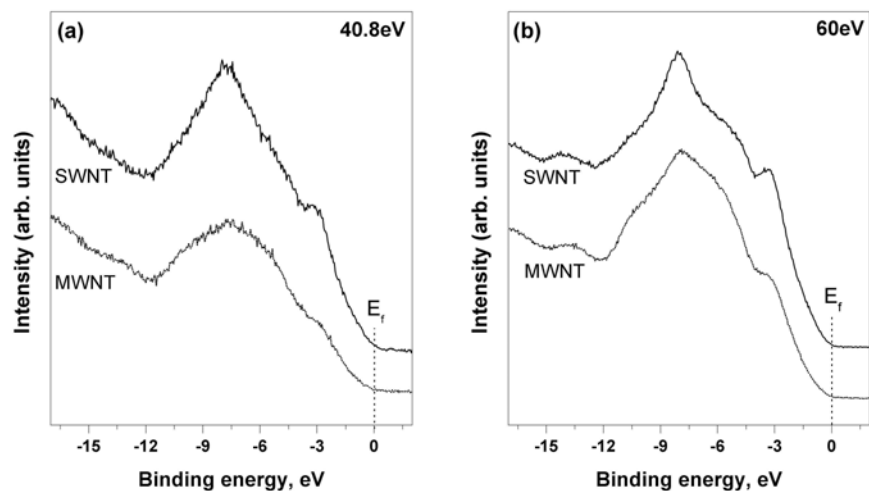


**Figure 4.12.** Valence band (VB) spectra of purified SWNT and MWNT using (a) 40.8eV and (b) 60eV photon energies.

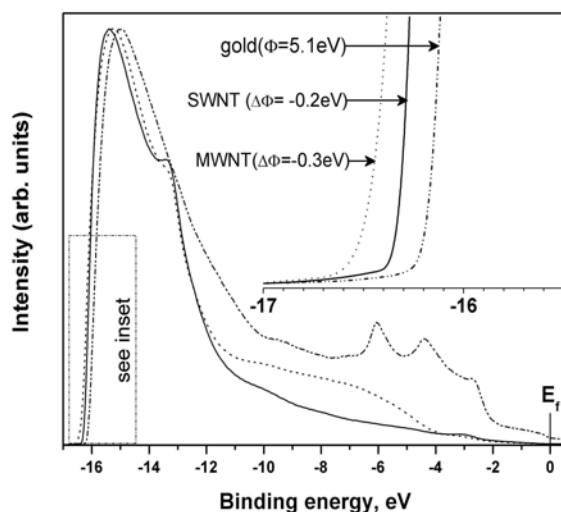


**Figure 4.13.** Secondary electron tail threshold of SWNT (solid line), MWNT (dashed line) and gold (dot-dash line) using He I source (21.2eV). *Inset:* Expanded view of the secondary electron tail threshold. *Gold film was used as an internal reference.*

#### **4.1.4. Formation mechanism of carbon nanotube**

Although arc discharge, laser ablation and CVD techniques have been successfully employed to synthesize SWNT and MWNT, the synthetic conditions are very different. For example, MWNTs are readily synthesized via direct vaporization of a graphite target

(temperature  $\sim 3000^{\circ}\text{C}$ ) in the arc discharge and laser ablation techniques and catalysts are not necessary in the process. For the CVD process, which requires relatively lower temperatures ( $\sim 700\text{-}1200^{\circ}\text{C}$ ), a catalyst is always needed for the synthesis of carbon nanotubes. On the other hand, the production of SWNT always needs a suitable catalyst regardless of the synthetic methods. Therefore, it is of great interests to ask whether the three different synthetic methods share the same growth mechanism of SWNT.

It is well accepted that a modified vapor-liquid-solid (VLS) growth mechanism is most likely to be operative in a SWNT growth process, regardless of synthetic methods. The VLS mechanism was introduced in the 1960s to explain the growth model of silicon whiskers<sup>28</sup>, and it was adopted to explain SWNT formation. The modified VLS mechanism is supported by TEM observations, which show that SWNT bundle germinates from metallic catalysts (size  $\sim 15\text{nm}$ ), and it tips can be encapsulated with the metal catalysts (size  $< 5\text{nm}$ ). The most active catalysts for the SWNT formation are the transition metals iron, cobalt and nickel, which have high carbon solubility<sup>29</sup>, irrespective of synthetic methods. After the decomposition of the carbon-bearing precursor on the surface of the metal catalyst, the carbon species dissolve into the melt catalysts (nanosized liquid droplet) forming a super-saturated solution at high temperatures. Upon cooling, the solubility limit of carbon decreases and carbon atoms start to precipitate out unidirectionally in the form of tubules. Homma et al.<sup>30</sup> proposed that the bulk metals (Fe, Co and Ni) have a eutectic phase diagram with carbon at  $\sim 1300^{\circ}\text{C}$ . Due to the nanosized of the catalysts, the eutectic point of carbon-metal liquid droplet is reduced to  $\sim 700\text{-}800^{\circ}\text{C}$ . Additionally, electron diffraction investigation of catalytic particles at the tips of carbon nanotubes indicates the formation of carbide species after nanotube growth<sup>31</sup>. Quantum molecular dynamics simulations<sup>32</sup> indicate that the incorporation of pentagon carbon defects at an early stage of SWNT nucleation is energetically favorable because they reduce the number of dangling bonds and facilitate curvature of the structure and bonding to the metallic catalysts.

## References

- [1] M. Wang, X.Q. Wang, Z.H. Li, Z.Y. Liu, P. He, *Mater. Chem. Phys.* 97, 243 (2006).
- [2] M. Kusaba, Y. Tsunawaki, *Thin Solid Films* 506, 255 (2006).
- [3] S. Tang, Z. Zhong, Z. Xiong, L. Sun, L. Liu, J. Lin, Z.X. Shen, K.L. Tan, *Chem. Phys. Lett.* 350, 19 (2001).
- [4] T.T. Chen, Y.M. Liu, Y. Sung, H.T. Wang, M.D. Ger, *Mater. Chem. Phys.* 97, 511 (2006).
- [5] S. Honda, Y.G. Baek, K.Y. Lee, T. Ikuno, T. Kuzuoka, J.T. Ryu, S. Ohkura, M. Katayama, K. Aoki, T. Hirao, K. Oura, *Thin Solid Films* 464, 290 (2004).
- [6] S. Maruyama, E. Einarsson, Y. Murakami, T. Edamura, *Chem. Phys. Lett.* 403, 320 (2005).
- [7] M.J. Bronikowski, P.A. Willis, D.T. Colbert, K.A. Smith, R.E. Smalley, *J. Vac. Sci. Technol. A*, 19, 1800 (2001).
- [8] H. Pan, H. Gao, S.H. Lim, Y.P. Feng, J. Lin, *J. Nanosci. Nanotechnol.* 4, 1014 (2004).
- [9] M. Meyyappan, L. Delzeit, A. Cassell and D. Hash, *Plasma Sources Sci. Technol.* 12, 205 (2003).
- [10] R. Andrews, D. Jacques, A.M. Rao, F. Derbyshire, D. Qian, X. Fan, E.C. Dicky and J. Chen, *Chem. Phys. Lett.* 303, 467 (1999). <http://www.ntp.com.cn/>
- [11] W. Alvarez, B. Kitiyanan, A. Borgna and D. Resasco, *Carbon*, 39, 547 (2001).
- [12] M. Shiraishi, T. Takenobu, A. Yamada, M. Ata and H. Kataura, *Chem. Phys. Lett.* 358, 213, (2002).
- [13] X. B. Wu, P. Chen, J. Lin, K. L. Tan, *Int. J. Hydrogen Energy* 25, 261 (2000).
- [14] A.G. Rinzler, J. Liu, H. Dai, P. Nikolaev, C.B. Huffman, F.J. Rodriguez-Macias, P.J. Boul, A.H. Lu, D. Heymann, D.T. Colbert, R.S. Lee, J.E. Fischer, A.M. Rao, P.C. Eklund, R.E. Smalley, *Appl. Phys. A* 67, 29 (1998).
- [15] E. Mizoguti, F. Nihey, M. Yudasaka, S. Iijima, T. Ichihashi and K. Nakamura, *Chem. Phys. Lett.* 321, 297 (2000).
- [16] H. Kataura, Y. Kumazawa, Y. Maniwa, I. Umezu, S. Suzuki, Y. Ohtsuka, and Y. Achiba, *Synth. Met.* 103, 2555 (1999).
- [17] M.S. Strano, *J. Am. Chem. Soc.* 125, 16148 (2003).
- [18] M. S. Dresselhaus, G. Dresselhaus, R. Saito, and A. Jorio, *Phys. Rep.* 409, 47 (2005).
- [19] M.S. Dresselhaus, P.C. Eklund, *Adv. Phys.* 49, 705 (2000).
- [20] T. Hayashi, Y.A. Kim, T. Matoba, M. Esaka, K. Nishimura, T. Tsukada, M. Endo, M. S. Dresselhaus, *Nano Lett.* 3, 887 (2003).
- [21] G.S. Duesberg, I. Loa, M. Burghard, K. Syassen and S. Roth, *Phys. Rev. Lett.* 85, 5436 (2000).



- [22] P. Chen, X. Wu, X. Sun, J. Lin, W. Ji, K.L. Tan, *Phys. Rev. Lett.* 82, 2548 (1999).
- [23] P. Delaney, H.J. Choi, J. Ihm, S.G. Louie, M.L. Cohen, *Nature* 391, 466 (1998).
- [24] J. Chen, X. Wan, J. Dong, *Phys. Stat. Sol (b)* 239, 152 (2003).
- [25] S. Suzuki, C. Bower, Y. Matanabe, O. Zhou, *Appl. Phys. Lett.* 76, 4007 (2000).
- [26] H. Ago, T. Kugler, F. Cacialli, W.R. Salaneck, M.P. Shaffer, A.H. Windle, R.H. Friend, *J. Phys. Chem. B* 103, 8116 (1999).
- [27] S. Suzuki, Y. Watanabe, Y. Homma, S. Fukuba, S. Heun, A. Locatelli, *Appl. Phys. Lett.* 85, 127 (2004).
- [28] R.S. Wagner, W.C. Ellis, *Appl. Phys. Lett.* 4, 89 (1964).
- [29] R.C. Ruhl, M. Cohen, *Scr. Metall.* 1, 73 (1967).
- [30] Y. Homma, Y. Kobayashi, T. Ogino, D. Takagi, R. Ito, Y.J. Jung, P.M. Ajayan, *J. Phys. Chem. B.* 107, 12161 (2003).
- [31] O.M. Gur'yanova, E.F. Kukovitsky, S.G. L'vov, N.A. Sainov, V.A. Shustov, *Phys. Solid State* 44, 473 (2002).

## **Chapter 5. Growth of vertically aligned carbon nanotube**

### *Summary*

A parametric study of the growth of vertically aligned carbon nanotubes (VACNTs) was carried out with radio-frequency plasma-enhanced chemical vapor deposition. The usage of relatively low H<sub>2</sub> plasma power ( $\leq 50\text{W}$ ) synthesizes less defective VACNTs. The lowest temperature for the growth of VACNT is at 450°C. Simultaneous H<sub>2</sub>-plasma etching and sample heating is found to be beneficial to significantly reduce the average diameter of the nanotubes. The presence of metallic underlayers greatly affects the growth of VACNTs. Current-voltage (I-V) measurements were also carried out for these VACNTs grown on metallic underlayers.

## **Chapter 5.1. Plasma-enhanced chemical vapor deposition**

### *Introduction*

Alignment of the carbon nanotubes is particularly important to enable both fundamental studies and applications, such as cold-cathode flat panel displays, vacuum microelectronics and interconnects. The growth of vertically aligned carbon nanotubes (VACNTs) on a flat substrate was demonstrated using the catalytic plasma-enhanced chemical vapor deposition (PE-CVD). The utilization of PE-CVD has the advantages to control the location, diameter, length, shape, chemical composition, and orientation of VACNT during synthesis.

Although both thermal CVD and PE-CVD use gaseous feedstock, heat is used to activate the gas in thermal CVD while PE-CVD uses electron impact to activate the gas. The main purpose of using PE-CVD is to reduce the energy activation for the deposition process. Standard semiconductor integrated circuit technology requires the substrate to withstand temperatures up to 450°C for a limited time without major degradation of electronic performance. Likewise, the fabrication of field emission display with soda glass substrates requires a fabrication temperature below 500°C. Therefore the reduction of the growth temperature of VACNTs using PE-CVD techniques is highly desirable and currently is an active research topic<sup>1-3</sup>.

Figure 5.1 shows a radio-frequency PE-CVD system used in this thesis for the synthesis of VACNTs. It consists of a vacuum chamber, vacuum pumps, and a pressure control system, gas manifolds for gas mixing, mass flow controllers, a shower head for uniform gas distribution over the 8 inch sample stage and a radio-frequency source which is coupled to the plasma via a parallel-plate capacitor. Other sources of plasma such as direct-current (dc PE-CVD), hot-filament dc (HF- dc PE-CVD), inductively coupled plasma (ICP PE-CVD), microwave PE-CVD, electron cyclotron resonance (ECR PE-CVD), hollow cathode gas discharge (HCGD), and corona discharge plasma. A detailed description of each plasma system can be found in reference [3].

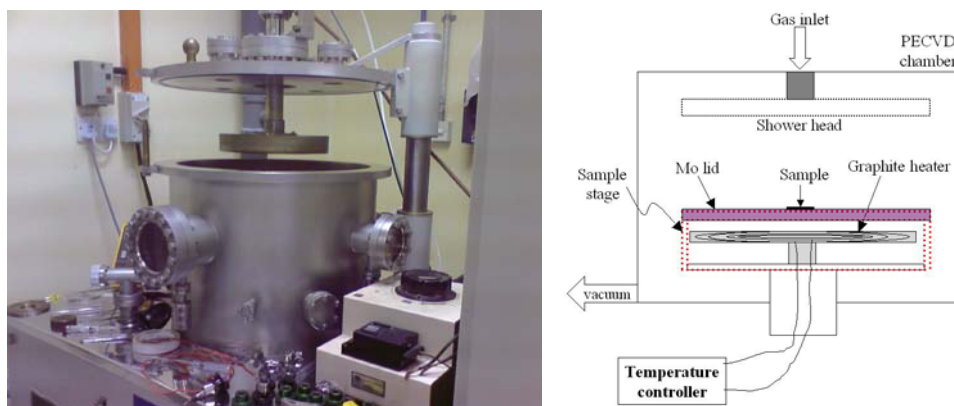


**Figure 5.1.** (Left panel) A radio-frequency plasma-enhanced chemical vapor deposition system. (Right panel) A schematic diagram of the main components of PE-CVD system. *Diagram not drawn to scale.*

### **5.1.1. Growth procedures and patterning of VACNT**

#### *Deposition of catalysts*

Silicon wafers were used as substrates for the growth of VACNT. The native  $\text{SiO}_2$  was not removed from the wafer. The main catalyst used for the growth of carbon nanotubes is 4nm Fe film, unless otherwise stated. The substrate was sonicated in iso-propanol and blew dry with a jet of  $\text{N}_2$  gas. Electron beam evaporation or magnetron sputtering was used to deposit the metal layers on the substrates.

#### *Growth procedure*

Vertically aligned carbon nanotubes were synthesized using a radio frequency (13.56MHz) plasma-enhanced chemical vapor deposition (PECVD) as shown in Fig 5.1. Ethylene ( $\text{C}_2\text{H}_4$ ) and hydrogen ( $\text{H}_2$ ) gases were used as the carbon source and etchant respectively. Other gases such as  $\text{CO}_2$  and  $\text{N}_2$  were also available as diluents. The sample chamber was evacuated to a pressure of  $\sim 10^{-5}$  Pa using a turbo pump in conjunction with a rough vacuum pump to remove the atmospheric impurities. A 20sccm of  $\text{H}_2$  gas was introduced into the chamber and the pressure

was manually adjusted to stabilize at  $133 \pm 5$  Pa (i.e.  $\sim 1$  Torr). The temperature of the graphite heater was ramped from the initial temperature to the final temperature at a rate of  $100^\circ\text{C}/\text{min}$ . Once the final temperature was reached, the radio frequency power was switched on to activate the hydrogen plasma and the etching of the 4nm Fe film will take place for the desired duration. After that, 40sccm of ethylene ( $\text{C}_2\text{H}_4$ ) was introduced and the CNT growth time commenced.

#### *Patterning of VACNT - Photolithography*

The positive photoresist resist layer (AZ7220) was spin-coated on the substrate at a rotational speed of 4000rpm for 30 seconds. The photoresist thickness was  $\sim 3.6\mu\text{m}$ . The excess photoresist solvent was removed by heating the photoresist-coated substrate at  $110^\circ\text{C}$  for 4 minutes on a hot plate. The mask aligner (Karl Suss MA6) is a double-sided contact and proximity mask aligner system, which is capable of patterning resolution down to  $1\mu\text{m}$ . A broadband UV source with emission wavelengths between 350nm and 450nm was used for the exposure. The Dark-Field plastic mask was used and patterned with circular spots of  $20\mu\text{m}$  diameter and regularly spaced  $100\mu\text{m}$  apart. The mask was pre-designed using the Leit version 8 software.

After the mask alignment and UV exposure steps, the substrate was washed in a developer for 40s to dissolve the softer photoresist regions. The developer consists of AZ400K and deionised water in a volume ratio of 2:5 respectively. The developed substrate was heated at  $110^\circ\text{C}$  for 3 min on a hot plate to remove any residual water on the photoresist and to improve the photoresist adhesion.

#### **5.1.2. “Standard” conditions for VACNT growth**

The following conditions were defined as the “standard” conditions for the growth of VACNT using a 4nm Fe catalyst:

- i. Pressure =  $133 \pm 5$  Pa
- ii. Temperature of sample stage (graphite heater) =  $600^{\circ}\text{C}$  ( $750^{\circ}\text{C}$ )<sup>†</sup>
- iii. Flow rate of  $\text{H}_2:\text{C}_2\text{H}_4 = 20:40$ sccm
- iv.  $\text{H}_2$  plasma etching time = 10min
- v. RF power = 100W
- vi. Nanotube growth duration = 20min

<sup>†</sup>see section 5.1.3

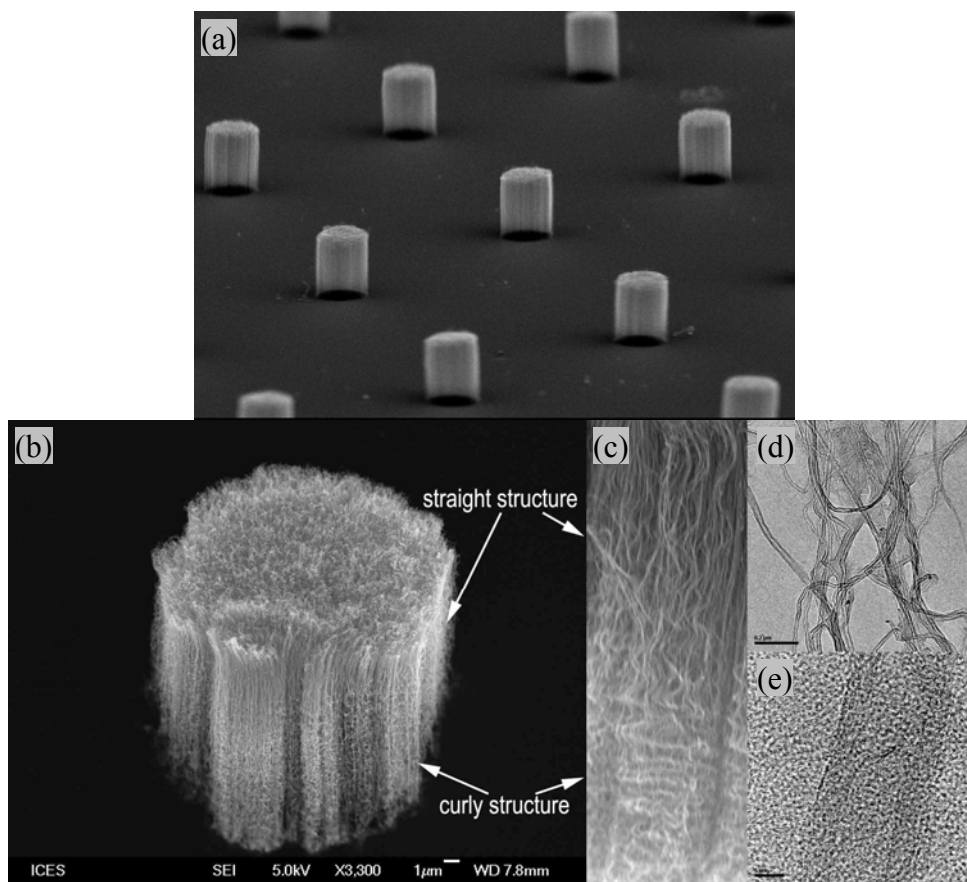


**Figure 5.2.** (a-c) SEM and (d,e) TEM images of VACNTs synthesized at “standard” conditions.

These “standard” conditions were found by trials and errors to give the best growth of VACNTs. The electron micrographs of typical VACNT samples are displayed in Figure 5.2. The

average diameter and length of a VACNT are 15 nm and 23  $\mu\text{m}$  respectively. The upper section of the VACNTs is straight, whereas the lower section is curly (see Fig 5.2b-c). These straight-and-curly segmented VACNTs were also observed in microwave PECVD synthesis of VACNT<sup>4,5</sup>. The curly structure has been attributed to the thermal CVD effects after the plasma is turned off.<sup>4</sup> Another possible reason is due to the decrease in the local temperature when the plasma is turned off, which results in the growth of curly nanotubes<sup>5</sup>. The vertical alignment of carbon nanotubes is due to the dense ‘forest’ arrangement whereby each tube supports one and other.

To understand how the temperature, flow rate, plasma pre-treatment, addition of other gas diluents and how metallic underlayers affect the growth of VACNTs, the experimental parameters were changed individually one at a time while the others remain at the fixed values.

### **5.1.3. Effects of temperature**

#### *Temperature calibration*

As shown schematically in Figure 5.1, the graphite heater is located  $\sim 1\text{cm}$  below the sample stage, which is made up of a stainless steel body and a  $\sim 30\text{mm}$  thick molybdenum lid. Therefore it is important to calibrate the temperatures of the sample stage and Si substrate with respect to the temperature of the graphite heater. The tip of a K-type thermocouple was placed on the sample stage and on top of the Si wafer to measure the temperatures of the sample stage and Si wafer respectively. Each temperature point was allowed to equilibrate for  $\sim 20\text{-}30$  minutes. The average temperatures were measured at 1 Torr of pressure and 20 sccm of  $\text{H}_2$  flow, which was similar to experimental conditions. The results are presented in Figure 5.3.

The measured average temperatures of the sample stage and Si wafer were significantly lower than the temperature of the graphite heater. The temperature difference between the sample stage and Si wafer was  $\sim 30^\circ\text{C}$  when  $T_{\text{graphite}} > 700^\circ\text{C}$  but became smaller  $\sim 10^\circ\text{C}$  when  $T_{\text{graphite}} < 600^\circ\text{C}$ . Therefore the values of temperature reported in this chapter are the temperatures of the sample stage, which is  $10\text{-}30^\circ\text{C}$  higher than the corresponding sample temperature.

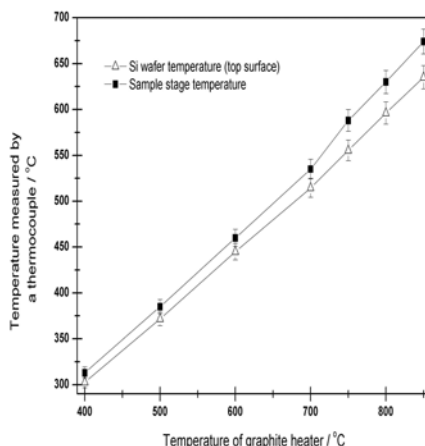


**Figure 5.3.** The temperature of sample stage (■■■) and silicon wafer (△△△) with respect to the temperature of the graphite heater.

*Low temperature growth of VACNTs ( $600^{\circ}\text{C} \rightarrow 450^{\circ}\text{C} \rightarrow 400^{\circ}\text{C} \rightarrow 380^{\circ}\text{C}$ )*

One of the challenges of VACNT growth is to lower the sample temperatures to  $< 450^{\circ}\text{C}$ . The feasibility of growing carbon nanotubes at temperatures lower than  $600^{\circ}\text{C}$  was explored. Firstly all Si substrates deposited with 4 nm Fe films were treated at 1 Torr of 100W  $\text{H}_2$  plasma at  $600^{\circ}\text{C}$  for 10 min. Secondly the  $\text{H}_2$  plasma was switched off and the sample stage was cooled down to the desired temperatures. Thirdly, once the lower temperature reached equilibrium, the VACNT was synthesized in a similar fashion as the “standard” conditions. In this manner, the etched Fe catalyst was assumed to be uniform and the growth of the carbon nanotubes was solely dependent on the external temperature and not the size of the Fe catalysts.

Figure 5.4. shows the SEM images of VACNTs synthesized at  $600^{\circ}\text{C}$ ,  $450^{\circ}\text{C}$ ,  $400^{\circ}\text{C}$  and  $380^{\circ}\text{C}$ . Dense VACNTs can be synthesized at  $450^{\circ}\text{C}$  respectively, but the average length of the VACNTs is about  $3\mu\text{m}$  as shown in Fig. 5.4c-d. When the temperature is further decreased to  $400^{\circ}\text{C}$ , very short and randomly oriented carbon nanotubes were observed (see Fig. 5.4e-f). However at  $380^{\circ}\text{C}$ , CNT did not grow on the substrate (Fig 5.4g). Hence the lowest temperature for CNTs growth (random orientation only) is about  $400^{\circ}\text{C}$ , while the lowest temperature for the



VACNT growth is at 450°C. Many attempts have been made to grow VACNT at 400°C but to no avail. The synthesis of VACNT at 450°C was studied further and the results were presented in the next section 5.1.4.

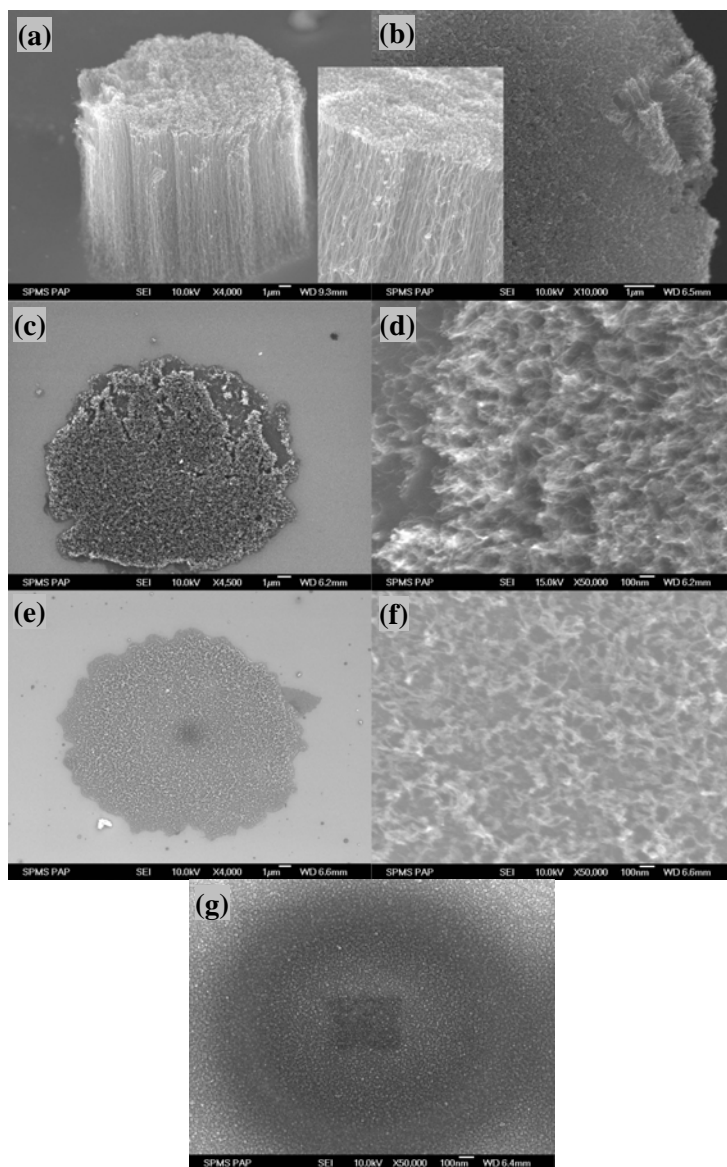


**Figure 5.4.** SEM images of CNTs synthesized at (a, b) 600°C, (c, d) 450°C, (e, f) 400°C and (g) 380°C using a 4 nm-thick Fe catalyst. All the Fe catalysts are pre-treated at 600°C, 1 Torr and 100W H<sub>2</sub> plasma power for 10 min.

#### **5.1.4. Optimized growth of VACNTs at 450°C**

##### *H<sub>2</sub> plasma power and etching duration*

To improve the growth of VACNTs at 450°C, I have studied the pre-treatment conditions of the 4nm Fe catalysts. However this time the Fe catalyst was exposed to 1 Torr of H<sub>2</sub> plasma at 450°C instead of 600°C, while the etching duration and plasma power were varied. The VACNT is grown at 450°C at the same plasma power used for the etching (likewise a 40 sccm C<sub>2</sub>H<sub>4</sub>, 1 Torr, and 20 min growth time are used). The results are displayed as Figure 5.5.

On the basis of Figure 5.5a, the H<sub>2</sub> plasma power and exposure duration are important parameters for the growth of VACNTs at 450°C. At high plasma power of 200W, the growth of VACNT becomes worse as the etching time is increased from 5 to 10min. Furthermore, no VACNT is observed when the 4nm Fe catalyst is etched for 60min at 200W plasma, and SEM study shows that the Si substrate is bare and there is no trace of Fe nanoparticles. Therefore, it is surmised that 200W H<sub>2</sub>-plasma is too strong to control the etching process and the 4nm Fe catalyst can be removed completely at longer duration. On the other hand, as the H<sub>2</sub>-plasma power is reduced to 25-50W, a long etching time (10-60min) is needed in order to grow better VACNTs (see Figure 5.6 below).

The Raman spectra of the VACNTs synthesized at 50W, 100W and 150W plasma power are shown in Figure 5.5b. The I<sub>D</sub>/I<sub>G</sub> ratios of VACNTs at 50W, 100W and 150W are 0.82, 1.05 and 1.23 respectively. In other words, there are more defects in VACNT which is synthesized using a stronger plasma intensity. This could be attributed to the more intense ion bombardment on the carbon nanotubes when the plasma power becomes stronger. Therefore the use of lower plasma power is favored for the growth of good quality VACNTs.

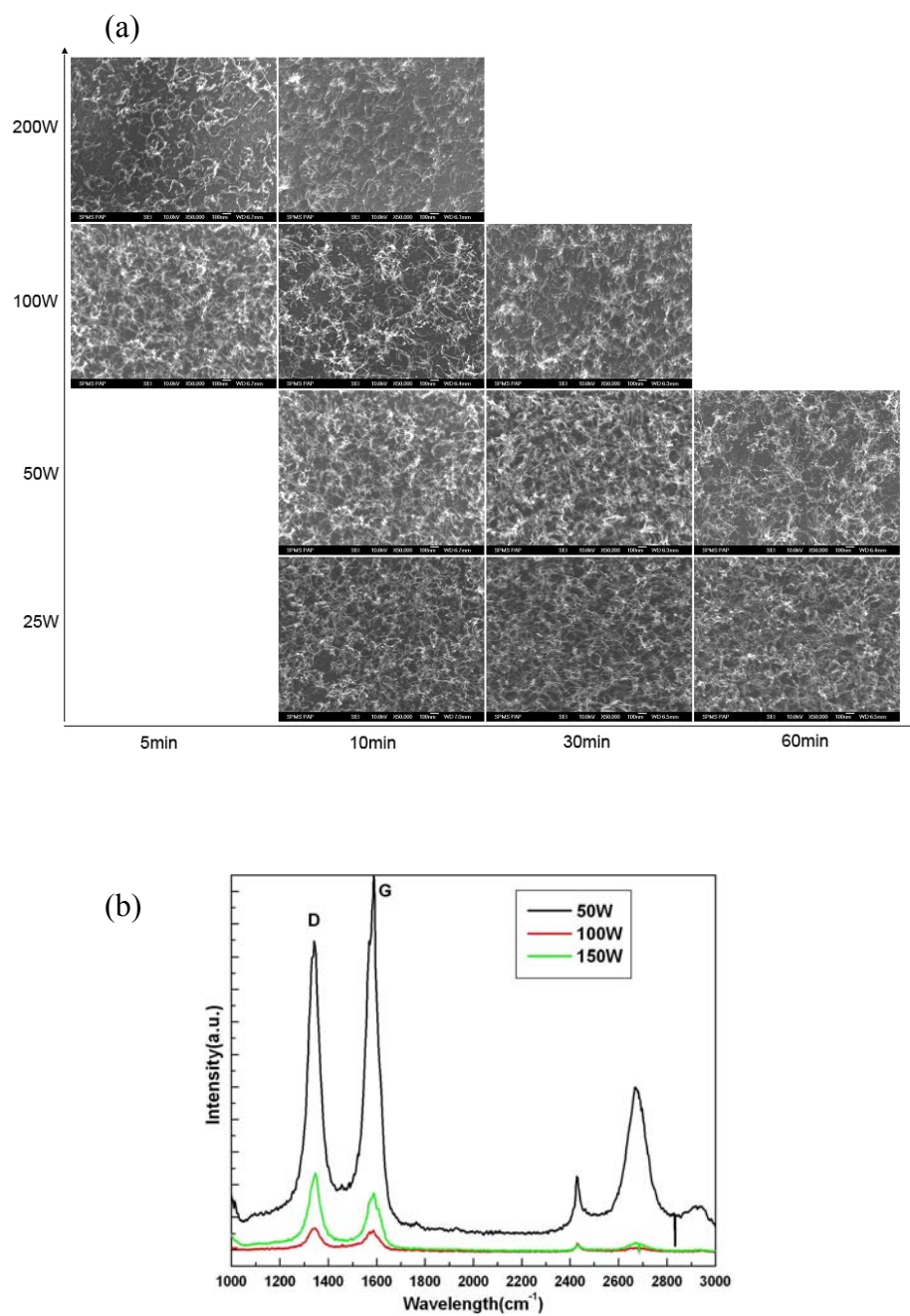


**Figure 5.5.** (a) SEM images (top views) of VACNTs synthesized at  $450^{\circ}\text{C}$  and 1Torr using a 4nm-thick Fe catalyst which is pre-treated at different  $\text{H}_2$  plasma power and duration. (b) Raman spectra of VACNTs synthesized at 50W, 100W and 150W plasma.

Figure 5.6 shows the SEM images of VACNTs synthesized at lower plasma power (50W and 25W) at 450°C. At 50W plasma, a uniform growth of VACNT is achieved when the etching process is set at 10min (Fig 5.6a). When the etching time is extended to 30min, the 50W plasma might have removed a portion of the 4nm Fe catalysts and non-uniform growth of VACNTs is observed (Fig 5.6b). For 25W of plasma, the observations are just the opposite. A longer etching time of 60min is needed to achieve uniform growth of VACNTs (compare Fig 5.6c and Fig 5.6d). Therefore, a low H<sub>2</sub> plasma intensity (with proper etching timing) favors the growth of uniform and good quality VACNTs at 450°C.

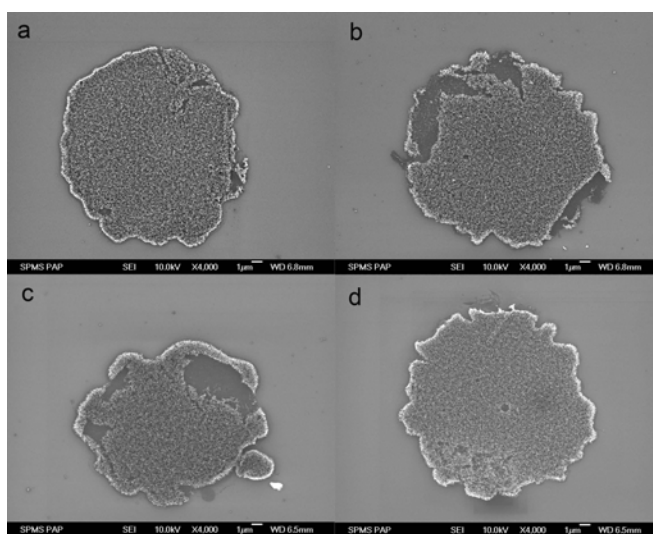


**Figure 5.6.** SEM images (top views) of VACNTs synthesized at 450°C with optimized pretreatment of the 4nm Fe catalysts: (a) 50W, 10min; (b) 50W, 30min; (c) 25W, 30min; and (d) 25W, 60min.

### 5.1.5. Effects of H<sub>2</sub>: C<sub>2</sub>H<sub>4</sub> flow ratio and pressure

#### *Effects of the flow rate of H<sub>2</sub>: C<sub>2</sub>H<sub>4</sub>*

The flow rate of H<sub>2</sub> and C<sub>2</sub>H<sub>4</sub> was increased to twice the flow rate of the “standard” conditions. However, at high H<sub>2</sub>/C<sub>2</sub>H<sub>4</sub> flow ratio of 40 sccm/80 sccm, the flow rate is too large to

synthesize proper VACNTs arrays. As shown in Fig 5.7, the increased flow rate uprooted and blew away some of the VACNTs. This indirectly implied that the adhesion of VACNTs to the substrate is weak and that they can be easily removed mechanically.

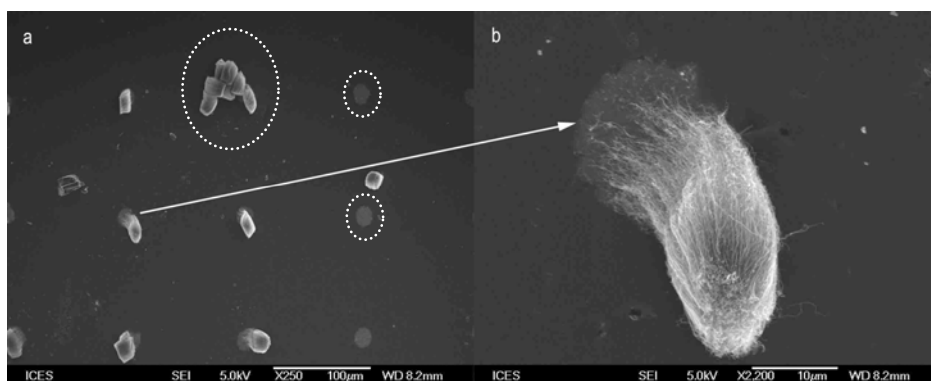


**Figure 5.7.** SEM images of VACNTs synthesized at higher flow rate of  $H_2:C_2H_4=40\text{sccm}:80\text{sccm}$ .

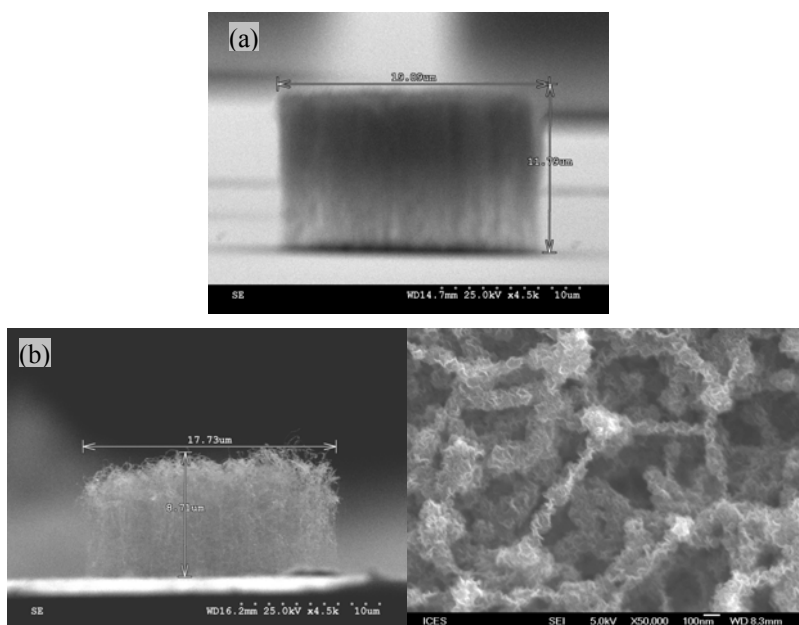


**Figure 5.8.** SEM images of VACNTs synthesized at (a) 0.3 Torr and (b) 5 Torr of pressures.

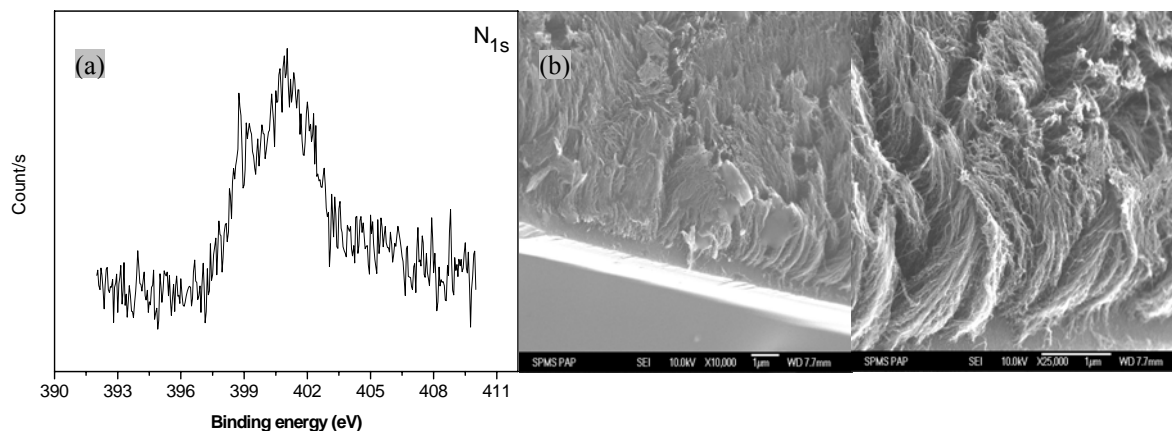
*Effects of pressure*

Figure 5.8 shows the SEM images of VACNTs synthesized at 0.3 and 5 Torr of pressures while the rest of the parameters are kept similar to the “standard” conditions ( $H_2:C_2H_4=20:40$  sccm,  $600^\circ C$ , 100W). The heights of the VACNTs are  $12\mu m$  and  $8.7\mu m$  at 0.3 Torr and 5 Torr of pressures respectively. At 5 Torr of pressure, closer examinations show that the exteriors of the VACNTs are coated with small flakes of graphitic platelets (see Fig 5.8b). At 0.3 Torr of pressure, the supplied carbon radical might be relatively lesser than the amount of carbon radical generated at 1 Torr. While at 5 Torr, there was an excess amount of carbon radical being supplied. The deposition of graphitic platelets at 5 Torr stunted the growth of VACNT and limited its height to  $8.7\mu m$ .

**5.1.6. Effects of other gas diluents**

The effects of  $CO_2$  diluent on the growth of VACNTs were investigated in this section. Several literatures reported that  $CO_2$  diluent lowers the growth temperature of carbon nanotubes and enhances its growth rate in a thermal CVD process, though the mechanism is not clear at present<sup>6-8</sup>. In our studies, we have added 0.1-10 sccm of  $CO_2$  diluent for the growth of VACNTs under various conditions but there’s no noticeable enhancement of the VACNT growth. On the other hand, Figure 5.9b shows the SEM images of the VACNTs synthesized at “standard” conditions but an additional 5sccm of  $N_2$  is introduced during the growth. The average height of the VACNTs is significant reduced to about  $1.8\mu m$  and the nanotubes are slightly bowed. XPS analysis (Fig 5.9a) reveals that nitrogen impurities are doped into the carbon nanotubes. The core level  $N1s$  of nitrogen-doped VACNT has several peaks located at 399eV and 401eV, and a shoulder at 405eV. The peak at  $\sim 399$  eV which is less abundant is attributed to  $N-sp^3-C$  bonding configuration while that at  $\sim 401$  eV to  $N-sp^2-C$ . The XPS analysis gave  $\sim 2at\%$  of nitrogen being

doped into the carbon nanotubes. The study of highly nitrogen doped (12at%) carbon nanotubes was conducted in Chapter 6, page 148.



**Figure 5.9.** (a) XPS  $N_{1s}$  peak and (b) SEM images of VACNTs synthesized at “standard” conditions with an additional 10 sccm of  $N_2$ .

### ***5.1.7. VACNT growth on 1nm Fe catalyst.***

The growth of VACNT was also studied using 1nm Fe catalyst using e-beam evaporator (deposited at Micromachine Centre, NTU). Preliminary results indicate that the growth of VACNTs using 1nm Fe catalysts is almost the same as those obtained using 4nm Fe catalysts. However I have changed the “standard”  $H_2$ -plasma treatment process whereby this time the  $H_2$  plasma etching and sample heating are carried out simultaneously. TEM images of Figure 5.10a and 5.10b shows that simultaneous heating and  $H_2$ -plasma treating significantly reduced the diameters of the VACNTs from  $\sim 15$ nm to less than 5nm. Likewise SEM images of Figure 10.c indicate that the average diameters of the nanotubes are greatly reduced to less than 5nm. Raman spectrum of Figure 5.10d shows that several radial breathing modes (RBMs) are observed at 179, 204, 248, 264 and  $275\text{cm}^{-1}$ , which indicates the presence of single-walled carbon nanotubes. The diameters of the single-walled carbon nanotubes range from 0.9-1.3nm. However, there is a mixture of multi-walled and single-walled carbon nanotubes.

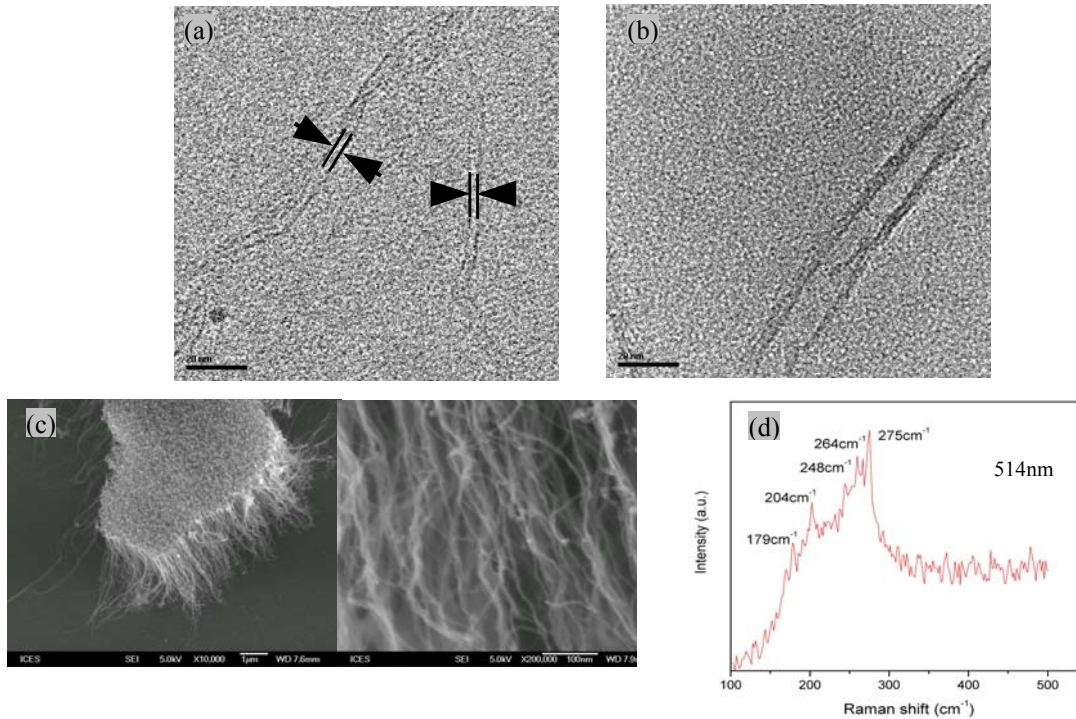


**Figure 5.10.** TEM images of VACNT synthesized by (a) simultaneous heating and H<sub>2</sub>-plasma treating, and (b) heated then followed by H<sub>2</sub>-plasma. (c) SEM images and (d) Raman spectrum of the VACNTs synthesized using simultaneous H<sub>2</sub> plasma etching and heating. Catalyst is 1nm Fe.

### **5.1.8. Effects of metallic underlayers and electrical measurement**

Previously, the growth of VACNT was conducted with Fe catalyst deposited on Si wafer with a native SiO<sub>2</sub>. In general, catalysts are supported on an oxide layer which prevents it from sintering. For examples, the use of Fe/Al<sub>2</sub>O<sub>3</sub> and Co-Mo/SiO<sub>2</sub> are very popular choices for the growth of VACNTs. These examples demonstrate the synergy between the active catalyst and the right oxide supports. However the presence of non-conducting oxide layers hinder the potential application of VACNT in electronic devices such as interconnects and the growth of VACNT on metallic underlayers will be of interests.



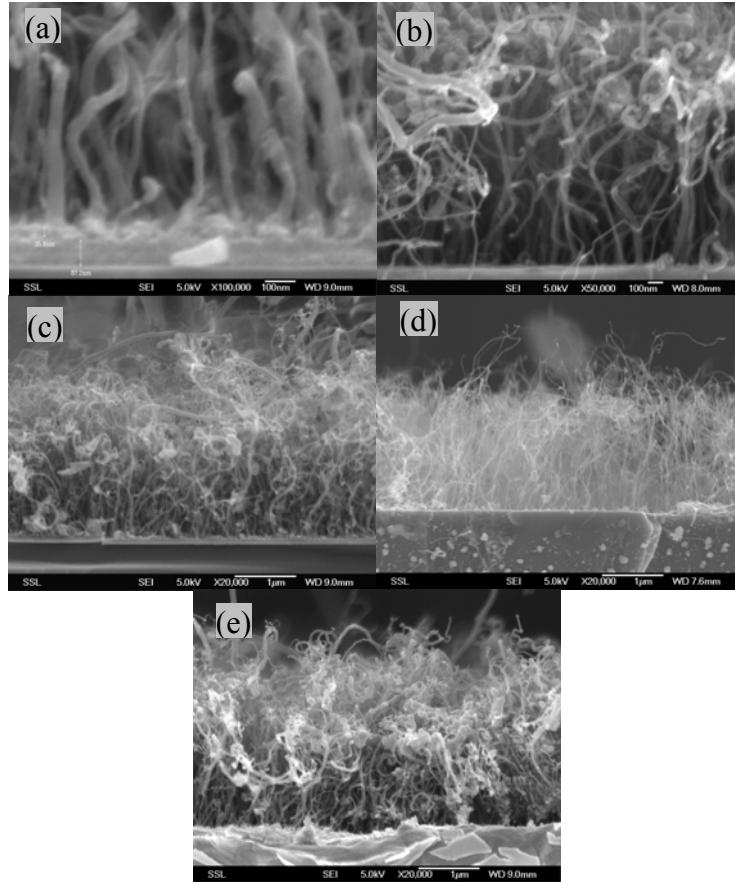


**Figure 5.11.** SEM images of CNT synthesized at “standard” conditions with 20 nm Fe catalyst deposited on (a) 60nmTa/Si, (b) 50nmTi/60nmTa/Si, (c) 60nmTa/500nmCu/Si, (d) 120nmTa/500nmCu/Si, (e) 50nmTi/120nmTa/Cu underlayers.

Transition metals like nickel, iron and cobalt are well known to be very active in their ability to break and re-form carbon-carbon bonds. On the other hand, other transition metals such as copper, tantalum, and titanium are non-catalytic and they might affect carbon diffusion and reaction rates. In order to investigate the effects of non-catalytic metallic underlayers (MU) on the growth of VACNTs, Cu, Ta and Ti were chosen and used as MU in the following combinations of Fe/UM/Si:

- Sample (a): Fe (20nm) / Ta (60nm) / Si wafer
- Sample (b): Fe (20nm) / Ti (50nm) / Ta (60nm) / Si wafer
- Sample (c): Fe (20nm) / Ta (60nm) / Cu (500nm) / Si wafer

- Sample (d): Fe (20nm) / Ta (120nm) / Cu (500nm) / Si wafer
- Sample (e): Fe (20nm) / Ti (50nm) / Ta (120nm) / Cu (500nm) / Si wafer

The deposition of the metal layers was carried out using a magnetron sputtering system. However, unlike e-beam evaporation, it is difficult to deposit very thin metal layers (<5nm) and control the film thickness using a magnetron sputtering.

Figure 5.11 shows the SEM images of samples (a)-(e) synthesized using the “standard” conditions. The diameters of the VACNTs were ~50-90nm which was larger than the VACNTs synthesized with 4nm Fe catalyst. The lengths of the VACNTs were also greatly reduced to about 1 $\mu$ m. The alignment of these VACNTs was also significantly affected by the non-catalytic metallic underlayers.

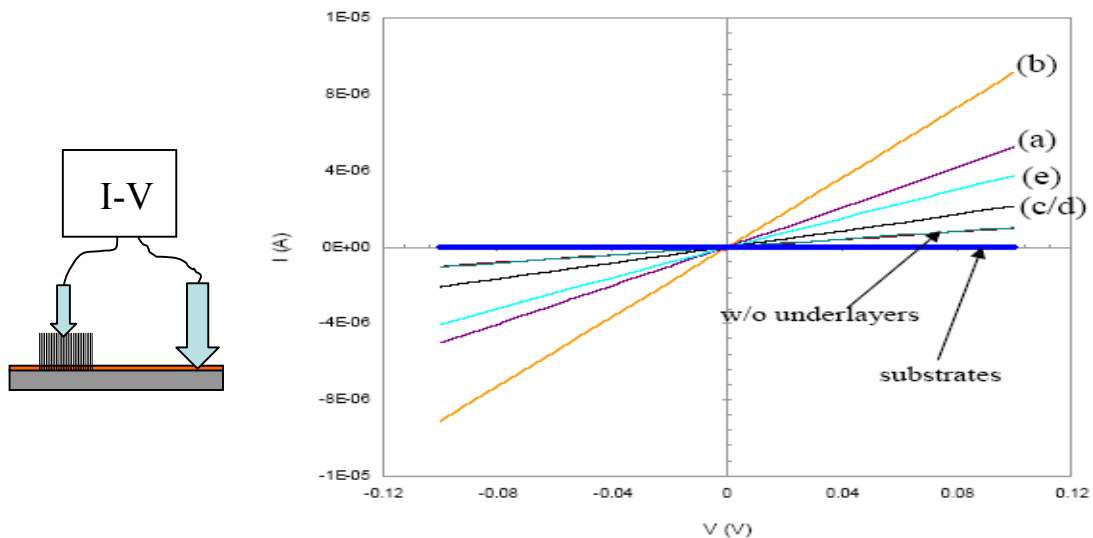


**Figure 5.12.** (Left panel) Schematic setup of the two-terminal I-V measurements. (Right panel) Typical I-V measurements of VACNT samples.

In order to study the electrical properties of the grown VACNTs, two-terminal current-voltage (*I-V*) electrical measurements were performed using a testing circuit schematically shown in Figure. 5.12 (left panel). Copper probes with cross section areas of 0.55 mm<sup>2</sup> were used as electrodes. One Cu electrode was in contact with the metal underlayer, while another electrode

was moved down very slowly until it touches the nanotubes, which was indicated by a surge in the current. The (*I-V*) characteristics of the VACNTs synthesized with metal underlayers and VACNTs with 4nm Fe catalysts were measured in vacuum. The absolute values of the resistance of the VACNTs varied with each measurement but the order of magnitude of the resistance of the samples was quite consistent. Typical *I-V* measurements of the samples were displayed in Figure 5.12 (right panel). The resistance of VACNTs synthesized with 4nm Fe catalysts (without any metallic underlayers) is larger than the VACNTs synthesized with metallic underlayers, even though the quality of the VACNTs (grown with 4nm Fe) was better. The resistances of VACNTs with metallic underlayers in increasing order were sample (b), (a), (e) and (c) or (d). The presence of Ti seems to reduce the resistance of VACNTs. This is in good agreement with *ab initio* calculations<sup>9</sup> which indicate that Ti atom wets the carbon nanotubes surface better than Ta or Cu, and the formation of titanium carbide might also reduce the contact resistance<sup>10</sup>.

### **5.1.9. Conclusions**

By optimizing the growth conditions such as H<sub>2</sub> plasma power and etching duration I have been able to achieve low-temperature growth (450°C) of VACNTs. The synthesis temperature has been reduced from 600°C to 450°C on 4nm Fe catalyst using PE-CVD techniques, with a low 25W H<sub>2</sub>-plasma power and 60 min etching time for pre-treating the catalyst. If the Fe catalyst was H<sub>2</sub>-plasma treated while the sample was heated up, the average diameter of the resulting VACNTs was significantly reduced from typically 15nm to <5 nm. Raman spectroscopy revealed that single-walled carbon nanotubes were present in the VACNTs synthesized using this type of treatment. Metallic underlayers were built below the catalyst in order to achieve CNTs as on chip interconnect. The *I-V* properties of these VACNTs with metallic underlayers were measured, indicating that Ti underlayers was better than Cu and Ta, in terms of lower resistance of the VACNTs/metallic underlayer/Si wafer systems.

## References

- [1] M.S. Bell, K.B.K. Teo, R.G. Lacerda, W.I. Milne, D.B. Hash, M. Meyyappan, *Pure Appl. Chem.* 78, 1117 (2006).
- [2] M. Meyyappan, L. Delzeit, A. Cassell, D. Hash, *Plasma Sources Sci. Technol.* 12, 205 (2003).
- [3] A.V. Melechko, V.I. Merkulov, T.E. McKnight, M.A. Guillom, K.L. Klein, D.H. Lowndes, M.L. Simpson, *J. Appl. Phys.* 97, 041301 (2005).
- [4] C. Bower, O. Zhou, W. Zhu, D.J. Werder, S.H. Jin, *Appl. Phys. Lett.* 77, 2767 (2000).
- [5] H. Sato, H. Takegawa, Y. Saito, *J. Vac. Technol. B* 21, 2564 (2003).
- [6] A.G. Nasibulin, D.P. Brown, P. Queipo, D. Gonzalez, H. Jiang, E.I. Kauppinen, *Chem. Phys. Lett.* 417, 179 (2006).
- [7] A. Magrez, J.W. Seo, V.L. Kuznetsov, L. Forro, *Angew. Chem, Int, Ed.* 46, 44 (2007).
- [8] Q. Wen, W. Qian, F. Wei, Y. Liu, G. Ning, Q. Zhang, *Chem. Mater.* 19, 1226 (2007).
- [9] E. Durgun, S. Dag, V.M.K. Bagci, O. Gulseren, T. Yildirim, S. Ciraci, *Phys. Rev. B.* 67, 201401R (2003).
- [10] M. Nihei, M. Honbe, A. Kawabata, Y. Awano, *Jpn. J. Appl. Phys., Part 1* 43, 1856 (2004).

## **Chapter 6. Nitrogen-doped carbon nanotubes**

### *Summary*

The electronic and optical properties of highly nitrogen-doped carbon nanotubes were studied experimentally. The nitrogen-doped carbon nanotubes were characterized using electron microscopy, Raman spectroscopy, photoelectron spectroscopy, x-ray absorption and pump-probe measurements. Nitrogen-doped CNT has a better ultrafast saturable absorption than pristine carbon nanotube.

## **6.1. Synthesis and characterizations of nitrogen-doped carbon nanotubes**

### *Introduction*

The electronic properties of single-wall carbon nanotube (SWNT) are greatly dependent on their tubular diameter and chirality. Theoretical and experimental studies show that SWNTs can behave from being metallic to semi-conducting ones<sup>1-3</sup>, while multi-walled carbon nanotubes (MWNTs) depend on the features of each coaxial carbon shell<sup>4</sup>. The highly varied electronic structures of carbon nanotubes greatly hinder the specific application of CNT in electronic devices, and a general method to manipulate its electronic properties will be desirable.

The deliberate introduction of defects<sup>5,6</sup> and impurities (dopants) into carbon nanotubes could offer a possible route to change and tune its electronic properties. The creation of new energy levels in the band gap with associated electronic states is an important step to make electronic devices. For instance, the intercalation of alkali metals into SWNT bundles has been shown to increase the conductivity<sup>7</sup>. The substitution of carbon atoms by boron or (and) nitrogen dopants has modified the electrical and structural properties of carbon nanotubes, giving them characteristic bamboo-shaped structures<sup>8-15</sup>. Hence the synthesis, characterization and applications of doped CNT will be of great interest.

The synthesis of carbon nitride (CN) nanotubes is of particular interest because they are expected to be metallic, independent of the tube diameter and chirality. This is motivated by theoretical prediction of the existence of stable CN tubular structures which are metallic<sup>16</sup>. Thus various approaches have been made to incorporate nitrogen atoms into carbon nanotubes, including magnetron sputtering<sup>9</sup>, pyrolysis of nitrogen-rich organic chemicals<sup>10-12</sup>, and arc-discharge in nitrogen atmosphere<sup>13</sup>. But the synthesized CN<sub>x</sub> nanotubes are still far from the canonical carbon nitride tubule stoichiometric CN. The solubility of nitrogen in graphite layers is reported to be <5 at% in most of the bulk CN<sub>x</sub> nanotubes<sup>13</sup>. However high N-content (10-19at%) CN<sub>x</sub> nanotubes were also identified<sup>11,17</sup> and some nanodomains may contain nitrogen

concentration up to 30at%<sup>9</sup>. Even those CN<sub>x</sub> nanotubes at low doping level already exhibit different electronic and structural properties.

The synthesis, characterization and application of nitrogen-doped multi-walled carbon nanotubes will be discussed in this chapter 6. TEM, Raman, XPS, UPS and x-ray absorption techniques (using synchrotron radiation source) were employed for this purpose. The potential application of CN<sub>x</sub> nanotubes as a saturable absorber was studied using ultrafast pump-probe measurements. Previously, H. I. Elim et al<sup>18</sup> have reported the degenerate pump-probe measurements of pristine MWNTs deposited on a quartz substrate and showed that MWNTs were potential ultrafast optical switching materials. However there is no report on the optical-electronic properties of N-doped MWNT. Thus it is of great interests to examine the effects of nitrogen dopants on the carbon nanotube optical-electronic properties using ultrafast pump-probe techniques. A saturable absorption is the property of a material whereby its absorption of light decreases as the light intensity increases. Saturable absorber devices can offer a potentially simple and cost effective solution for passive optical regeneration, error-free periodically amplified optical transmission and laser mode locking.

### **6.1.1. Synthesis of CN<sub>x</sub> nanotube**

The CN<sub>x</sub> nanotubes were synthesized by chemical vapour deposition (CVD) technique using the same Co<sub>0.05</sub>Mo<sub>0.025</sub> catalysts as described in Chapter 4, page 107. In place of a methane source, an organic solvent (acetonitrile (CH<sub>3</sub>CN)) was chosen as the carbon and nitrogen sources for the CN<sub>x</sub> nanotube growth. The CH<sub>3</sub>CN solvent was heated to ~60°C to generate vapor and was carried into the furnace by a helium (99.9995% purity) flow of 60 sccm (see Fig 4.1, page 106). The synthesis temperature was set to 700°C. The as-synthesized CN<sub>x</sub> samples were purified via the 5-step purification process (Figure 4.2, page108).

### 6.1.2. Characterizations of $CN_x$ nanotubes

#### *Electron microscopy*

The  $CN_x$  nanotubes possess a characteristic bamboo-shaped morphology (see Figure. 6.1). They can be considered as polymerised carbon nitride nanobells, whereby each nano-compartment is linked together to form the tube. A detailed TEM-measurement of the diameter distribution was conducted. The outer diameters of  $CN_x$ NT were between 9 and 13nm, with few bamboo-shaped  $CN_x$  nanotubes having diameters smaller than 8nm.

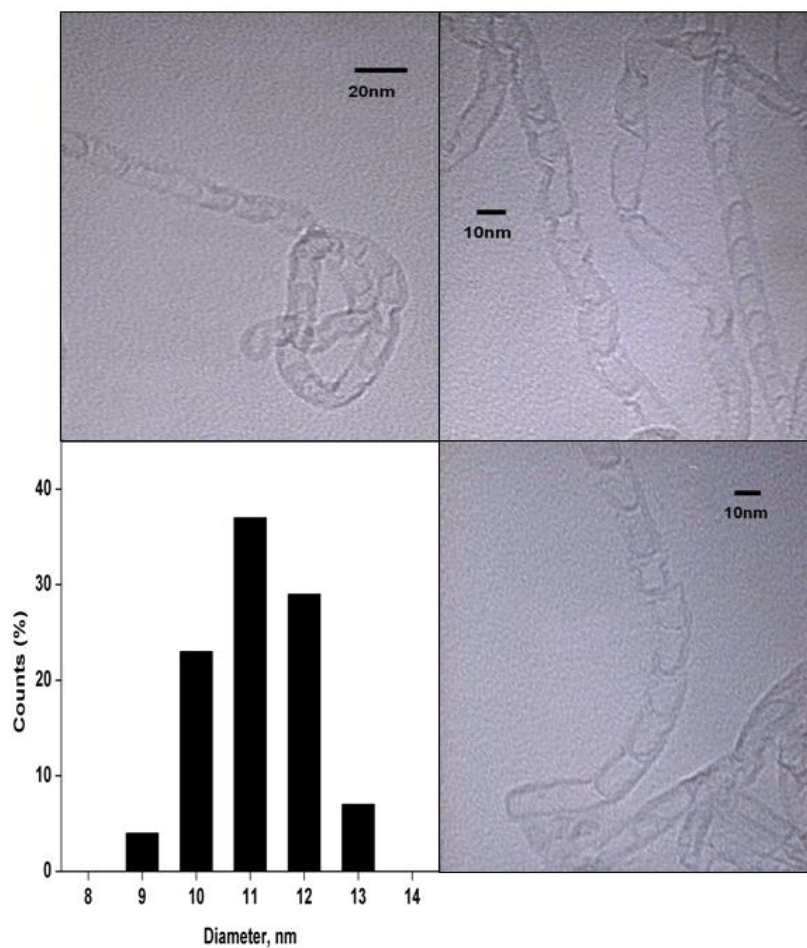


**Figure 6.1.** Typical TEM images of bamboo-shaped nitrogen-doped carbon nanotubes and a diameter-distribution bar chart.



The same  $\text{Co}_{0.05}\text{Mo}_{0.025}$  catalyst was used for the synthesis of SWNT via decomposition of methane. However when they were employed for the synthesis of N-doped nanotube, only  $\text{CN}_x$  multi-walled nanotubes were obtained, but no bundle of SWNT. Zhang et al<sup>19</sup> had also attempted to synthesize N-doped SWNT using laser ablation technique but the SWNT was not nitrogenated. Nitrogen doping can only be found on the amorphous carbon materials. Based on the theoretical calculation of vacancy-mediated N substitution, D. Srivastava et al<sup>20</sup> show that pyridine-like vacancy defects and N substitution are favored on the surface of nanotubes with diameters larger than 8nm. For carbon nanotubes with diameters <8nm, N chemisorption or fused pentagon-type defects occurs. Thus it can be surmised that most of our  $\text{CN}_x$  nanotubes contains pyridine-like vacancy defects due to N-doping.

#### *Raman spectroscopy*

Raman spectra (Reinshaw micro-Raman 2000 system, with an excitation laser of 514nm) of the pristine MWNT and  $\text{CN}_x$  nanotubes were shown in Figure 6.2. They all consisted of the D-mode ( $\sim 1300\text{cm}^{-1}$ ) and the G-mode ( $\sim 1600\text{cm}^{-1}$ ) peaks. The D-mode is defect-induced and associated with optical phonons close to the  $\kappa$  point of the Brillouin zone of carbon nanotubes. The G-mode is a Raman-allowed  $\Gamma$ -point vibration corresponding to the phonon modes of  $E_{2g}$  symmetry and it is known as the tangential mode for carbon nanotubes.

For the estimation of the defect (dopant) concentration in  $\text{CN}_x$  nanotubes and its related Raman process, the D-mode intensity is normalized with respect to the intensity of the G-mode. As shown in Figure 6.2, the peak area ratio ( $I_D/I_G$ ) of  $\text{CN}_x\text{NT}$  and pristine MWNT were 0.96 and 0.36 respectively. The higher  $I_D/I_G$  ratio of  $\text{CN}_x$  nanotubes strongly implies the presence of nitrogen dopants and more defects. The G-band of pristine MWNT, and  $\text{CN}_x\text{NT}$  are located at  $1589\text{cm}^{-1}$  and  $1580\text{cm}^{-1}$ , respectively. The downshift of the G-bands indicates a charge-transfer from the nitrogen dopants to the carbon atoms<sup>21</sup>.

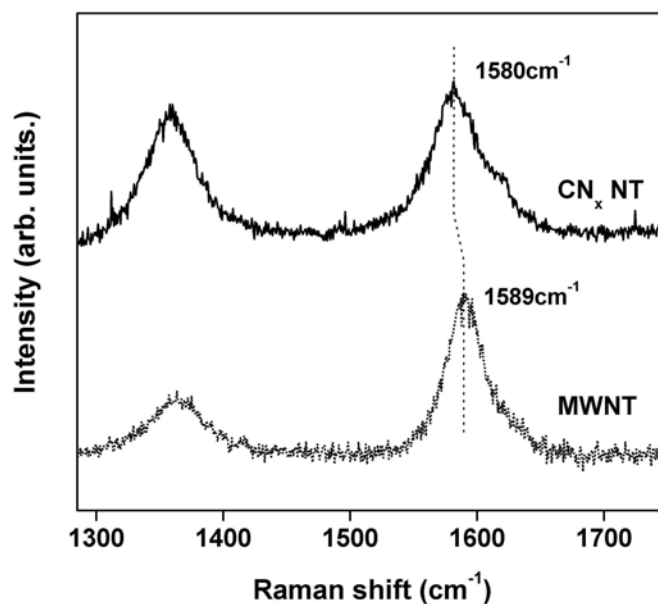


**Figure 6.2.** First-order Raman spectra of  $\text{CN}_x$  nanotubes and pristine MWNT.

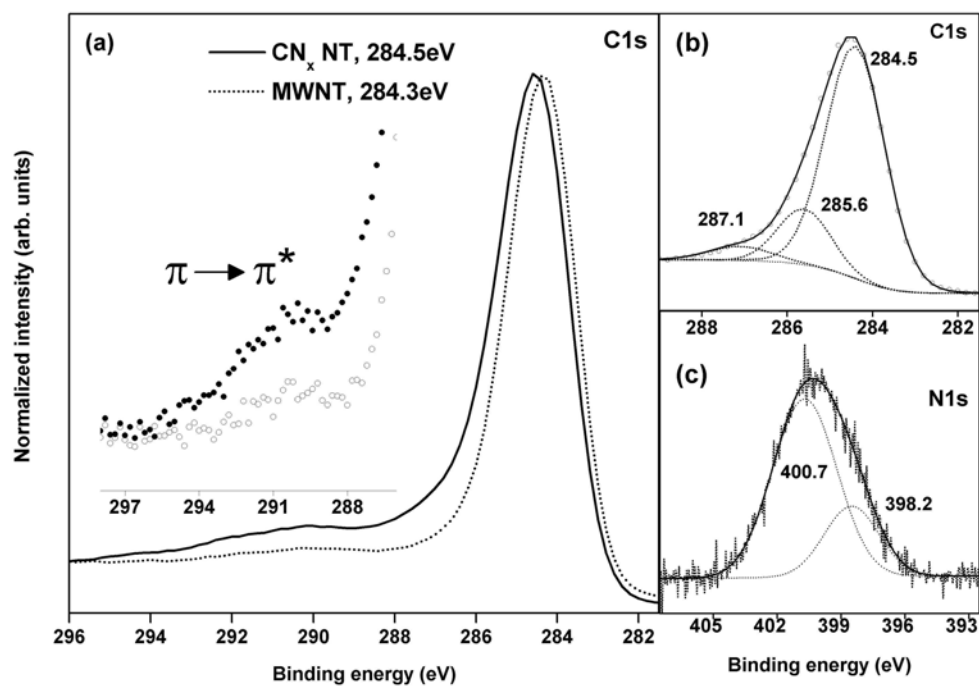


**Figure 6.3.** (a) XPS  $\text{C1s}$  core level spectra for pristine MWNT (dotted line) and  $\text{CN}_x$  nanotube (solid line) with 12at% N-dopant. *Inset:* Energy loss due to  $\pi \rightarrow \pi^*$  transition. (b-c) Deconvoluted  $\text{C1s}$  and  $\text{N1s}$  core-level spectra for  $\text{CN}_x\text{NT}$ ,  $x \approx 12\text{at}\%$ .

*Photoelectron spectroscopy: XPS, UPS, XANES*

XPS, UPS and XANES measurements were performed at the Singapore Synchrotron Light Source (SSLS), using photon energy of 700eV for core levels, 40.8 eV for valence band, and 60 eV for work function studies respectively. The samples were biased by  $-10\text{V}$  during the work function measurements to accelerate the low energy secondary electrons. A comparison of pristine MWNT and  $\text{CN}_x$  nanotube was conducted in order to elucidate the effects of nitrogen dopants had on the electronic structures of nanotubes.

The pristine MWNT sample is free from atmospheric contaminants, showing no signals of XPS  $\text{O}1s$  and  $\text{N}1s$  core energy levels. The  $\text{C}1s$  spectra for the MWNT and  $\text{CN}_x\text{NT}$  are normalized and displayed in Figure 6.3a. A chemical up-shift of 0.2eV and an asymmetric broadening in the high binding energy tail are observable for the  $\text{CN}_x$  nanotube  $\text{C}1s$  core-level spectrum (solid line). The up-shift of the  $\text{C}1s$  line may result from the presence of N atoms which induce a charge transfer from the less electronegative C to more electronegative N. As such, some homopolar C-C bonds are replaced by heteropolar C-N bonds and caused a shift in the  $\text{C}1s$  core levels towards higher binding energy<sup>22</sup>. The asymmetric broadening of the  $\text{C}1s$  peak of the  $\text{CN}_x$  nanotubes suggests the existence of various carbon species in the higher binding energy regions. By peak analysis two additional peaks can be fitted at 285.6 and 287.1 eV, in addition to the major peak at 284.5 eV (graphite-like C-C bond, see Fig 6.3b). It is noted that the  $\text{N}1s$  peak can also be fitted with 2 Gaussian lines located at 398.2 and 400.7eV (see Fig. 6.3c). According to the suggestion of Marton et al<sup>23</sup>, there are two carbon-nitride phases. In Phase 1, which corresponds to the  $\text{C}1s$  level at 287.1 eV and  $\text{N}1s$  at 398.2 eV, N atoms are in a  $\text{sp}^3$  bonding configuration with an isolated electron lone pair (similar to  $\beta\text{-Si}_3\text{N}_4$ ). Phase 2 corresponds to the  $\text{C}1s$  line at 285.6 eV and  $\text{N}1s$  at 400.7 eV, which represents substitutional N atoms in a  $\text{sp}^2$  graphitelike configuration. From the peak intensity analysis a high nitrogen content of  $\sim 12\text{at}\%$  can be estimated. Noted that M. Glerup et al.<sup>11</sup> had attained 16-19.6 at% N-doped carbon

nanotubes using acetonitrile-tetrahydrofuran mixture as the precursor while M. Nath et al.<sup>17</sup> had prepared C<sub>10</sub>N nanotubes from the pyrolysis of pyridine over Fe/SiO<sub>2</sub>.

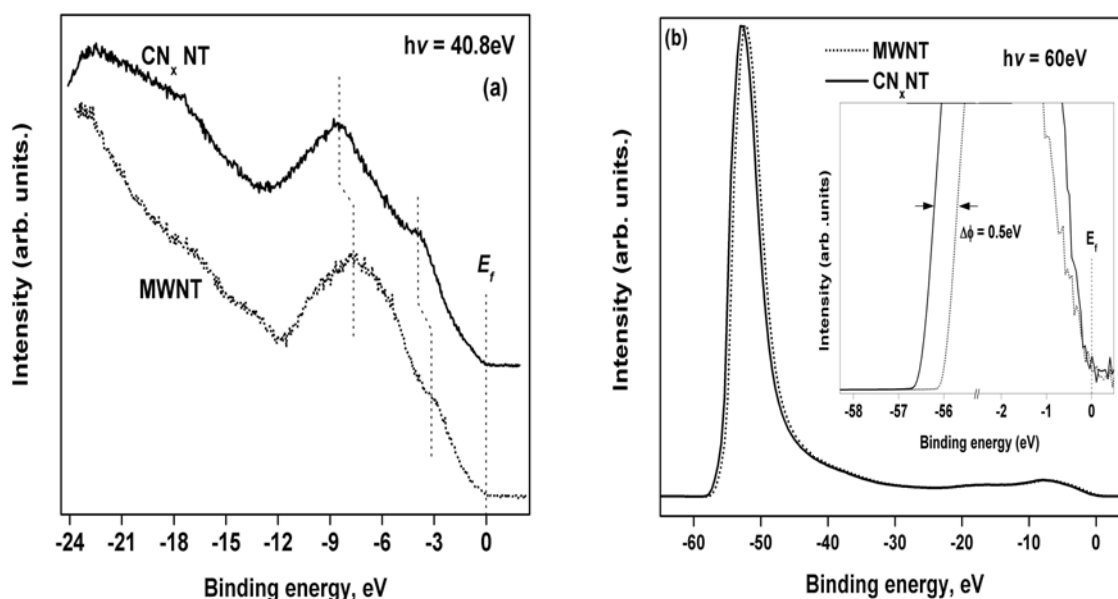


**Figure 6.4.** (a) UPS He II (40.8eV) valence band spectra of pristine MWNT and CN<sub>x</sub> nanotube. (b) Secondary electron tail threshold spectra of pristine MWNT and CN<sub>x</sub> nanotube using photon energy = 60eV. *Inset:* Expanded view of the secondary electron tail threshold and top valence band regions.

Because of the one extra  $2p$  electron of each substitutional N atom (as compared to the carbon atoms) N-doped carbon nanotubes are expected to show stronger  $\pi$  bonds of aromatic rings<sup>22,23</sup>. This can be observed in our UPS valence-band (VB) studies. In Figure 6.4a the VB spectrum of the MWNT sample exhibits two bands located at binding energies 3.1 and 7.6 eV, which correspond to the C $2p$   $\pi$ - and  $\sigma$ -electrons respectively as reported in the literature<sup>24</sup>. Upon doping with  $\sim 12\text{at}\%$  nitrogen, both  $\pi$  and  $\sigma$  bands shift rigidly towards higher binding energies by  $\sim 0.5$  eV. This shift can be attributed to the rise of Fermi level due to N-doping. Each nitrogen

atom has five valence electrons vs. four per carbon. The substitution of electron-rich nitrogen into the carbon network therefore would include a donor level near the bottom of the conduction band, raising the Fermi level<sup>25</sup>. After correction of the Fermi level shift, the intensity enhancement of the  $\pi$ -derived peak at  $\sim 3$  eV is obvious in the  $CN_x$  spectrum. The enhancement of the  $\pi$ -peak is related to the fact that each  $sp^2$  N atom can contribute two electrons to the  $\pi$  system as compared to one  $\pi$  electron per network carbon atom. The  $\sigma$ -like peak at 7 eV decreases its intensity whereas an increase in the intensity around 17 eV is evident too. This may also reflect the substitution of C-C bonds by C-N bonds<sup>26,27</sup>. One more XPS evidence of the N substitution is the observation of an extra energy loss peak in the C1s region, which is located  $\sim 6$ eV at the higher binding energy and corresponds to  $\pi \rightarrow \pi^*$  electron transition (see Fig 6.3a inset). A similar observation was reported for amorphous a- $CN_x:H$  film as its nitrogen content was increased<sup>22</sup>.

The secondary electron tail threshold regions of pristine MWNTs and  $CN_x$  nanotubes were presented in Figure 6.4b. The secondary electron tail threshold of the  $CN_x$  nanotubes is shifted 0.5eV towards higher binding energy in comparison to that of MWNT, which means a reduction of the work function by 0.5eV. This is consistent to the rise of Fermi level (in Fig. 6.4a) due to the N-doping. Additionally as shown in the inset of Figure 6.4b, the nitrogen substitution has enhanced the leading edge of the valence band in the binding energy up to 3eV, which may be associated to the N lone pair<sup>26</sup>. Both the reduction in work function and the enhancement of the electron density at the top valence band bear great importance to improve the field-emission properties of CNTs<sup>10</sup>. Our results are in good agreement with first-principles calculations of nitrogenated SWNTs, which predict a 0.18 eV reduction in the work function of CNT when a nitrogen atom is substituted in the nanotube tip<sup>27,28</sup>. The greater reduction in work function as determined by us could be due to the unique polymerized nanobell structures of  $CN_x$  nanotubes

whereby the linking compartmentalized regions are usually enriched with nitrogen and reduced the work function more as compared to tip substitution.

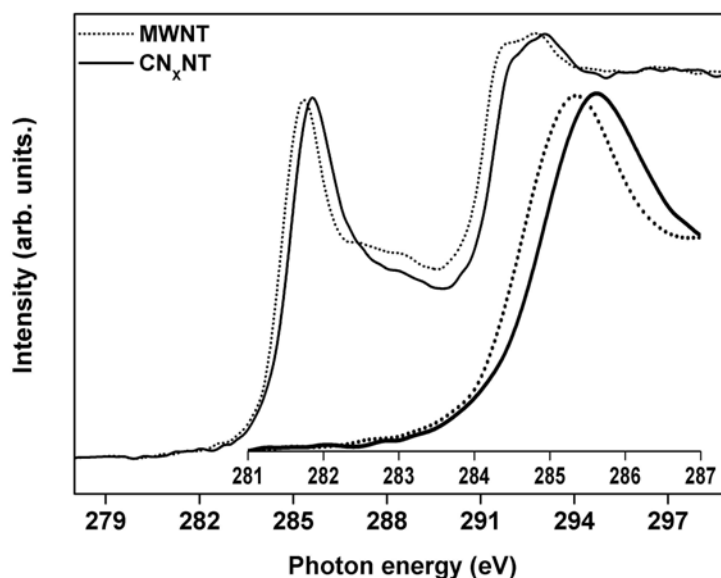


**Figure 6.5.** XANES  $C1s$  K-edge absorption spectra of pristine MWNTs (dotted lines) and  $CN_x$  nanotubes (solid lines). *Inset:* An expanded view of the graphitic  $C1s \rightarrow \pi^*$  resonance.

X-ray absorption near-edge spectroscopy (XANES) is employed to further probe the electronic structure of the  $CN_x$  nanotubes. Figure 6.5 shows the carbon K-edge of the MWNT and  $CN_x$ NT. Both spectra exhibit two peaks at  $\sim 285$ eV and  $\sim 290$ eV, which are related to the graphitic  $C1s-C2p\pi^*$  and  $C1s-C2p\sigma^*$  resonance, respectively. A detailed observation of XANES shows that the  $C1s \rightarrow \pi^*$  peak of the  $CN_x$  nanotubes (solid line in Figure 6.5 inset) is up-shifted by 0.3eV. By considering the 0.5 eV rising of the Fermi level in the  $CN_x$  nanotubes, both  $C1s$  and  $C2p\pi^*$  in the  $CN_x$  nanotubes are actually shifted up by 0.3 eV as compared to those of pristine MWNTs. This can be attributed to the upward band bending. Substituting N atoms

behave as dopants of the  $n$ -type semiconductor on one hand, but, since N is more electronegative than carbon atoms, they can provide acceptor-like state on the other hand. This would result in upward band bending.

### **6.1.3. $CN_x$ nanotubes with improved ultrafast saturable absorption**

#### *Ultrafast pump-probe measurements*

For ultrafast pump-probe measurements, drops of the nanotube dispersion in isopropanol were cast onto a quartz slide to form a film. A comparison between pristine MWNT and  $CN_x$  nanotube was carried out to elucidate the effects of nitrogen-dopants have on the ultrafast responses of the nanotubes. Figure 6.6 shows the typical one-color pump-probe results of the pristine MWNT and  $CN_x$  nanotube samples taken at the same wavelength of 780 nm with increasing irradiance of 8, 37, 70 and 110  $\text{GW}/\text{cm}^2$ . All the signals show a positive change in transmission, which is related to photoinduced bleaching. Furthermore, the transient signals clearly show there are two components. By using a two-exponential component model:

$$Y = A \exp\left(\frac{-X}{\tau_1}\right) + B \exp\left(\frac{-X}{\tau_2}\right) \quad [6.1]$$

where  $A$  and  $B$  are arbitrary constants,  $\tau_1$  and  $\tau_2$  correspond to the fast and slow response time respectively.

The best fits (solid lines in Fig 6.6a-b) produce  $\tau_1 = 130$  fs and  $\tau_2 = 1$  ps. We believe that  $\tau_1$  is the autocorrelation of the laser pulses used<sup>18</sup>. The  $\tau_2$  component is the recovery time of the excited  $\pi$ -electrons in the  $CN_x$  nanotubes film. It should be pointed out that the relaxation dynamics are not dependent on the pump irradiance, including the saturation regime. Its time scale is comparable to the findings for SWCNTs<sup>29a</sup>.

However, as shown in Fig 6.6c, we have observed that the pump irradiance dependence of the maximum value of  $\Delta T/T$  in the  $CN_x$ NT nanotubes is greater than that in MWNT. This

confirms the results that the larger third-order susceptibility of  $\text{CN}_x$  nanotubes is due to the presence of nitrogen dopants. The observed larger third-order susceptibility is attributed to higher-density  $\pi$ -electrons of  $\text{CN}_x$  nanotubes as elucidated by XPS energy loss and valence band spectra (Figs. 6.3a and 6.4a).

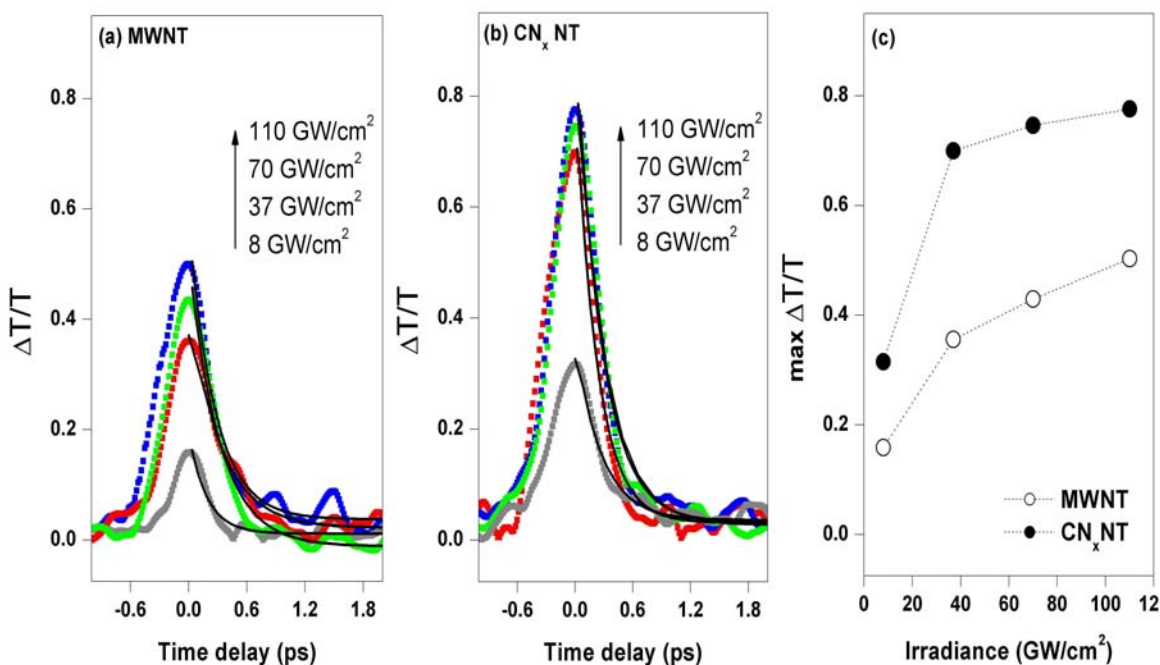


**Figure 6.6.** Degenerate 130-fs-time-resolved pump-probe measurements of (a) pristine MWNT and (b)  $\text{CN}_x$  nanotube performed at 780 nm with increasing irradiance. All the solid lines are two-exponential fitting curves with  $\tau_1=130$  fs and  $\tau_2=1$  ps. (c) A plot of maximum  $\Delta T/T$  against irradiance for MWNT ( $\circ\circ\circ$ ) and  $\text{CN}_x$ NT ( $\bullet\bullet\bullet$ ).

It is observed that the positive  $\Delta T/T$  signals develop as the irradiances increase. However when the irradiances increase from 37 to 110  $\text{GW}/\text{cm}^2$ , the maximum  $\Delta T/T$  signals of  $\text{CN}_x$ NT remain almost the same. Figure 6.6 gives a clear sign of saturation in  $\text{CN}_x$ NT sample. In this saturation regime, most of the carrier states of  $\text{CN}_x$  nanotubes are filled and thus the sample absorption is completely quenched. A similar observation has been made on semiconducting



SWNT in a very low fluence of  $1\text{mJ}/\text{cm}^2$  ( $\sim 7\text{GW}/\text{cm}^2$ ). On the other hands, pristine MWNT did not show clear absorption saturation.

The better ultrafast saturable absorption of  $\text{CN}_x$  nanotubes suggests that these  $\text{CN}_x$  nanotubes can be used as saturable absorber devices. With improved fabrication techniques, saturable absorber devices based on  $\text{CN}_x$  nanotubes can offer a potential solution for passive optical regeneration, error-free transmission distances of periodically amplified optical transmission systems, laser mode locking based on saturable absorber, and high noise suppression capability. For examples, Set et al.<sup>29</sup> and Yamashita et al.<sup>30</sup> have already explored the application of saturable absorbers involving SWNTs.

#### **6.1.4. Conclusion**

In short, nitrogen-doped carbon nanotubes ( $\sim 12\text{at}\%$ ) were synthesized by pyrolysis of acetonitrile on Co-Mo catalysts. Photoemission studies show that the whole valence band is shifted to deeper binding energy due to the nitrogen doping which causes Fermi level shifts to conduction band edge. The work function of nitrogen-doped carbon nanotubes is reduced by  $0.5\text{eV}$ . The enhancement of electron density near the top of valence band, the rise of the valence band  $\pi$  peak and the decay of the valence band  $\sigma$  peak are all related to the N-substitution to the carbon network. Consequently the richer density of  $\pi$ -electrons in  $\text{CN}_x\text{NT}$  endows it with larger third-order susceptibility and better ultrafast saturable absorption.

**References**

- [1] J.W. Mintmire, B.I. Dunlap, C.T. White, *Phys. Rev. Lett.* 68, 631(1992).
- [2] N. Hamada, S. Sawada, A. Oshiyama, *Phys. Rev. Lett.* 68, 1579 (1992).
- [3] T.W. Odom, J. Huang, P. Kim, C.M. Lieber, *Science* 281, 62 (1998).
- [4] M. Ge, K. Sattler, *Science* 260, 515 (1993).
- [5] J. E. Fischer, *Acc. Chem. Res.* 35, 1079 (2002).
- [6] M. Ouyang, J-L. Huang, C.M. Lieber, *Acc. Chem. Res.* 35, 1079 (2002).
- [7] R.S. Lee, H.J. Kim, J.E. Fischer, A. Thess, R.E. Smalley, *Nature* 388, 255 (1997).
- [8] R. Sen, B.C. Satishkumar, A. Govindaraj, K.R. Harikumar, G. Raina, J. Zhang, A.K. Cheetham, C.N.R. Rao, *Chem. Phys. Lett.* 287, 671 (1998).
- [9] K. Suenage, M.P. Johansson, N. Hellgren, E. Broitman, L.R. Wallenberg, C. Colliex, J. Sundgren, L. Hultman, *Chem. Phys. Lett.* 300, 695 (1999).
- [10] C. Tang, D. Golberg, Y. Bando, F. Xu, B. Liu, *Chem. Commun.* 3050 (2003).
- [11] M. Glerup, M. Castignolles, M. Holzinger, G. Hug, A. Loiseau, P. Bernier. *Chem. Commun.* 2542 (2003).
- [12] S. Trasobares, O. Stephan, C. Colliex, W.K. Hsu, H.W. Kroto, *J. Chem. Phys.* 116, 8966 (2002).
- [13] R. Droppa Jr, C.T.M. Ribeiro, A.R. Zanatta, M.C. dos Santos, F. Alvarez, *Phys. Rev. B.* 69, 045405 (2004).
- [14] G.G. Fuentes, E. Borowiak-Palen, M. Knupfer, T. Pichler, J. Fink, *Phys. Rev. B.* 69 (2004) 245403.
- [15] D. Golberg, Y. Bando, L. Bourgeois, K. Kurashima, T. Sato, *Carbon* 38, 2017 (2000).
- [16] Y. Miyamoto, M.L. Cohen, S.G. Louie, *Solid State Commun.* 102, 605 (1997).
- [17] M. Nath, B.C. Satishkumar, A. Govindaraj, C.P. Vinod, C.N.R. Rao, *Chem. Phys. Lett.* 322, 333 (2000).
- [18] H.I. Elim, W. Ji, G.H. Ma, K. Y. Lim, C.H. Sow, C.H.A. Huan, *Appl. Phys. Lett.* 85, 1799 (2004).
- [19] Y. Zhang, H. Gu, S. Iijima, *Appl. Phys. Lett.* 73, 3827 (1998).
- [20] D. Srivastava, M. Menon, C. Daraio, S. Jin, B. Sadanadan, A.M. Rao, *Phys. Rev. B* 69, 153414 (2004).
- [21] P.W. Chiu, G.S. Duesberg, U. Dettlaff-Weglikowska, S. Roth, *Appl. Phys. Lett.* 80, 3811 (2002).
- [22] A. Mansour, D. Ugolini, *Phys. Rev. B* 47, 10201 (1993).

- [23] D. Marton, K. J. Boyd, A.H. Al-Bayati, S.S. Todorov, J.W. Rabalais, *Phys. Rev. Lett.* 73, 118 (1994).
- [24] J. Ago, T. Kugler, F. Cacialli, W.R. Salaneck, M.S.P. Shaffer, A.H. Windle, R.H. Friend, *J. Phys. Chem. B* 103, 8116 (1999).
- [25] R. Czerw, M. Terrones, J.-C. Charlier, X. Blase, B. Foley, R. Kamalakaran, N. Grobert, H. Terrones, D. Tekleab, P. M. Ajayan, W. Blau, M. Ru2hle and D. L. Carroll, *Nano Letts* 9, 457 (2001).
- [26] S. Souto, M. Pickholz, M.C. dos Santos, F. Alvarez, *Phys. Rev. B* 57, 2536 (1998).
- [27] G. Zhang, W. Duan, B. Gu, *Appl. Phys. Lett.* 80, 2589 (2002).
- [28] J.C. Charlier, M. Terrones, M. Baxendale, V. Meunier, T. Zacharia, N.L. Rupesinghe, W. K. Hsu, N. Grobert, H. Terrones, G. A. J. Amaratunga, *Nano Lett.* 2, 1191 (2002).
- [29] S.Y. Set, H. Yaguchi, Y. Tanaka, and M. Jablonski, *J. Lightwave Tech.* 22, 51 (2004).
- [30] S. Yamashita, Y. Inoue, S. Maruyama, Y. Murakami, H. Yaguchi, M. Jablonski and S.Y. Set, *Opt. Lett.* 29, 1581 (2004).

## Chapter 7. Pore structure modification and hydrogen storage

### *Summary*

A brief introduction to the H<sub>2</sub> storage and technique was presented in section (7.1). In section (7.2), the H<sub>2</sub> storage of pore-modified carbon nanotubes was investigated. The pore structures of carbon nanotubes were modified by potassium hydroxide activation and nitrogen doping. In section (7.3-7.4), H<sub>2</sub> uptakes of boron nitride and TiO<sub>2</sub> nanotubes (~2wt%) are measured to be higher than carbon nanotubes ( $\leq 0.5\text{wt}\%$ ) at 300K. The studies of H<sub>2</sub> adsorption of BN and TiO<sub>2</sub> nanotubes give important insights on the factors which enhance H<sub>2</sub> uptakes. The syntheses and characterizations of BN and TiO<sub>2</sub> nanotubes are given in the appendix.

## **7.1. Hydrogen storage of nanostructured materials**

### **7.1.1. Introduction**

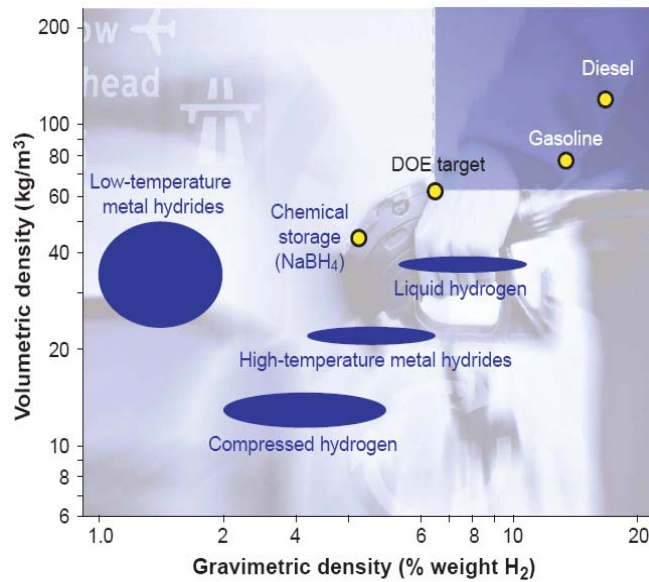
The ever increasing demand for energy and depleting fossil fuel supply have triggered a grand challenge<sup>1-3</sup> to look for technically viable and socially acceptable alternative energy sources. Hydrogen as an alternative energy has stand out among the proposed renewable and sustainable energy sources, because it is relatively safe, easy to produce, and non-polluting when coupled with fuel cell technology.

The development of H<sub>2</sub>-powered vehicle coupled with a fuel cell engine is highly desirable due to its higher efficiency. An internal combustion of H<sub>2</sub> and O<sub>2</sub> in an engine is limited by the Carnot efficiency (~25%), but when H<sub>2</sub> is electrochemically driven to react with O<sub>2</sub> in a fuel cell engine the efficiency can reach 50-60%. For on-board H<sub>2</sub> storage, vehicles require compact, lightweight and affordable containment. A commercially available car built solely for mobility burns about 24kg of petrol in a combustion engine and covers a distance of 400km. In order for H<sub>2</sub>-powered vehicles to cover the same distance, 4kg (8kg) of hydrogen are needed to power the fuel cell engine (H<sub>2</sub>-O<sub>2</sub> combustion engine version). Thus on-board storage of H<sub>2</sub> is an important issue of hydrogen technology.

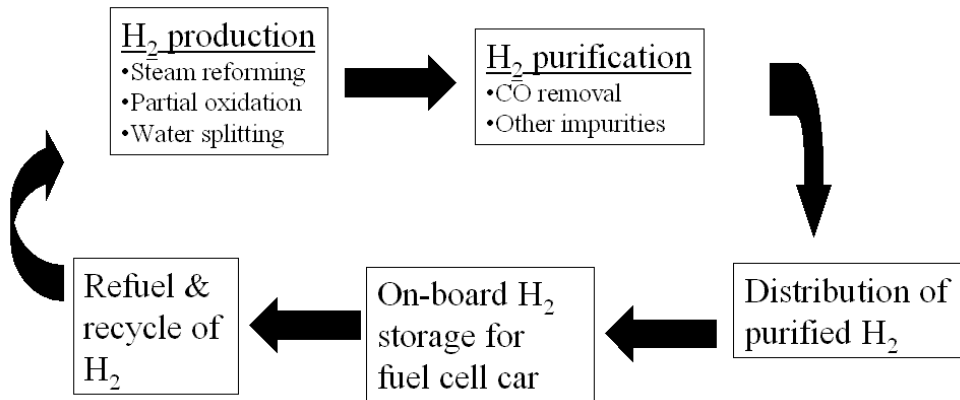
The US department of energy (DOE) hydrogen plan for fuel cell powered vehicle requires a gravimetric density of 6.5wt% or equivalent to a volumetric density of 62 kgH<sub>2</sub>m<sup>-3</sup> (720 ml(STP)/g<sub>adsorbent</sub>) (see Figure 7.1). Conventional storage and transportation of H<sub>2</sub> include (i) compressed gas, (ii) liquefaction, (iii) chemisorption (metal hydrides and complex hydrides) and (iv) physisorption, but none of these techniques have yet achieved the DOE target satisfactorily.

Figure 7.2 shows the overview of H<sub>2</sub> technology as an alternative energy source. The production of H<sub>2</sub> can be achieved using steam reforming<sup>4</sup>, partial oxidation<sup>5</sup> and water splitting techniques<sup>6</sup>. Purification of hydrogen gas requires the removal of carbon monoxide which tends to poison the nanosized Pt catalysts used in the fuel cell electrodes. The setting up of H<sub>2</sub>-refill stations island-wide ensures fuel cell drivers can always refill their vehicles with purified

hydrogen. On the basis of Figure 7.2, H<sub>2</sub> storage is just one of the many aspects of the H<sub>2</sub> technology. The on-board H<sub>2</sub> storage for fuel cell car is a major technological hurdle, which needs immediate attentions, and innovative methods and concepts have been proposed to address this issue.



**Figure 7.1.** Current H<sub>2</sub> storage technologies compared to DOE target and petroleum performance<sup>2</sup>. *The upper right box indicates future H<sub>2</sub> storage technological breakthrough.*



**Figure 7.2.** An overview of H<sub>2</sub> technology as an alternative energy source.

### **7.1.2. Modes of H<sub>2</sub> storage**

#### *Compression*

4kg of H<sub>2</sub> occupies a volume of 45m<sup>3</sup> at 300K and atmospheric pressure, which render it hardly practical for vehicular transportation. The most direct and easy way to store H<sub>2</sub> is to compress hydrogen in a cylinder at high pressure up to 70MPa. A better-designed, safe and lightweight gas cylinder (~110kg) is needed to withstand high pressure up to 70MPa to reach gravimetric density of 6wt% (volumetric density 30kgH<sub>2</sub>m<sup>-3</sup>). However it is estimated theoretically that the compression of hydrogen up to 80MPa consumes lots of energy (~2.21kWh/kg), similar to the case of H<sub>2</sub> liquefaction. Hence this method is not likely to be used commercially to store H<sub>2</sub> for mobile transportation.

#### *H<sub>2</sub> Liquefaction*

Condensation of H<sub>2</sub> into liquid or even solid state is attractive from the viewpoint of increasing mass per container volume ( $\rho_{\text{liq}}=70.8\text{kgm}^{-3}$ ,  $\rho_{\text{solid}}=70.6\text{kgm}^{-3}$ ). However the efficiency of liquefaction and boil-off are two major obstacles which limit the utilization of this method. The technical work necessary to liquefy H<sub>2</sub> gas at room temperature is ~15.2kWh/kg which is much larger than the theoretical estimate of 3.23kWh/kg. The condensation temperature of H<sub>2</sub> at 1bar is 21.2K and boil-off of liquid H<sub>2</sub> is inevitable inside a cryogenic container. Furthermore the critical temperature of hydrogen is 33.2K (above this temperature liquid H<sub>2</sub> cannot exist), and liquid hydrogen can only be stored in an open system to prevent strong overpressure as high as 1000MPa. This mode of H<sub>2</sub> storage is suitable for cases where cost of hydrogen is not an important issue and the hydrogen is consumed in a short time such as air and space applications.

#### *Chemisorption (Metal & complex hydrides)*

Some metals are known to form hydrides such as PdH<sub>0.6</sub> (0.56wt%), MgH<sub>2</sub> (7.6wt%) and TiH<sub>2</sub> (4wt%). Intermetallic alloys (e.g. LaNi<sub>5</sub>H<sub>6</sub> (1.4wt%), ZrV<sub>2</sub>H<sub>5.5</sub> (3wt%), FeTiH<sub>2</sub> (1.8wt%),

etc) are also known to store hydrogen with high volumetric density ( $\sim 100\text{-}150\text{kgH}_2/\text{m}^3$ ) but suffer from low gravimetric density ( $\sim 1.4\text{-}3\text{wt}\%$ ) due to presence of heavy elements.

Complex hydrides usually consist of Group I, II and III elements such as Li, Mg, B and Al to build a wide variety of metal-hydrogen complexes such as alanates and borohydrides. Some of the promising complex hydrides with high gravimetric density include  $\text{LiBH}_4$  (18wt%),  $\text{Al}(\text{BH}_4)_3$  (17wt%),  $\text{TiO}_2$ -doped  $\text{LiAlH}_4$  (7.9wt%) and new comer lithium nitride ( $\text{Li}_3\text{NH}_4$ , 9.3wt%).

Although the chemical storage of hydrogen using metal and complex hydrides may be able to achieve DOE targets, it seriously faces the practical issues of reaction kinetics, thermodynamic equilibrium, and reversibility, which are often not commercially attractive. For instance, the typical heat of adsorption (desorption) in chemisorption is about 2-3eV, which is too high and incompatible with the waste heat of fuel cells (0.2-0.8eV). Various physical and chemical pretreatments such as ball milling to reduce particle size, increasing defect concentration and shortening diffusion paths, surface modifications and doping of catalysts can be applied to improve its  $\text{H}_2$  sorption properties.

### *Physisorption*

The physisorption of hydrogen on porous solid with large specific surface area (SSA) presents a simple, highly reversible and clean storage method. Thus it is highly desirable to find a  $\text{H}_2$ -storing material which is behaving much like a sponge soaking up water. The heat of adsorption (desorption) in physisorption is typically between 5-500meV, largely depends on the nature of the adsorbate-adsorbent in question. The physisorptive hydrogen uptakes of zeolites (e.g. ZSM-5,  $\text{SSA}\approx 430\text{m}^2/\text{g}$ ) and activated carbons (e.g. AX-21,  $\text{SSA}\approx 2600\text{m}^2/\text{g}$ ) have been extensively investigated. However the  $\text{H}_2$  uptakes of zeolites and activated carbons are usually very diluted ( $<1\text{wt}\%$ ) at room temperature, and appreciably amount of hydrogen can be stored at



low temperature (i.e. 77K). The best H<sub>2</sub> sorption of ZSM-5 and AX-21 were reported to be ~0.7wt% (77K, 1bar) and ~4-5wt% (77K, 10bar) respectively (see Fig A7.2 and Fig A7.3a, page 203).

Current research efforts have been directed to various nanostructured materials (e.g. carbon nanotubes<sup>7-12</sup>, BN nanotubes<sup>13-16</sup>, MoS<sub>2</sub> nanotube<sup>17</sup>, TiS<sub>2</sub> nanotubes<sup>18</sup>, ZnO nanowire<sup>19</sup>, SiC nanorod<sup>20</sup>) and highly porous novel materials (e.g. metal-organic-framework<sup>21</sup>, microporous polymers<sup>22</sup>, nanoporous carbon derived from carbide<sup>23</sup>, Prussian blue analogue<sup>24</sup>, nanoporous nickel phosphate<sup>25</sup>), which have been synthesized and tested for physisorptive hydrogen storage (see Table 7.4, page 199). Although the room temperature hydrogen uptakes of these novel materials are limited to ~1-4wt%, but it is noted that these nanostructured materials showed better H<sub>2</sub> sorption than its bulk counterparts and there are still room for further optimizations.

The synthesis and application of advanced nano-materials offer new promises for addressing the H<sub>2</sub> energy challenges. Therefore in this thesis, the synthesized and characterized nano-materials (carbon nanotubes, boron nitride nanotubes and TiO<sub>2</sub>-derived nanotubes) were tested for hydrogen storage. The hydrogen storage of these nano-materials was studied using pressure-composition (*P-C*) isotherms, temperature-programmed desorption (TPD), FTIR and N<sub>2</sub> adsorption isotherms at 77K (pore structure analysis).

### **7.1.3. Techniques for measuring H<sub>2</sub> uptake**

The hydrogen storage capacity can be determined using 3 commonly applied techniques:

#### (i) Volumetric technique

The volumetric technique measures pressure changes that are due to H<sub>2</sub> adsorption / desorption of the sample in a constant volume. In a volumetric apparatus, the H<sub>2</sub> pressures of up to ~10MPa are typically applied to study the sorption behavior. Leakage tests and temperature fluctuations have to be carefully tested and minimized in order to have reliable results.

#### (ii) Thermogravimetric analysis (TGA)

TGA measures the H<sub>2</sub> adsorption (desorption) by monitoring the increase (decrease) of sample weight with a very sensitive microbalance. Since very low sample mass is needed (typically ~100mg) and measurements are conducted with a hydrogen stream, buoyancy effects have to be corrected. However TGA is a non-selective analysis and extremely high purity and clean hydrogen source has to be used.

(iii) Thermal desorption spectroscopy (TDS)

This method relies on determining the amount of hydrogen desorbed from a hydrogenated sample, which is heated under high vacuum, using a mass spectroscopy. The sensitivity of TDS can be further improved using deuterium-loaded sample to reduce noise from other hydrogen-bearing adsorbates. In order to quantify the amount of hydrogen desorbed, the system must be calibrated carefully with respect to a “standard” material of known hydrogen content (e.g. TiH<sub>2</sub> with 4wt%). By measuring the H<sub>2</sub> desorption temperature at various heating rates, it is possible to use the Kissinger equation<sup>26</sup> for determining the activation energy of H<sub>2</sub> desorption.

In this thesis, the hydrogen storage of the samples was measured using only a volumetric gas reaction controller (GRC). Three different types of GRCs were used:

(i) A commercially available gas reaction controller provided by Advanced Materials Corporation, Pittsburgh was employed for H<sub>2</sub> storage measurements. This GRC automatically measures the pressure-composition (*P-C*) isotherm of the sample at constant temperature and operates up to a maximum hydrogen pressures of ~900PSI (~6Mpa). However the working temperature range is limited from -50°C to 500°C, and not suitable for low temperature (e.g. 77K) measurements. This GRC is calibrated with LaNi<sub>5</sub> as standard for H<sub>2</sub> uptake at room temperature. An expected 1.4wt% (LaNi<sub>5</sub>H<sub>6</sub>) of H<sub>2</sub> uptake is achieved which indicate that the PCI unit is reliable (see Appendix Figure A7.1, page 203). No gas leakage was found when the pressures of the PCI manifold and blank sample chamber were manually increased to pressures up to 900PSI. For an arbitrary pressure (800-900PSI), the pressure fluctuation was monitored

over a period of  $\geq 12$  hr. The drop in the pressure was always less than 2PSI (fluctuation of  $\pm 2$ PSI is within the sensitivity of the pressure gauge), which indicated that gas leakage is negligible. Furthermore, when the sample holder was loaded with SiO<sub>2</sub> granules (SiO<sub>2</sub> granules does not adsorb H<sub>2</sub>), the room temperature H<sub>2</sub> uptake was less than 0.1wt%.

(ii) A home-made gas reaction controller is specifically constructed to operate at liquid nitrogen temperature (77K) and room temperature with maximum H<sub>2</sub>-pressure of  $\sim 6$ MPa<sup>12</sup>. The hydrogen storage measurements were manually collected. The reliability and accuracy of this home-made GRC at 77K were calibrated with a well-studied H<sub>2</sub> uptake of an activated carbon (AX-21, Anderson Development Corp.). The maximal H<sub>2</sub> uptake of AX-21 was  $\sim 4.5$ wt% at 77K and 6MPa (see Appendix Figure A7.2, page 203), which is consistent with literature<sup>27,28</sup>.

(iii) Hydrogen adsorption isotherms at 77K (up to 1bar) were measured using self-modified equipment, NOVA3000. This NOVA3000, Quantachrome Corp., originally is used to measure the nitrogen uptake of powder samples at 77K. By changing the gas parameters to hydrogen, this NOVA3000 can be used to measure hydrogen adsorption isotherms at 77K. The gas non-ideality correction factors of  $2.2 \times 10^{-6}$  and  $1 \times 10^{-7} \text{ torr}^{-1}$  at 77K and 300K, respectively, were used in the program software. The cross sectional area parameter was changed to  $1.23 \text{ nm}^2$  per molecule for hydrogen gas. Likewise the accuracy of the H<sub>2</sub> uptake at 77K was checked with activated carbon (AX-21) and zeolite (HZSM-5). The H<sub>2</sub> uptake of AX-21 and HZSM-5 was  $265 \text{ ml(STP)/g}_{\text{adsorbent}}$  and  $79 \text{ ml(STP)/g}_{\text{adsorbent}}$ , respectively, which agreed well with literature data<sup>29</sup> (see Figure A7.3a, page 203).

## **7.2. H<sub>2</sub> storage of carbon nanotubes with modified pores**

### *Introduction*

Carbon adsorbents are attractive H<sub>2</sub>-storing materials due to its lightweight, relatively non-toxicity and low cost. Early efforts focused on activated carbon and fibers<sup>27-30</sup>, which possess large specific surface area and nanopores, as H<sub>2</sub>-storing materials. Strobel et al.<sup>30</sup> surveyed a wide range of activated carbons and fibers, and reported that the H<sub>2</sub> adsorption reached a value of ~1.5wt% at 23°C and 125bar. Experimental and theoretical considerations<sup>60,61</sup> have estimated that the binding energy and desorption temperature of H<sub>2</sub>-carbon system (gas-solid interaction) are ~40-50meV and 80K respectively. Therefore activated carbon only shows appreciable amount of H<sub>2</sub> uptake at low temperatures.

In this section, the hydrogen adsorption properties of chemically modified carbon nanotubes, (i) KOH-activated SWNT and (ii) CN<sub>x</sub> nanotubes, were compared with pristine carbon nanotubes, (iii) SWNT and (iv) MWNT. It is noted that chemically modified carbon nanotubes show higher H<sub>2</sub> uptakes than pristine carbon nanotubes (i.e. KOH-activated SWNT versus pristine SWNT and CN<sub>x</sub> nanotubes versus pristine MWNT). The specific surface area (SSA) and pore size distribution (PSD) of the samples were analyzed using the N<sub>2</sub> adsorption isotherms at 77K. The hydrogen isotherms were conducted at room temperature (300K) and 77K, and H<sub>2</sub> pressures up to ~6MPa. The H<sub>2</sub> adsorption isotherms at 77K and 300K of carbon nanotubes can be fitted with Langmuir models and Henry's Law, respectively. The isosteric heat of adsorption ( $q_{st}$ ) is evaluated using the Clausius-Clapeyron equation.

### **7.2.1. Samples preparation & H<sub>2</sub> storage measurement procedures**

All samples used for the hydrogen adsorption study had undergone the 5-step purification process. In addition, the samples were annealed in air at 500°C for 30min to open the tips of the nanotubes before the H<sub>2</sub> sorption tests.

The SWNT was activated by potassium hydroxide (KOH) to increase its surface area and modify its pore structures. SWNT and KOH (mass ratio 1:4 respectively) were grinded manually inside a glove bag. The SWNT-KOH mixture was immediately loaded into the horizontal quartz and quickly heated from 300K to 1073K at 20min/K under flowing nitrogen (50ml/min). The activation was maintained at 1073K for 2hr, and the resulting activated SWNT was washed extensively with distilled water to remove the excess KOH. This chemically activated SWNT was labeled as *act*-SWNT. Pristine SWNT, pristine MWNT and nitrogen-doped CNT were labeled as *p*-SWNT, *p*-MWNT and CN<sub>x</sub>NT respectively. TEM images of the samples are presented in the Appendix A7.1 as Figure A7.4, page 204.

The mass of CNT samples typically used for H<sub>2</sub> storage measurements is about 200-500mg. The home-made GRC was employed to measure the H<sub>2</sub> sorption of CNT samples. The samples are degassed at 300°C and 1 x 10<sup>-3</sup>Pa for 2hr. To check for system leakage, roughly degassed samples are arbitrarily charged with high pressures of H<sub>2</sub>. If there is no H<sub>2</sub> leakage in the system, the sample is properly degassed again before the actual H<sub>2</sub> storage measurements. The hydrogen charging is allowed to equilibrate for 15-30min until there are no more pressure changes. The H<sub>2</sub> storage measurements are repeated with fresh samples of carbon nanotubes to ensure repeatability and reliability. Table 7.1 summarizes the porous texture and H<sub>2</sub> uptakes of the carbon nanotube samples.

**Table 7.1.** Adsorptive parameters of modified and pristine carbon nanotube samples.

Sample	SSA <sub>BET</sub> , m <sup>2</sup> /g	V <sub>mic</sub> , ml/g	V <sub>meso</sub> , ml/g	H <sub>2</sub> uptake at 6MPa (77K / r.t.), wt%	q <sub>st</sub> , kJ/mol
<i>p</i> -SWNT	423	0.107	0.646	2.2 / 0.38	4.7
<i>act</i> -SWNT	806	0.309	0.456	3.7 / 0.78	5.4
<i>p</i> -MWNT	133	0.055	0.351	1.5 / 0.20	4.6
CN <sub>x</sub> NT	605	0.275	0.403	3.2 / 0.66	5.1

Specific surface area (SSA<sub>BET</sub>) is determined by BET method.

Micropore volume (V<sub>mic</sub>) is determined using Dubinin-Radushkevich (DR) method.

Total pore volume (V<sub>T</sub>) is determined at P/P<sub>0</sub>=0.98

Mesopore volume (V<sub>meso</sub>) is obtained by V<sub>T</sub> - V<sub>mic</sub>.

Isotheric heat of adsorption, q<sub>st</sub>, is evaluated by Clausius-Clapeyron equation

### 7.2.2. Nitrogen adsorption isotherms at 77K

The porous texture of the nanotubes was studied by nitrogen adsorption isotherms at 77K (see Figure 7.3a). The nanotube samples exhibit a cross between Type II and IV isotherms with hysteresis loops in the IUPAC classification. The presence of a hysteresis loop is typical of a mesoporous material whereby desorption requires higher energy than adsorption (i.e. filling and emptying processes of the mesopores by capillary condensation). The hysteresis loops of the carbon nanotube samples close at P/P<sub>0</sub> ~0.4, and the hysteresis loops of *act*-SWNT and CN<sub>x</sub>NT are more pronounced, which is attributed to the development of new pore structures. Importantly, both *act*-SWNT and CN<sub>x</sub>NT have higher N<sub>2</sub> uptakes below P/P<sub>0</sub> =0.1, which suggests the development of micropores. To evaluate the specific surface area (SSA) of the carbon nanotubes, the Brunauer, Emmet and Teller (BET) model was applied to the N<sub>2</sub> adsorption data at P/P<sub>0</sub> range of ~0.05 to 0.35, which is the typical BET multi-layer adsorption. The total pore volume is obtained from the amount of N<sub>2</sub> adsorbed at P/P<sub>0</sub> = 0.98. It is noted that CN<sub>x</sub>NT has higher SSA than pristine MWNT, while KOH activation increases the SSA of the SWNT by ~2 times (Table 7.1).

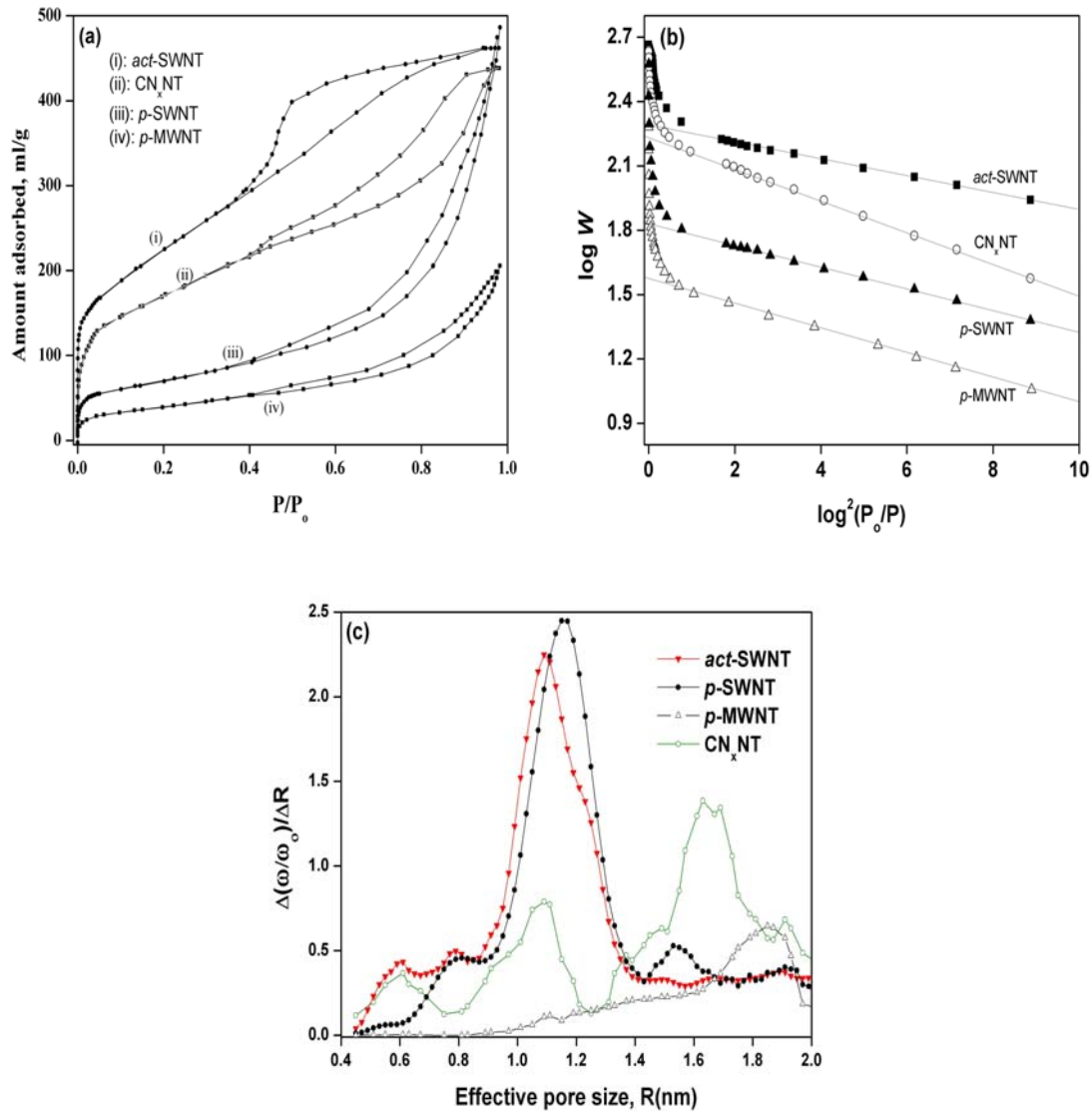


**Figure 7.3.** (a) N<sub>2</sub> adsorption isotherms at 77K, (b) DR plots and (c) HK plots of *p*-SWNT, *act*-SWNT, *p*-MWNT and CN<sub>x</sub>NT.

The extent and development of the micropore volume brought about by chemical modifications are evaluated by Dubinin-Radushkevich (DR) equation:

$$\log w = \log w_0 - \left( \frac{RT}{\beta E_0} \right)^2 \log^2 \left( \frac{P_0}{P} \right) \quad [7.1]$$

where  $w$  is the volume adsorbed at temperature  $T$ ,  $w_o$  is the micropore volume,  $P_o/P$  is the inverse relative pressure,  $\beta$  is the affinity coefficient (0.34 for  $N_2$  adsorbate),  $R$  is the universal gas constant, and  $E_o$  is the characteristic energy. The DR plots of the nanotubes are displayed as Figure 7.3b. Both Fig 7.3b and Table 7.1 indicate that  $CN_xNT$  has a larger amount of micropore volume than pristine MWNT, while KOH-activated SWNT also possesses larger micropore volumes than the non-activated ones. The increment of micropore volumes bear great importance to the hydrogen adsorptive properties (vide infra). Texier-Madoki et al.<sup>27</sup> and Kijkamp et al.<sup>29</sup> show that the  $H_2$  adsorption capacity of activated carbons is well-related to its micropore volumes. Of particular interests, the existence of subnanopores ( $<0.56nm$ ) has been reported to be beneficial for  $H_2$  physisorption<sup>12,33</sup>.

The Horvath-Kawazoe (HK) method<sup>34</sup> was used to compute the pore size distribution ( $PSD_{HK}$ ) for micropore size between 0.35nm-2nm. Numerical expression of HK method is given as follows:

$$\ln\left(\frac{P}{P_o}\right) = \frac{62.38}{(l - 0.64)} + \left(\frac{1.895 \times 10^{-3}}{(l - 0.32)^3}\right) - \left(\frac{2.7087 \times 10^{-7}}{(l - 0.32)^9}\right) - 0.05014 \quad [7.2]$$

where  $P/P_o$  is the relative pressure of the  $N_2$  adsorption isotherms,  $l$  is the defined as the distance between nuclei of two layers (e.g. a slit).

The calculation of  $PSD_{HK}$  involves finding the following function:

$$\omega/\omega_o = f(l - d_a) \quad [7.3]$$

where  $\omega_o$  is the maximum amount of  $N_2$  adsorbed at  $P/P_o=0.9$ ,  $d_a=0.34nm$  is the diameter of a carbon atom, and the term  $(l - d_a)$  is the effective pore size in nanometers. Suitable values of  $(l - d_a)$  between 0.35nm and 2nm are chosen and the respective  $l$  values are substituted into equation [7.2] to determine the corresponding  $(P/P_o)$  values. Then  $\omega$  is the amount of  $N_2$  adsorbed at  $P/P_o$ .



for a particular  $l$  value. Plotting the derivatives of  $(\omega/\omega_\infty)$  against  $(l - d_a)$  gives the effective pore size distribution.

The results of  $PSD_{HK}$  are presented in Figure 7.3c. The  $PSD_{HK}$  of  $p$ -SWNT consists of 0.8nm, 1.17nm and 1.54nm pore sizes. The pore size of  $p$ -SWNT at 1.17nm is very close to the average diameter as determined by Raman spectroscopy (page 118). When  $p$ -SWNT was activated with KOH, a small peak appears at  $\sim 0.6$ nm and extends to 0.35nm. This indicates that KOH-activation lead to the development of subnanopores. The  $p$ -MWNT contains a few micropores of size  $\sim 1.8$ nm, which might be the grooves due to the randomly criss-crossing network of nanotubes. On the other hand,  $CN_xNT$  exhibits more microporous features at  $\sim 0.6$ nm, 1.1nm and 1.7nm pore sizes than the pristine MWNT. From TEM images (Fig A7.4), the tubular walls of  $CN_xNT$  have many kinks and buckling compared to  $p$ -MWNT. These defects of multi-walled carbon nanotubes are viewed as important binding sites for  $H_2$  molecules<sup>12</sup>.

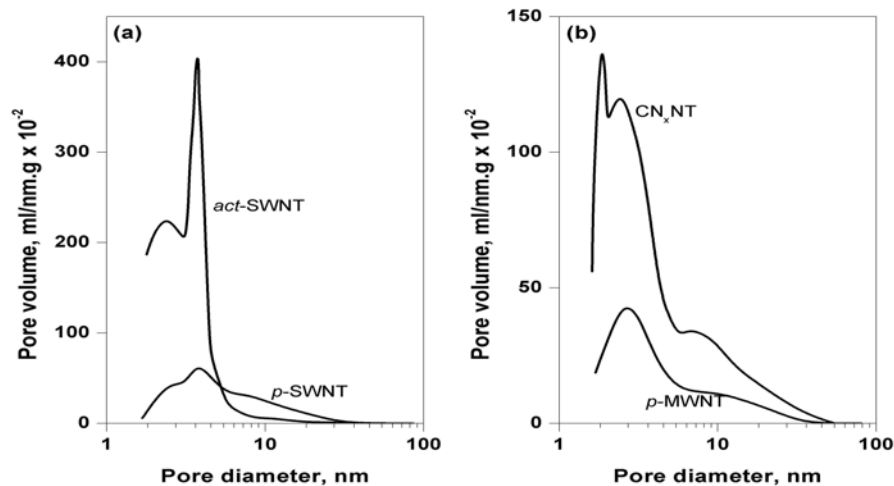


**Figure 7.4.** BJH mesopore size distribution of (a) single-walled and (b) multi-walled carbon nanotube samples.

The Barret, Joyner, and Halenda (BJH) mesopore size distribution (2-50nm) of the samples is presented as Figure 7.4. Likewise chemical modification of carbon nanotubes

increases the mesoporous volume and changes its mesoporous distributions. Although the modified carbon nanotubes possess more microporous texture, the fraction of microporous is relatively low and the modified nanotubes still belong to mesoporous materials (see Table 7.1).

### **7.2.3. Hydrogen adsorption isotherms**

Figure 7.5 shows the hydrogen adsorption isotherms of the SWNT and MWNT samples. The desorption branch follows the adsorption branch which indicates that H<sub>2</sub> adsorption isotherm of CNT is completely reversible (see also Figure A7.3b, page 203). At room temperature, the hydrogen storage of the samples displayed a linear relationship of pressure, which can be explained by Henry's Law. There is no abrupt increase in the H<sub>2</sub> storage at a particular pressure, as in the case of metal hydride compounds, which strongly suggests that room temperature H<sub>2</sub> storage in the carbon nanotubes is physisorption rather than chemisorption. The adsorbed hydrogen layer is extremely diluted at room temperature (<1wt%). The H<sub>2</sub> storage of *act*-SWNT and CN<sub>x</sub>NT have better performance as compared to its pristine counterparts (see Fig 7.5 and Table 7.1), 0.78wt% (vs. 0.38wt%) and 0.66wt% (vs. 0.20wt%), respectively, at room temperature and 6MPa.

At cryogenic temperature (77K), the H<sub>2</sub> adsorption capacity of SWNT and MWNT samples increased rapidly with pressure up to ~2MPa. The H<sub>2</sub> adsorption capacity of the chemically modified nanotubes is also higher than the pristine nanotubes at 77K. The cryogenic isotherms of the nanotubes are type I isotherms with adsorption saturation taking place, and can be fitted with a Langmuir model<sup>35</sup>,

$$M = M_s \frac{aP}{1 + aP} \quad [7.4]$$

where is M<sub>s</sub> the saturated adsorption capacity, P is the pressure, and *a* is a constant. The experimental excess H<sub>2</sub> adsorption above 2MPa is attributed to the increase in the effective monolayer adsorption pores and decrease in the chemical potential of hydrogen at higher pressure (vide infra). In addition, at higher pressures, H<sub>2</sub> molecules can be compressed in void space of the

carbon nanotubes and increases the overall H<sub>2</sub> uptakes<sup>36</sup>. The experimental H<sub>2</sub> uptakes are qualitatively consistent with the Monte Carlo simulation results on the H<sub>2</sub>/SWNT bundles in Chapter 3.4.

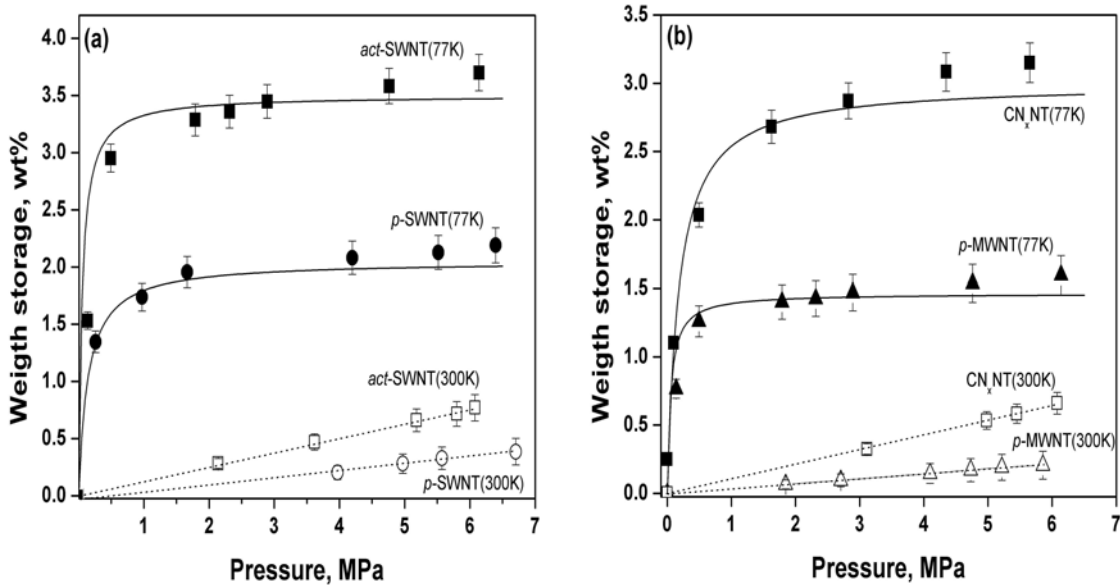


**Figure 7.5.** Hydrogen adsorption isotherms at room temperature (open symbols) and 77K (filled symbols) for (a) *act*-SWNT and *p*-SWNT and (b) CN<sub>x</sub>NT and *p*-MWNT samples. Isotherms at 300K and 77K are fitted with Henry's Law and Langmuir model respectively.

The isosteric heat of adsorption ( $q_{st}$ ) reflects the strength of interaction between gas molecules and adsorbent. The isosteric heat of adsorption is defined by Clausius-Clapeyron equation<sup>37</sup>:

$$q_{st} = -R \left( \frac{\partial(\ln p)}{\partial(1/T)} \right)_n \quad [7.5]$$

where  $P$  is the pressure,  $T$  is the temperature,  $R$  is the universal gas constant and  $n$  is the amount of H<sub>2</sub> adsorbed. Since the H<sub>2</sub> adsorption isotherms of CNTs are completely reversible, the heat of adsorption is equal to the heat of desorption.

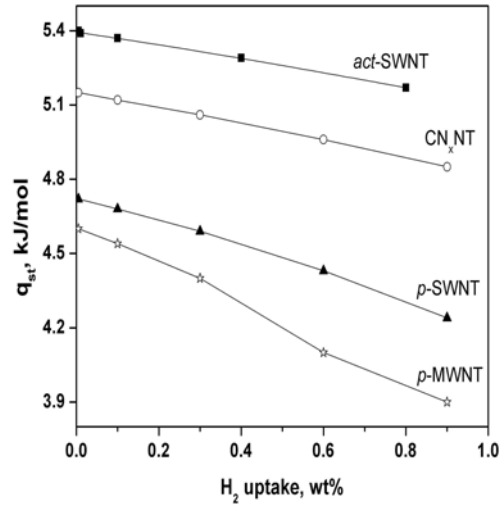


**Figure 7.6.** Variation of isosteric heat of adsorption with the amount of  $H_2$  adsorbed.

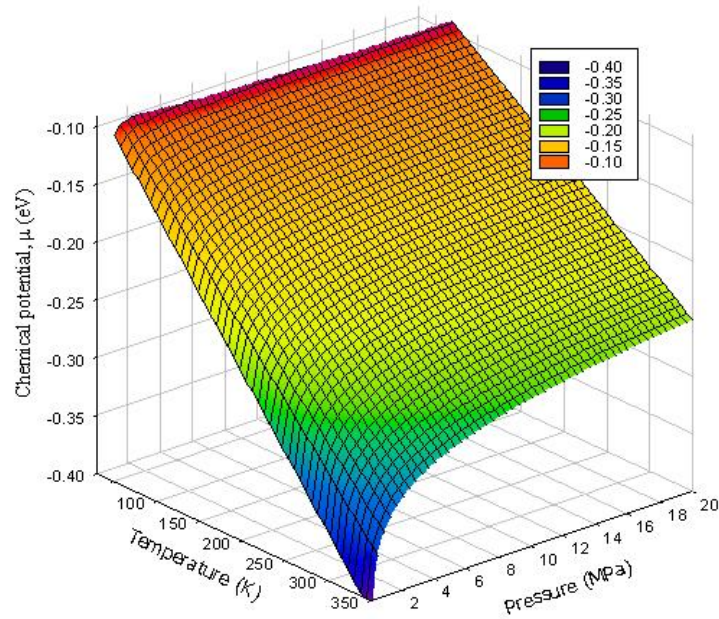


**Figure 7.7.** Variation of chemical potential of  $H_2$  ( $\mu$ ) with pressure and temperature. Legends are divided into 5 color bands (from  $-0.1\text{eV}$  to  $-0.4\text{eV}$ ).

Figure 7.6 shows the variation of isosteric heat of carbon nanotube samples with the amount of H<sub>2</sub> adsorbed. The evaluated  $q_{st}$  values range between 4.6-5.4kJ/mol (~48-56meV), which is within the physisorption range and similar to the reported adsorption energy of activated carbon<sup>28,31</sup> (40-50meV, see Table 7.1). Nonetheless, the evaluated  $q_{st}$  values are larger for chemically modified carbon nanotubes (i.e. *act*-SWNT and CN<sub>x</sub>NT) than pristine carbon nanotubes. Noteworthy, the  $q_{st}$  values of pristine carbon nanotubes tend to decrease faster than the modified carbon nanotubes, which indicate that modified carbon nanotubes might be able to store more H<sub>2</sub> at higher pressures >6MPa.

When the adsorption potential of the adsorbent ( $\epsilon_{\text{carbon}}$ ) is more stable than the chemical potential of the adsorbate ( $\mu_{\text{hydrogen}}$ ), adsorption then favorably occurs. Therefore it is of great importance to determine  $\epsilon$  and  $\mu$  for the solid-gas physisorption. Figure 7.7 shows the temperature- and pressure-dependence of the H<sub>2</sub> chemical potential ( $\mu$ ) calculated by using the experimental values of enthalpy (H) and entropy (S)<sup>38</sup>. Generally, a low temperature and high pressure reduce the chemical potential of hydrogen. On the basis of Figure 7.7, it is difficult to adsorb significant amount of H<sub>2</sub> with carbon at ambient temperature and even at high pressures of ~20 MPa because  $\mu$  is large ~200-300 meV (blue-greenish region of Fig 7.7), and  $\epsilon$  of activated carbon is ~50 meV. On the other hand, at 77K the chemical potential of H<sub>2</sub> is reduced to ~100 meV (orange region of Fig 7.7), which is closer to the adsorption potential of carbon materials. This qualitatively agreed with the works of Strobel et al.<sup>30</sup> and Nijkamp et al.<sup>29</sup> on activated carbons. Hence, in comparison with literature, the H<sub>2</sub> adsorption isotherms of carbon nanotubes are similar to activated carbons. Nonetheless, KOH-activated and N-doped carbon nanotubes exhibit higher H<sub>2</sub> uptakes than pristine carbon nanotubes.

The enhanced H<sub>2</sub> uptakes of the chemically modified carbon nanotubes (*act*-SWNT and CN<sub>x</sub>NT) strongly suggest that optimization of the pore structures, specific surface area and chemical bonding are crucial parameters. Both *act*-SWNT and CN<sub>x</sub>NT have larger SSA,

increased amount of micropore volume and more suitable micropore sizes than pristine carbon nanotubes, which contributed to higher H<sub>2</sub> uptakes. The charge transfer of N-atoms to C-atoms polarizes the H<sub>2</sub> molecules and might be responsible for a higher H<sub>2</sub> uptake. The defective exterior walls of CN<sub>x</sub>NT provide stronger and more adsorption sites for H<sub>2</sub> molecules than *p*-MWNT (see Figure A7.4, page 204).

At present, there's no direct evidence to indicate whether KOH activation changes the interstitial channel spacing of SWNT bundles because N<sub>2</sub> molecules (kinetic diameter ~0.36nm) cannot access the assumed 0.32nm channel spacing. In other words, the analysis obtained from the N<sub>2</sub> adsorption isotherms at 77K gives mostly about the exterior texture of the SWNT bundles and MWNT samples. The kinetic diameter of H<sub>2</sub> molecule is ~0.29nm and seems likely to penetrate into the interstitial channels of a SWNT bundle. However Deng et al.<sup>39</sup> demonstrated theoretically that the ~0.34nm interstitial channels spacing (interlayer distance) of SWNT bundle (graphene sheets) solely contributes diluted amount of H<sub>2</sub> uptake of 0.2wt% at 50bar and 300K (zero H<sub>2</sub> uptake for graphene sheets). When the interstitial channel spacing (interlayer distance) from 0.34nm to 0.8nm, the H<sub>2</sub> uptake of SWNT bundle (graphene sheets) is slightly enhanced to 0.5wt% at 50bar and 300K. However the SWNT bundles are held together by strong van der Waals forces over its entire length, unless the interstitial channel spacing has been pillared by foreign dopants which prevent the channels from collapsing. Hence it is reasonable to surmise that the interstitial channel spacing of *act*-SWNT is about the same as *p*-SWNT because there is no intercalatant in *act*-SWNT. Furthermore, <sup>13</sup>C NMR shows that at ambient conditions He atoms could access the interstitial sites of SWNT bundles whereas H<sub>2</sub> and N<sub>2</sub> molecules could not<sup>40</sup>. Inelastic neutron scattering study<sup>41</sup> of H<sub>2</sub>-loaded SWNT bundle suggests that the location of the physisorbed H<sub>2</sub> is most likely at the exterior surface and similar to activated carbon. Therefore the higher H<sub>2</sub> uptake of *act*-SWNT is attributed mainly to its larger SSA and micropore volume than *p*-SWNT.

#### **7.2.4. Conclusions**

In short, the H<sub>2</sub> adsorption behavior of carbon nanotube is similar to activated carbon, which show appreciable H<sub>2</sub> uptake at low temperatures. Therefore, it is imperative to modify carbon nanotubes to achieve larger SSA, micropore volume and size, and q<sub>st</sub> value for better physisorption of H<sub>2</sub>. Thus N doping and KOH activation is a favorable method to enhance the H<sub>2</sub> uptakes of CNTs, though the H<sub>2</sub> adsorption is still dominated by the presence of large SSA and microporous texture. The creation of defects via plasma etching<sup>42</sup> and special synthetic methods<sup>12</sup> have also been shown to improve the H<sub>2</sub> uptakes. Likewise the deliberate introduction of dopants such as Li and solvated Li cations<sup>39</sup> to increase the interstitial channels spacing of CNTs, modify the q<sub>st</sub> values, and the charge transfer from the metal dopant to the nanotube polarizes the H<sub>2</sub> molecule and enhances the H<sub>2</sub> uptake.

### 7.3. Room temperature H<sub>2</sub> uptakes of TiO<sub>2</sub> nanotubes

Since H<sub>2</sub> uptakes of CNTs are diluted (<1wt%) at room temperature, two new candidates with better room temperature H<sub>2</sub> uptakes have been proposed in this dissertation. TiO<sub>2</sub> and BN nanotubes are relatively good candidates for room temperature H<sub>2</sub> uptakes of ~2wt%. Therefore, the pressure-composition isotherms of TiO<sub>2</sub> and BN nanotubes are mainly focused on room temperature.

Our research group<sup>43</sup> was the first to investigate multi-layered TiO<sub>2</sub> nanotubes as a new candidate for hydrogen storage. This is motivated by the interstitial spacing between layers ( $d_{\text{layer}}=0.72\text{nm}$ , see Appendix Figure A7.16, page 224) of TiO<sub>2</sub> nanotubes which is larger than the kinetic diameter of free H<sub>2</sub> molecules ( $d_{\text{hydrogen}}=0.29\text{nm}$ ) and the interlayer distance of MWNT ( $d_{\text{MWNT}}=0.34\text{nm}$ ). In addition, the non-seamless structures of open-tipped TiO<sub>2</sub> nanotubes imply that H<sub>2</sub> molecules can enter the interlayer domain via the tips and sidewall defects. This is an added advantage because H<sub>2</sub> molecules can intercalate between layers in the walls of TiO<sub>2</sub> nanotubes forming host-guest compounds TiO<sub>2</sub>·xH<sub>2</sub>. The H<sub>2</sub> uptakes of TiO<sub>2</sub> nanotubes were determined from pressure-composition (*P-C*) isotherms. The specific surface area and pore structure of TiO<sub>2</sub> nanotube were determined from nitrogen adsorption isotherm at 77K. Temperature-programmed desorption (TPD) and FTIR techniques were employed to elucidate the H<sub>2</sub> sorption properties of TiO<sub>2</sub> nanotubes.

**Table 7.2.** Adsorptive parameters of bulk TiO<sub>2</sub> and titania nanotubes.

Sample	SSA <sub>BET</sub> , m <sup>2</sup> /g	V <sub>mic</sub> , ml/g	V <sub>meso</sub> , ml/g	H <sub>2</sub> uptake at 6MPa, wt%	E <sub>a</sub> , kJ/mol
TiO <sub>2</sub> nanotube (~10nm)	197	0.274	0.379	2.0	15
Bulk TiO <sub>2</sub> (50-600nm)	16	-	0.030	0.8	-

Specific surface area (SSA<sub>BET</sub>) is determined by BET method.

Micropore volume (V<sub>mic</sub>) is determined using DR method.

Total pore volume (V<sub>T</sub>) is determined at P/P<sub>0</sub>=0.98

Mesopore volume (V<sub>meso</sub>) is obtained by V<sub>T</sub> - V<sub>mic</sub>.

Activation energy, E<sub>a</sub>, is evaluated by Kissinger method



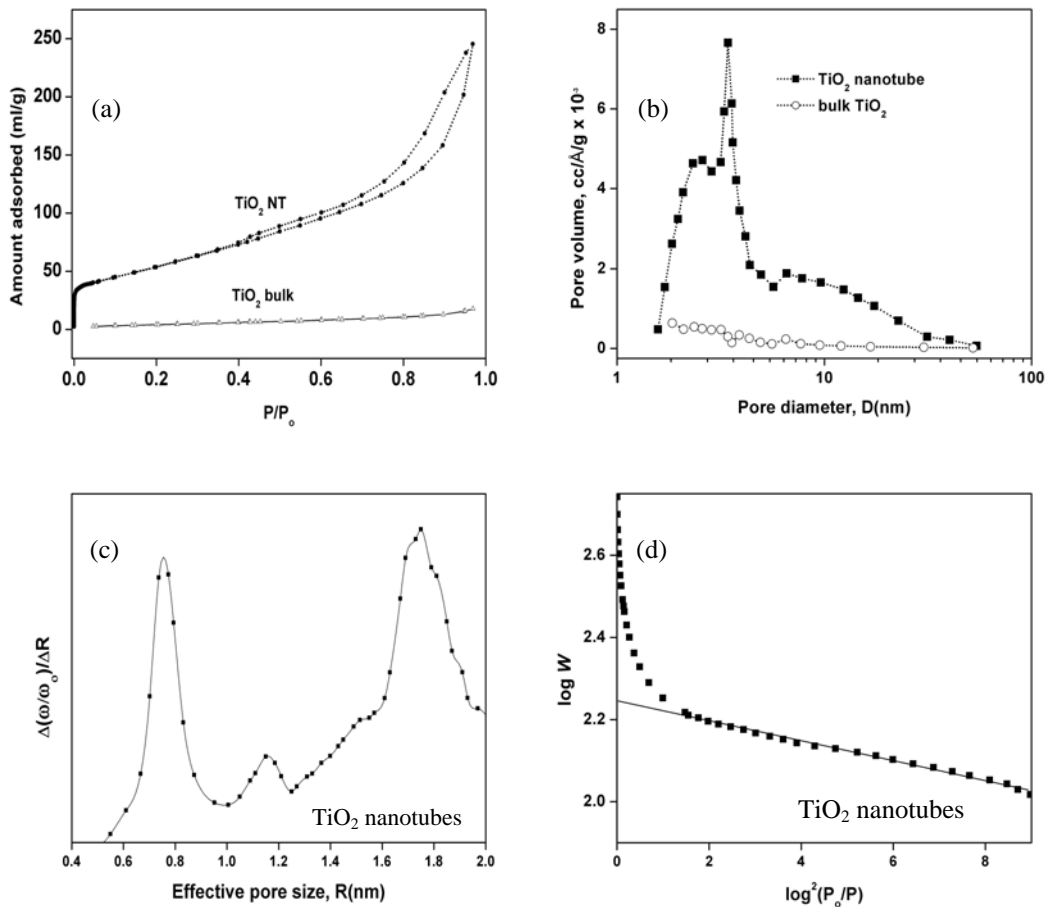
### **7.3.1. Nitrogen adsorption isotherms at 77K**

Table 7.2 compares the adsorptive properties of bulk TiO<sub>2</sub> and TiO<sub>2</sub> nanotubes. The pore structures of TiO<sub>2</sub> samples were studied using N<sub>2</sub> adsorption isotherm at 77K. The micropore volume of TiO<sub>2</sub> nanotube was evaluated by Dubinin-Radushkevich (DR) equation. The pore size distribution (PSD) was analyzed by using the Barret, Joyner, and Halenda (BJH) and Horvath-Kawazoe (HK) method. The results of the N<sub>2</sub> adsorption isotherms studies are presented as Figure 7.8.

The N<sub>2</sub> adsorption isotherm of TiO<sub>2</sub> NT is typical of type IV isotherm according to the IUPAC classification. The adsorption-desorption hysteresis loop is observed at  $P/P_0 \approx 0.43$ , indicating capillary condensation inside the nanotubes (innermost cavity). A smaller N<sub>2</sub> adsorption load is observed for the bulk TiO<sub>2</sub> with no hysteresis loop (see Figure 7.8a). The specific surface area (SSA) of the TiO<sub>2</sub> sample is determined by Brunauer-Emmet-Teller (BET) measurements in the  $P/P_0$  range of 0.05 to 0.43, which is a typical BET multi-layer adsorption. A 12-fold increase in SSA is noted when the bulk TiO<sub>2</sub> adopts a nano-tubular structure, from 16 to 197 m<sup>2</sup>/g.

The BJH plots of bulk TiO<sub>2</sub> and TiO<sub>2</sub> nanotubes were presented as Figure 7.8b. Three BJH peaks located at ~6.7nm, 3.4nm and 2.4nm are observed for TiO<sub>2</sub> NT. The broad peak centered ~6.7nm is attributed to the inner cavities and pores formed inside the aggregates of the TiO<sub>2</sub> NTs. It is supposed that the 10M NaOH solution exfoliates the anatase crystallites into layered sheets at ~120°C. The rolling-up of these unstable layered crystalline sheets results in non-seamless multiple-walled TiO<sub>2</sub> nanotubes. Thus the layers of the TiO<sub>2</sub> nanotubes contain defects, and extensive rinsing of 0.1M HCl gives rise to the observed smaller pore sizes of 2.4nm and 3.4nm.

Figure 7.8c shows the HK plot for pore size distribution between 0.35nm-2nm. The pore size at 0.8nm is very close to the interstitial spacings between layers of TiO<sub>2</sub> nanotubes. Similar to MWNT, the pore size at ~1.2-1.8nm is attributed to the grooves created from the randomly criss-crossing of TiO<sub>2</sub> nanotubes. However, subnanopores (<0.56nm) is absence from TiO<sub>2</sub> nanotubes. The micropore volume of TiO<sub>2</sub> nanotubes is evaluated using DR method, which yields  $V_{mic}=0.274\text{ml/g}$  (see Table 7.2).



**Figure 7.8.** (a) N<sub>2</sub> adsorption isotherms at 77K, (b) BJH pore size distribution of TiO<sub>2</sub> nanotube and bulk anatase, (c) effective pore size distribution by HK method, and (d) DR plot.

### 7.3.2. Hydrogen adsorption isotherms

The hydrogen uptake by TiO<sub>2</sub> systems was measured with a commercial pressure-composition (*P-C*) isotherm unit (see Figure 7.9). The TiO<sub>2</sub> sample of ~300-500mg was first degassed at 250°C and  $1 \times 10^{-3}$  Pa for at least 2hr. When the sample was cooled to room temperature, the hydrogen sorption process began. As shown in Figure 7.9a, the hydrogen concentration gradually increases as the pressure increases. At room temperature and pressure of ~900 PSI (~6MPa) the H<sub>2</sub> uptake was ~2.0wt% H<sub>2</sub> for TiO<sub>2</sub> NT. A much lower hydrogen concentration of ~0.8wt% is noted for the bulk forms (see Figure 7.9a blue symbol profile).

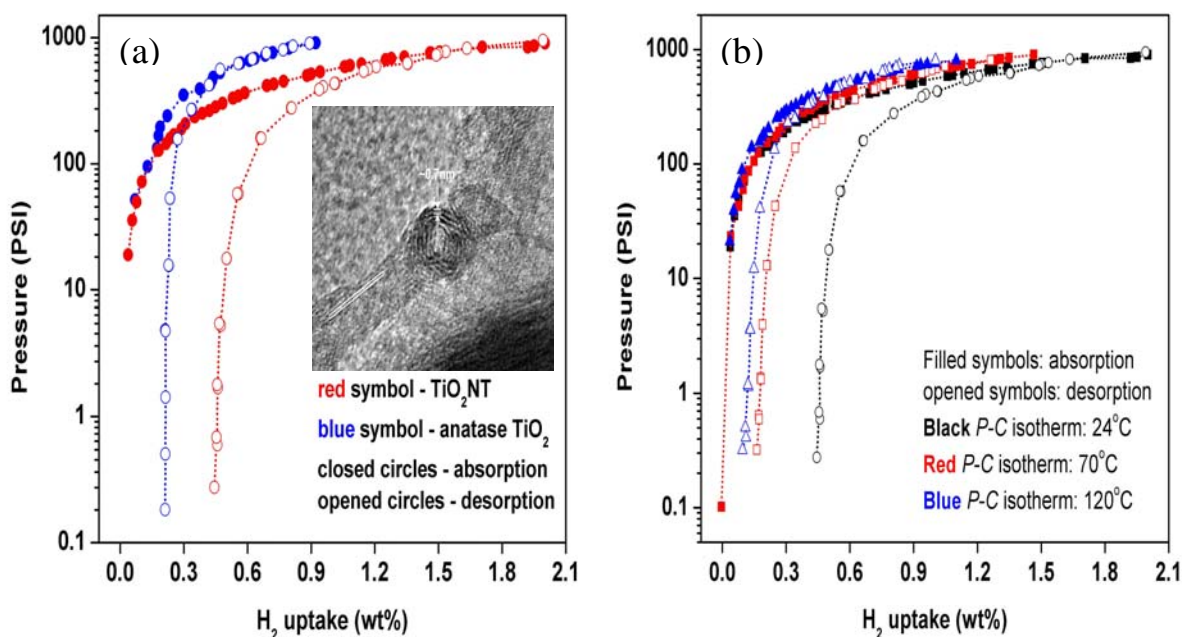


**Figure 7.9.** (a) *P-C* isotherms of TiO<sub>2</sub> nanotubes and bulk TiO<sub>2</sub> at room temperature. (b) *P-C* isotherms of TiO<sub>2</sub> nanotubes at 24°C, 70°C and 120°C.

Preliminary tests of 10 consecutive cycles of H<sub>2</sub> adsorption and desorption (each cycle is accompanied with degassing at 250°C) at 25°C, the hydrogen-storage capacity of TiO<sub>2</sub> NT decreased by ~7%, indicating a reasonably good recyclability in the H<sub>2</sub> adsorption and desorption

process. The desorption curves of bulk and nanotubular TiO<sub>2</sub> samples does not coincide with the adsorption curves as the H<sub>2</sub> pressure is reduced. Only ~75% of the stored hydrogen can be released when the hydrogen pressure is lowered to atmospheric conditions, revealing the irreversible nature of the process. Obviously the hydrogen molecules which can be released simply by reducing the pressure are physically adsorbed, while the ~25% of adsorbed hydrogen molecules, which are held on the sample at lower pressures, are chemically adsorbed and desorption may occur upon heating it. This behavior is similar to the hydrogen sorption of ZnO nanowires<sup>19</sup> and TiS<sub>2</sub> nanotubes<sup>18</sup>, whereby it is estimated that 30-40% of the hydrogen is chemisorbed and can be released at elevated temperature of 75-185°C.

The better hydrogen uptake of TiO<sub>2</sub> NT can be attributed to its unique nano-tubular morphology and larger SSA such that sorption takes place both on external wall and interstitial channels. It should be noted that nearly perfect oxide surfaces are essentially inert to molecular H<sub>2</sub> and sorption at room temperature usually takes place at defect sites<sup>44</sup>. The enhanced physisorption of TiO<sub>2</sub> NTs can be rationale from the HRTEM images taken by us (see Fig 7.9 inset, and Figure A7.16 page 224) and Yao et al.<sup>45</sup> which revealed the shells of TiO<sub>2</sub> NTs are not seamless since the tube structure was formed by rolling up titania single-layer sheets. Therefore there are more defects on TiO<sub>2</sub> NTs, which give rise to better hydrogen sorption than bulk TiO<sub>2</sub>. In addition, the intercalation of H<sub>2</sub> molecules into the interstitial sites of the walls of TiO<sub>2</sub> nanotube and giving rise to a host-guest compound (TiO<sub>2</sub>·xH<sub>2</sub>) increases its H<sub>2</sub> uptake capacity. The formation of a host-guest compound (TiO<sub>2</sub>·xH<sub>2</sub>) has been verified by Bavykin et al.<sup>46</sup> using solid-state <sup>1</sup>H MAS NMR, which showed a signal of intercalated molecular H<sub>2</sub> at 4.5ppm. Bavykin et al.<sup>46</sup> estimated the coefficient of self-diffusion of H<sub>2</sub> inside the walls of TiO<sub>2</sub> NT at room temperature to be 2.8 x 10<sup>-13</sup> cm<sup>2</sup>s<sup>-1</sup>. However, these intercalated H<sub>2</sub> molecules are weakly chemisorbed onto the TiO<sub>2</sub> nanotubes and can be released upon heating at 70°C (vide infra).

The *P-C* isotherms of TiO<sub>2</sub> NT were repeated at 2 elevated temperatures of 70°C and 120°C (Figure 7.9b). It is noted that the maximum H<sub>2</sub> uptake is reduced, with 1.45wt% and 1.10wt% hydrogen uptakes at 70°C and 120°C respectively. The desorption-curves return closer to the absorption-curves, with 0.25wt% and 0.13wt% H<sub>2</sub> remain for the 70°C and 120°C *P-C* isotherms respectively. TPD and FTIR were further employed to understand the H<sub>2</sub> adsorption-desorption mechanism of TiO<sub>2</sub> nanotube.

### **7.3.3. TPD and FTIR studies of H<sub>2</sub>-soaked TiO<sub>2</sub> nanotubes**

TPD was performed on a home-built stainless steel microreactor equipped with an online mass spectrometer (HPR20 mass spectrometer, Hiden Analytical Ltd). ~100mg of TiO<sub>2</sub> nanotube was loaded into the middle of the microreactor and vacuum degassed at 250°C for 2hr. The TiO<sub>2</sub> nanotube was then soaked at ~9MPa of H<sub>2</sub> pressure (purity 99.9995%) for 2hr at room temperature. Once the pressure returned to ambient conditions, the microreactor was purged with purified argon (flow rate=50ml/min) for 2hr to remove residual H<sub>2</sub> before measuring the desorption process. The desorption process of the H<sub>2</sub>-soaked TiO<sub>2</sub> nanotube was conducted from room temperature to higher temperatures at various heating rate with argon as the carrier gas. During TPD measurements, H<sub>2</sub>, N<sub>2</sub>, O<sub>2</sub> and H<sub>2</sub>O desorption were monitored simultaneously. Nitrogen and oxygen gases desorption signals were not observed.

From TPD process, the H<sub>2</sub> desorption peaks shifted towards higher temperatures (from 70°C to 119°C) as the heating rate was increased (10K/min to 25K/min, see Fig 7.10a). This strongly suggests that some hydrogen molecules were chemisorbed onto the TiO<sub>2</sub> NT and therefore would not be released at room temperature so that the PCI desorption curve did not follow the adsorption curve.

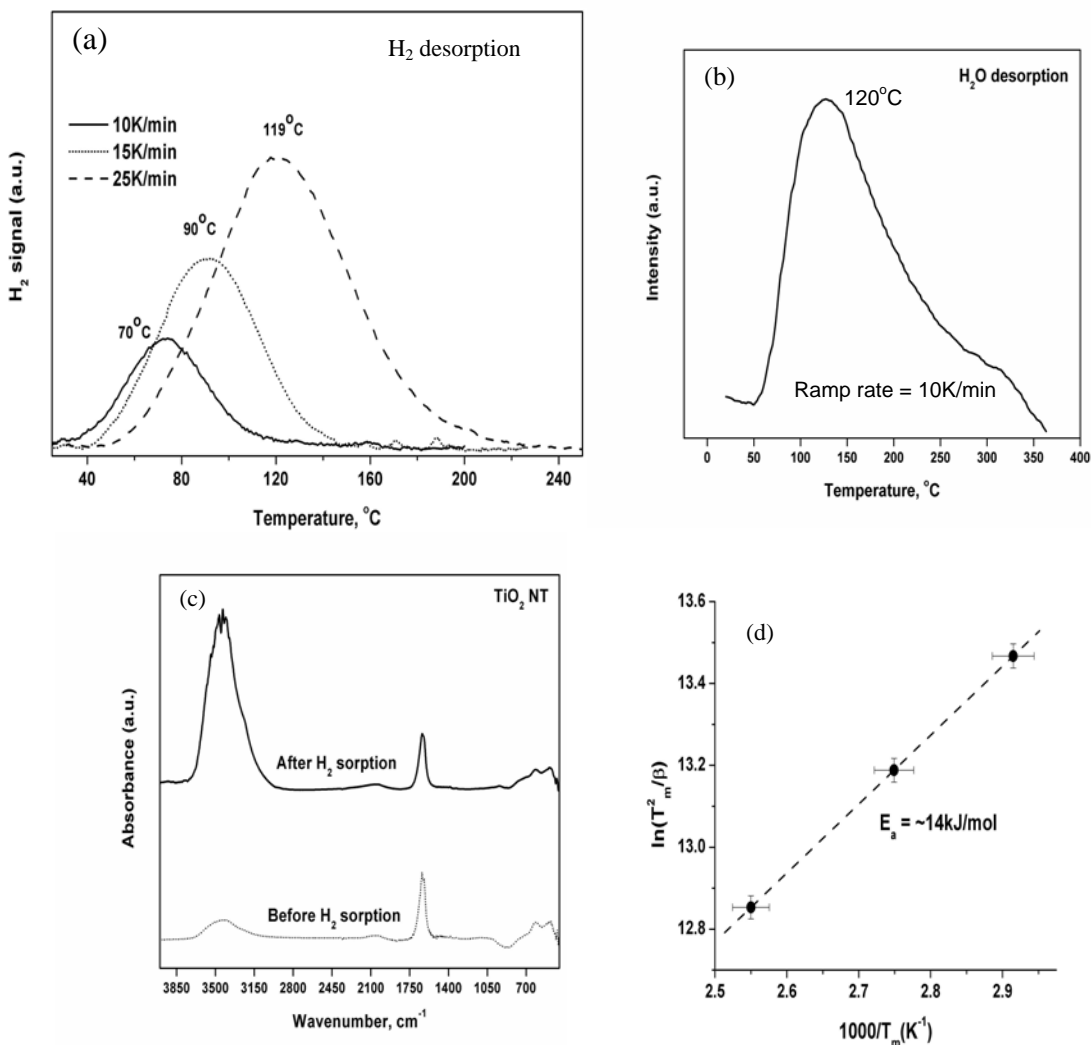


**Figure 7.10.** (a) H<sub>2</sub> desorption and (b) H<sub>2</sub>O desorption process during TPD of hydrogenated TiO<sub>2</sub> nanotubes at indicated ramp rate, using argon as carrier. (c) FTIR spectra of TiO<sub>2</sub> nanotubes before and after H<sub>2</sub> sorption. (d) Kissinger's plot of H<sub>2</sub> desorption of TiO<sub>2</sub> nanotubes.

Some hydrogen molecules are dissociatively adsorbed and bonded to the oxide ions can be released inevitably as H<sub>2</sub>O at a higher temperature of 120-200 °C when the OH bonds are ruptured. Figure 7.10b shows the H<sub>2</sub>O desorption of the H<sub>2</sub>-soaked TiO<sub>2</sub> nanotubes. The observed H<sub>2</sub>O desorption is due to the breaking of -OH bond from the hydrogenated TiO<sub>2</sub> nanotubes. This is not due to moisture in the H<sub>2</sub> supply (or gas line) because a separate experiment was carried out using multi-walled carbon nanotube as a H<sub>2</sub> storage material and there was no H<sub>2</sub>O desorption

peak. Furthermore, FTIR spectra of TiO<sub>2</sub> NT revealed that there was a significant increase in the –OH signal (3427cm<sup>-1</sup>) after the hydrogenation process (see Fig 7.10c). The H<sub>2</sub>-soaked TiO<sub>2</sub> NT was transferred into a glove bag (filled with dried nitrogen atmosphere) and pelletized with KBr for FTIR measurements. The adsorption of moisture is therefore minimized. The observation of the enhanced –OH infrared band is due to the chemisorbed H<sub>2</sub> in TiO<sub>2</sub> nanotubes.

Since the adsorption branch does not coincide with the desorption branch (both physisorption and chemisorption is involved), the Kissinger's equation<sup>26</sup> is used to evaluate the heat of desorption instead of the Clausius-Clapeyron equation. The activation energy involved in the desorption of hydrogen from H<sub>2</sub>-soaked TiO<sub>2</sub> nanotube is given by Kissinger Equation:

$$-\frac{E_a}{R} = \frac{\partial \ln(\beta/T_m^2)}{\partial(1/T_m)} \quad [7.6]$$

where T<sub>m</sub> is the temperature at which the maximum reaction rate peaks, β is the heating rate, E<sub>a</sub> is the activation energy and R the universal gas constant.

Figure 7.10d shows the Kissinger's plot of H<sub>2</sub>-soaked TiO<sub>2</sub> nanotubes at different heating rates. The slope is fitted to obtain the value of E<sub>a</sub>/R. Thus the activation energy for hydrogen desorption for H<sub>2</sub>-loaded TiO<sub>2</sub> nanotube was E<sub>a</sub> ~14kJ/mol (~145meV). This value is much higher than the heat of adsorption of carbon nanotubes (~50meV), which indicates that chemisorption is involved for hydrogen-titania nanotube interactions. However this E<sub>a</sub> value of TiO<sub>2</sub> NT is lower than those of common metal hybrids<sup>47</sup>.

#### **7.3.4. Conclusions**

In short, nanotubular form of TiO<sub>2</sub> has H<sub>2</sub> sorption capacity of ~2wt% at room temperature and 6MPa, which is much higher than carbon nanotubes. Among them 75% are physisorbed and can be reversibly released upon the pressure reduction. On the basis of *P-C* isotherms and TPD, it is estimated that ~13% are weakly chemisorbed and can be released at 70°C while ~12% are strongly chemisorbed and released only at temperatures above 120°C.

### **7.4. Room temperature H<sub>2</sub> uptakes of BN nanotubes**

Boron nitride is isoelectronic and isostructure to graphite, except for the presence of ionic B-N bonds in boron nitride compared to covalent C-C bonds in carbon. Boron nitride nanofibers, bamboo-shaped BN nanotubes, and collapsed BN nanotubes have been demonstrated to store ~2-4wt% of H<sub>2</sub> at room temperature and modest pressures. The large difference in electron affinity of the B-N bonds suggest that polarization of H<sub>2</sub> molecules might be important for binding H<sub>2</sub> onto the BN nanotube surfaces. The observed higher H<sub>2</sub> uptake of BN nanotube than carbon nanotube warrants a further investigation. Therefore BN nanotubes were synthesized using a catalyzed mechano-chemical method (Appendix A7.2, page 205) and tested for H<sub>2</sub> sorption. Likewise, the pressure-composition (*P-C*) isotherms, N<sub>2</sub> adsorption at 77K, and temperature-programmed desorption (TPD) were employed to elucidate the H<sub>2</sub> sorption behavior of BN nanotubes.

**Table 7.3.** Adsorptive parameters of BN nanotubes and bulk BN.

Sample	SSA <sub>BET</sub> , m <sup>2</sup> /g	V <sub>mic</sub> , ml/g	V <sub>meso</sub> , ml/g	H <sub>2</sub> uptake at 6MPa, wt%	E <sub>a</sub> , kJ/mol
BN nanotube (~10nm)	129	0.203	0.411	2.2	19.7
Bulk BN (~1μm)	15	-	0.01	0.1	-

Specific surface area (SSA<sub>BET</sub>) is determined by BET method.

Micropore volume (V<sub>mic</sub>) is determined using DR method.

Total pore volume (V<sub>T</sub>) is determined at P/P<sub>0</sub>=0.98

Mesopore volume (V<sub>meso</sub>) is obtained by V<sub>T</sub> - V<sub>mic</sub>.

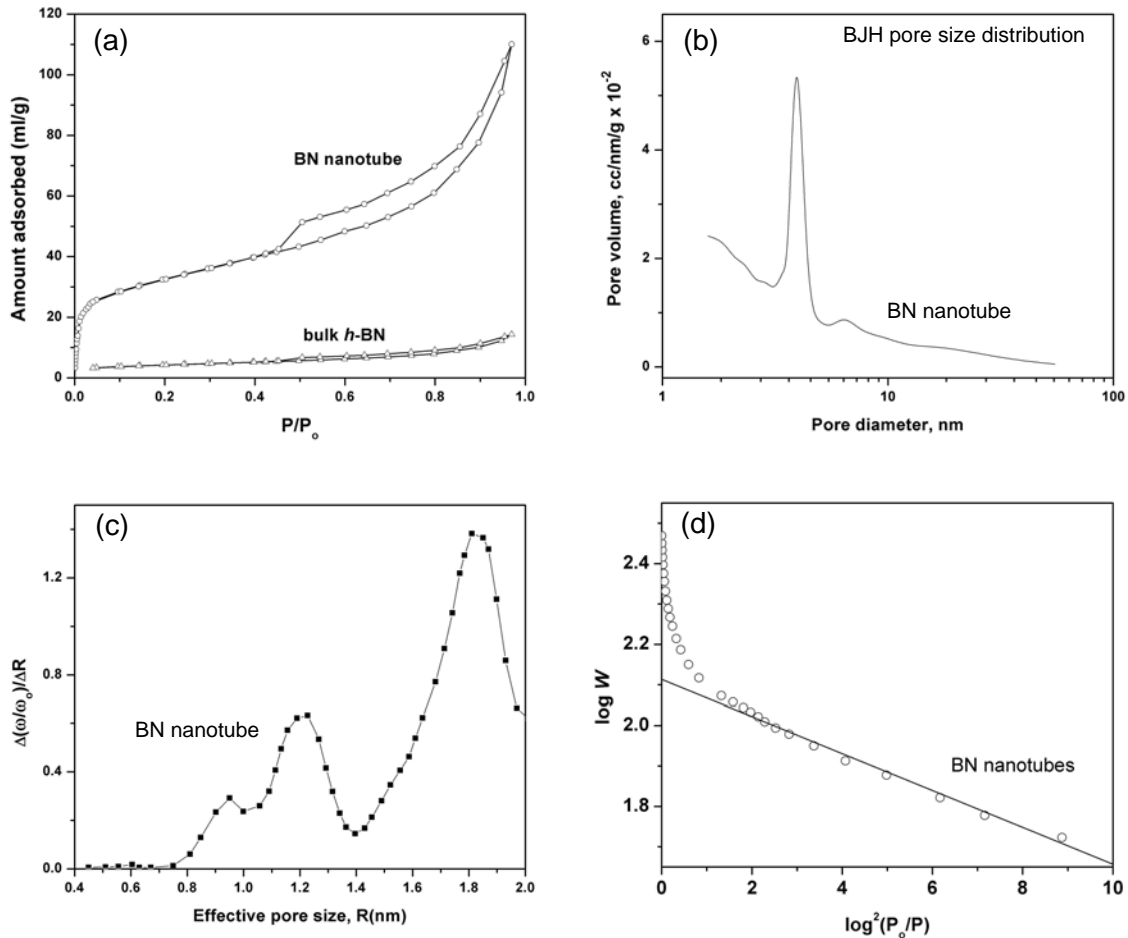
Activation energy, E<sub>a</sub>, is evaluated by Kissinger method

#### **7.4.1. Nitrogen adsorption isotherms at 77K**

Table 7.3 compares the adsorptive properties of bulk BN and BN nanotubes. The N<sub>2</sub> adsorption isotherm of BNNT is typical of type IV isotherm according to the IUPAC classification. The adsorption-desorption hysteresis loop is observed at P/P<sub>0</sub> ≈ 0.43, indicating



capillary condensation inside the nanotubes (innermost cavity). A smaller  $N_2$  adsorption load is observed for the bulk BN with no hysteresis loop (see Figure 7.11a). The Brunauer, Emmett, and Teller (BET) measurements show that the specific surface area (SSA) of the BN nanotube is determined to be  $129\text{m}^2/\text{g}$ , at least 8 times larger than that of bulk  $h\text{-BN}$  ( $15\text{m}^2/\text{g}$ ). The pore size distribution (PSD) was likewise analyzed by using the Barrett-Joyner-Halenda (BJH) method. A prominent PSD peak was observed at  $\sim 4\text{nm}$ , which can be attributed to the interstitial sites of the BN nanotube agglomerates.



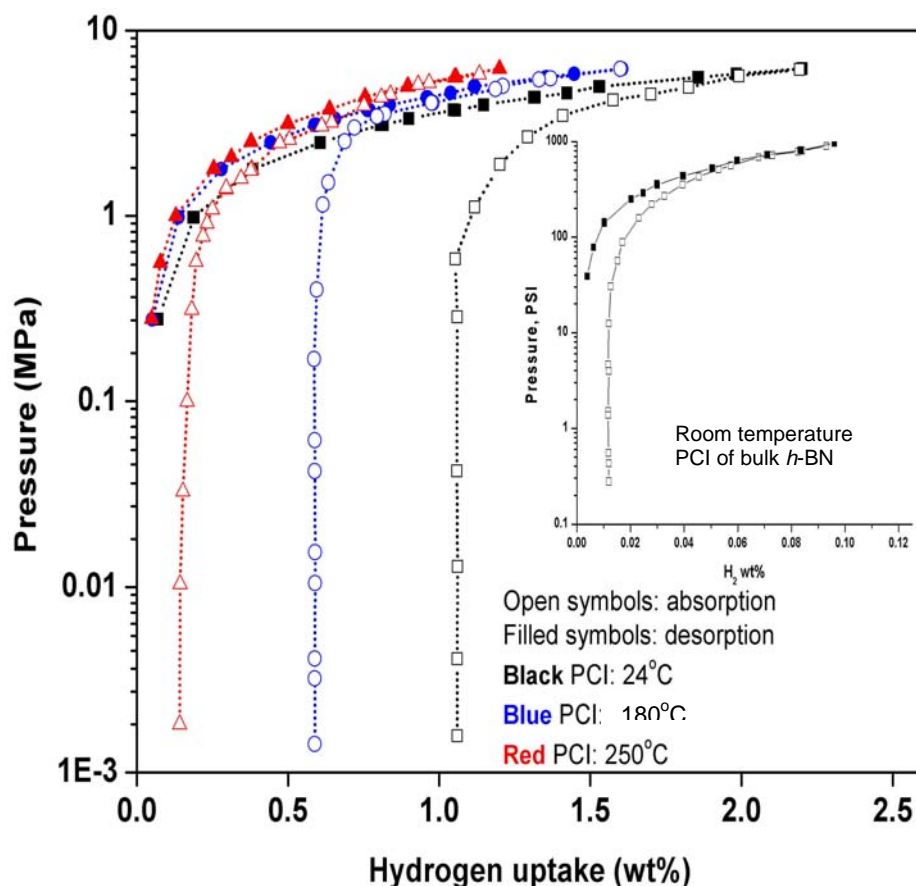
**Figure 7.11.** (a)  $N_2$  adsorption isotherms at 77K and (b) BJH pore size distribution of BN nanotube. (c) Effective pore size distribution by HK method, and (d) DR plot.

Figure 7.11c shows the micropore size distribution ( $PSD_{HK}$ , 0.36-2nm) of BNNT as determined by Horvath-Kawazoe (HK) method. The micropores of BNNT are mainly found at ~1.8nm, 1.2nm and 0.9nm, which is very similar to MWNT samples. No subnanopore can be found on BN nanotubes, this is in contrast to  $CN_x$  nanotubes.

The micropore volume of BN nanotubes is likewise evaluated using Dubinin-Radushkevich (DR) method, which yields  $V_{mic}=0.203\text{ml/g}$  (see Table 7.3). BN nanotubes are noted to possess a higher amount of micropore volume than pristine MWNT ( $V_{mic}=0.055\text{ml/g}$ ), but fewer amount of micropore volume than  $CN_x\text{NT}$  ( $V_{mic}=0.275\text{ml/g}$ ). This might be due to the mixture of bamboo-shaped and concentric hollow BN nanotubes.

#### **7.4.2. Hydrogen adsorption isotherms**

The hydrogen uptake of BN nanotube was carried out in similar fashion as  $TiO_2$  nanotube. Briefly, the BN samples of ~300-500mg were degassed at  $350^\circ\text{C}$  and  $1 \times 10^{-3}$  Pa for at least 2hr. When the samples had cooled to room temperature, the hydrogen sorption process began. Figure 7.12 shows the pressure-composition isotherms of the BN nanotube at  $24^\circ\text{C}$ ,  $180^\circ\text{C}$  and  $250^\circ\text{C}$ . The  $H_2$  uptake of the BN nanotube was 2.2wt% at room temperature and 6MPa. This value is much higher than those of bulk BN (~0.1wt%, see inset of Fig. 7.12). As seen in Figure 7.12, the  $H_2$  desorption curves of the BN nanotubes do not coincide with the adsorption curves and these strongly suggest the presence of  $H_2$ -chemisorption. At  $180^\circ\text{C}$  and  $250^\circ\text{C}$  the maximal  $H_2$  uptakes were reduced to 1.6wt% and 1.2wt% respectively. The desorption curves returned closer to the adsorption curves at higher temperatures. Preliminary tests of 10 consecutive cycles of  $H_2$  adsorption and desorption (each cycle is accompanied with degassing at  $350^\circ\text{C}$ ) at  $25^\circ\text{C}$ , the hydrogen-storage capacity of BNNT still retain a  $H_2$  uptake of ~2.2wt%, indicating a reasonably good recyclability in the  $H_2$  adsorption and desorption process.



**Figure 7.12.** *P-C* isotherms of BN nanotubes at 24°C (black curves), 180°C (blue curves) and 250°C (red curves). *Inset:* *P-C* isotherm of bulk BN powder at room temperature.

The higher  $H_2$  storage of BN nanotube can be attributed to its nano-morphology, larger specific surface area and the presence of heteropolar B-N bonding<sup>48</sup>. The ionic B-N bonding may induce an extra dipole moment and hence stronger adsorption of hydrogen, since the induced dipole moment of hydrogen molecules is sensitive to local electric fields. The binding energy of  $H_2$  on the BN sheet is calculated to be about 90 meV, significantly higher than 60 meV on graphite<sup>48</sup>. The buckling structure in BN nanotubes may induce extra dipole moment so that on BNNTs the calculated binding energy of  $H_2$  can be as high as 110, 85 and 100 meV, respectively, on the top of  $B_3N_3$  hexagon center, boron atom, and nitrogen atom<sup>48</sup>. From first principles<sup>49</sup>, it is found that radial deformation on BN nanotubes can modify the  $H_2$  adsorption energy and site. For

small defects, hydrogen prefers to adsorb on the boron atom. While for large defects, hydrogen prefers to adsorb on the nitrogen atoms in the high curvature regions. Therefore, from TEM images (see page 207), it is surmised that the BN nanotubes prepared by the present method are defective and some possessed a bamboo shape, and the presence of defects enhanced its H<sub>2</sub> adsorption.

#### **7.4.3. TPD of H<sub>2</sub>-soaked BN nanotube**

The TPD measurement of H<sub>2</sub>-soaked of BN nanotube was performed in a similar fashion as TiO<sub>2</sub> nanotube. Briefly, ~100mg of BN nanotube was degassed at 400°C for 2hr before the BN nanotube was soaked in ~9MPa of H<sub>2</sub> pressure. Figure 7.13 shows the TPD of the H<sub>2</sub>-soaked BN nanotube at different ramp rate. A H<sub>2</sub> desorption peak of chemisorbed hydrogen was observed at ~180°C and the H<sub>2</sub> desorption extended to 300°C for ramp rate=10K/min using Ar as carrier gas. However, FTIR measurement of the H<sub>2</sub>-soaked BN nanotube did not observed any B-H or N-H bonds. Wang et al.<sup>50</sup> had investigated mechanically milled hexagonal BN-H system (i.e. *h*-BN powder milled in H<sub>2</sub> atmosphere for 80hr), and observed from FTIR spectra and TPD that H<sub>2</sub> was partially released from B-H (~500K) and N-H (~1000K) bonds. Since the H<sub>2</sub> desorption temperature of BN nanotube occurs at ~180°C, it is assumed that the H<sub>2</sub> molecules are adsorbed onto BNNT via a relatively weaker chemisorption process without dissociation. Thus on the basis of TPD and P-C isotherms, it is estimated that ~50% of the adsorbed hydrogen on the BN nanotube is chemisorbed.

Likewise Kissinger's method<sup>26</sup> was employed in determining the activation energy involved in the desorption of hydrogen from H<sub>2</sub>-soaked BN nanotube. The inset of Figure 7.13 shows the Kissinger's plot of BN nanotubes at different heating rates. The slope is similarly fitted to obtain the value of E<sub>a</sub>/R. Thus the activation energy for hydrogen desorption for H<sub>2</sub>-loaded BN nanotube was ~19.7kJ/mol (~204meV). This value is much higher than the heat of adsorption of carbon nanotubes (~50meV) and TiO<sub>2</sub> nanotubes (~145meV), which indicates that relatively

stronger chemisorption is involved for hydrogen-BN nanotube interactions. Therefore the H<sub>2</sub> desorption of BNNT occurs at higher temperatures.

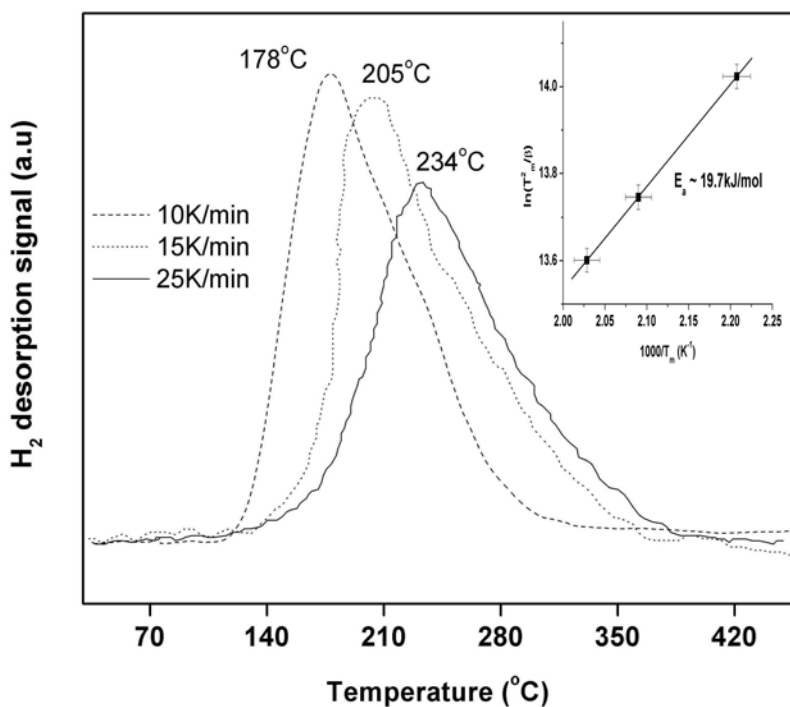


**Figure 7.13.** H<sub>2</sub> desorption process during TPD of hydrogenated BN nanotubes at indicated ramp rate, using argon as carrier. *Inset:* Kissinger's plot.

#### 7.4.4. Conclusions

In short, BN nanotube has H<sub>2</sub> storage of 2.2wt% at room temperature and 6MPa. It is estimated that ~50% of the sorption is chemisorption-like and the remaining is physisorption. Desorption of the chemisorbed H<sub>2</sub> occurs at ~180-250°C and the activation energy of H<sub>2</sub>-desorption is determined to be ~204meV. The mechano-chemical synthesis yields defective BN nanotubes, which is beneficial to H<sub>2</sub> uptakes.

### **7.5. Insights into H<sub>2</sub> physisorption – concluding remarks**

The H<sub>2</sub> storage studies of carbon nanotubes, TiO<sub>2</sub> nanotubes and BN nanotubes give useful insights into the mechanism involved, the adsorptive properties pertinent to H<sub>2</sub> uptakes and post-synthesis treatment to enhance the H<sub>2</sub> storage. The creation of micropores (0.56nm-2nm), and increment of micropore volume are noted to be beneficial to H<sub>2</sub> storage capacity. The morphology of the nanosized materials, to certain extent, seems to affect the H<sub>2</sub> storage. For example, bamboo-shaped N-doped carbon nanotubes have larger SSA and higher H<sub>2</sub> storage than the pristine concentric-shaped carbon nanotubes. This implicitly indicates that the choice of synthetic technique is important for the producing the nano-materials with the desire traits. For example, H. Gao et. al.<sup>12</sup> has used a template method to synthesize open-tipped insufficiently graphitized MWNTs, which possess many defects and subnanopores, and these defective MWNTs have a H<sub>2</sub> storage of ~6.5wt% at 10MPa and 77K. Defects are crucial for increasing the H<sub>2</sub> storage capacity. Defects can be manifested as missing bonds or atoms, kinks and buckles of the structures, nanosized cracks or crevices. Theoretical investigations indicate that H<sub>2</sub> binds more favorably at defective sites<sup>49,50</sup>. Noteworthy, wedging the interlayer distance of lamellar nano-materials to larger spacing presents a novel method to store H<sub>2</sub>. As indicated by the study of multilayered TiO<sub>2</sub> nanotubes, the non-seamless sidewalls provide easy access to H<sub>2</sub> molecules and allow formation of host-guest compound, TiO<sub>2</sub>.xH<sub>2</sub>. Hetero-atomic materials such as BN, doped carbon nanotubes and hypothetical B<sub>2</sub>O<sub>3</sub> nanosheets<sup>51</sup> bind H<sub>2</sub> molecules more strongly. The heterogeneity of the molecular surface provides more H<sub>2</sub> binding sites with different degree of strength (compare the case of BN and pure C nanotubes). Hence the above-mentioned criteria can guide us to investigate and search for new H<sub>2</sub> storage nano-materials.

Table 7.4 shows the hydrogen storage of nanomaterials, novel porous adsorbents, and hypothetical materials. The literature is chosen based on recent experimental and theoretical findings, novelty of the materials and potential H<sub>2</sub> sorption capacity that warrants further investigations. The H<sub>2</sub> storage studies of carbon nanotubes and BN nanotubes strongly suggest

that post-synthesis treatments (high temperature annealing, surface modifications and chemical treatments), presence of defects and even the choice of synthetic techniques are important factors which can affect the H<sub>2</sub> sorption capacity. The synthesis and characterizations of new nanomaterials open up new possibility of storing H<sub>2</sub> via novel mechanism. Furthermore it is interesting to study the H<sub>2</sub> sorption properties of a family of nanomaterials synthesized using dissimilar synthetic methods. As an illustration, as indicated in Table 7.4, the family of BN nanomaterials have H<sub>2</sub> uptakes of ~1-4wt% depending on the synthetic methods and post-treatment.

Metal-organic-framework<sup>21</sup> (e.g. MOF-5) and microporous polymers<sup>22</sup> are currently attracting great attentions as potential H<sub>2</sub> storage materials because the important parameters such structural framework, porosity and specific surface area can be well-controlled and tailored accordingly. A judicious choice of framework might render a MOF with selective gas sorption properties.

Hypothetical materials such as Ti-modified SWNT<sup>52</sup>, alkali-doped pillared SWNT<sup>39</sup> and Ti-modified C60<sup>53</sup> give new insights to H<sub>2</sub> sorption mechanism of SWNT and C60. These theoretical calculations serve as guide and motivations to modify existing materials for better H<sub>2</sub> storage.

**Table 7.4.** A comparison of H<sub>2</sub> uptake by various nanostructured materials.

	Ref	Sample	H <sub>2</sub> uptake / wt%	Conditions
Carbon nanotubes	7	SWNT (diameter ~ 1.85nm)	2.4-4.2	10MPa, r.t.
	8	Purified SWNT	0.01 (1.0)	Ambient pressure, r.t (77K)
	9	Purified SWNT	5.1	Atomic H, desorbed 600°C
	10	Purified MWNT	0.25	Ambient pressure, 25-400°C
	11	Alkali-doped MWNTs	~2.0	Ambient pressure, 20-500°C
	12	MWNT (template-synthesized)	1.1 (6.4)	10MPa, r.t. (77K)
	<i>a</i>	<i>SWNT &amp; MWNT samples</i>	<i>0.2-0.78 (1.5-3.7)</i>	<i>6MPa, r.t. (77K)</i>
Carbon	54	Mesoporous carbon	1.78	0.11MPa, 77K
	55	K-doped superactivated carbon	1.6	5MPa, r.t.
	56	Nickel/graphite composite	2.7	70atm, 77K
	23	Carbide-derived carbons	1.9-3.0	1atm, 77K
Boron nitride	13	BN nanofibers	2.9	9MPa, r.t
	14	BN nanotubes	1.8–2.6	10MPa, r.t
	15	Collapsed BN nanotubes	4.2	10MPa, r.t.
	16	BN nanotubes, cages, capsules	1–3	Ambient pressure, 20–300°C
	50	Milled <i>h</i> -BN powder	2.6	Ball-milled in H <sub>2</sub> atmosphere
	<i>a</i>	<i>BN nanotubes</i>	<i>2.2</i>	<i>6MPa, r.t.</i>
Inorganic nanomaterials	17	MoS <sub>2</sub> nanotubes	1.2	3MPa, r.t.
	18	TiS <sub>2</sub> nanotubes	2.5	4MPa, r.t.
	19	ZnO nanowires	0.83	3.03MPa, r.t.
	20	SiC nanorods	2.5	6MPa, r.t.
	<i>a</i>	<i>TiO<sub>2</sub> nanotubes</i>	<i>2.0</i>	<i>6MPa, r.t.</i>
Novel porous adsorbents	21	Metal-organic-framework, MOF-5	1.0 (4.5)	20bar, r.t. (78K)
	22	Microporous polymers	1.44-1.70	10bar, 77K
	24	Prussian blue analogues	1.4-1.8	890Torr, 77K
	25	Nanoporous nickel phosphate	1.26	600Torr, 77K
Hypothetical materials	52	Ti-doped SWNT	2.85-7.50	Dissociative & molecular adsorption
	39	Alkali-doped pillared SWNT	6.0	50bars, r.t.
	53	Ti-clustered C60	8.0	Dissociative & molecular adsorption

<sup>a</sup> this thesis

r.t. denotes room temperature

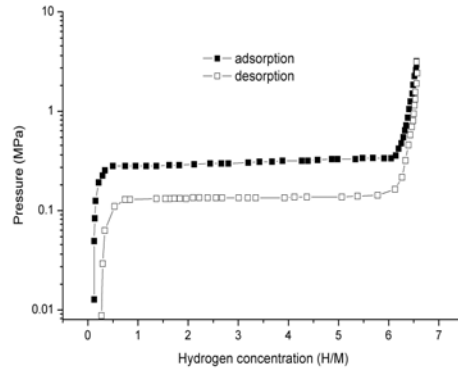
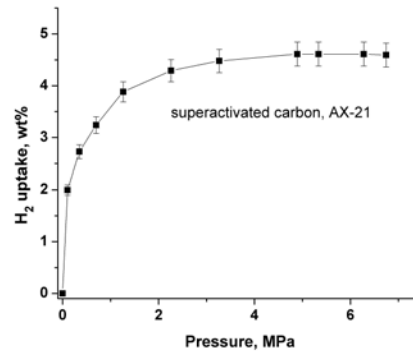
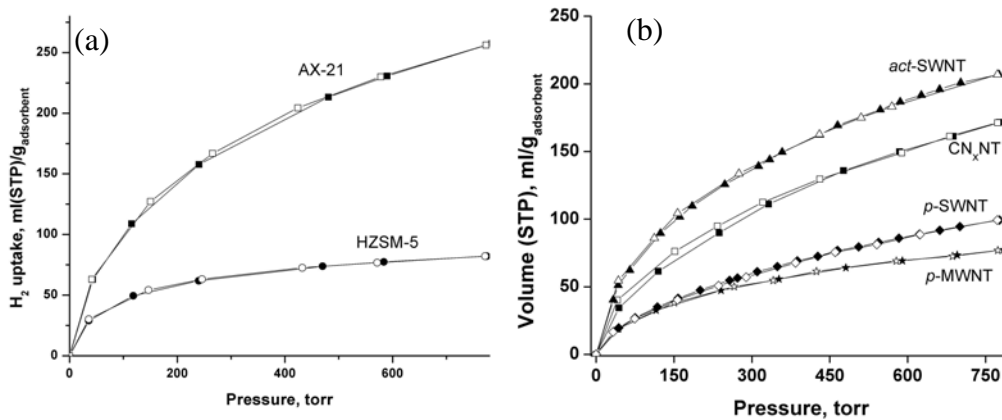


## References

- [1] L. Schlappbach, A. Zuttel, *Nature (London)* 414, 353 (2001).
- [2] R.F. Service, *Science* 305, 958 (2004).
- [3] L. Zhou, *Renew. Sust. Energ. Rev.* 9, 395 (2005).
- [4] S. Rakass, H. Oudghiri-Hassani, P. Rowntree, N. Abatzoglou, *J. Power Sources* 158, 485 (2006).
- [5] (a) A.T. Ashcroft, A.K. Cheetham, M. L. H. Green, P.D.F. Vernon, *Nature* 352, 225 (1991).  
(b) J.S.J. Hargreaves, G.J. Hutchings, R.W. Joyner, *Nature*, 348, 428 (1990).
- [6] J.A. Turner, *Science* 305, 972 (2004).
- [7] C. Liu, Y.Y. Fan, M. Liu, H.T. Cong, H.M. Cheng, M.S. Dresselhaus, *Science* 286, 1127 (1999).
- [8] A. Anson, M.A. Callejas, A.M. Benito, W.K. Maser, M.T. Izquierdo, B. Rubio, J. Jagiello, M. Thommes, J.B. Parra, M.T. Martinez, *Carbon* 42, 1243 (2004).
- [9] A. Nikitin, H. Ogasawara, D. Mann, R. Dencke, Z. Zhang, H. Dai, K. Cho, A. Nilsson, *Phys. Rev. Lett.* 95, 225507 (2005).
- [10] X.B. Wu, P. Chen, J. Lin, K.L. Tan, *Intl. J. of Hydrogen Energy*, 25, 261 (2000).
- [11] R.T. Yang, *Carbon* 38, 623 (2000).
- [12] H. Gao, X.B. Wu, J.T. Li, G.T. Wu, J.Y. Lin, K. Wu, S.D. Xu, *Appl. Phys. Lett.* 83, 3389 (2003)
- [13] R. Ma, Y. Bando, T. Sato, D. Golberg, H. Zhu, C. Xu, D. Wu, *Appl. Phys. Lett.* 81, 5225 (2002).
- [14] R. Ma, Y. Bando, H. Zhu, T. Sato, C. Xu, D. Wu, *J. Am. Chem. Soc.* 124, 7672 (2002).
- [15] C. Tang, Y. Bando, X. Ding, S. Qi, D. Golberg, *J. Am. Chem. Soc.* 124, 14550 (2002).
- [16] T. Oku, M. Kuno, I. Narita, *J. Phys. Chem. Solids.* 65, 549 (2004).
- [17] J. Chen, Z. L. Li, J. Tao, *J. Alloys Compd.* 413 (2003) 356.
- [18] J. Chen, S. L. Li, Z. L. Tao, Y. T. Shen, C. X. Cui, *J. Am. Chem. Soc.* 125 (2003) 5284.
- [19] Q. Wan, C. L. Lin, X. B. Yu, T. H. Wang, *Appl. Phys. Lett.* 84, 124 (2004).
- [20] V.G. Pol, S.V. Pol, A. Gedanken, S.H. Lim, Z. Zhong, J. Lin, *J. Phys. Chem. B*, 110, 11237 (2006).
- [21] N.L. Rosi, J. Eckert, M. Eddaoudi, D.T. Vodak, J. Kim, M. Keefe, O.M. Yaghi, *Science* 300, 1127 (2003).
- [22] N.B. McKeown, B. Gahnem, K.J. Msayib, P.M. Budd, C.E. Tattershall, K. Mahmood, S. Tan, D. Book, H.W. Langmi, A. Walton, *Angew. Chem. Int. Ed.* 45, 1804 (2006).

- [23] Y. Gogotsi, R.K. Dash, G. Yushin, T. Yildirim, G. Laudisio, J.E. Fischer, *J. Am. Chem. Soc.* 127, 16006 (2005).
- [24] S.S. Kaye, J.R. Long, *J. Am. Chem. Soc.* 127, 6506 (2005).
- [25] P.M. Forster, J. Eckert, J.S. Chang, S.E. Park, G. Ferey, A.K. Cheetham, *J. Am. Chem. Soc.* 125, 1309 (2003).
- [26] H.E. Kissinger, *J. Res. Nat. Bur. Stand.* 57, 217 (1956); H.E. Kissinger, *Anal. Chem.* 29, 1702 (1957).
- [27] N. Texier-Mandoki, J. Dentzer, T. Piqero, S. Saadallah, P. David, C. Vix-Guterl, *Carbon* 42, 2735 (2004).
- [28] P. Benard, R. Chahine, *Langmuir* 17, 1950 (2001).
- [29] M.G. Nijkamp, J.E.M.J. Raaymakers, A.J. van Dillen, K.P. de Jong, *Appl. Phys. A.* 72, 619 (2001).
- [30] R. Strobel, L. Jorissen, T. Schliermann, V. Trapp, W. Schutz, K. Bohmhammel, G. Wolf, J. Garce, *J. Power Sources* 84, 221 (1999).
- [31] Vidali G, Ihm G, Kim H Y, Cole M W 1991 *Surf. Sci. Rep.* 12 133
- [32] S.H. Jhi, Y. K. Kwon, K. Bradley, J.C.P. Gabriel, *Solid State Commun.* 129, 769 (2004).
- [33] K. Kadono, H. Kajiura, M. Shiraishi, *Appl. Phys. Lett.* 83, 3392 (2003).
- [34] G. Horvath, K. Kawazoe, *J. Chem. Eng. Jpn* 16, 470 (1983).
- [35] I. Langmuir, *J. Am. Chem. Soc.* 59, 2400 (1937).
- [36] L. Zhou, Y.P. Zhou, Y. Sun, *Int. J. Hydrogen Energy* 29, 319 (2004).
- [37] W. Gopel, G. Rucker, R. Feierabend, *Phys. Rev. B.* 28, 3427 (1983).
- [38] *Smithsonian Physical Tables*, 9<sup>th</sup> ed. edited by W. E. Forsythe ~Smithsonian Institute, Washington, 1964.
- [39] W.Q. Deng, X. Xu, W.A. Goddard, *Phys. Rev. Lett.* 92, 66103-1 (2004).
- [40] A. Kleinhammes, S.H. Mao, X.J. Yang, X.P. Tang, H. Shimoda, P. Lu, O. Zhou, Y. Wu, *Phys. Rev. B.* 68, 075418 (2003).
- [41] H.G. Schimmel, J.K. Gordon, M.G. Nijkamp, C.T. Visser, K.P. de Jong, F.M. Mulder, *Chem. Eur. J.* 9, 4764 (2003)
- [42] K.S. Han, H.S. Kim, M.S. Song, M.S. Park, S.S. Han, J.Y. Lee, J.K. Kang, *Appl. Phys. Lett.* 86, 263105 (2005).
- [43] S.H. Lim, J. Luo, Z. Zhong, J. Lin, *Inorganic Chem.* 44, 4124 (2005).
- [44] W. Gopel, G. Rucker, R. Feierabend, *Phys. Rev. B.* 28, 3427 (1983).
- [45] B.D. Yao, Y.F. Chan, X.Y. Zhang, W.F. Zhang, Z.Y. Yang, N. Wang, N. Appl. Phys. Lett. 82, 281 (2003).

- [46] D.V. Bavykin, A.A. Lapkin, P.K. Plucinski, J.M. Friedrich, F.C. Walsh, *J. Phys. Chem. B.* 109, 19422 (2005).
- [47] H. Kawano, Y. Zhu, A. Tanaka, S. Sugimoto, *Thermochim. Acta* 371, 155 (2001).
- [48] S. Jhi, Y. Kwon, *Phys. Rev. B.* 69, 245407 (2004).
- [49] X. Wu, J. Yang, J. G. Hou, Q. Zhu, *Phys. Rev. B.* 69, 153411 (2004).
- [50] P. Wang, S. Orimo, H. Fujii, *Appl. Phys. A.* 78, 1235 (2004).
- [51] Y. Xia, J.Z. Zhu, M. Zhao, F. Li, B. Huang, Y. Ji, X. Liu, Z. Tan, C. Song, Y. Yin, *Phys. Rev. B.* 71, 075412 (2005).
- [52] S. Jhi, Y. Kwon, *Phys. Rev. B.* 71, 035408 (2005).
- [53] T. Yildirim, S. Ciraci, *Phys. Rev. Lett* 94, 175501 (2005).
- [54] O. Sun, Q. Wang, P. Jena, Y. Kawazoe, *J. Am. Chem. Soc.* 127, 14582 (2005).
- [55] J. Peng, J.E. Hampsey, Z. Wu, Q. Hu, Y. Lu, *Appl. Phys. Lett.* 85, 4887 (2004).
- [56] Y. Kojima, N. Suzuki, *Appl. Phys. Lett.* 84, 4113 (2004).
- [57] Z.Y. Zhong, Z.T. Xiong, L.F. Sun, J.Z. Luo, P. Chen, X. Wu, J. Lin, K.L. Tan, *J. Phys. Chem. B.* 106, 9507 (2002).

**Appendix A7.1****Figure A7.1.** P-C isotherm of LaNi<sub>5</sub>H<sub>6</sub> alloy at room temperature**Figure A7.2.** H<sub>2</sub> uptake of super-activated AX-21 carbon at 77K using the home-made GRC.**Figure A7.3.** H<sub>2</sub> uptakes of (a) AX-21 and HZSM-5, and (b) various carbon nanotubes at 77K and pressures up to 770torr. The isotherms are completely reversible. *Open symbols (adsorption), and filled symbols (desorption).*

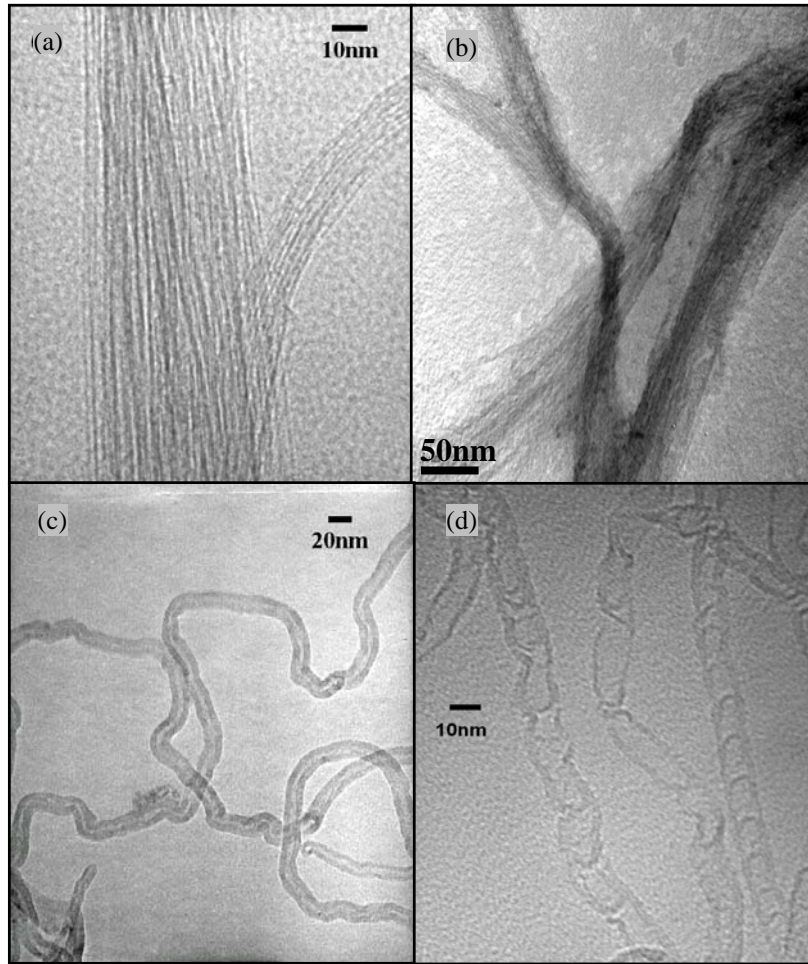


**Figure A7.4.** Transmission electron micrographs of (a) *p*-SWNT, (b) *act*-SWNT, (c) *p*-MWNT, and (d) CN<sub>x</sub>NT.

## **Appendix A7.2. Synthesis and characterizations of boron nitride nanotube**

### *Introduction*

Boron nitride nanotube is isoelectronic and isostructural to carbon nanotube. Unlike carbon nanotube which can be metallic or semiconducting, BNNT is semiconducting with a bandgap of  $\sim 5\text{eV}$  and that the gap is nearly independent of the tube diameter, chirality and the number of BN layers; a phenomenon that has been attributed to the ionic origin of the BN bonding. The uniform semiconducting property of BNNT implies that it has great advantages for electronic applications. BN nanotube has been successfully synthesized using similar techniques applied for the growth of CNT, such as arc-discharge, laser ablation and chemical vapor deposition (CVD)<sup>1-3</sup>. However most of the methods reported may require sophisticated equipment, usage of harmful precursors such as borazine and ammonia, and high synthesis temperatures  $\geq 1400^\circ\text{C}$ . In light of its interesting electronic properties and potential applications of BNNT, a simple and scalable synthesis method will be desirable. In this appendix A7.2, boron nitride nanotube (BNNT) was synthesized using a catalyzed mechano-chemical reaction. The BNNT was characterized with electron microscopy, x-ray diffraction (XRD), x-ray photoelectron spectroscopy (XPS), Fourier Transform infrared (FTIR) and Raman spectroscopy.

### **A7.2.1. Synthesis of BNNT: Catalyzed mechano-chemical process**

#### *Preparation of nickel-boron catalyst*

The nickel-boron catalyst was prepared by ball-milling nickel boride ( $\text{NiB}_x$ ) and boron powders. The nickel boride was prepared by the reduction of nickel chloride with potassium tetrahydridoborate ( $\text{KBH}_4$ ). 300mM of  $\text{KBH}_4$  aqueous solution and 50mM of  $\text{NiCl}_2$  solution ( $\text{NiCl}_2 \cdot 6\text{H}_2\text{O}$  was dissolved in methanol/water, 1:1 volume ratio, solution) were prepared separately. 200ml of  $\text{KBH}_4$  solution was added dropwise to 400ml of  $\text{NiCl}_2$  solution under vigorous stirring. The resulting  $\text{NiB}_x$  powder were filtered and rinsed with distilled water. The

molar ratio of boron to  $\text{NiB}_x$  catalyst was 4:1 respectively, and the mixture was ball-milled in air atmosphere for 48 hours at 180rpm (Planetary ballmill, Fristsch Pulverisette 5). The ball-milled Ni-B powder was loaded into a horizontal quartz tube reactor flowing with a mixture of  $\text{N}_2:\text{H}_2$  gases with their flow rates at 15 vs 35 ml/min respectively. The continuous supply of  $\text{H}_2$  is noted to be crucial for the efficient growth of the BN nanotube. The reactor was heated up at  $7.5^\circ\text{C}/\text{min}$  to a maximum temperature of  $1025^\circ\text{C}$  and held for 2 hour. The as-prepared BNNT was sonicated in 8M HCl acid to remove the residual Ni particles. The acid-treated BNNT was rinsed with distilled water and dried at  $80^\circ\text{C}$  overnight.

#### **A7.2.2. Characterizations of boron nitride nanotube**

##### *Electron microscopy*

Figure A7.5 shows the electron micrographs of the BN nanotubes. The diameters of BN nanotubes ranged from 20-50nm, while the lengths were widely distributed from  $>250\text{nm}$  to a few micrometers. The BN nanotubes have non-uniform and irregular morphology. Ni nanoparticles encased at the tip of the BNNT can be observed from the TEM micrographs. The short lengths of BNNT might be due to the relatively lower synthetic temperature used ( $1150^\circ\text{C}$  is the safety limit of the tube furnace). The BNNT has defective exterior and some of the nanotubes have a bamboo-shaped core. Defective BNNT is an attractive nano-material for hydrogen storage, which has been discussed in Chapter 7, page 191.

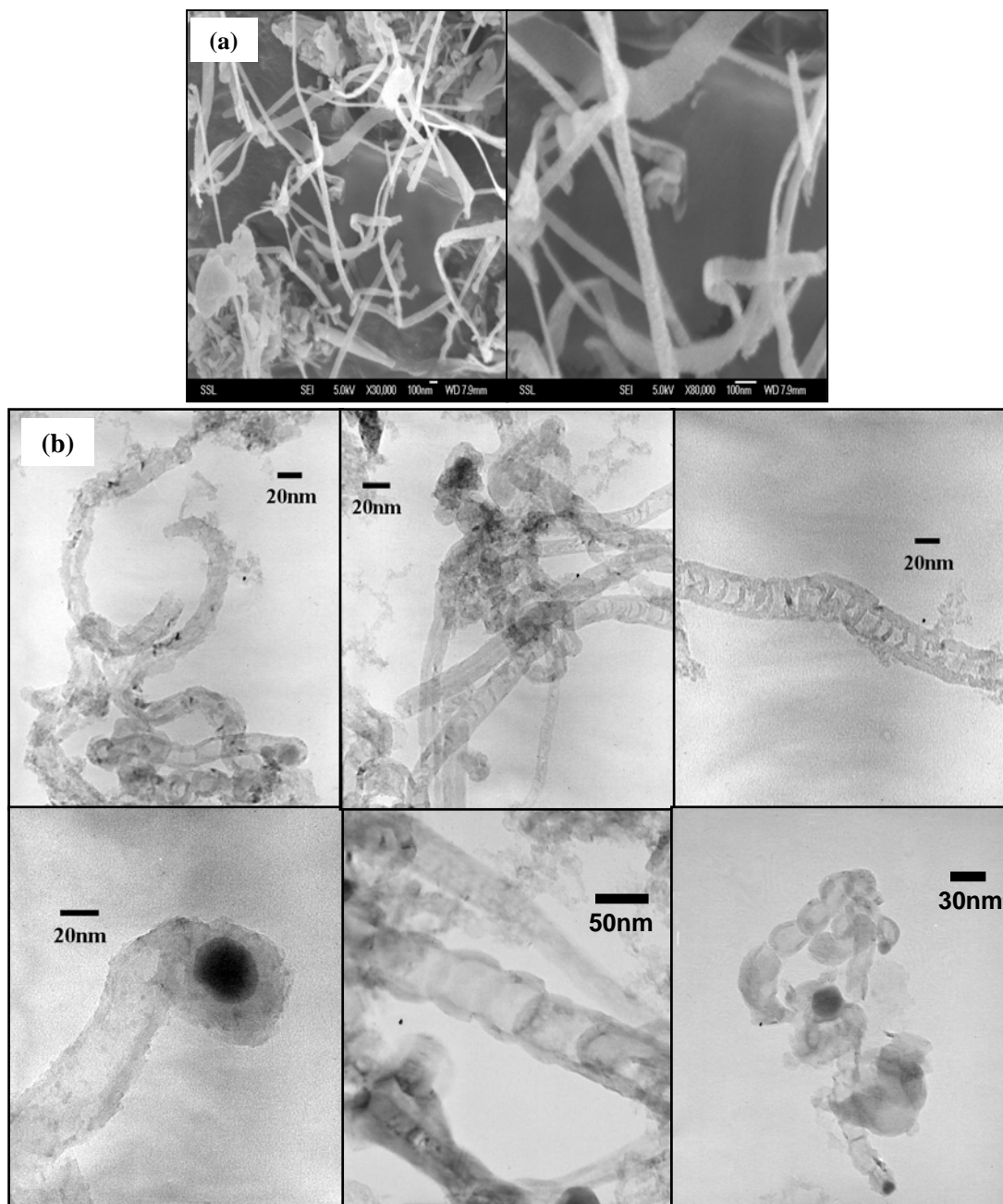


**Figure A7.5.** (a) SEM and (b) TEM images of boron nitride nanotubes synthesized from a ball-milled nickel-boron catalyst and heated in nitrogen-hydrogen gas mixture at 1025°C.

#### *Powder x-ray diffraction (XRD)*

The typical XRD patterns of the BN nanotube and bulk BN are shown in Figure A7.6. All reflection peaks can be indexed as hexagonal-phase boron nitride with lattice constants of  $a =$



2.48Å and  $c = 6.79\text{Å}$ , which are consistent with literature (JPDCS, No. 45-895,  $a = 2.5044\text{Å}$  and  $c = 6.6562\text{Å}$ ). The (002) peak indicates the presence of well-stacked layered structures in hexagonal BN. Furthermore the (002) peak of BNNT is slightly shifted to lower angle as compared to bulk  $h$ -BN crystal, indicating a slight expansion of the interplanar spacing (from 3.33 to 3.40Å) in nanometric tube-like morphology. The broadening of the (002) peak is due to the reduced domain size in the direction that is perpendicular to the (00 $l$ ) plane. The (00 $l$ ) reflections are associated with the orderly stacking along the  $c$ -axis, while the ( $hk0$ ) reflections indicate the ordering in the basal  $ab$  planes.

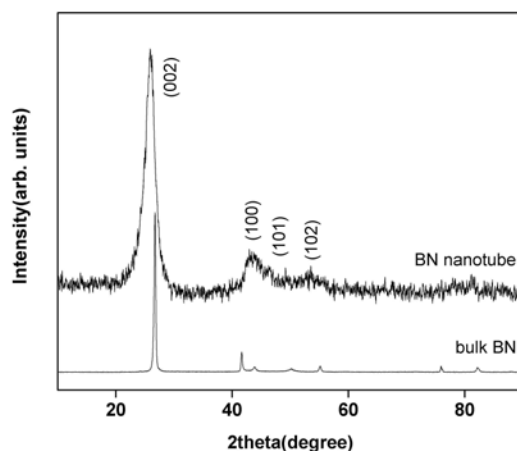


**Figure A7.6.** XRD patterns of BN nanotube and bulk BN powders.

#### *FTIR and Raman spectroscopy*

The FTIR spectrum of BN nanotube exhibits two strong characteristic peaks located at  $\sim 1380$  and  $\sim 805\text{ cm}^{-1}$  (Figure A7.7a). The former is the B-N vibration along the axis of the nanotubes, while the latter is the B-N vibration perpendicular to the axis<sup>4</sup>. Computational simulations<sup>5</sup> and LEED study<sup>6</sup> have shown the substantial buckling of B-N bonds in the bulk  $sp^2$ -based layered structure. Outward displacement of nitrogen atoms has been predicted and experimentally observed. Due to the curvature of the BN nanotube this buckling becomes more

evident. This structural buckling results in some  $sp^3$  admixture in  $sp^2$  BN bonding so that the softening of the FTIR vibration modes can be observed. Indeed in comparison with bulk  $h$ -BN, the B-N vibration perpendicular to the axis of the BNNT is shifted to lower frequency (from 811 to  $805\text{cm}^{-1}$ ) by  $6\text{cm}^{-1}$ , indicating the buckled structure in BNNT.

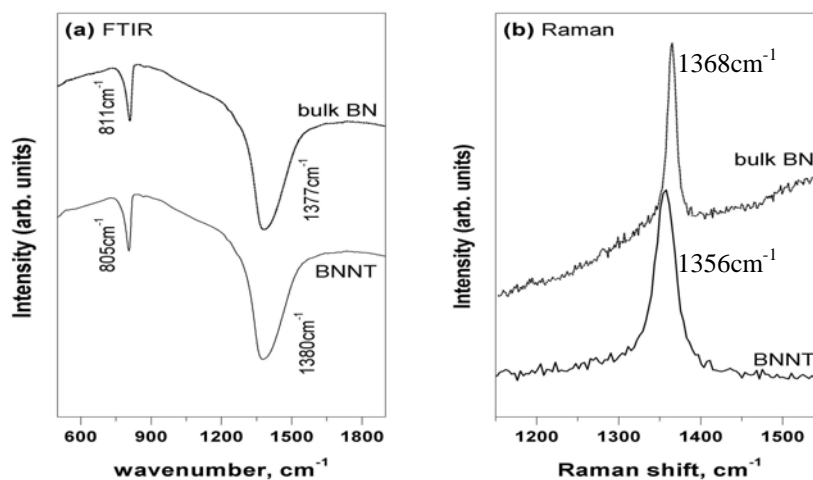


**Figure A7.7.** (a) FTIR and (b) Raman spectra of the purified BNNT

The Raman scattering spectrum of BN nanotube exhibits only one Raman active mode,  $E_{2g}$ , in the range of  $1100\text{-}1600\text{cm}^{-1}$  (Fig A7.7b). The  $E_{2g}$  mode of boron nitride is due to the in-plane atomic displacement of B and N atoms against each other. This peak is located at  $1356\text{cm}^{-1}$  for the BN nanotube and the full-width at half maximum (FWHM) is  $\sim 32\text{cm}^{-1}$ . The  $E_{2g}$  Raman peak of BN nanotube, compared to bulk BN, was broader and downshifted by  $12\text{cm}^{-1}$ . This is attributed to the buckled structure of BN nanotubes.

#### *X-ray photoelectron spectroscopy (XPS)*

XPS was employed to determine the chemical composition of the BN nanotube (see Figure A7.8). The elemental composition of the BNNT was determined as followed:

$$\%X = (A_x/S_x) / \sum_{i=1}^N (A_i/S_i) \quad [\text{A7.1}]$$

where X is the element,  $A_x$  the area under the peak of element X in the spectrum, and  $S_x$  is the sensitivity factor. The sensitivity factor of nitrogen and boron are 0.42 and 0.13 respectively. The average atomic ratio of B:N is around 1.04:1 on the basis of quantification of the  $B1s$  and  $N1s$  peaks. The slightly higher B content might be due to residual boron. The  $B1s$  peak and  $N1s$  peaks are located at 190.5eV and 398.3eV, respectively, which are in good agreement with the values of bulk BN. The  $O1s$  peak might be due to the adsorption of  $CO_2$ ,  $O_2$  and  $H_2O$  impurities onto the surface of the sample.

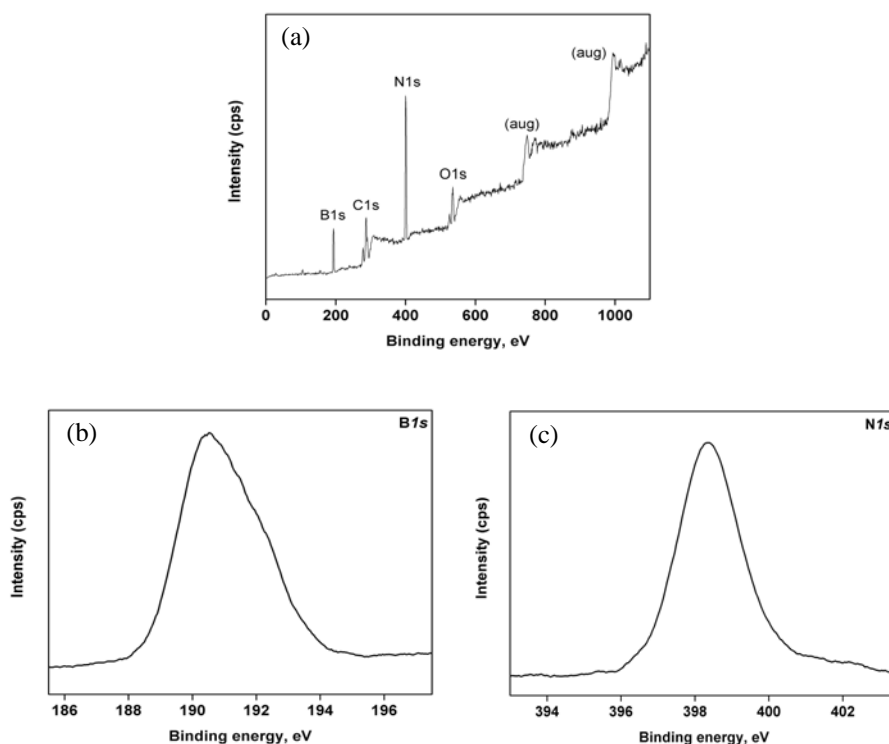


**Figure A7.8.** XPS spectra of boron nitride nanotubes: (a) survey scan, (b) core-level  $B1s$  and (c)  $N1s$  scans.

### A7.2.3. Formation mechanism of BNNT via mechano-chemical process

Ammonia gas is not essential since it is reported that  $NH_3$  decomposes into  $N_2$  and  $H_2$  gases at  $>550^\circ C$ <sup>7</sup>. It is inferred that extensive ball-milling of boron and  $NiB_x$  powders resulted in a nanometric boron-nickel mixture, which is essential for the synthesis of BN nanotubes. It is

noted that H<sub>2</sub> gas is crucial to the efficient growth of BN nanotubes in terms of the activation of the metallic Ni, which could absorb nitrogen into the B-Ni alloy. At 1025°C the formation of Ni-BN eutectics yields anisotropic growth of BN nanotubes. However the formation mechanism of the present BN nanotubes is unlikely explained by VSL model, mainly due to the transport of boron atoms into the NiB<sub>x</sub> catalyst. The synthetic temperature of 1025°C is too low to melt boron and generate boron-containing vapor.

Chen et al.<sup>2</sup> has also employed a similar mechano-thermal technique to synthesize BN nanotubes. The nitrogenated boron powder was achieved via ball-milling in ammonia atmosphere, and heating the resulting powders at ≥1200°C in N<sub>2</sub> gas to yield multi-walled boron nitride nanotubes. Chen et al.<sup>2</sup> has proposed a solid-liquid-solid (SLS) mechanism for the formation of BN nanotube. However it should be noted that the extensive ball-milling process has introduced metallic impurities such as Fe nanoparticles into the milled boron matrix; Fe nanoparticles can be seen encased at the BN nanotube tips in Chen et al. report<sup>2</sup>. In addition, to the best of my knowledge, there is no report that boron powder reacts directly with nitrogen gas to form BN without the presence of a catalytic impurity. Due to the introduction of Fe nanoparticles in the milling process, B-N layers are able to germinate anisotropically out of the nitrated boron matrix to yield nanotubes.

However, in my synthesis of BN nanotube, the boron-NiB<sub>x</sub> mixture was not nitrogenated during the ballmill process. The nitrogenation process takes place when the B-NiB<sub>x</sub> catalyst was heated at 1025°C under nitrogen-hydrogen flow. The nitrogen atom and boron atoms (from the milled boron) diffuse into the Ni catalyst and precipitate out BN sheets unidirectionally. Therefore the likely formation mechanism of the present BN nanotube using a catalysed mechano-chemical synthesis is an intermediate of SLS and VLS process.

### **Appendix A7.3 Synthesis and characterizations of TiO<sub>2</sub>-derived nanotubes**

#### *Introduction*

The preparation of one-dimensional (1D) TiO<sub>2</sub>-related materials (nanotubes, nanowires, nanobelts and nanorods) is of great importance because of their unique morphologies, properties and promising applications. However there are disagreements in literature regarding the chemical structure of the TiO<sub>2</sub>-derived nanotubes synthesized via a hydrothermal process. Therefore in this section A7.3, the disputed chemical structure of these TiO<sub>2</sub>-derived nanotubes will be discussed.

Kasuga et al.<sup>8</sup> first reported the observation of TiO<sub>2</sub>-derived multi-walled nanotubes (NT), which were synthesized via a hydrothermal process between bulk TiO<sub>2</sub> powder and 10M NaOH solution at 120°C. Yao and Wang et al.<sup>9,10</sup> repeated the experiment and concluded that the observed multi-walled nanotubes were TiO<sub>2</sub>. In addition, based on Ti L-edge EELS study of various types of titanium oxides, Akita et al.<sup>11</sup> likewise suggested that the TiO<sub>2</sub>-derived nanotubes had coordinated bonds the same as TiO<sub>2</sub>, in which 6 oxygen atoms surround the Ti atoms. They proposed that when bulk TiO<sub>2</sub> was treated with 10M NaOH at 120°C, some of the Ti-O-Ti bonds were broken, and Ti-O-Na and Ti-OH bonds are formed. Subsequent treatment with diluted HCl and distilled water removed both Ti-O-Na and Ti-OH bonds, and formed new Ti-O-Ti bonds. At this stage, the metastable anatase phase rolled up to form the tubular structures by the soft chemical reaction.

On the other hands, other research groups also repeated the synthesis but reported that the formation mechanism are better described by layered titanate. Both H-form layered titanate (H<sub>2</sub>Ti<sub>3</sub>O<sub>7</sub>·nH<sub>2</sub>O n ≈ 0.5–3, H<sub>2</sub>Ti<sub>4</sub>O<sub>9</sub>·H<sub>2</sub>O, H<sub>x</sub>Ti<sub>2-x/4</sub>□<sub>x/4</sub>O<sub>4</sub> x ≈ 0.7, □: vacancy and H<sub>2</sub>Ti<sub>2</sub>O<sub>4</sub>(OH)<sub>2</sub>)<sup>12-18</sup> and salt-form layered titanate (Na<sub>x</sub>H<sub>2-x</sub>Ti<sub>3</sub>O<sub>7</sub> x ≈ 0.5 – 0.75)<sup>19,20</sup> nanotubes had been suggested to be the final products. This proposed formation mechanism of TiO<sub>2</sub>-derived nanotube from a layered titanate is very similar to other inorganic nanotubes synthesized from lamellar precursors<sup>21</sup>.

Nonetheless, it should be noted that all the above-mentioned final products of TiO<sub>2</sub> hydrothermal synthesis, titania and titanate nanotubes, are important 1D TiO<sub>2</sub>-related materials worthy of studying. For example, titania nanostructured materials can be applied as photocatalysts for the purification of air and aqueous pollutions<sup>22</sup>, while trititanate (H<sub>2</sub>Ti<sub>3</sub>O<sub>7</sub>) nanotube would be a potential proton-conducting fuel cell electrolyte and Li-battery electrode<sup>23</sup>. Likewise TiO<sub>2</sub>(B) (a polymorph of TiO<sub>2</sub>) nanotube is a promising Li intercalation host material because of its low density and tunnel structures<sup>24-26</sup>. Ion exchangeable sodium titanate (Na<sub>x</sub>H<sub>2-x</sub>Ti<sub>3</sub>O<sub>7</sub>) nanotube can be applied as a novel 1D cation exchanger and sorbent for the control and management of radioactive wastes<sup>27</sup>.

It would be more useful if one could properly control the types of TiO<sub>2</sub>-related nanostructured materials as the final products. A careful study on the synthetic conditions of TiO<sub>2</sub>-derived nanomaterials was conducted to address the conflicting issues mentioned above. Post-synthesis treatments such as 0.1M HCl acid washing and air annealing are found to be key experimental parameters. It is demonstrated that under appropriate conditions various types of TiO<sub>2</sub>-derived nanostructured materials including trititanate, sodium titanate, TiO<sub>2</sub>(B) nanotubes, anatase nanotubes and anatase nanowires / nanorods could be selectively synthesized.

#### **A7.3.1. Synthetic procedure: Hydrothermal method**

A systematic hydrothermal process was carried out throughout the whole experiments. Typically 1g of commercially available bulk TiO<sub>2</sub> (Merck, anatase) were refluxed in 100ml of 10M NaOH. The temperature and reaction time were fixed at 120°C and 48hr respectively. All acid washing process was carried out with 0.1M HCl at room temperature. The TiO<sub>2</sub>-derived nanotube was recovered by centrifugation. One set of the TiO<sub>2</sub>-derived nanotube was washed thoroughly with distilled water only. Another set of the TiO<sub>2</sub>-derived nanotube was washed with copious amount of 0.1M HCl acid (2L), pickled in fresh 500ml 0.1M HCl overnight and followed by washing with distilled water. The acid washing was considered as a proton exchange process

in our experiments. All the samples were air dried overnight at 80°C. Subsequent air annealing was carried out in a well-ventilated furnace. Figure A7.9 summarizes the synthetic routes and post-synthesis treatments of TiO<sub>2</sub>-derived nanomaterials.

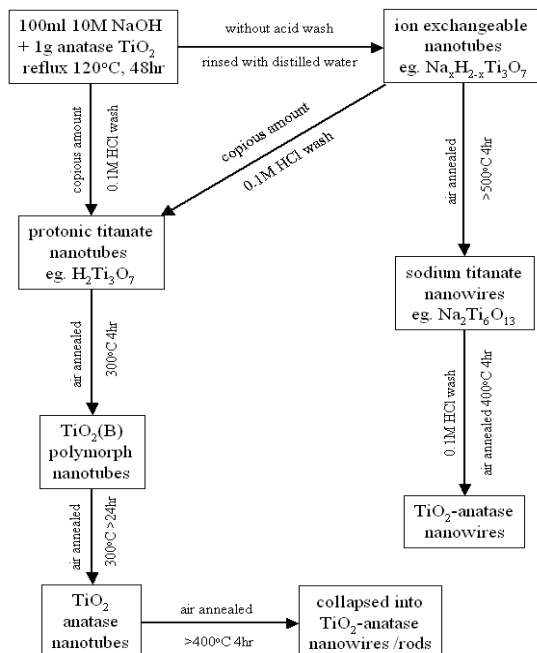


**Figure. A7.9.** Synthetic pathways and post-synthesis treatments of TiO<sub>2</sub>-derived nanomaterials.

### A7.3.2. Characterizations of TiO<sub>2</sub>-derived nanotubes.

#### *Electron microscopy*

From electron microscopy (see Figure A7.10 and Figure A7.11), TiO<sub>2</sub>-derived multi-walled nanotubes were obtained from the hydrothermal process with and without acid wash. This implied that tubular structures were already formed during the extended hydrothermal process. Based on our experimental studies (vide infra), we had labeled the nanotubes obtained without acid washing as ion exchangeable sodium titanate nanotubes, eg. Na<sub>x</sub>H<sub>2-x</sub>Ti<sub>3</sub>O<sub>7</sub> where  $x \approx 0.5-0.75$ , as suggested by Sun and Yoshida et al.<sup>19,20</sup> On the other hands, the TiO<sub>2</sub>-derived nanotubes which were washed with copious amount of 0.1M HCl acid can be better labeled as layered protonic titanate, eg. trititanate nanotubes (H<sub>2</sub>Ti<sub>3</sub>O<sub>7</sub>·nH<sub>2</sub>O) as suggested by Suzuki et al<sup>13</sup>.

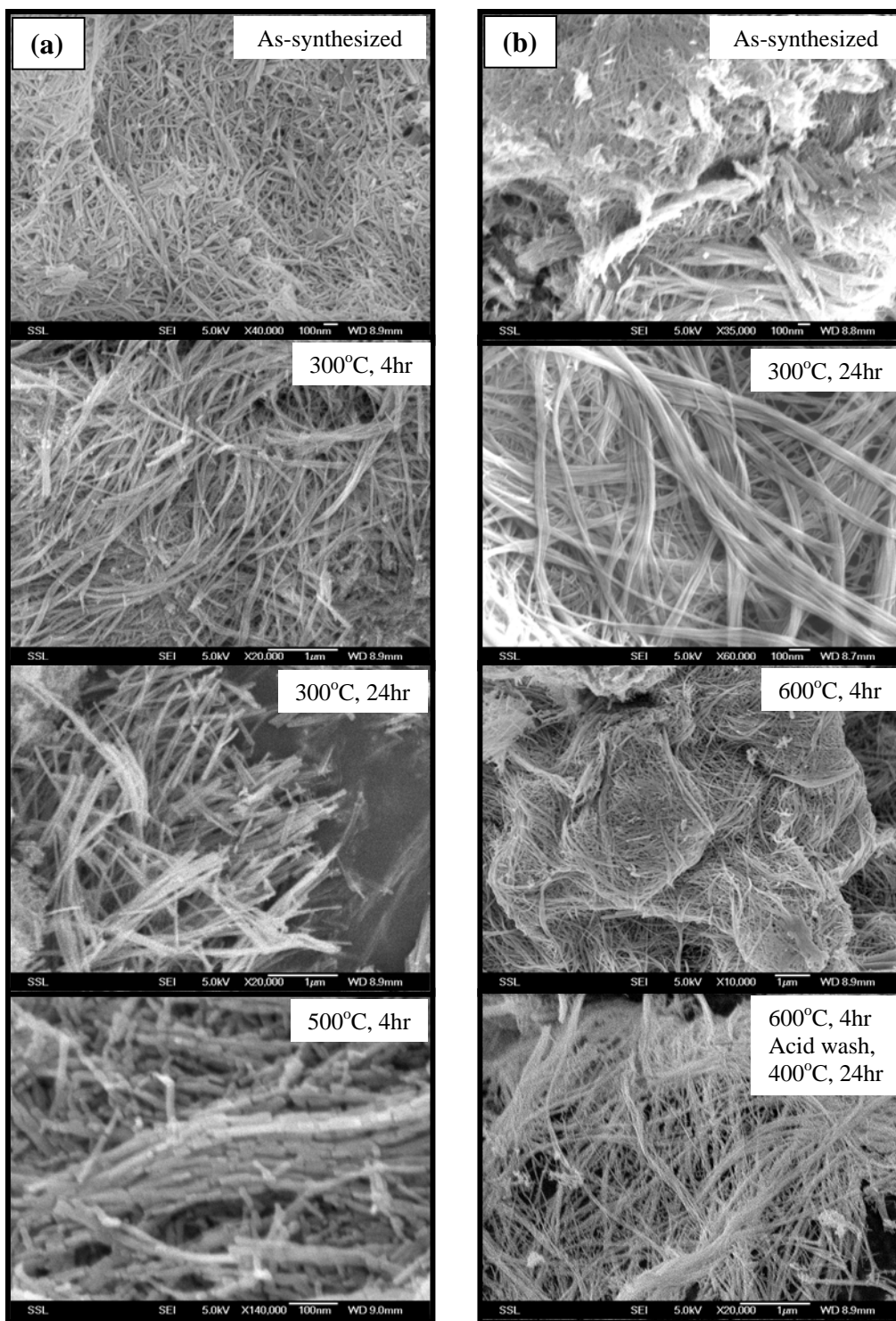


**Figure A7.10.** SEM images of TiO<sub>2</sub>-derived nanotubes (column a) with acid wash and (column b) without acid wash. *Post-synthesis treatments were indicated on the images.*



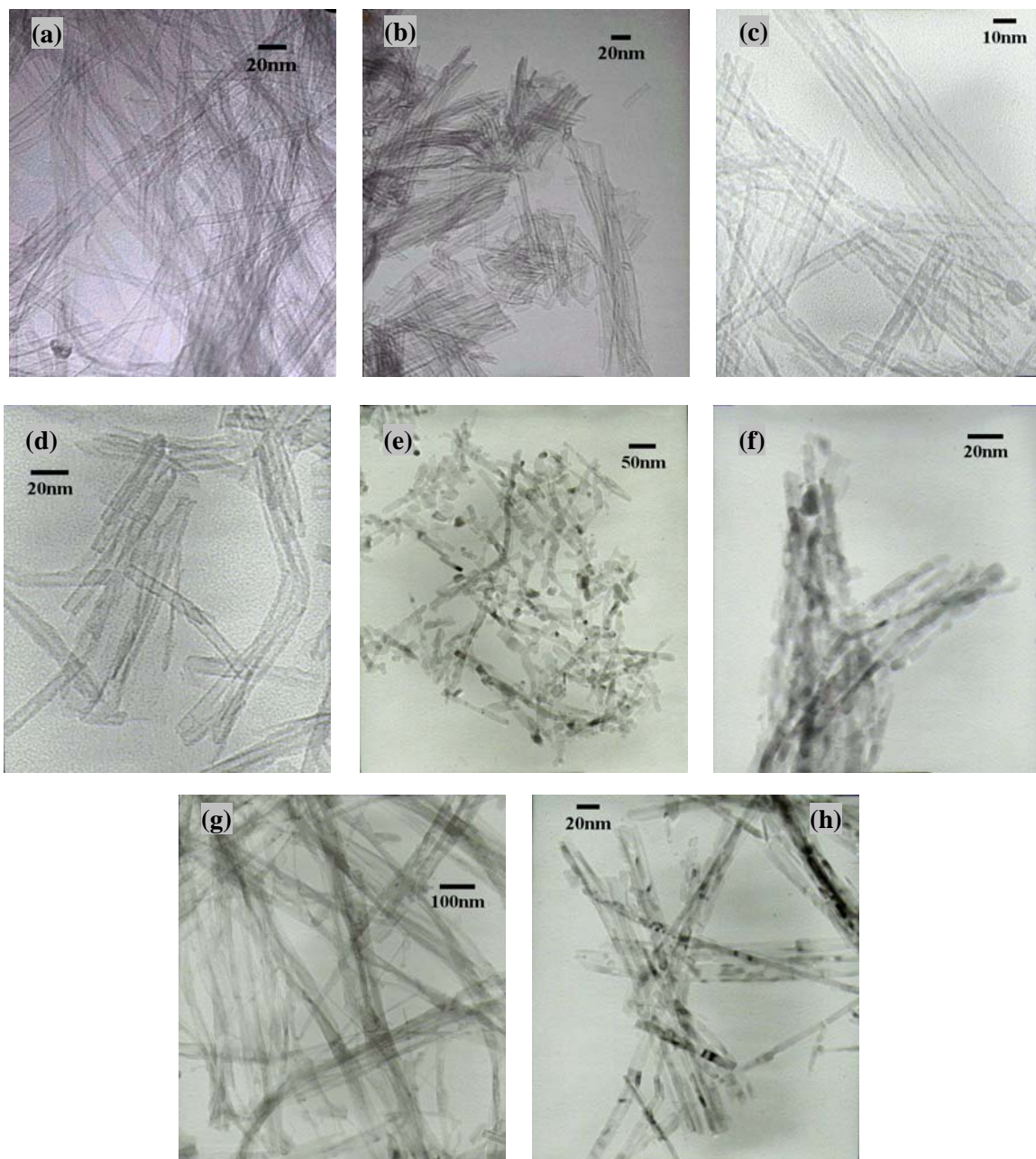


**Figure. A7.11.** TEM images of (a) as-synthesized trititanate nanotubes, (b)  $\text{Na}_x\text{H}_{2-x}\text{Ti}_3\text{O}_7$  nanotubes annealed at 300°C for 32hr, (c)  $\text{TiO}_2(\text{B})$  nanotubes, (d)  $\text{TiO}_2$ -anatase nanotubes, (e-f) collapsed  $\text{TiO}_2$ -anatase nanowires / nanorods after calcination at 500°C for 4hr, (g) sodium titanate nanowires and (h)  $\text{TiO}_2$ -anatase nanowires after proton exchanged and calcination of  $\text{Na}_2\text{Ti}_9\text{O}_{19}$  nanotubes at 400°C.

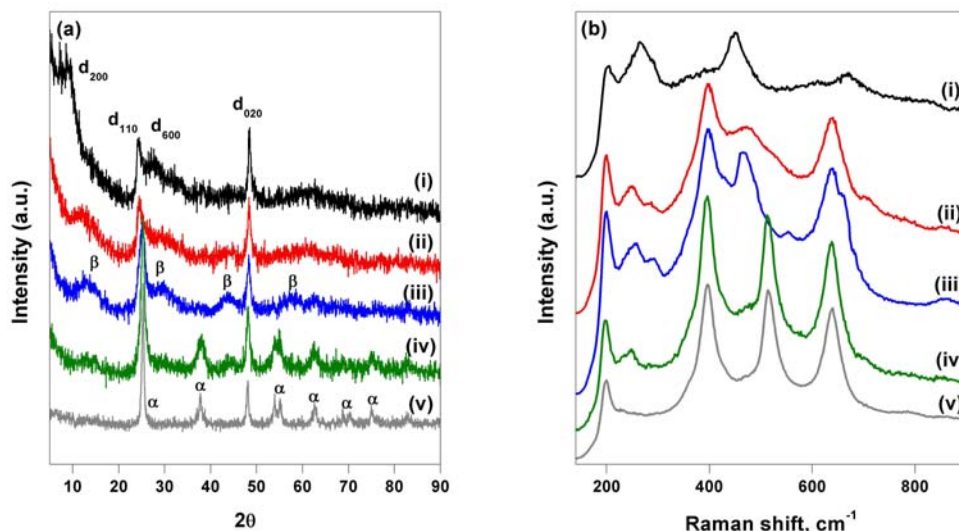


**Figure. A7.12.** (a) XRD patterns and (b) Raman spectra of (i) trititanate nanotubes with acid wash, (ii) after calcination at  $200^{\circ}\text{C}$  for 4hr, (iii) obtained  $\text{TiO}_2(\text{B})$  nanotubes after calcination at  $300^{\circ}\text{C}$  for 4hr, (iv) anatase phase observed after calcination at  $300^{\circ}\text{C}$  for  $\geq 24$ hr, (v) collapsed of nanotubes into  $\text{TiO}_2$ -anatase nanowires and nanorods at  $500^{\circ}\text{C}$  for 4hr.  $\text{TiO}_2(\text{B})$  and anatase are indexed as  $\beta$  and  $\alpha$  respectively in the XRD patterns.

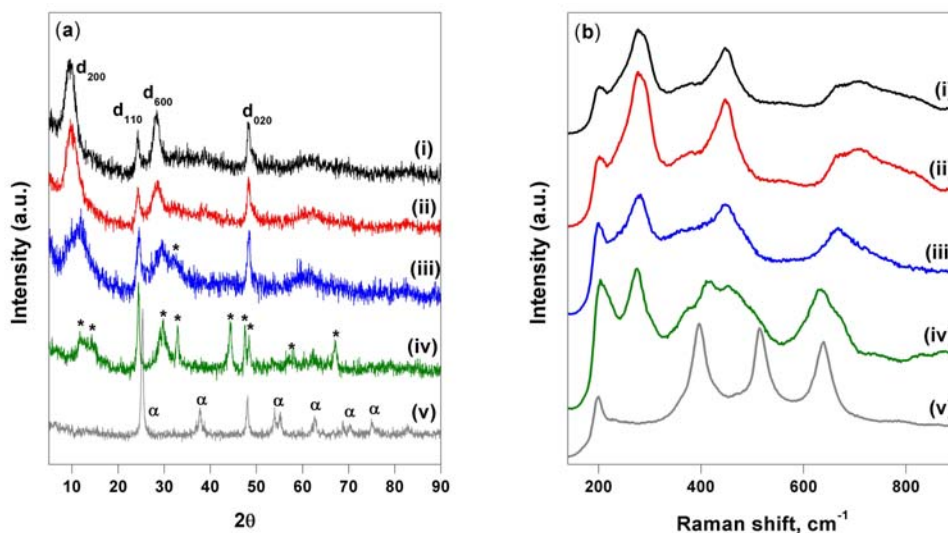


**Figure. A7.13.** (a) XRD patterns and (b) Raman spectra of (i)  $\text{Na}_x\text{H}_{2-x}\text{Ti}_3\text{O}_7$  nanotubes without acid wash, (ii) after calcination at  $300^{\circ}\text{C}$  for up to 32hr, (iii) after calcinations at  $500^{\circ}\text{C}$  for 4hr, (iv) obtained sodium titanate ( $\text{Na}_2\text{Ti}_6\text{O}_{13}$ ) nanowires after calcination at  $600^{\circ}\text{C}$  for 4hr and (v)  $\text{TiO}_2$ -anatase nanowires were obtained after acid washing and annealing  $\text{Na}_2\text{Ti}_6\text{O}_{13}$  nanowires.  $\text{Na}_2\text{Ti}_6\text{O}_{13}$  and anatase are indexed as  $*$  and  $\alpha$  respectively in the XRD patterns.

*Powder x-ray diffraction (XRD)*

Nevertheless XRD study shows that the nanotubes obtained from different post-synthesis treatments may have different crystalline structures. As indicated in Figure A7.12a-i (tritanate NT) and Figure A7.13a-i ( $\text{Na}_x\text{H}_{2-x}\text{Ti}_3\text{O}_7$  NT), acid washing has a drastic effect on the XRD patterns of the  $\text{TiO}_2$ -derived nanotubes. Clearly, the XRD peak intensities of (200), (110) and (600) are affected by the acid washing process, which may be attributed to the replacement of  $\text{Na}^+$  ions by  $\text{H}^+$  ions in the  $\text{TiO}_2$ -derived nanotubes. The Raman spectra of the as-synthesized trititanate and  $\text{Na}_x\text{H}_{2-x}\text{Ti}_3\text{O}_7$  nanotubes were alike (see Fig A7.12b-i & A7.13b-i respectively) and very hard to differentiate them apart. However their differences in thermal stability and related XRD and Raman patterns helped us to identify the types of titanate nanotubes.

It has been reported that proton exchange and subsequent dehydration of layered titanates with the formula  $\text{A}_2\text{Ti}_n\text{O}_{2n+1}$  ( $\text{A} = \text{Na}, \text{K}, \text{Cs}; 3 \leq n \leq 6$ ) yield  $\text{TiO}_2(\text{B})$  at temperatures below  $350^\circ\text{C}$ .<sup>28</sup> In other words, calcination of  $\text{H}_2\text{Ti}_3\text{O}_7$  at  $\leq 350^\circ\text{C}$  converts it into  $\text{TiO}_2(\text{B})$ . From Figure A7.12a-ii, upon heating the acid-washed nanotubes to  $200^\circ\text{C}$  for 4hr, the weak XRD  $d_{002}$  peak of the nanotubes downshifted from  $\sim 9^\circ$  to  $\sim 11^\circ$ . This  $d_{200}$  peak downshifted further from  $\sim 11^\circ$  to  $\sim 14^\circ$  when the nanotubes were heated at  $300^\circ\text{C}$  for 4hr. The resulting XRD pattern of the acid-washed nanotubes calcined at  $300^\circ\text{C}$  can be satisfactorily indexed as  $\text{TiO}_2(\text{B})$  structure (JCPD PDF No. 35-0088).

When  $\text{TiO}_2(\text{B})$  was annealed at  $300^\circ\text{C}$  for a prolonged period ( $\geq 24\text{hr}$ ), however, the  $d_{200}$  intensity was greatly reduced (but still discernible and remained at  $\sim 14^\circ$ ) and anatase phase was observed. Therefore the duration of calcination has a drastic effect on the structures of  $\text{TiO}_2(\text{B})$  nanotubes, which convert to  $\text{TiO}_2$ -anatase nanotubes (see XRD Fig A7.12a-iv). When the trititanate nanotubes were calcined at  $500^\circ\text{C}$  for 4hr, the  $d_{200}$  peak diminished and XRD pattern can be indexed as an anatase structure (Fig A7.12a-v). We believed that at  $>400^\circ\text{C}$ , the  $\text{TiO}_2(\text{B})$  nano-tubular structures started to collapse and break up into shorter anatase nanowires and

nanorods. This is supported by Fig A7.10 and Fig A7.11e-f, which show the images of segmented TiO<sub>2</sub>-anatase nanowires and nanorods calcined at 500°C for 4hr.

Ion exchangeable sodium titanate (Na<sub>x</sub>H<sub>2-x</sub>Ti<sub>3</sub>O<sub>7</sub>) nanotubes had better thermal stability than trititanate nanotubes because of the presence of Na<sup>+</sup> ions. In a similar fashion, we had calcined the Na<sub>x</sub>H<sub>2-x</sub>Ti<sub>3</sub>O<sub>7</sub> nanotubes at 300°C (32hr), 500°C (4hr) and 600°C (4hr) and studied the corresponding XRD and Raman spectra.

In Figure A7.13a, the XRD pattern of Na<sub>x</sub>H<sub>2-x</sub>Ti<sub>3</sub>O<sub>7</sub> nanotubes calcined at 300°C for 32hr was essentially the same as the starting material. TEM images of Fig A7.11b shows that the nanotubular structures are still preserved after 32hr of 300°C annealing. This is in sharp contrast to trititanate nanotubes which dehydrate into TiO<sub>2</sub>(B) and subsequently to anatase nanotubes for prolonged calcination. Thus this strongly suggests that there is no degradation of the crystal structure of the sodium titanate framework and the thermal stability of the nanotubes was strongly dependent on the presence of Na<sup>+</sup> ions.

When Na<sub>x</sub>H<sub>2-x</sub>Ti<sub>3</sub>O<sub>7</sub> nanotubes were heated at 500°C for 4hr, some new peaks began to develop in the XRD pattern (see Fig A7.13a-iii). The d<sub>200</sub> peak broadened and downshifted slightly from ~10° to ~12°, and a new peak located at ~32° was noted. Upon further heating to 600°C for 4hr, these new phases were fully developed (Fig A7.13a-iv). These new XRD peaks can be satisfactorily indexed as Na<sub>2</sub>Ti<sub>6</sub>O<sub>13</sub> (JCPD PDF No. 14-277). TEM images (Fig A7.11g-h) revealed that at ≥500°C the Na<sub>x</sub>H<sub>2-x</sub>Ti<sub>3</sub>O<sub>7</sub> nanotubes had transformed to nanowires. It is also noted that there are fewer nanorods when Na<sub>x</sub>H<sub>2-x</sub>Ti<sub>3</sub>O<sub>7</sub> nanotubes are collapsed into nanowires. In addition, these so-called Na<sub>2</sub>Ti<sub>6</sub>O<sub>13</sub> nanowires can be transformed into TiO<sub>2</sub>-anatase nanowires via a similar 0.1M HCl washing and calcination at 400°C for 4hr. This is confirmed by XRD and Raman spectra which indicate that an anatase phase when the Na<sub>2</sub>Ti<sub>6</sub>O<sub>13</sub> nanowires was proton exchanged and calcined at 400°C for 4hr (see Fig A7.13a-v and Fig A7.13b-v).

*Raman spectroscopy*

The exact assignment of the Raman modes for these TiO<sub>2</sub>-derived nanotubes is currently not well established in literature. This is because the Raman modes of the TiO<sub>2</sub>-derived nanotubes were different from the bulk anatase and rutile phase, which show 6 and 4 active Raman modes respectively. However Raman spectroscopy can still be applied effectively to elucidate the presence of TiO<sub>2</sub>(B) and anatase phase after the annealing process.

In good agreement with the XRD results, after calcination at 200-300°C for 4hr the Raman spectrum of the H<sub>2</sub>Ti<sub>3</sub>O<sub>7</sub> nanotubes (Fig. A7.12b-i) changes greatly, with the new spectra of Fig. A7.12b-ii and Fig A7.12b-iii similar to that reported for bulk TiO<sub>2</sub>(B)<sup>24</sup>. When TiO<sub>2</sub>(B) was annealed at 300°C for a prolonged period (≥24hr) or at 500°C for 4hr, the Raman spectrum is dominated by an anatase phase, which was characterized by E<sub>g</sub> (198cm<sup>-1</sup>, 637cm<sup>-1</sup>), B<sub>1g</sub> (395cm<sup>-1</sup>, 513cm<sup>-1</sup>) and A<sub>1g</sub> (513cm<sup>-1</sup>) modes. For Na<sub>x</sub>H<sub>2-x</sub>Ti<sub>3</sub>O<sub>7</sub> nanotubes, there is no major change in the Raman spectra (Figs. A7.13b) after heating it for 32hr at 300°C or for 4hr at 500°C. When sodium titanate nanowires were acid-washed and calcined at 400°C for 4hr, the formation of anatase phase is observable by Raman study as displayed in Fig. A7.13b-v.

*Thermogravimetric analysis (TGA)*

Figure A7.14 is the thermogravimetric analysis (TGA) of the TiO<sub>2</sub>-derived nanotubes. All TG samples were purged with purified air at 80°C for 2hr before the TG graphs were collected from 30°C to 800°C at a ramp rate of 5°C/min. From the TG curve (Fig A7.14-iii), it was estimated that ~11%wt of H<sub>2</sub>O was released from the trititanate nanotubes. This is higher than the expected dehydration process of the bulk trititanate, H<sub>2</sub>Ti<sub>3</sub>O<sub>7</sub> → H<sub>2</sub>O + 3TiO<sub>2</sub>; a loss of ~7wt% H<sub>2</sub>O<sup>28</sup>. We accounted for the observed higher weight lost due to swelling via water intercalation into the (200) plane of H<sub>2</sub>Ti<sub>3</sub>O<sub>7</sub> nanotubes. Water molecules might be intercalated between the interlayer of the nanotubes when the Na<sup>+</sup> ions were proton exchanged. This assumption agrees well with the XRD data which indicate that the d<sub>200</sub> value of as-synthesized

$\text{H}_2\text{Ti}_3\text{O}_7$  nanotube is  $\sim 9.67\text{\AA}$ ; larger than  $7.87\text{\AA}$  of bulk  $\text{H}_2\text{Ti}_3\text{O}_7$ .<sup>26,28</sup> When the trititanate nanotubes were heated up to  $200^\circ\text{C}$ , the  $d_{200}$  correspondingly moved from  $\sim 9.67\text{\AA}$  to  $\sim 7.62\text{\AA}$  which was closer to bulk  $\text{H}_2\text{Ti}_3\text{O}_7$ . Therefore based on XRD and TGA studies, the trititanate nanotubes may be formulated as  $\text{H}_2\text{Ti}_3\text{O}_7 \cdot 0.5\text{H}_2\text{O}$ . On the other hands,  $\text{TiO}_2(\text{B})$  nanotubes had a loss of only  $\sim 1\text{wt}\%$ . Thus the  $\text{TiO}_2$ -derived nanotubes after proton exchanged can be described as layered trititanate ( $\text{H}_2\text{Ti}_3\text{O}_7 \cdot 0.5\text{H}_2\text{O}$ ) nanotubes and dehydrate into  $\text{TiO}_2(\text{B})$  nanotubes at  $300^\circ\text{C}$  for 4hr. The TGA profile of  $\text{Na}_x\text{H}_{2-x}\text{Ti}_3\text{O}_7$  nanotube was also displayed in Fig A7.14. A weight loss of  $\sim 8.3\%$  is noted for the  $\text{Na}_x\text{H}_{2-x}\text{Ti}_3\text{O}_7$  nanotube.

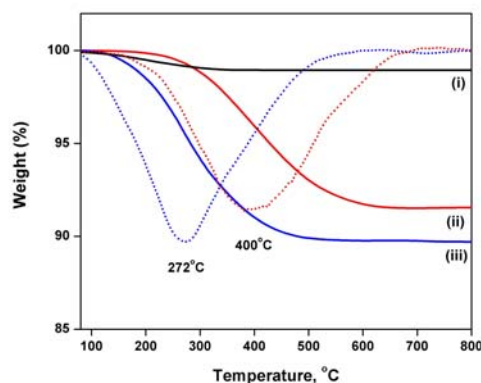


**Figure. A7.14.** TG analysis of (i)  $\text{TiO}_2(\text{B})$  nanotubes, (ii),  $\text{Na}_x\text{H}_{2-x}\text{Ti}_3\text{O}_7$  nanotubes pre-annealed at  $300^\circ\text{C}$  for 32hr, and (iii) as-synthesized trititanate nanotubes. Differentiated TG (DTG) curves were presented as dotted lines.

The TGA of  $\text{Na}_x\text{H}_{2-x}\text{Ti}_3\text{O}_7$  nanotube has a gentler slope than trititanate nanotube. Furthermore, the differentiated TG (DTG) curves showed that the temperature of weight loss for trititanate nanotubes started at  $272^\circ\text{C}$ , while  $\text{Na}_x\text{H}_{2-x}\text{Ti}_3\text{O}_7$  nanotube was at  $400^\circ\text{C}$ . This is consistent with the XRD studies that  $\text{Na}_x\text{H}_{2-x}\text{Ti}_3\text{O}_7$  nanotubes were more thermally stable than trititanate nanotubes.

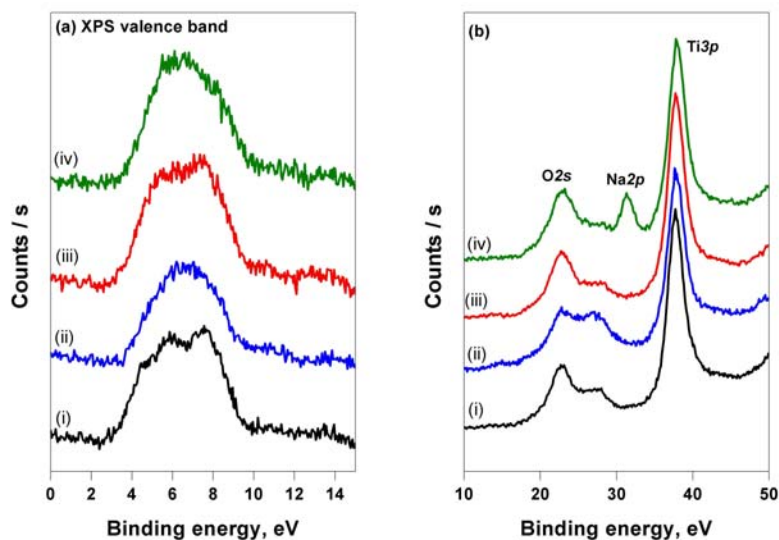


**Figure. A7.15.** XPS (a) valence band (VB) and (b) core levels emission spectra of (i) bulk anatase  $\text{TiO}_2$ , (ii) trititanate nanotubes, (iii)  $\text{TiO}_2(\text{B})$  nanotubes and (iv)  $\text{Na}_x\text{H}_{2-x}\text{Ti}_3\text{O}_7$  nanotubes. *Inset: core-level  $\text{Na}1s$  of  $\text{Na}_x\text{H}_{2-x}\text{Ti}_3\text{O}_7$  nanotube. XPS core levels emission spectra were normalized using the  $\text{Ti}3p$  peak. The valence band spectra were offset for clarity of presentation.*

#### *X-ray photoelectron spectroscopy (XPS)*

From the XPS photoelectron spectra in the binding energy region between 10 and 50eV (see Fig. A7.15b), a  $\text{Na}2p$  peak can be observed for the  $\text{Na}_x\text{H}_{2-x}\text{Ti}_3\text{O}_7$  nanotubes without acid wash (Fig. A7.15b-iv), which is not observed for the  $\text{H}_2\text{Ti}_3\text{O}_7$  nanotubes with extensive acid wash. Additionally a strong  $\text{Na}1s$  peak located at  $\sim 1073\text{eV}$  was detected for  $\text{Na}_x\text{H}_{2-x}\text{Ti}_3\text{O}_7$  nanotubes (inset of Fig A7.15b) and we estimated that  $x \approx 0.7$ . This provides a clear evidence that acid washing is a proton exchange process and affects the types of titanate nanotubes to be obtained. A stronger shoulder of the  $\text{O}2s$  peak is observed for  $\text{H}_2\text{Ti}_3\text{O}_7$  (see Fig. A7.15b-ii) due to the chemical shift of oxygen in  $\text{H}_2\text{O}$ . The XPS valence band (VB) structures these  $\text{TiO}_2$ -derived nanotubes were compared with bulk anatase. The  $\text{O} 2p$ -derived valence band of the bulk anatase is characterized by a VB width of  $\sim 4.7\text{eV}$  (estimated from the high and low binding energy limits at the inflection points of the VB) and 2 peaks centred at  $\sim 5.9\text{eV}$  and  $\sim 7.6\text{eV}$ , which are associated to  $\pi$  (nonbonding) and  $\sigma$  (bonding)  $\text{O}2p$  orbitals<sup>29,30</sup>. But the valence band of the



trititanate nanotubes,  $\text{H}_2\text{Ti}_3\text{O}_7$ , which had been calcined at  $200^\circ\text{C}$  for 4hr, exhibits only 1 main peak at  $\sim 7\text{eV}$  and the VB width is reduced to  $\sim 3.7\text{eV}$ , which suggests a combination of  $\pi$  and  $\sigma$   $\text{O}2p$  orbitals. On the other hands,  $\text{TiO}_2(\text{B})$  and  $\text{Na}_x\text{H}_{2-x}\text{Ti}_3\text{O}_7$  nanotubes exhibit a stronger  $\pi$ - and  $\sigma$   $\text{O}2p$  emission intensities respectively. The VB width of  $\text{TiO}_2(\text{B})$  and  $\text{Na}_x\text{H}_{2-x}\text{Ti}_3\text{O}_7$  nanotubes are estimated to be about  $4.7\text{eV}$  and  $4.5\text{eV}$  respectively. Of particular interest is the valence band of  $\text{TiO}_2(\text{B})$  nanotubes which is quasi-resemble that of bulk  $\text{TiO}_2$ -anatase. This is expected because the electronic structure of bulk  $\text{TiO}_2(\text{B})$  was calculated to be an  $n$ -type semiconductor with a band gap  $3\text{-}3.2\text{eV}$ , which is similar to anatase or rutile<sup>31,32</sup>.

On the basis of XRD, Raman, TGA and XPS results, one can propose that  $\text{TiO}_2$ -derived nanotubes that had undergone extensive proton exchange (acid washing) could be suitably labeled as trititanate ( $\text{H}_2\text{Ti}_3\text{O}_7$ ) nanotubes. Calcination of trititanate nanotubes at  $300^\circ\text{C}$  for 4hr, dehydrate it to  $\text{TiO}_2(\text{B})$  nanotubes. When the  $\text{TiO}_2(\text{B})$  nanotubes were calcined at  $300^\circ\text{C} \geq 24\text{hr}$ , however, it converted to  $\text{TiO}_2$ -anatase nanotubes. Upon further calcination  $>400^\circ\text{C}$ , the tubular structures collapsed and formed  $\text{TiO}_2$ -anatase nanowires / nanorods. On the other hands, the  $\text{TiO}_2$ -derived nanotubes obtained with water wash only can be labeled as ion exchangeable  $\text{Na}_x\text{H}_{2-x}\text{Ti}_3\text{O}_7$  nanotubes. These  $\text{Na}_x\text{H}_{2-x}\text{Ti}_3\text{O}_7$  nanotubes are thermally more stable than trititanate nanotubes. At  $>500^\circ\text{C}$ ,  $\text{Na}_x\text{H}_{2-x}\text{Ti}_3\text{O}_7$  nanotubes likewise collapsed into nanowires. Hence a careful control of the synthetic pathway allows one to select the types of  $\text{TiO}_2$ -related nanostructured materials as the final products.

### **A7.3.3. Formation mechanism of titania nanotube.**

Figure A7.16 shows the TEM images of the products at different stages of the hydrothermal process. Stage 0 refers to the starting  $\text{TiO}_2$  materials. After  $\sim 6\text{-}10\text{hr}$  of  $10\text{M}$   $\text{NaOH}$  hydrothermal process at  $120^\circ\text{C}$  (stage 1), step-like structures and nanosheets exfoliated from bulk  $\text{TiO}_2$  are observed. This strongly suggests a sheet-folding process is involved. Curling and



scrolling of the nanosheets can be observed at Stage 2 (~18hr). At stage 3 (~24hr) of the hydrothermal process, formation of TiO<sub>2</sub>-derived nanotubes occurred. At stage 4, the final products were washed with 0.1M HCl and HRTEM showed that the TiO<sub>2</sub> nanotubes possess multi-layered structures.

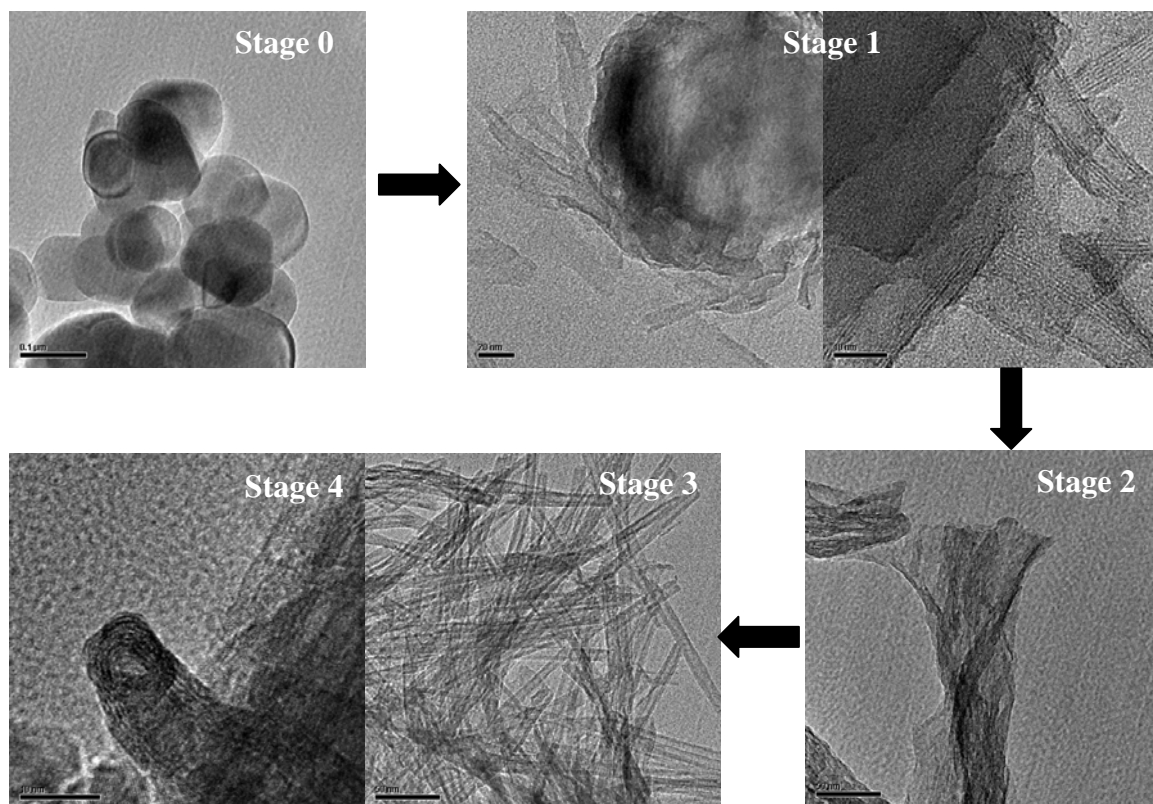


**Figure A7.16.** TEM observations of titania nanotubes at different stages of the hydrothermal process.

### Appendix - References

- [1] Y. Saito, M. Maida, T. Matsumoto, *Jpn. J. Appl. Phys.* 38, 159 (1999).
- [2] Y. Chen, M. Conway, J.S. Williams, J. Zou, *J. Mater. Res.* 17, 1896 (2002).
- [3] O.R. Lourie, C.R. Jones, B.M. Bartlett, P.C. Gibbons, R.S. Ruoff, W.E. Buhro, *Chem. Mater.* 12, 1808 (2000).
- [4] E. Borowiak-Palen, T. Pichler, G.G. Fuentes, B. Bendjenmil, X. Liu, A. Graff, G. Behr, R.J. Kalenczuk, M. Knupfer, J. Fink, *Chem. Commun.* 1, 82 (2003).
- [5] X. Blasé, A. Rubio, S.G. Louie, M.L. Cohen, *Europhys. Lett.* 28, 335 (1994).
- [6] M. Menon, D. Srivastava, *Chem. Phys. Lett.* 307, 407 (1999).
- [7] C.H. Shin, G. Bugli, G. Djega-Mariadassou, *J. Solid State Chem.* 95, 145 (1991).
- [8] T. Kasuga, M. Hiramatsu, A. Hoson, T. Sekino, K. Niihara, *Adv. Mater.* 11, 1307 (1999).
- [9] B.D. Yao, Y.F. Chan, X.Y. Zhang, W.F. Zhang, Z.Y. Yang, N. Wang, *Appl. Phys. Lett.* 82, 281 (2003).
- [10] W. Wang, O.K. Varghese, M. Paulose, G.A. Grimes, *J. Mater. Res.* 19, 417 (2004).
- [11] T. Akita, M. Okumura, K. Tanaka, K. Ohkuma, M. Kohyama, T. Koyanagi, M. Data, S. Tsubota, M. Haruta, *Surf. Interface Anal.* 37, 265 (2005).
- [12] Q. Chen, W. Zhou, G. Du, L.M. Peng, *Adv. Mater.* 14, 1208 (2002).
- [13] Y. Suzuki, S. Yoshikawa, *J. Mater. Res.* 19, 962 (2004).
- [14] G. H. Du, Q. Chen, R. C. Che, Z.Y. Yuan, L.M. Peng, *Appl. Phys. Lett.* 79, 3702 (2001).
- [15] S. Zhang, L.M. Peng, Q. Chen, G.H. Du, D. Dawson, W.Z. Zhou, *Phys. Rev. Lett.* 25, 256103-1 (2003).
- [16] A. Nakahira, W. Kato, M. Tamai, T. Isshiki, K. Nishio, *J. Mater. Sci.* 39, 4239 (2004).
- [17] R. Ma, Y. Bando, T. Sasaki, *Chem. Phys. Lett.* 80, 577 (2003)
- [18] M. Zhang, Z. S. Jin, J.W. Zhang, X.Y. Guo, J.J. Yang, W. Li, X.D. Wang, Z.J. Zhang, *J. Molec. Catal. A: Chem.* 217, 203 (2004).
- [19] X. Sun, Y. Li, *Chem. Eur. J.* 9, 2229 (2003).
- [20] R. Yoshida, Y. Suzuki, S. Yoshikawa, *Mater. Chem. Phys.* 91, 409 (2005).
- [21] J. Wang, Y. Li, *Adv. Mater.* 15, 445 (2003).
- [22] A. Fujishima, T.N. Rao, D.A. Tryk, *J. Photochem. Photobiol. C: Photochem. Rev.* 1, 1 (2000).
- [23] D.J.D. Corcoran, D.P. Tunstall, J.T.S. Irvine, *Solid State Ionics*, 136, 297 (2000).
- [24] G. Armstrong, A.R. Armstrong, J. Canales, P.G. Bruce, *Chem. Commun.* 19, 2454 (2005).
- [25] G. Armstrong, A.R. Armstrong, J. Canales, P.G. Bruce, *Angew. Chem. Int. Ed.* 43, 2286 (2004).

- [26] M. Zkalova, M. Kalbac, L. Kavan, I. Exnar, M. Graetzel, *Chem. Mater.* 17, 1248 (2005).
- [27] I.M. Ali, *J. Radioanal. Nucl. Chem.* 260, 149 (2004).
- [28] T.P. Feist, P.K. Davies, *J. Solid State Chem.* 101, 275 (1992).
- [29] R. Sanjines, H. Tang, H. Berger, F. Gozzo, G. Margaritondo, F. Levy, *J. Appl. Phys.* 75, 2945 (1994).
- [30] R. Heise, R. Courths, S. Witzel, *Solid State Commun.* 84, 599 (1992).
- [31] G. Nuspl, K. Yoshizawa, T. Yanabe, *J. Mater. Chem.* 7, 2529 (1997).
- [32] S. Yin, J. Wu, M. Aki, T. Sato, *Int. J. Inorg. Mater.* 2, 325 (2000).

## **Chapter 8. Carbon nanotube-nanoparticle hybrids**

### *Summary*

The exterior walls of carbon nanotubes (CNTs) are decorated with metallic nanoparticles (NPs), and these CNT-NP hybrids are useful platforms for anchoring bio-molecules. In section (8.2), Pd nanoparticle and glucose oxidase enzyme are co-electrodeposited on Nafion-solubilized MWNT film. This Pd nanoparticle-oxidase-Nafion-MWNT hybrid is fabricated into a glucose sensor. In section (8.3), a genosensor based on Au nanoparticle-MWNT hybrid is investigated to detect hybridization events of complementary and mismatched DNA strands.

## **8.1. Bio-electrochemistry of carbon nanotube**

### **8.1.1. Introduction**

Although carbon nanotubes possess many interesting properties, the attachment of foreign nanoparticles may endow it with special properties which CNTs do not have. CNT has a large specific surface area and offers a rich surface chemistry, thus it is an excellent carbon support for the deposition of useful nanoparticles. The tips, inner cavities and exterior surfaces of CNTs have been successfully attached with foreign nanoparticles<sup>1-3</sup>. In addition, CNT has been used as (sacrificial) template for the synthesis of other nanostructured materials<sup>4,5</sup>.

Therefore it is of great interests to find potential applications of these carbon nanotube-nanoparticle hybrids. For examples, platinum nanoparticles deposited on CNTs have been widely studied as catalysts for H<sub>2</sub>-powered fuel cell technology<sup>6</sup>. CNT-gold nanoparticle array has been shown to possess better field emission current<sup>7</sup>. Carbon nanotubes coated with conformal layers of gold or silver showed enhanced optical limiting behaviour<sup>8</sup>. Therefore by combining the individual properties of nanoparticles and carbon nanotubes, these hybrids are very attractive novel materials for technological applications.

The synergy of CNT and nanoparticles has been expanded to include bio-molecules such as proteins and deoxyribonucleic acid (DNA). S. C. Tsang et al.<sup>9</sup> investigated the interactions between open-tipped MWNTs and various small sized proteins (Zn<sub>2</sub>-Cd<sub>5</sub>-metallothionein, cytochrome c<sub>3</sub> and β-lactamase I). High-resolution TEM studies revealed that single protein molecules and their associated forms were immobilized inside the cavities of open-tipped MWNTs. Further investigations showed that enzymes can also be immobilized onto the exterior surfaces of SWNT which had been functionalized with carboxylic acid and succinimidyl ester<sup>10</sup> groups. Importantly, the immobilized enzymes still remained catalytically active and showed no sign of drastic conformational deformation.

K. A. Williams et al.<sup>11</sup> also demonstrated that both ends of SWNT strands, which were terminated by carboxylic acid, can be covalently coupled to peptide nucleic acid (PNA). These PNA-derived SWNTs readily hybridized with complementary single-stranded DNA. The oligonucleotide adducts endow CNTs with DNA recognition properties which could be used to fabricate DNA hybridization sensors or genosensors.

Since CNT possesses excellent electrochemical properties and interacts with bio-molecules, it is palpable to study the electrochemical biosensing properties of CNT hybrids. In this thesis, CNT-nanoparticle hybrids are attached with specific bio-molecules for biosensing purposes. The role of nanoparticles serves as anchoring points for the bio-molecules, while CNTs serve as electrodes for transducing the interaction signals. A glucose biosensor based on MWNT/nano-palladium hybrid and a MWNT/nano-gold genosensor were investigated respectively.

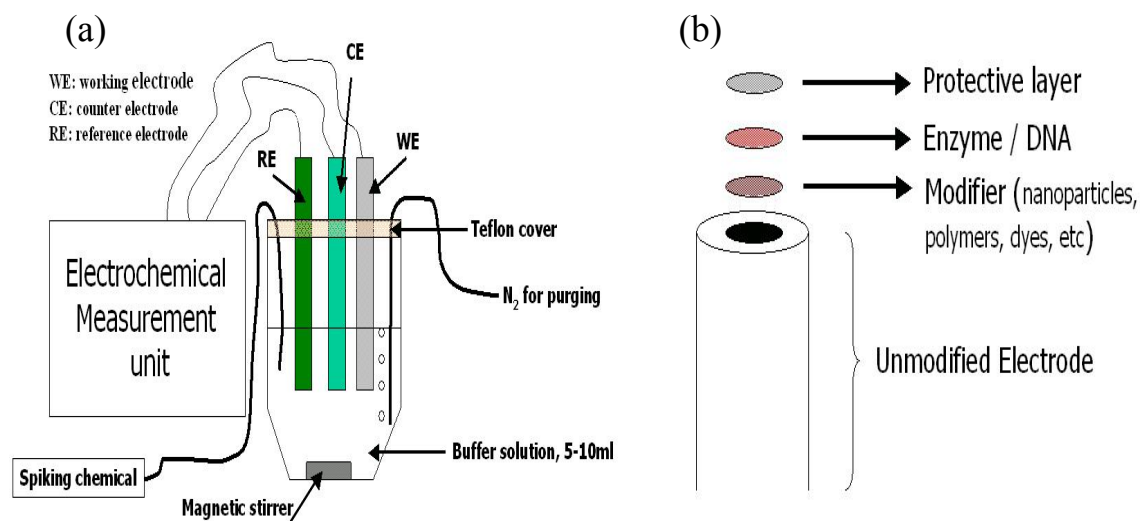


**Figure 8.1.** A schematic set-up of (a) the electrochemical unit used for biosensing tests, and (b) a chemically modified electrode.

### **8.1.2. Concepts of electrochemical biosensing**

When a bio-molecule participates in a bio-chemical reaction, the occurrence of the reaction can usually be monitored. Depending on the techniques used to detect the bio-chemical reactions, a biosensor can be constructed to effectively monitor the overall reactions. Biosensors<sup>12</sup> based on magnetic, optical, thermal and electrochemical effects can be fabricated; each type of biosensors has its own merits. Nonetheless, biosensors base on electrochemistry stands out among the device fabrication. This is because electrochemical biosensor is highly sensitive, inexpensive and relatively easier to fabricate.

Figure 8.1 shows the schematic setup of the electrochemical unit used for biosensing tests. It is a 3-electrode electrochemical cell, which consists of a working electrode (WE, glassy carbon electrode), counter electrode (CE, platinum wire) and a reference electrode (RE, saturated calomel or Ag/AgCl electrode). The 3 electrodes are immersed in 5-10ml of buffer medium. The bio-reaction of interest takes place at the WE interface, which is registered as electrical signals by the electrochemical measurement unit. Very often, the working electrode is modified before the attachment of bio-molecules (e.g. enzymes or DNA). Figure 8.1b demonstrates how the surface of the working electrode can be modified by the deposition of nanoparticles (e.g. MnO<sub>2</sub> nanoparticles), fullerene, polymers, surfactants, adsorption of special dyes and attachment of functional groups (such as thiolated / amine alky chains for gold electrode)<sup>13</sup>. The usefulness of modifying the working electrode is three-fold. Firstly, without the modifier, the direct attachment of a bio-molecule to the working electrode may ‘poison’ or block the active surface of the electrode and hinder effective detection. Secondly, with the modifier, the attachment of the bio-molecule can be carried out in a more control fashion, in contrast to mere physical adsorption. Thirdly, the bio-molecule can be protected in a conducive environment in order to extend its catalytic properties, which is important for device fabrication.

The modification of the working electrode with carbon nanotube film would present a useful and simple technique to enhance the electrochemical properties of the working electrode.

Generally, a homogenous CNT solution is used to cast a thin film of CNT onto the surface of the working electrode. For example, a significantly superior oxidative behaviour of dopamine<sup>14</sup> (an important neurotransmitter) was observed for CNT-modified electrodes as compared to conventional electrodes. Another interesting aspect of CNT-modified electrode was the direct observation of protein electrochemistry, which is normally not observable or hard to detect in unmodified electrodes. J. J. Davis et al.<sup>15</sup> showed that CNT-modified electrodes allow the observation of direct electron transfer (DET) of important enzymes such as cytochrome c and glucose oxidase without the assistance of mediators. Consequently, it is possible to fabricate a DET-based biosensor using carbon nanotubes. Therefore MWNT-modified glassy carbon electrodes have been chosen in this work to co-electrodeposit glucose oxidase enzymes and Pd nanoparticles for the fabrication of glucose biosensors (see section 4.3.1).

The fine powdery nature of bulk CNT makes it very suitable to be used as powder microelectrode<sup>16</sup>. A powder microelectrode was fabricated by etching the tip of the Pt (diameter of Pt: 50-150µm) microdisk electrode in saturated CaCl<sub>2</sub> solution, so that a microcavity is formed at the tip. The microcavity is filled with the CNT powder for electroanalysis. A minute amount of CNT is loaded into the micro-sized cavity of the microelectrode. Due to its very simple preparation, CNT-powder microelectrode can be applied as a single-use detector. The “expended” CNT can be easily removed via ultrasonication and reloaded with “fresh” CNT powder. This technique has been employed to fabricate a DNA hybridization sensor based on gold nanoparticle-CNT hybrid (see section 4.3.2).

The electrochemical measurements were conducted in the form of cyclic voltammographs (CV), hydrodynamics voltammographs (HDV), electro-impedance spectroscopy (EIS) and alternating current voltammographs (ACV). A brief description of each technique will be outlined in this thesis. An in-depth discussion of the techniques is given in references<sup>17</sup>.

A cyclic voltammograph is collection of current-vs-voltage graphs, whereby a lower potential is sweep linearly to a higher potential and back. The cycle can be repeated for several



times. The potential is defined with respect to a reference electrode used in the electrochemical cell. In electrochemistry, a CV plot can be viewed as an oxidation-reduction process. This can be compounds added to the electrolyte (e.g. glucose in equation [8.1] page 233 or  $\text{Ru}(\text{bpy})_3^{2+}$  in equation [8.3] page 255) being oxidized or reduced at the WE surface. Generally, when the applied potential is sweep from a lower potential to a higher potential it is an oxidation process, and vice versa.

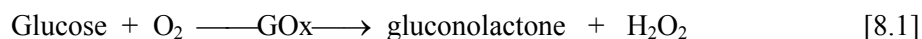
A hydrodynamic voltammograph is collected by applying a fixed potential and allowing the current to decay to a stable state (usually within 30-90s). The HDV is collected at discrete potential points. However, the buffer solution is mechanically stirred at a defined rotational speed while collecting the HDV. Note that in CV measurements the buffer solution is not agitated.

Electro-impedance spectroscopy is a special technique which probes the surface resistance of the electrodes. This technique has been widely exploited by I. Willner and co-workers<sup>18</sup> for the fabrication of highly sensitive DNA biosensors. This is because the immobilization of a foreign entity onto the surface of the electrodes will change its interfacial resistance. Therefore EIS technique is most useful for monitoring the attachment of DNA molecules onto the electrode surfaces because single-stranded DNA has negative charges. Therefore any changes in the electrode interfacial resistance is closely linked to the hybridization events of DNA.

Alternating current voltammograph (ACV) is similar to a CV measurement, except that a small-amplitude sinusoidal potential with a frequency of 10 Hz-100 kHz is superimposed onto linear potential sweep used in a d.c. cyclic voltammetry. The most important aspect of ACV is the magnitude of the a.c. perturbation that is regarded to be small in comparison to the overall change in voltage occurring during the sweep. A typical amplitude of 5 mV or less is employed in AC measurements. ACV is an extremely sensitive technique and it is very suitable for detecting small or weak electrochemical signals.

## **8.2. A glucose biosensor based on co-electrodeposition of palladium nanoparticles and glucose oxidase onto Nafion-solubilized carbon nanotube electrode.**

Among all the enzyme-based biosensors, the glucose biosensor is the most widely studied because of its importance in the monitoring of blood glucose for the treatment and control of diabetes. Most of the amperometric glucose biosensors are based on the glucose oxidase (GOx) enzyme, which catalyzes the oxidation of glucose to gluconolactone:



The quantification of glucose can be achieved via electrochemical detection of the enzymatically-liberated  $\text{H}_2\text{O}_2$ . This is the basic principle of first generation glucose biosensors. However, the overvoltage necessary for the oxidation or reduction of  $\text{H}_2\text{O}_2$  at solid electrodes is rather high, which might make the quantification of glucose highly unspecific due to interference from reducing agents such as uric acid and ascorbic acid. For example the oxidation of  $\text{H}_2\text{O}_2$  for a plain glassy carbon electrode (GCE) occurs at about +0.8V, which is too high. Thus in the refinement of these first generation glucose biosensors, the modification of the electrodes is carried out such that the  $\text{H}_2\text{O}_2$  oxidation / reduction overvoltage is considerably lowered to about +0.3V. A good strategy is the application of metallized enzyme electrodes, at which noble metals such as palladium, platinum, gold, copper and iridium and GOx are simultaneously entrapped onto the electrode surface, and such metallized enzyme electrodes have been demonstrated to lower the  $\text{H}_2\text{O}_2$  oxidation / reduction overvoltage efficiently<sup>19</sup>.

In this section, the fabrication, characterizations and analytical performance of a glucose biosensor based on electrochemical co-deposition of Pd and GOx onto a carbon nanotube film will be discussed. Glucose oxidase has been demonstrated to covalently attach on CNT via carbodiimide activation<sup>20</sup> and physical adsorption<sup>21</sup>. However, our approach modifies the surfaces of MWNTs with Pd-GOx biocomposites using electrochemical co-deposition and there is not a need for any chemical linkages. The influence of palladium and GOx composition and common

interferents (uric and ascorbic acids) on the sensor performance is also evaluated. In addition, Pd-GOx biocomposite was incorporated into Nafion-solubilized MWNT matrix and successfully applied as a glucose biosensor. When the Nafion-MWNT bioelectrodes are coated with an extra Nafion membrane, it eliminates interfering signals of uric and ascorbic acids and possesses enhanced storage time and performance, in comparison to the biosensors made without Nafion.

### **8.2.1. Experimental procedures**

Acid purified multi-wall carbon nanotubes (MWNTs, diameter 10-30nm) were used in this work. Glucose oxidase (GOx) (EC 1.1.3.4, *Aspergillus niger*, >100U/mg) was purchased from Amresco and used as received. D-(+)-glucose was purchased from Sigma and the glucose stock solution was allowed to mutarotate for 24 h at room temperature prior to use and subsequently stored at 4°C. Palladium chloride was obtained from Merck and a 5.6 mM PdCl<sub>2</sub> stock solution of pH 5.6 was prepared for co-deposition of Pd and GOx. The supporting electrolyte was 0.1M phosphate buffer at pH 7, unless otherwise stated.

The electrochemical measurements were performed with Solartron SI 1280B Potentiostat / Galvanostats. A platinum wire, Ag/AgCl (3 M NaCl) reference electrode and glassy carbon electrode (GCE, circular diameter 3 mm) were inserted into a modified 5-10 ml cell (BAS, Model MF-2040) for the measurements. All potentials are referred to the Ag/AgCl reference electrode. A magnetic stirrer provided the convective transport at 300 rpm during the amperometric measurements and the background current was allowed to decay to a steady state value before spiking the equilibrated β-D-glucose.

The multi-walled carbon nanotubes were sonicated in toluene to give a concentration of ~1 mg/ml. 4 μl of the MWNT suspension was film-cast onto the surface of the glassy carbon electrode (GCE) and allowed to dry slowly. Electrodeposition of palladium and GOx was carried out in a pH 5.6 electroplating bath<sup>22</sup>. The composition of the palladium-GOx electroplating bath

consists of ~0.5—3mM of PdCl<sub>2</sub> and ~300—1500U of GOx, making a total volume of 10ml. MWNT-modified GCE were immersed in the plating bath and a constant potential of -0.9V was applied for 10min under gentle stirring condition. The electrodes were rinsed with pH 7 buffer and stored in the buffer at 4°C prior to use.

### **8.2.2. Solubilization of MWNT via wrapping of Nafion polymer**

1mg/ml of MWNTs were solubilized in 0.5% Nafion solution (99.5% ethanol) via mild sonication and subsequently film-cast onto the surface of the GCE. Films formed from the Nafion-solubilized MWNTs are more uniform and stable than those cast from organic solvents. Nafion assists the dispersion of MWNTs, whereby the MWNTs do not sediment for more than a week (see inset of Figure 8.2). On the other hands, MWNTs sonicated in organic solvents, without Nafion, tend to aggregate after the sonication has stopped. Furthermore these Nafion-solubilized MWNT film adhered to the GCE much better than MWNT film that was cast from toluene. The amount of MWNT film cast onto the GCE is more controllable and reproducible since it is cast from a homogeneous Nafion-MWNT solution. This is crucial for amperometric measurement under stirring conditions because the Nafion-MWNT biosensing area remains intact and whole. The electrodeposition of Pd-GOx onto Nafion-MWNT film was carried out in a similar fashion. After the co-deposition of Pd-GOx, these Nafion-MWNT bioelectrodes were coated with an extra 2.5µl layer of 0.5% Nafion.

### **8.2.3. Electron micrographs of MWNT- nanoparticle hybrids**

The TEM images were obtained on a transmission electron microscope (TEM, JEOL JEM-2010F). The electrodeposited Pd-GOx MWNT and Pd-GOx Nafion-solubilized MWNT films were sonicated in distilled water, just enough to peel the films off from the GCE. A vortex

mixer is used to agitate and disperse the films in distilled water before the films were cast onto formvar coated copper grids.

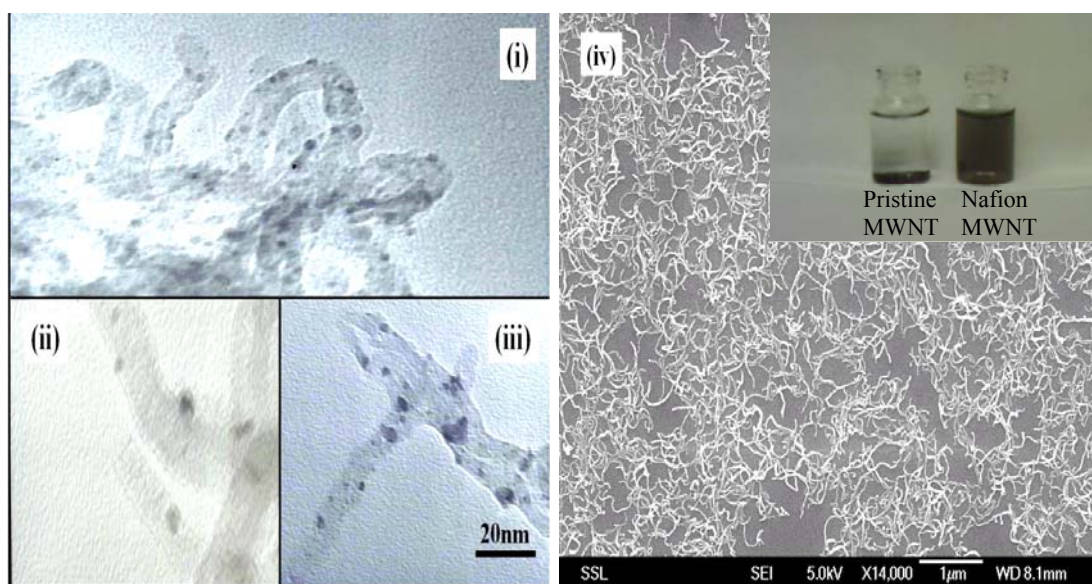


**Figure 8.2** TEM images of electrodeposited (i) Pd-GOx on MWNT, (ii) Pd nanoparticles on MWNT without GOx and (iii) Pd-GOx on Nafion-solubilized MWNT. (iv) SEM images of Nafion-solubilized MWNT cast onto a Si substrate.

From the TEM images (Figure 8.2), roughly spherical Pd nanoparticles (~2-6nm) are randomly decorated on the walls of the various MWNTs. It is interesting to note that Pd nanoparticles are formed instead of a conformal Pd coating. The acidic purification of the CNTs introduced relatively large amount of carboxylic acids moieties (-COOH) at defect sites located at the sidewalls of the nanotubes. Palladium ions might be anchored to these -COOH sites and formed Pd nanoparticles when a -0.9V potential was applied. The entrapment and adsorption of GOx (diameter 4-5nm) onto the Pd nanoparticles cannot be inferred directly from the TEM images. However from the results of the FTIR and HDV measurements (vide infra), it is clear that GOx is present along with the deposited Pd nanoparticles. It is possible that the TEM preparation which involves sonication and agitation has dislodged the GOx enzymes from the Pd

nanoparticles. The formation of Pd nanoparticles on Nafion-MWNT film indicates that the MWNT sidewalls are not entirely masked by the Nafion and there are accessible areas for the co-deposition of Pd-GOx biocomposites. Otherwise the Nafion has no pore big enough for the deposition of the GOx. It has been suggested that the solubilization action of Nafion is very similar to other polymeric materials bearing polar side chains, which ‘wrap’ around the MWNTs, and the electrocatalytic properties of MWNTs are not impaired by Nafion under optimal conditions<sup>23</sup>. Therefore dispersing MWNTs in 0.5% Nafion ensures that the amount of MWNTs are controllably cast onto GCE and the MWNTs still retain its electrocatalytic carbon surface. Figure 8.2(iv) shows the SEM image of Nafion-solubilized MWNT cast onto a Si substrate. It is assumed that the Nafion-MWNT film deposited on GCE is similar to Figure 8.2(iv). It can be seen that the film is very thin and composed only a few layer of MWNTs.

#### ***8.2.4. XRD patterns and FTIR spectroscopy***

Due to the fact that Pd nanoparticles were deposited onto a very small area of MWNT electrode ( $\sim 7\text{mm}^2$ ), it was very difficult to collect its powder XRD pattern. Hence to collect the XRD pattern of the Pd-MWNT hybrid, MWNT powder was pressed into a thin MWNT sheet. A thin copper wire was attached to the pressed MWNT sheet (using epoxy) and soaked in the  $\text{PdCl}_2$  solution for an hour. The electrodeposition of Pd nanoparticles (without GOx) was carried out in a similar fashion. The resulting Pd nanoparticle-MWNT sheet was rinsed with distilled water and air-dried before detaching the copper wire.

The attachment of GOx enzymes to the Pd nanoparticles is confirmed by the presence of the amide infrared (IR) mode, which a signature of protein. After the electrodeposition of GOx-Pd nanoparticles onto the MWNT film (In this case, we do not use Nafion), the electrode is rinsed thoroughly with distilled water and air-dried. The GOx-Pd-MWNT is scrapped off from the electrode and mixed with KBr for FTIR transmittance measurements.

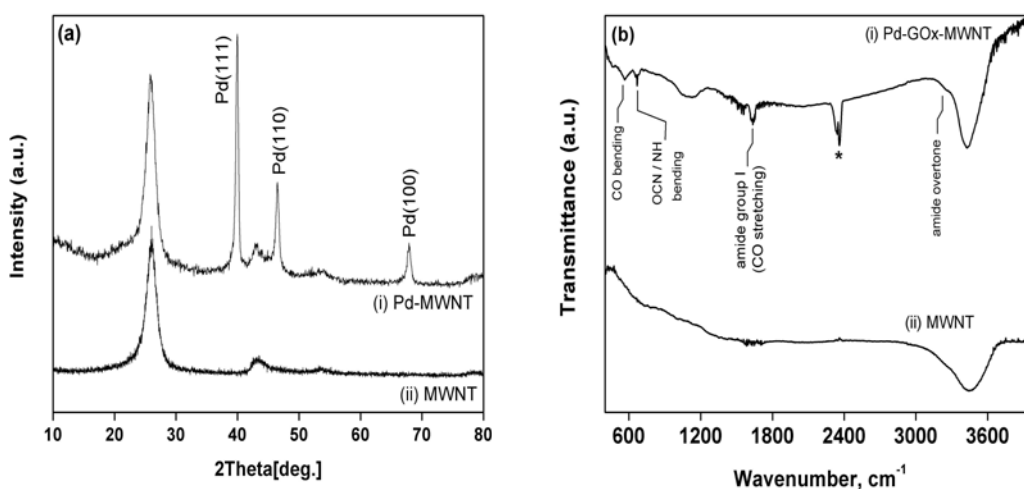


**Figure 8.3.** (a) XRD patterns and (b) FTIR spectra of (i) electrodeposited Pd nanoparticle-MWNT hybrid (with GOx for IR spectrum) and (ii) pristine MWNT. (Asterisk\* denotes interfering IR signal of CO<sub>2</sub>)

The XRD pattern of the electrodeposited Pd-MWNT composite is shown in Figure 8.3a. The major diffraction peaks of Pd nanoparticles can be indexed as the Pd face-centered cubic (fcc) phase based on the JCPDS data. The diffraction peaks of Pd nanoparticles at 39.9°, 46.4° and 67.9° can be assigned to (111), (110) and (110) crystalline planes respectively. The average size of the Pd nanoparticles is calculated by the Scherrer formula:

$$D_{\text{ave}} = K\lambda / \beta_{1/2} \cdot \cos\theta \quad [8.2]$$

where  $K$  is a constant (often taken as unity),  $\theta$  is the scattering angle,  $\beta_{1/2}$  is the full width at half maximum (FWHM) of the XRD peak,  $\lambda$  is wavelength of Cu K <sub>$\alpha$ 1</sub> (0.15418nm) x-ray source. Using the FWHM of the narrow Debye-Scherrer line at  $2\theta=39.948^\circ$ , which corresponds to Bragg diffraction from Pd(111) planes for the calculation. The value of  $D_{\text{ave}}$  is estimated to be 5nm, which is consistent with TEM observations.

FTIR is a useful tool to illustrate the co-electrodeposition of GOx-Pd onto the MWNTs. The FTIR results were displayed in Figure 8.3b. It is well known that the IR spectroscopy of proteins exhibits strong amide bands<sup>24</sup>, particularly the so-called amide I band which is the most

intense and useful. The amide I band represent primarily the C=O stretching vibration of the amine groups, coupled to in-plane bending of the N-H and stretching of the C-N bonds. For GOx-Pd-MWNT sample, the observed IR signals were located at  $\sim 565\text{cm}^{-1}$  (out-of-plane CO bending),  $668\text{cm}^{-1}$  (out-of-plane NH bending),  $1634\text{cm}^{-1}$  (CO stretching) and  $3240\text{cm}^{-1}$  (NH stretching with amide II overtone) were attributed to the characteristic IR bands of the peptide linkage of a protein. The IR transmittance of pristine MWNT is almost featureless, except a broad  $\sim 3444\text{cm}^{-1}$  band which is ascribed to adsorbed water molecules.

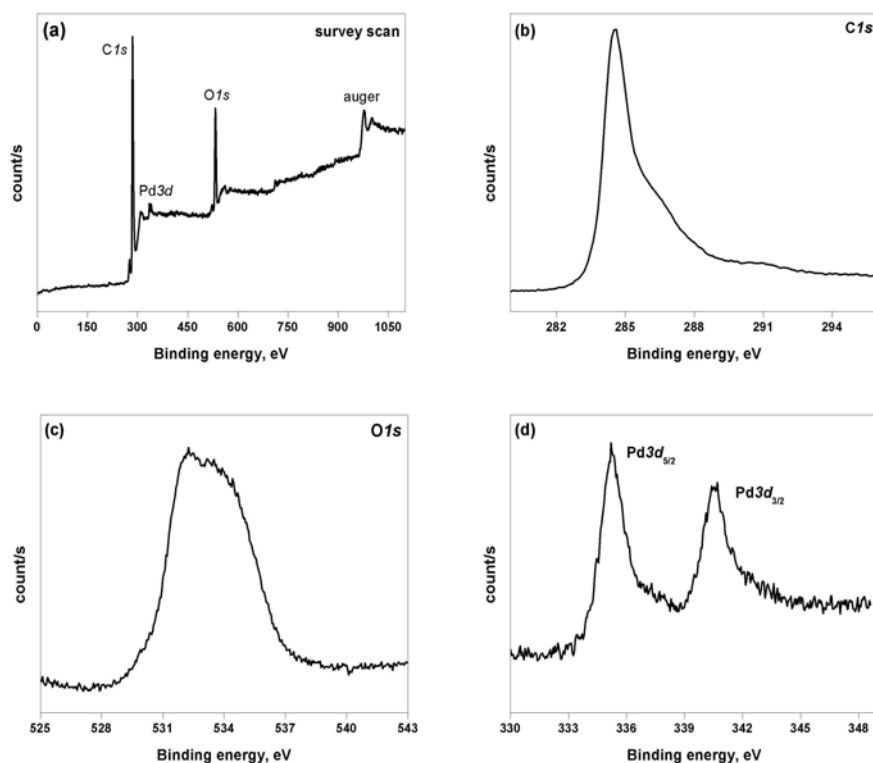


**Figure 8.4.** XPS spectra of Pd-MWNT composite (a) survey scan, (b) *C 1s*, (c) *O 1s*, and (d) *Pd 3d*.

### 8.2.5. XPS analysis

For XPS analysis, the MWNT powder was sonicated extensively in acetone until it became paste-like. The MWNT paste was cast onto the conducting XPS stud to form a film which adheres firmly to the stud. The electrodeposition of Pd nanoparticles (without GOx) was conducted directly using this MWNT-on-stud.

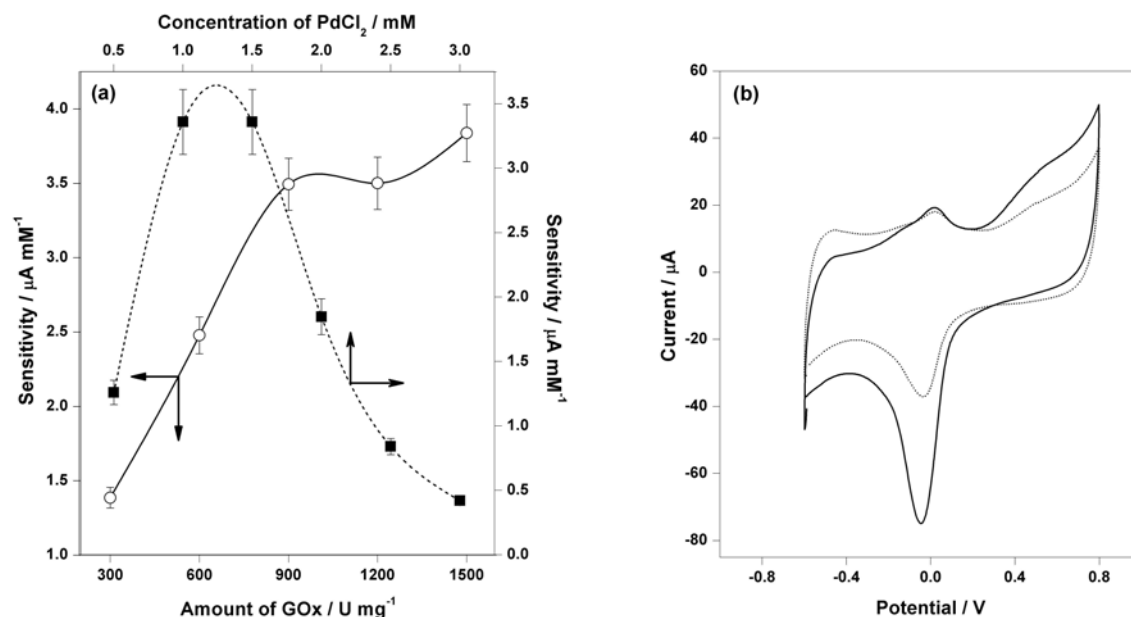


Figure 8.4 shows the XPS spectra of the electrodeposited Pd-MWNTs composite, without GOx enzyme. The binding energies for the Pd 3d<sub>5/2</sub> and 3d<sub>3/2</sub> peaks were located at 335.2 and 340.5eV respectively. The FWHM of the Pd 3d-doublet is ~1.1eV. The Pd 3d-doublet corresponds well to those of metallic Pd(0) from the standard spectra of elemental Pd. Thus the results of XRD and XPS confirmed the complete reduction of Pd<sup>2+</sup> anions and the formation of Pd(0) nanoparticles on MWNTs.

#### **8.2.6. Glucose quantification of GOx-Pd-MWNT-Nafion composite**

The optimization of the fabricated biosensor sensitivity towards the enzymatically liberated H<sub>2</sub>O<sub>2</sub> is studied primarily on MWNT-modified GCE and then the optimal conditions are applied to the Nafion-solubilized MWNT electrode. The amperometric response of the bioelectrodes towards 5mM glucose is monitored at an applied potential of +0.3V. A potential of +0.3V is judiciously chosen based on CV and HDV results (vide infra, Fig 8.5b & Fig 8.6). The influence of the composition of Pd and GOx on the analytical performance of the biosensor is presented as Figure 8.5a. It is noted that for a fixed amount of GOx (~1000U/mg), a concentration of ~1 to 1.5mM PdCl<sub>2</sub> gave a better detection towards hydrogen peroxide. But higher concentration of PdCl<sub>2</sub> (>1.5mM) resulted in the decrease of the biosensor performance. It is probable that at higher palladium salt concentration, the palladium ions started to compete with the GOx at the electrode surface or displaced GOx already adsorbed<sup>25</sup>. On the other hand, for a fixed concentration of 1mM of PdCl<sub>2</sub>, the performance of the biosensor shows a better performance of glucose sensing as the amount of GOx is increased in the electroplating bath. Still it is not feasible to use large amount of GOx in the fabrication of the biosensor, as this will increase its cost. Accordingly we have chosen electrodeposition conditions of ~1mM of PdCl<sub>2</sub> and ~1000U/mg of GOx as our optimal conditions. A slightly lower concentration of ~1mM PdCl<sub>2</sub> is used because at higher concentration of PdCl<sub>2</sub> the fabricated biosensor tends to have shorter storage stability period. In the case of Nafion-solubilized CNT electrode, the deposited

Pd-GOx biocomposite is observed to be a more durable and has better selectivity. Therefore we will focus primarily on this Pd-GOx-Nafion CNT electrode in the following discussion.



**Figure 8.5.** (a) Influence of the composition of  $\text{PdCl}_2$  and GOx on the biosensor performance towards  $5\text{ mM}$  glucose at an applied  $+0.3\text{ V}$ . For a fixed  $1000\text{ U/mg}$  of GOx, the results are shown as (■). For a fixed  $1\text{ mM}$   $\text{PdCl}_2$ , the results are shown as (○). (b) Cyclic voltammograms of Pd-GOx-Nafion MWNT before (dotted line) and after (solid line) adding  $0.25\text{ mM}$  of  $\text{H}_2\text{O}_2$  at a sweep rate of  $25\text{ mVs}^{-1}$ .

The cyclic voltammetric (CV) response of Pd-GOx-Nafion MWNT electrode towards the enzymatically liberated  $\text{H}_2\text{O}_2$  is simulated by adding  $0.25\text{ mM H}_2\text{O}_2$  at pH 7 buffer and it is illustrated as Figure 8.5b. It is well established that the oxidation of  $\text{H}_2\text{O}_2$  at a plain glassy carbon electrode starts close to  $+0.8\text{ V}$ <sup>22,25</sup>. But in the case of Pd-GOx-Nafion CNT electrode, an appreciable oxidation current begin at  $+0.3\text{ V}$ . This catalytic effect is attributed to the presence of Pd nanoparticles, which has substantially lowered the overvoltage oxidation of  $\text{H}_2\text{O}_2$  by about  $+0.5\text{ V}$ . This result is consistent with literature for other palladium-based electrodes and Pd-

electrodeposited electrodes<sup>22,25</sup>. In addition, we do not exclude the possibility that the Nafion-solubilized CNT itself also contributes to the enhanced detection towards  $\text{H}_2\text{O}_2$ <sup>23</sup>.

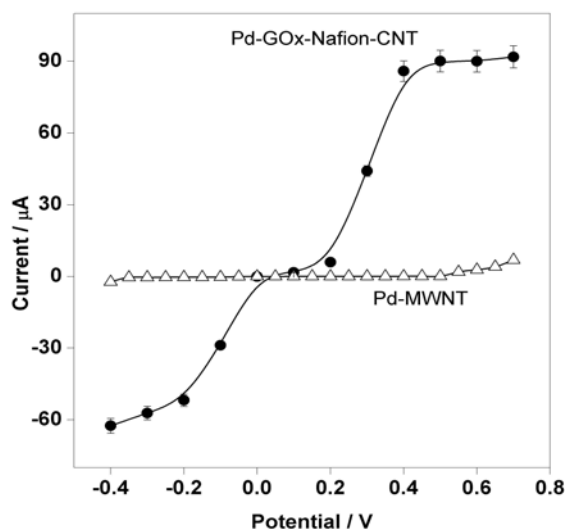


**Figure 8.6.** Hydrodynamic voltammograms of Pd-MWNT ( $\Delta$ ) and Pd-GOx-Nafion MWNT ( $\bullet$ ) electrodes in 15mM glucose.

The hydrodynamic voltammograms (HDV) for 15mM glucose at Pd-GOx-Nafion MWNT electrode is displayed as Figure 8.6. For the fabricated Pd-GOx-Nafion MWNT electrode, the oxidation of the enzymatically formed  $\text{H}_2\text{O}_2$  starts at potentials more positive than +0.2V and reaches a plateau around +0.4V to +0.8V, while the reduction starts at potentials more negative than 0V and reaches a maximum at about -0.3V. This indicates that the fabricated biosensor has a flexible operating potential range for the monitoring of the oxidation / reduction of  $\text{H}_2\text{O}_2$ . And by choosing the appropriate operating potential window, commonly encountered electroactive interferents can be selectively avoided. In the absence of GOx, the electrodeposited Pd-Nafion MWNT electrode is almost amperometrically insensitive to the presence of glucose,

save at higher potential ( $> +0.7V$ ) at which direct oxidation of glucose might take place. Hence the response of the Pd-GOx-Nafion MWNT electrode is due to the entrapped GOx enzymes.

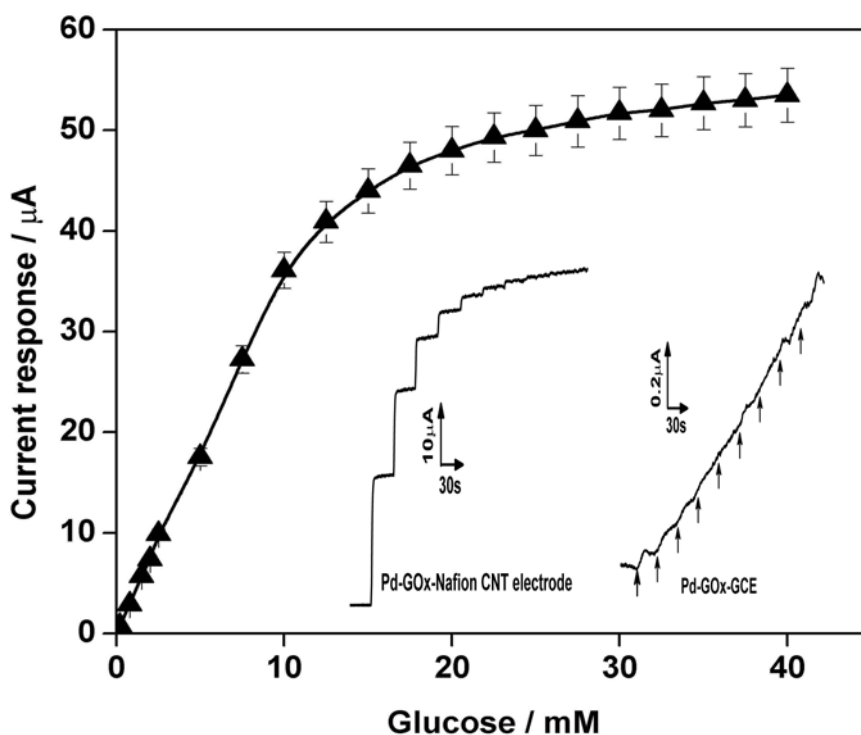


**Figure 8.7.** Calibration curve of the optimized Pd-GOx-Nafion MWNT bioelectrode. *Inset:* A comparative chronoamperometric response of Pd-GOx-Nafion MWNT and Pd-GOx GCE bioelectrodes upon successive addition of 5mM glucose at +0.3V.

The inset of Figure 8.7 shows the typical chronoamperometric responses of Pd-GOx GCE and Pd-GOx-Nafion MWNT electrodes for the successive addition of 5mM glucose at an applied potential of +0.3V. The Pd-GOx GCE is fabricated under identical conditions as the Pd-GOx-Nafion MWNT electrode. It can be seen that the absence of a CNT film greatly affects the conditions for the co-deposition of Pd-GOx and the glucose sensing capability. The Pd-GOx GCE gave a poor amperometric response of glucose. It did not exhibit sharp step-like responses and the

current signals were much smaller than those of MWNT-based bioelectrodes. Clearly, the presence of a MWNT film has resulted in a better performing glucose sensor. The co-deposition of Pd-GOx onto a plain GCE at pH 5.6 is considered futile and has been pointed out<sup>25</sup>. However when the co-deposition of Pd-GOx onto a Nafion-MWNT film is carried out under identical experimental conditions, the resulting Pd-GOx-Nafion MWNT electrode responds rapidly ( $t_{95\%} \approx 3$ s) to changes in the glucose level. The steady state calibration curve (Figure 8.7) exhibits a linearity up to  $\sim 12$ mM and the detection limit being 0.15mM (S/N=3).

The influence of common interfering electroactive substances such as uric acid (UA) and ascorbic (AA) is assessed and presented in Figure 8.8a. For Pd-GOx MWNT electrode, the interfering signals of 0.5mM UA and AA are significant and undermine glucose quantification at +0.3V. On the other hands, the interfering effects of adding 0.5mM UA and AA are eliminated for the Pd-GOx-Nafion MWNT electrode coated with an extra layer of 0.5% Nafion. If the Pd-GOx-Nafion MWNT electrode is not coated with an extra 0.5% Nafion membrane, the electrodes shows a slight response to the addition of 0.5mM UA / AA but the interfering signals are much weaker than Pd-GOx MWNT electrode. It is well known that Nafion is a negatively charged ployelectrolyte matrix and it reduces the permeability of negatively charged substrates<sup>26</sup>.

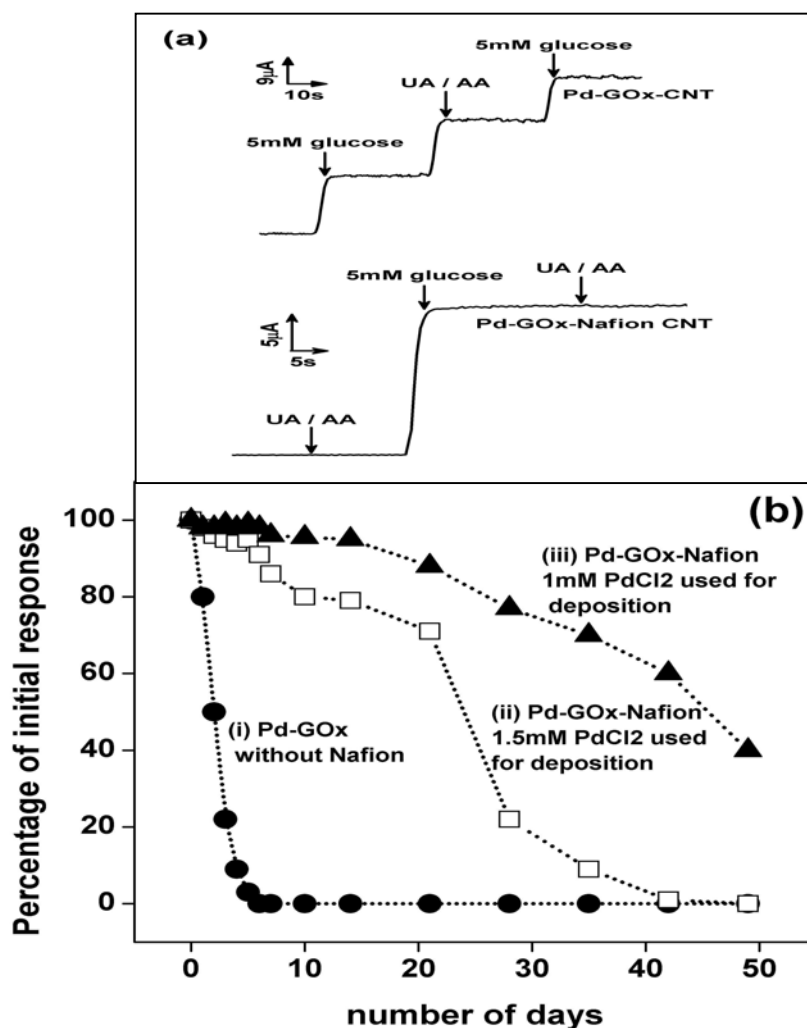


**Figure 8.8.** (a) Effects of interfering signals of 0.5mM uric acid (UA) and ascorbic acid (AA) on the performance of Pd-GOx-MWNT and Pd-GOx-Nafion MWNT bioelectrodes at +0.3V in 0.1M phosphate buffer pH 7; stirring rate: 300rpm. (b) Long term storage stability of the (i) Pd(1mM)-GOx MWNT, (ii) Pd(1.5mM)-GOx-Nafion MWNT and (iii) Pd(1mM)-GOx-Nafion MWNT bioelectrodes toward the sensing of 5mM glucose during a storage period of 50 days. Dotted lines are drawn for visual aid only.

The operational stability of the optimised Pd(1mM)-GOx-Nafion MWNT electrode was measured at +0.3V in 0.1M phosphate pH 7 buffer containing 5mM glucose. The relative deviation for ten times continuous determinations of 5mM glucose is less than ~3%, which indicates that the optimised Pd(1mM)-GOx-Nafion MWNT electrode has a good operational stability. The long-term storage stability of 3 different bio-electrodes was studied by measuring

the response to 5mM glucose and the results were presented in Figure 8.8b. The optimised Pd(1mM)-GOx-Nafion MWNT electrode lost at most ~5% of the initial response after a storage period of 14 days. But after 50 days of storage, the Pd(1mM)-GOx-Nafion MWNT electrode gradually began to lose its initial response and drop to ~40%. When a higher concentration of PdCl<sub>2</sub> (1.5mM) is used for the co-deposition of GOx onto Nafion-MWNT film, the as-fabricated Pd(1.5mM)-GOx-Nafion MWNT electrodes lost more than 5% of its initial response after a storage period of about 6 days. In the case of co-deposited Pd(1mM)-GOx onto plain MWNT film (without Nafion), the electrodes lost ~20% of its initial response just after 1 day of storage. It completely lost its biosensing capability after 6 days storage. The loss of activity response of the electrodes due to fouling is unlikely because there is no significant shift in the overpotentials of the HDV for the 3 bio-electrodes. The HDV plateau of Pd-GOx-Nafion-MWNT electrodes remain fairly constant but the HDV plateau of Pd-GOx-MWNT electrode is reduced, which indicates that small fragments of the MWNT film are broken off. The slow loss and denaturation of GOx enzymes due to temperature changes undergone from storage to room temperature may also contribute to the loss of sensitivity of the bioelectrodes<sup>26</sup>.

### **8.2.7. Conclusions**

A more controllable, stable and reproducible depositing of CNT film onto GCE can be achieved using homogeneous solution of (0.5%)Nafion-MWNT. The sidewalls of the MWNTs are not completely masked by the 0.5% Nafion and there are accessible sites for the incorporation of Pd-GOx biocomposites. The optimized Pd-GOx-Nafion MWNT bioelectrodes has a good glucose biosensing capability. An extra 0.5% Nafion coating is needed to completely suppress the interfering signals from UA and AA during the electrocatalytic oxidation of glucose at +0.3 V. It may be anticipated that other biomaterials and / or mediators can be incorporated in the Nafion-MWNT matrix for the fabrication of other useful biosensors.

### **8.3. Electrochemical genosensor based on gold nanoparticle-carbon nanotube hybrid**

The development of a DNA hybridization biosensor or genosensor involves the assembly of single stranded nucleic acid probes over a suitable solid support and transducing the hybridization events when the probes selectively capture its complementary target nucleic acids. Therefore the solid support should offer good surface chemistry for the systematic attachment of DNA or an affinity for DNA adsorption, and be compatible with the detection techniques.

An important issue in the fabrication of an electrochemical genosensor is the configurational freedom of the immobilized nucleic acid probes<sup>27</sup>. When hybridization events happen, the probe and target oligonucleotides must be free to hybridize with each other. Thus for a good genosensor, care must be taken to minimize the restriction of the immobilized probes configurational freedom in order to realize efficient hybridization.

DNA has been successfully attached to a great variety of surfaces and materials which are suitable for electrochemistry. They include mercury drops, carbon and gold materials, indium tin oxides (ITO) glass and conducting polymers<sup>27-29</sup>. Additionally, gold nanoparticles modified electrodes have been successfully used to immobilize thiolated nucleic acid<sup>30,31</sup> via the well-known gold-sulfur linkage.

Hence a hybrid of gold nanoparticles and CNTs will be a compatible heterostructure with many biological systems. Jiang et. al.<sup>32</sup> have attached gold nanoparticles to N-doped CNTs which have been functionalized with carboxylic acid groups via H<sub>2</sub>SO<sub>4</sub>-HNO<sub>3</sub> treatment. Hydrophobic interactions between octanethiol-capped gold nanoclusters and acetone-activated CNTs are also employed for the attachment of gold nanoparticles<sup>33</sup>. CNT modified with cationic polyethyleneamine, anionic citric acid and heating in NH<sub>3</sub> atmosphere has been shown to facilitate gold nanoparticles attachment<sup>34</sup>. Liu L. et al.<sup>35</sup>, on the other hand, utilize thiol-terminated pyrene which anchored on CNT via  $\pi$ - $\pi$  stacking interaction and the thiol terminals act



as interlinkers for the self-assembly of gold nanoparticles to CNT surfaces. However there is a lack of report on the application and performance of these Au-CNT hybrids.

Therefore it is the aim of this work to demonstrate the electrochemical genosensing properties of Au-MWNT hybrid. Single stranded thiolated oligonucleotide probes are immobilized onto the Au-MWNT hybrid through gold-sulfur linkage. The Au-MWNT hybrid is further modified with 6-mercapto-1-hexanol (MCH, SH-(CH<sub>2</sub>)<sub>6</sub>-OH) to enhance the efficiency of hybridization events by providing the oligonucleotide probes better configurational freedom<sup>27</sup>.

### **8.3.1. Experimental procedures**

The immobilization and hybridization events of the oligonucleotides are monitored using electrochemical impedance spectroscopy (EIS), cyclic voltammetry (CV) and a.c. voltammetry (ACV) techniques. Particularly, the hybridization events are detected with tris(2,2'-bipyridyl) ruthenium(II) mediated guanine oxidation<sup>36,37</sup>. Differentiation of complementary and mismatched hybridization events can be realized using Ru(bpy)<sub>3</sub><sup>2+</sup> as mediator for the oxidation of extra guanine residues attached to the oligonucleotides with mismatched bases.

The single-stranded oligonucleotides come with and without mercaptohexyl group at the 5'-phosphate end and the sequences are as follow:

(1) SH-(CH<sub>2</sub>)<sub>6</sub>-5' -TTTACTTTAATCAACTAT - 3' (Probe)

(2) 5' -ATAGTTGCTTACAGTAAA - 3' (complementary)

(3) 5' -GGATAGTTGCAAAACAGTAAA - 3' (2-mismatch)

(4) 5' -GGGATAGTTGCAA TACAGTAAA - 3' (1-mismatch)

Oligonucleotides (2'), (3'), and (4') with mercaptohexyl group at the 5'-phosphate end were used for CV measurements (see Figure 8.14).

The attachment of gold nanoparticles to MWNTs was carried out using citric acid (CA). The MWNT and citric acid (2:1 mass ratio) was sonicated extensively in distilled water. The excess water was evaporated until a MWNT paste was obtained. This MWNT paste was placed in

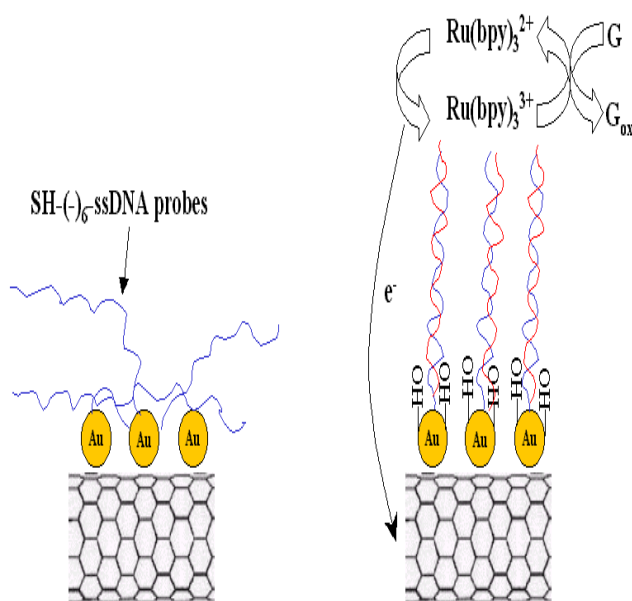
a pre-heated furnace at 300°C for 2 h. This process creates plenty of C-O, C=O and COOH moieties on the MWNT surfaces, and enhances the MWNT dispersion in water (vide infra, XPS spectrum). Typically, 10mg of the modified MWNT was dispersed and stirred in 50ml of 0.2g auric chloride solution at 70°C for 1 h. 50ml of 0.1g citric acid was added dropwise and continued stirring for another 4 h. The resulting products were filtered, washed with distilled water and dried.

Electrochemical impedance spectroscopy (EIS), cyclic voltammetry (CV) and a.c. voltammetry (ACV) techniques were performed with a Solartron SI 1280B Potentiostat / Galvanostats. A 3-electrode system was used: A homemade MWNT powder  $\mu$ -electrode as the working electrode. It was made of a  $\sim$ 100 $\mu$ m diameter platinum wire sealed in a glass tube. A cavity of  $\sim$ 25 $\mu$ m was controllably etched by applying an alternating voltage of 20–30V in concentrated CaCl<sub>2</sub> solution, with a graphite rod as the opposite electrode. The Ag/AgCl (3M) electrode was used as the reference electrode and a platinum coil as the counter electrode. EIS measurements were conducted in the presence of 10mM K<sub>3</sub>[Fe(CN)<sub>6</sub>]/K<sub>4</sub>Fe(CN)<sub>6</sub>] (1:1) mixture as a redox probe. A bias potential of 0.17V in the frequency range of 10mHz to 20kHz and an alternating voltage 10mV were used for the EIS measurements. All CV measurements were taken with a single scan at 25mVs<sup>-1</sup> for the oxidation of guanine via Ru(bpy)<sub>3</sub><sup>2+</sup> mediator within a potential range of 0V to 1.2V. Likewise the ACVs were recorded for a single scan at 5Hz and 10mV amplitude.

For electrochemical measurements, the Au-MWNT powder was packed into the  $\mu$ -electrode and polished with a weighing paper. The Au-MWNT  $\mu$ -electrode was immersed in 1.5 $\mu$ M solution of probe (*I*) in a 0.5M PBS buffer for 2 h at 25°C and then rinsed with purified water. The Au-MWNT  $\mu$ -electrode modified with immobilized probe (*I*) was treated in 1mM 6-mercapto-1-hexanol (MCH) for 2 h to mask the unmodified gold nanoparticles. In addition, the

negative dipole of the –OH terminus helps to project the negatively charged DNA backbone into the solution, rendering it greater configurational freedom<sup>38</sup>.

The modified Au-MWNT-probe(1)  $\mu$ -electrode was immersed in a hybridization buffer (Tris buffer 1M NaCl pH 8.5) containing the 1.5 $\mu$ M complementary oligonucleotides (2) for different exposure time (see Figure 8.13). It was then rinsed with purified water before each voltammetric measurements.



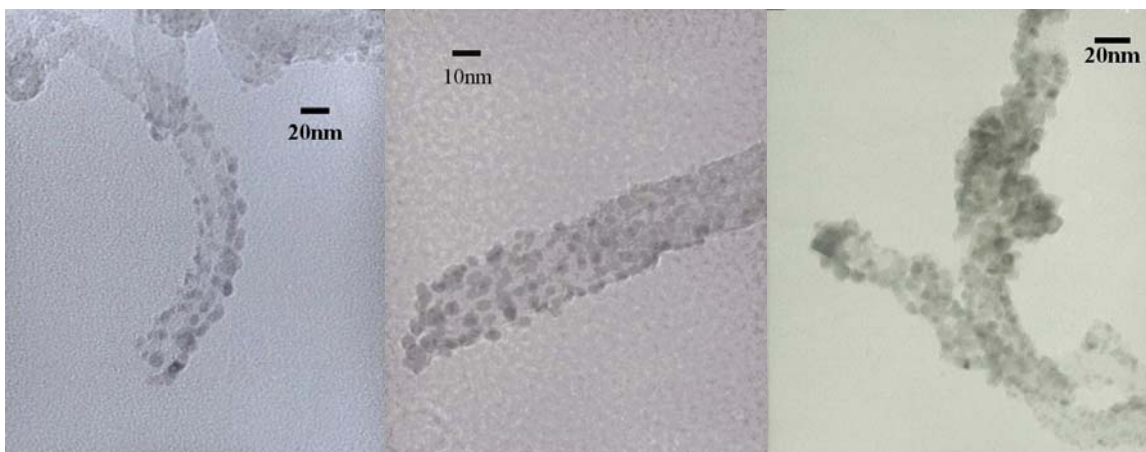
**Figure 8.9.** Schematic illustration of self-assembly of thiolated oligonucleotides onto Au-MWNT hybrid. The use of MCH assists the erection of *ss*DNA and facilitates hybridization of complementary oligonucleotides, which is detected via mediator  $\text{Ru}(\text{bpy})_3^{2+}$ . (*ss* denotes single stranded)

Figure 8.9 is the schematic illustration of the self-assembly of thiolated oligonucleotide probes (1) onto Au-CNT hybrid. Post-treatment by a spacer thiol, mercaptohexanol (MCH), not only helps to displace non-specifically adsorbed HS-*ss*DNA molecules but also erects the DNA molecules, making it more accessible for specific hybridization<sup>27,28,38</sup>. In a neutron reflectivity

studies by Levicky et al.<sup>39</sup>, thiolated ss-DNA was self-assembled onto a gold surface and it was shown that the ss-DNA was lying flat on the gold surface with multiple adsorption points. In this case, the hybridization efficiency was <10% as the probe DNA had limited configurational freedom. When gold surface was modified with MCH, the hybridization efficiency was enhanced to almost 100%. Likewise we believe that the modification of the gold nanoparticles with MCH has similar effects, though we did not rigorously prove it.

### **8.3.2. Electron micrographs of gold nanoparticle-MWNT hybrid**

The Au-MWNT powder was dispersed in water and transferred to a formvar coated Cu grid for TEM observation. The TEM image shows that gold nanoparticles are successfully bound to the MWNTs (Figure 8.10). The diameter distribution of the gold nanoparticle is ~5-9nm. Large clusters of Au nanoparticles deposited on MWNT can also be observed.



**Figure 8.10.** TEM images of gold nanoparticle-MWNT hybrids

### 8.3.3. XRD patterns & UV-vis spectroscopy

The UV-vis absorption spectrum of Au nanoparticle-MWNT composite was measured using Cary 50 Bio UV-vis Spectrophotometer. As shown in Figure 8.11b, the UV-vis absorption spectrum of Au-CNT hybrid shows the presence of the surface plasmon band of gold nanoparticles at  $\sim 520\text{nm}$ .

The XRD pattern of the Au nanoparticle-MWNT hybrid is shown in Figure 8.11a. The major diffraction peaks of Au nanoparticles can be indexed as the Au face-centered cubic (fcc) phase based on the JCPDS data. The diffraction peaks of Au nanoparticles at  $39.9^\circ$ ,  $46.4^\circ$  and  $67.9^\circ$  can be assigned to (111), (200), (220) and (311) crystalline planes respectively. The average size of the Au nanoparticles is  $\sim 7\text{nm}$  as calculated by the Scherrer formula.

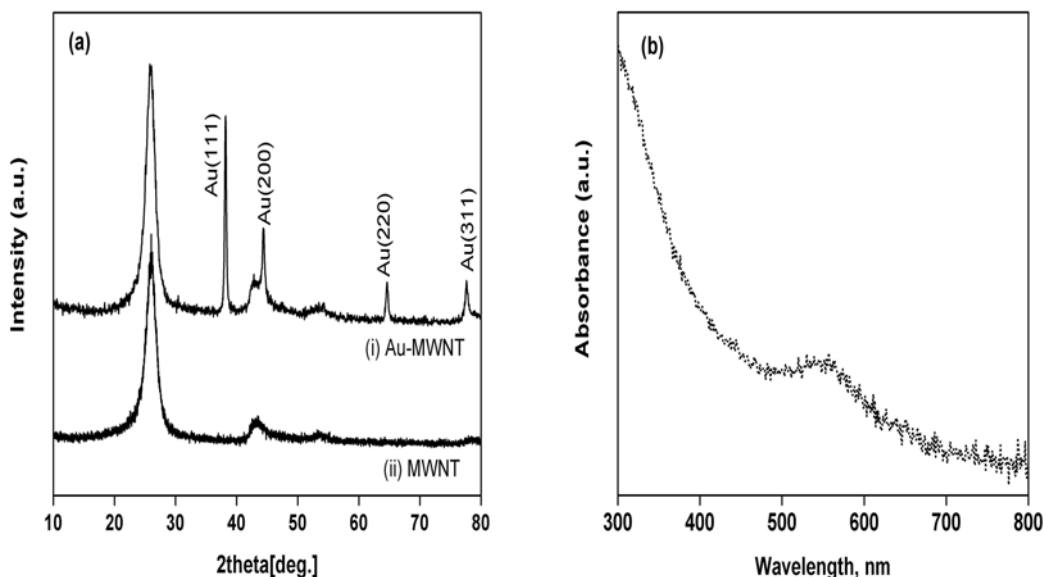


**Figure 8.11.** (a) XRD patterns of (i) Au nanoparticle-MWNT and (ii) pristine MWNT. (b) UV-vis absorption spectrum of MWNT bound with gold nanoparticles.

### 8.3.4. XPS analysis

Figure 8.12a shows the XPS core-level C1s of citric acid functionalized MWNT. The C1s spectrum of CA functionalized MWNT was deconvoluted into 284.5eV (C-C), 285.8eV (C-O), 288.2eV (C=O) and 290eV (COOH) peaks. The creation of surface oxygen functionalities is important for the attachment of gold nanoparticles onto the exterior wall of the MWNTs. The Au nanoparticle-MWNT hybrid exhibits binding energies for the Au 4f<sub>7/2</sub> and 4f<sub>5/2</sub> peaks were located at 84.0 and 87.7eV respectively. Thus the results of XRD and XPS confirmed the formation of Au nanoparticles on MWNTs.

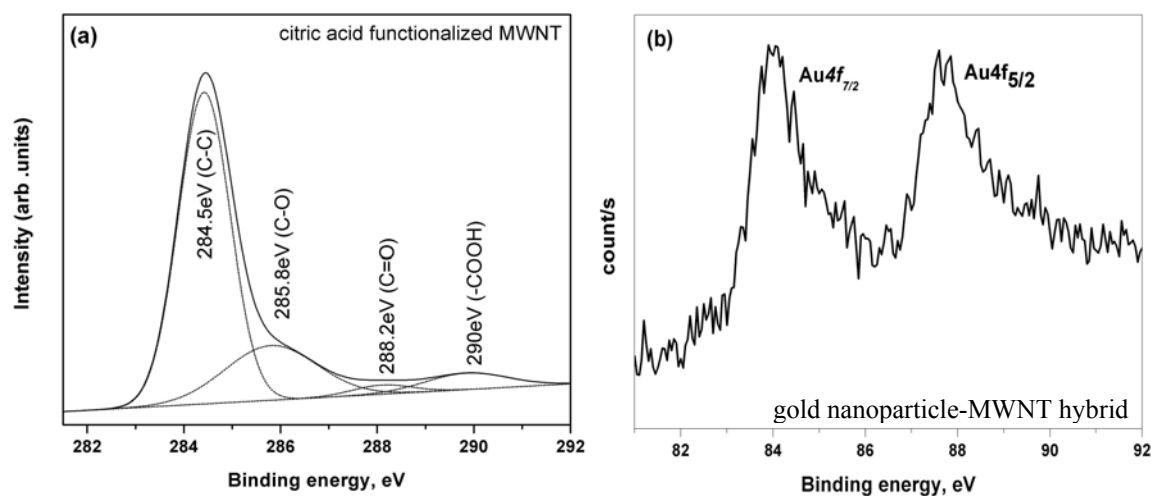


**Figure 8.12.** (a) XPS core-level C1s of citric acid functionalized-MWNT and (b) core-level Au4f of gold nanoparticle-MWNT hybrid.

### 8.3.5. Electrochemical impedance spectroscopy (EIS)

The immobilization and hybridization of the oligonucleotides can be effectively monitored using EIS techniques<sup>18</sup>. The assembly of negatively charged oligonucleotides complexes onto electrode supports greatly altered its interfacial properties such as capacitance and electron transfer resistance ( $R_{et}$ ). Consequently the EIS response of oligonucleotide-modified

electrodes in the presence of a highly negative charged solubilized redox probe,  $[\text{Fe}(\text{CN})_6]^{3-/4-}$  mixture, are expected to increase the  $R_{\text{et}}$  due to mutual repulsion of the oligonucleotide and the negatively charge redox probe.

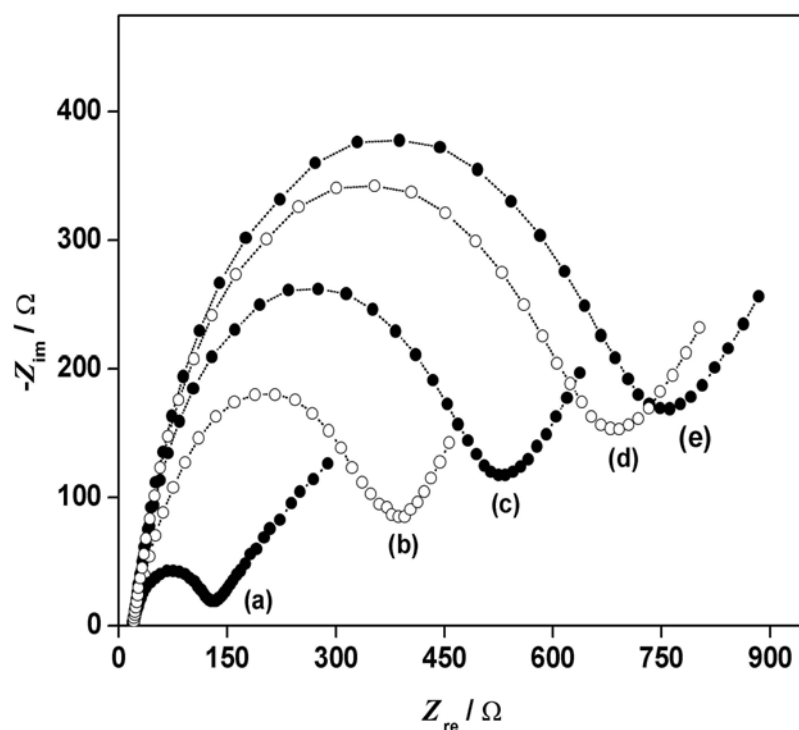


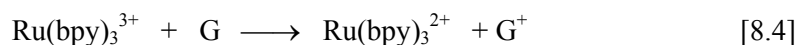
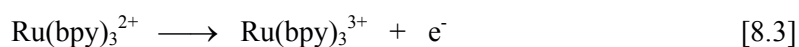
**Figure 8.13.** Nyquist diagram ( $Z_{\text{im}}$  vs  $Z_{\text{re}}$ ) for EIS measurements of Au-MWNT  $\mu$ -electrode in the presence of 10mM  $[\text{Fe}(\text{CN})_6]^{3-/4-}$  (1:1-mixture): (a) modified with MCH and without any attached oligonucleotides, (b) modified with oligonucleotide probes (**1**) and (c, d, e) duplexed with complementary oligonucleotides (**2**), 1.5 $\mu\text{M}$ , for 30, 90, 120mins respectively. The frequency range from 10mHz to 20kHz at an applied constant bias potential of +0.17V, with amplitude of alternating voltage at 10mV in 10mM PBS buffer, pH 7.0.

From Figure 8.13, it is clear that the attachment of oligonucleotides changes the  $R_{\text{et}}$  of the Au-MWNT  $\mu$ -electrode significantly. The  $R_{\text{et}}$  of MCH-Au-MWNT  $\mu$ -electrode, modified solely with MCH for 2 h, is  $\sim 125\Omega$ . But when the electrode is modified with the oligonucleotide probe (**1**) solution and MCH, the  $R_{\text{et}}$  is increased to  $\sim 385\Omega$ . The increment of  $R_{\text{et}}$  indicates that negatively charged single-stranded oligonucleotide probes (**1**) are self-assembled on the Au-

MWNT  $\mu$ -electrode. The hybridization events can be monitored progressively using EIS technique when the Au-MWNT-probe (1)  $\mu$ -electrode is exposed to the complementary strands (2) for different time intervals. It can be seen that the  $R_{et}$  increased for longer hybridization time and the  $R_{et}$  approached a maximum value of  $\sim 750\Omega$ . No further increment in the  $R_{et}$  when the hybridization time is extended beyond 2hr. Therefore a hybridization period of  $\sim 2$ hr is chosen for the duplexing of the complementary oligonucleotides. Although EIS measurements easily monitor hybridization events, it cannot differentiate target oligonucleotides with mismatches<sup>18,39</sup>. Our approach to distinguish base-pair mismatch is based on the catalytic oxidation of guanine using  $Ru(bpy)_3^{2+}$  as the mediator<sup>36,37</sup>, relying on voltammetric techniques.

### **8.3.6. Cyclic voltammetry – guanine oxidation**

It has been reported that electrochemical detection of DNA can be achieved using guanine (G) oxidation chemistry<sup>120,121</sup>. In this approach, a redox-active mediator such as  $Ru(bpy)_3^{2+}$  is used to mediate the oxidation of guanine, which can be described by a 2-step mechanism :



The Au-MWNT  $\mu$ -electrode oxidized the mediator to a  $Ru(bpy)_3^{3+}$  state, which is capable of removing an electron from guanine in DNA and converts it to an oxidized guanine. At the same time,  $Ru(bpy)_3^{2+}$  is re-generated and completed a catalytic cycle. The catalytic cycles repeat over a large number of times and deliver large electrical signals to the electrode. The main reason for the rapid electron transfer between  $Ru(bpy)_3^{2+}$  and guanine is that the oxidation of guanine is almost identical to that of  $Ru(bpy)_3^{2+}$ <sup>36,37</sup>.



In order to differentiate complementary and mismatched oligonucleotides, the CV responses of thiolated target oligonucleotides (**2'**), (**3'**), (**4'**) self-assembled onto Au-CNT  $\mu$ -electrode in the presence of  $\text{Ru}(\text{bpy})_3^{2+}$  mediator were studied (see Figure 8.14). Oligonucleotide probe (**I**) is not attached to the Au-CNT hybrid for these CV measurements since it does not contain guanine bases. For MCH-modified Au-MWNT  $\mu$ -electrode, whereby no oligonucleotide is attached, the redox potential of  $\text{Ru}(\text{bpy})_3^{2+}$  is detected at 1.05V which is consistent with literature<sup>36,37</sup>. Importantly, this suggests that MCH-Au-MWNT is a compatible interface for the electrochemistry of  $\text{Ru}(\text{bpy})_3^{2+}$ , which would not be the case with gold-thiol monolayers<sup>37</sup>.

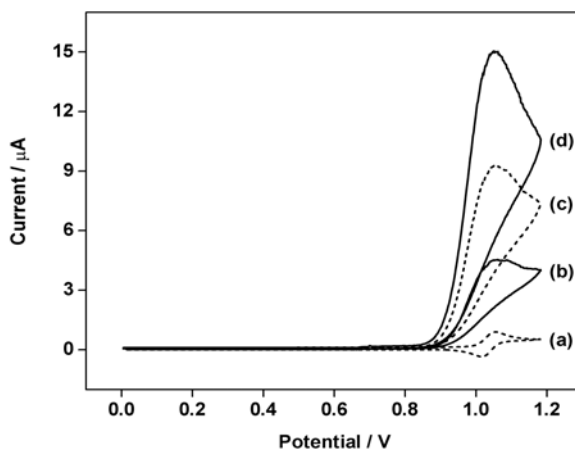


**Figure 8.14.** Cyclic voltammograms of  $\text{Ru}(\text{bpy})_3^{2+}$  ( $30\mu\text{M}$ ) in  $50\text{mM}$  phosphate buffer at  $\text{pH}$  7 with  $700\text{mM}$   $\text{NaCl}$  at  $25\text{mVs}^{-1}$ : When Au-MWNT  $\mu$ -electrode is modified with (a) MCH only, (b) complementary *ss*-oligonucleotide (**2'**), (c) 2 mismatched *ss*-oligonucleotide (**3'**) and (d) single mismatched *ss*-oligonucleotide (**4'**).

This is because even though the gold nanoparticles are modified with MCH but the CNT support permits access of  $\text{Ru}(\text{bpy})_3^{2+}$  and detection. Non-specific binding of oligonucleotides is tested with the non-thiolated target oligonucleotides (**2,3,4**). The Au-MWNT  $\mu$ -electrode is similarly exposed to the non-thiolated target oligonucleotides and followed by MCH treatment and did not observe any sharp increase for the oxidation current of  $\text{Ru}(\text{bpy})_3^{2+}$ . Therefore we can

omit non-specific binding of DNA because the assembly of thiolated DNA should proceed via gold-thiol linkage and the strong affinity of the thiol group on MCH for gold resulted in the displacement of non-specifically adsorbed DNA<sup>27,28,38</sup>. From Figure 8.14 it can be seen that the CV responses of the 3 target oligonucleotides are distinguishable, which is attributed to the different number of guanine residues they possess. Both mismatched target oligonucleotides (**3'**, **4'**) are given extra guanine bases so as to make them more electrochemically discernible. Thus it is possible to distinguish complementary, 2-mismatch and single-mismatch hybridization events. For this purpose, we use AC voltammetry techniques to improve the sensitivity. The probe (**1**) is attached to the Au-MWNT hybrid and followed by the hybridization of non-thiolated targets (**2,3,4**).

#### **8.3.7. a.c. voltammetry (ACV) – guanine oxidation**

Figure 8.15 shows the results of the ACV measurements in the presence of  $\text{Ru}(\text{bpy})_3^{2+}$ . When the Au-MWNT-probe(**1**)  $\mu$ -electrode is hybridized with the target oligonucleotides, a significant current increase is noted. This is anticipated from the CV measurements. Likewise the electron transfer from the guanines of the target oligonucleotides to the  $\text{Ru}(\text{bpy})_3^{2+}$  is responsible for the increase in the oxidation current. Furthermore, the ACV signals for each target strand (**2**), (**3**) and (**4**) are also distinguishable. The direct oxidation of guanine of the target oligonucleotides (**2,3,4**) using Au-MWNT  $\mu$ -electrode, without mediator  $\text{Ru}(\text{bpy})_3^{2+}$ , is very weak and did not show a clear distinction of electrochemical signals among the 3 target oligonucleotides. Thus it is not use for the detection of hybridization events. Nevertheless, the use of  $\text{Ru}(\text{bpy})_3^{2+}$  as mediator and deliberate attachment of extra guanine residues to the mismatched oligonucleotides has enabled us to tell apart complementary and mismatched hybridization events.

We have repeated the ACV measurements 10 times for each oligonucleotide (**1,2,3,4**) whereby the  $\mu$ -electrode is always loaded with fresh Au-CNT powder. This is to make sure that

the ACV results are not due to experimental artifacts. The inset of Fig 8.15 shows the results of the repeated ACV measurements. For modified Au-MWNT-probe(1), the ACV signal yields an oxidation peak value of  $0.335\mu\text{A}$  with a relative deviation of 11%. When it is hybridized with the target oligonucleotides, the ACV signals are increased to  $1.75\mu\text{A} \pm 10\%$ ,  $4.13\mu\text{A} \pm 13\%$  and  $7.22\mu\text{A} \pm 15\%$  for target oligonucleotides (2), (3) and (4) respectively. Although the relative deviation for the ACV signals is about 10-15%, it does not undermine the genosensing capability of the Au-CNT hybrid. This is because the ACV signals for the 3 different hybridization events are still distinguishable using  $\text{Ru}(\text{bpy})_3^{2+}$  as the mediator.

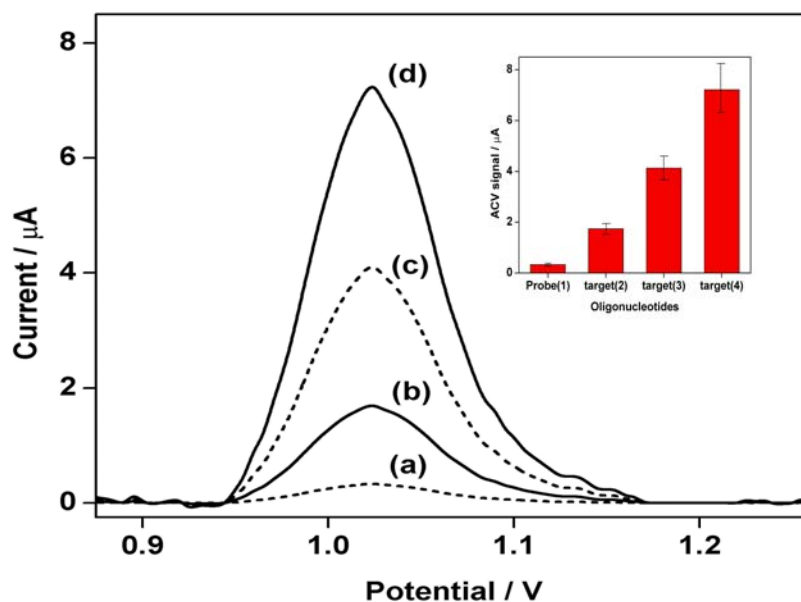


**Figure 8.15.** AC voltammetry measurements for Au-MWNT  $\mu$ -electrode (a) functionalized with probe oligonucleotides (1), (b) hybridized with complementary oligonucleotides (2), (c) with 2-mismatched target oligonucleotides (3) and (d) with 1-mismatched target oligonucleotides (4). ACVs are conducted with a sinusoidal wave of 5Hz and 10mV amplitude. *Inset:* Repeated ACV measurements for each oligonucleotide whereby the  $\mu$ -electrode is always loaded with fresh Au-MWNT powder.

Gold nanoparticle-carbon nanotube hybrid is a compatible heterostructure for the self-assembly of thiolated DNA and can be extended to other biomolecules such as RNA and enzymes. The gold nanoparticles act as the anchoring sites for the thiolated biomolecules such

that high chemical specificity in the immobilization of oligonucleotides can be achieved via stable gold-thiol linkages and the presence of MCH enhanced hybridization events and displaced non-specifically adsorbed DNA. Carbon nanotubes play a complementary role as a support which serves as a fast electron-transfer center and detected the catalytic oxidation current of  $\text{Ru}(\text{bpy})_3^{2+}$  mediator. Using sensitive ACV techniques, the Au-MWNT hybrid can be used as a reliable DNA hybridization biosensor.

### **8.3.8. Conclusions.**

A simple electrodeposition method has employed to attach Pd nanoparticles and glucose oxidase onto MWNT. This technique has been extended to Nafion-solubilized MWNT. The Pd-GOx-Nafion MWNT electrode shows excellent glucose sensing at relatively low voltage (+3V) due to the presence of Pd nanoparticles. An additional 0.5% Nafion membrane eliminates interfering effects of uric acid and ascorbic acid and improves the long term storage stability of the bio-electrode.

Carboxylic acid (-COOH) functionalized carbon nanotubes can be easily prepared using citric acid. XPS spectra show that -COOH moiety is created when CNT/citric acid paste is baked at 300°C. The gold nanoparticle-carbon nanotube hybrid was tested as a genosensor. Thiolated oligonucleotides can be anchored onto the gold nanoparticles via sulfur-gold linkage. The as-fabricated genosensor is able to differentiate complementary and mismatched oligonucleotides using highly sensitive electrochemical techniques such as ACV and EIS measurements.

Though not shown in this thesis, the citric acid treatment used in preparing nano-Au/CNT hybrid has been used in preparing the nano-Pt/CNT hybrid with Pt particle size of ~2-3nm. This well-dispersed Pt/CNT hybrid has been used as the electrodes (both anode and cathode) for  $\text{H}_2\text{-O}_2$  polymer electrolyte membrane (PEM) fuel cells and shown a 25% higher energy output density as compared to conventional Pt/carbon black electrodes under identical operation conditions.

**References**

- [1] J. Liu, A.G. Rinzler, H.J. Dai, J.H. Hafner, R.K. Bradley, P.J. Boul, A. Lu, T. Iverson, K. Shelimov, C.B. Huffman, F. Rodriguez-Macias, Y.S. Shon, T.R. Lee, D.T. Colbert, R.E. Smalley, *Science* 280, 1253 (1998).
- [2] P.M. Ajayan, T.W. Ebbesen, T. Ichihashi, S. Iijima, K. Tanigaki, H. Hiura, *Nature (London)* 362, 522 (1993).
- [3] B. Xue, P. Chen, Q. Hong, J. Lin, K.L. Tan, *J. Mater. Chem.* 11, 2378 (2001).
- [4] L. Qian, X.R. Yang, *Talanta* 69, 957 (2006).
- [5] Y. Bando, D. Golberg, M. Mitome, K. Kurashima, T. Sato, *Chem. Phys. Lett.* 346, 29 (2001).
- [6] M.M. Shaijumon, S. Ramaprabhu, N. Rajalakshmi, *Appl. Phys. Lett.* 88, 253105 (2006).
- [7] K. Kim, S.H. Lee, W. Yi, J. Kim, J.W. Choi, Y. Park, J. Jin, *Adv. Mater.* 15, 1618 (2003).
- [8] K.C. Chin, A. Gohel, W.Z. Chen, H.I. Elim, G.L. Chong, C.H. Sow, A.T.S. Wee, *Chem. Phys. Lett.* 409, 85 (2005).
- [9] S.C. Tang, J.J. Davis, M.L.H. Green, A.O. Hill, Y.C. Leung, P.J. Sadler, *J. Chem. Soc., Chem. Commun.* 1803 (1995).
- [10] (a) B.R. Azamian, J.J. Davis, K.S. Coleman, C.B. Bagshaw, M.L.H. Green, *J. Am. Chem. Soc.* 124, 12664 (2002). (b) R.J. Chen, Y. Zhang, D. Wang, H. Dai, *J. Am. Chem. Soc.* 123, 3838 (2001).
- [11] K.A. Williams, P.T.M. Veenhuizen, B.G. de la Torre, R. Eritja, C. Dekker, *Nature (London)* 420, 761 (2002).
- [12] See *Biosensors and Bioelectronics*, a principal international journal devoted to research, design development and application of biosensors and bioelectronics.
- [13] (a) X. Luo, J. Xu, W. Zhao, H. Chen, *Biosens. Bioelectron.* 19, 1295 (2004). (b) F. Patolsky, G. Tao, E. Katz, I. Willner, *J. Electroanal. Chem.* 454, 9 (1998). (c) H. Huang, N. Hu, Y. Zeng, G. Zhou, *Anal. Biochem.* 308, 141 (2002). (d) J.F. Rusling, A.F. Nassar, *J. Am. Chem. Soc.* 115, 11891 (1993). (e) A.A. Karyakin, A.K. Strakhova, E.E. Karyakina, S.D. Varfolomeyev, A.K. Yatsimirsky, *Synth. Met.* 60, 289 (1993). (f) C. Ramalechume, V. Yegnaraman, A.B. Mandal, *J. Solid State Electrochem.* 10, 499 (2006).
- [14] P.J. Britto, K.S.V. Santhanam, P.M. Ajayan, *Bioelectrochem. Bioenerg.* 41, 121 (1996).
- [15] J.J. Davis, R.J. Coles, H.A. Hill, *J. Electroanal. Chem.* 440, 279 (1997).
- [16] C.S. Cha, C.M. Li, H.X. Yang, P.F. Liu, *J. Electroanal. Chem.* 368, 47 (1994).
- [17] (a) Analytical applications of immobilized enzyme reactors, edited by S. Lam, G. Malikin. Blackie academic & Professional, Glasgow 1994. (b) Electroenzymology Coenzyme regeneration, edited by K. Nakamura, M. Aizawa, O. Miyawaki. Springer-Verlag 1988. (c) P.T.

Kissinger, W.R. Heineman, J. Chem. Edu. 60, 702 (1983). (d) E. Laviron, J. Electroanal. Chem. 101, 19 (1979).

[18] E. Katz, I. Willner, Electroanalysis 15, 913 (2003); and references therein.

[19] Y. Ikariyama, S. Yamauchi, J. Electrochem. Soc. 136, 702 (1989).

[20] H. Xue, W. Sun, B. He, Z. Shen, Synth. Met. 135, 831 (2003).

[21] A. Guiseppi-Eli, C. Lei, R.H. Baughman, Nanotechnology 13, 559 (2002).

[22] Q. Chi, S. Dong, Anal. Chim. Acta. 278, 17 (1993).

[23] J. Wang, M. Musameh, Y. Lin, J. Am. Chem. Soc. 125, 2408 (2003).

[24] Infrared analysis of peptides and proteins: principles and applications, edited by B.R. Singh. American Chemical Society 2000.

[25] H. Sakslund, J. Wang, J. Electroanal. Chem. 374, 71 (1994).

[26] D.R. Shankaran, N. Uehara, T. Nato, Biosens. Bioelectron. 18, 721 (2003).

[27] J.J. Gooding, Electroanalysis 14 (2002) 1149.

[28] M. C. Homs, Anal. Lett. 35 (2002) 1875.

[29] F. Lucarelli, G. Marrazza, A.P.F. Turner, M. Mascine, Biosens. Bioelectron. 19 (2004) 515.

[30] S. Liu, H. Ju, Biosens. Bioelectron. 19 (2003) 177.

[31] O. Lioubashevski, V.I. Chegel, F. Patolsky, E. Katz, I. Willner, J. Am. Chem. Soc. 126 (2004) 7133.

[32] K. Jiang, A. Eitan, L.S. Schadler, P.M. Ajayan, R.W. Siegel, Nano Lett 3 (2003) 275.

[33] A.V. Ellis, K. Vijayamohan, R. Goswami, N. Chakrapani, L.S. Ramanathan, P.M. Ajayan, G. Ramanath, Nano Lett. 3 (2003) 279.

[34] L. Jiang, L. Gao, Carbon 41 (2003) 2923.

[35] L. Liu, T. Wang, J. Li, Z. Guo, L. Dai, D. Zhang, D. Zhu, Chem. Phys. Lett 367 (2003) 747.

[36] H. H. Thorp, Trends Biotechnol. 16 (1998) 117.

[37] M.E. Napier, H. H. Thorp, Langmuir 13 (1997) 6342.

[38] R. Levicky, T.M. Herne, M.J. Tarlov, S.K. Satija, J. Am. Chem. Soc. 120 (1998) 9787.

[39] A. Bardea, F. Patolsky, A. Dagan, I. Willner, Chem. Commun. 1 (1999) 21.

## **Chapter 9. Functionalization of carbon nanotubes**

### *Summary*

Hydroxyl (-OH) functionalized single-walled carbon nanotubes were studied in section (9.1). Various spectroscopic techniques were employed to characterize these -OH functionalized SWNTs. In section (9.2), a gravitational-dependent, thermally-induced self-diffraction phenomenon of octadecylamine-grafted MWNTs was described.

## **9.1. Hydroxyl (-OH) functionalized single-walled carbon nanotubes**

### *Introduction*

The functionalization of single walled carbon nanotube (SWNT) not only gives insight into the fundamental chemistry of carbon nanotubes (CNT) but also allows one to chemically engineer its physical and chemical properties<sup>1</sup>. The sidewalls of carbon nanotubes have been demonstrated to undergo extensive covalent and non-covalent chemistry such as carbene chemistry, nitrene addition, hydrogenation via Birch reduction, fluorination, alkylation and 1,3-dipolar cycloaddition<sup>2,3</sup>. Besides wet chemistry, solid-phase mechanochemistry has also been applied for large scale functionalization and shortening of SWNTs<sup>4-7</sup>. Under optimal conditions, reactive gases (ammonia, chlorine, etc) and / or solid chemicals (KOH and cyclodextrins) are ball milled with carbon nanotube to achieve sidewall functionalization and solubilization<sup>4,6</sup>. This carbon nanotube chemistry has been monitored using spectroscopic techniques, which revealed that the electronic band structure of SWNTs could be selectively modified<sup>1-3</sup>.

Oxidizing acid etching, thermal oxidation, O<sub>2</sub> plasma treatment, ball milling with potassium hydroxide and ozonolysis have been used to functionalize SWNTs with oxygenated groups<sup>4,8,9</sup>, which may play a key role in the subsequent SWNT dissolution, purification and assembly<sup>2</sup>. Furthermore, the oxygenation of SWNTs was found to convert small-gapped (0.1-0.5 eV) semiconducting SWNTs to apparently metallic ones. About 0.1 electron charge was estimated to be transferred from the carbon nanotube to each oxygen atom, resulting in hole carriers and finite conductance<sup>10,11</sup>. The spectroscopic studies have been conducted on the electronic structure of the acid-oxidized<sup>8</sup>, hydrothermal modified<sup>12</sup> and ozonized SWNTs<sup>13</sup>, but not on hydroxyl (-OH) modified SWNT. Hence in this section, OH functionalization was conducted on SWNTs to introduce OH group onto its sidewall, and the electronic structure of OH-functionalized SWNTs was studied. Various spectroscopic techniques such as Raman spectroscopy, Fourier Transform Infrared (FTIR), ultra-violet photoelectron spectroscopy (UPS), and x-ray photoelectron spectroscopy (XPS) were used for the investigation.



### **9.1.1. Experimental procedures**

Since a large quantity of SWNT was needed in this experiment, a commercial grade SWNT was purchased from Shenzhen Nanoport<sup>14</sup>. The SWNT was briefly air-annealed at 500°C to remove 3% ash content as stated by the manufacture. The SWNT was soaked in 12M hydrochloric acid and subsequently annealed at 1000°C under argon protection to remove any surface oxides that could be formed due to the acidic purification. These purified SWNTs were subsequently ball-milled with potassium hydroxide (KOH). A mixture of SWNTs and KOH (mass ratio C:KOH = 1:20 weight ratio) was loaded into an agate capsule containing a milling ball. The capsule was set to vibrate violently for 0.5 h in dry air at room temperature. The resulting mixture was washed repeatedly with methanol until the KOH was completely removed. The morphology of the KOH-milled SWNT was checked with scanning electron microscope (SEM, JEOL JSM-6700F). For comparison, pristine SWNT was also ball-milled without KOH under identical conditions. The OH-functionalized SWNT was denoted as SWNT<sub>OH</sub>.

Photoelectron spectroscopy (PES) was carried out on a VG ESCALAB Mk II machine under UHV (better than  $3 \times 10^{-9}$  Torr) condition. XPS spectra were obtained using Mg  $K\alpha$  (1254.6eV) ionization source. Ultraviolet photoelectron spectroscopy (UPS) spectra were obtained using He II (40.8eV), and He I (21.2eV) resonance lines with an applied 10eV bias. A standard gold metal (5.1eV of work function) was used as a reference to determine the Fermi edge.

Optical spectroscopic characterizations were also employed to follow the functionalization process. FTIR spectra (Perkin-Elmer 2000 FTIR spectrometer) of the SWNT samples were collected using DRIFT method. Renishaw Raman system 1000B at 514.5nm laser wavelength was employed to explore structural defects and the presence of functional groups in the samples. Solution-phase optical absorption spectra of pristine and -OH functionalized SWNTs were collected with an UV-vis-NIR photospectrometer.

The optical limiting behavior of  $-OH$  functionalized SWNTs was investigated using 7ns laser at 532nm<sup>15</sup>. Pristine SWNT was sonicated in 1% Triton 100X and SWNToh was dissolved in water such that both had 70% transmittance for the optical limiting experiments.

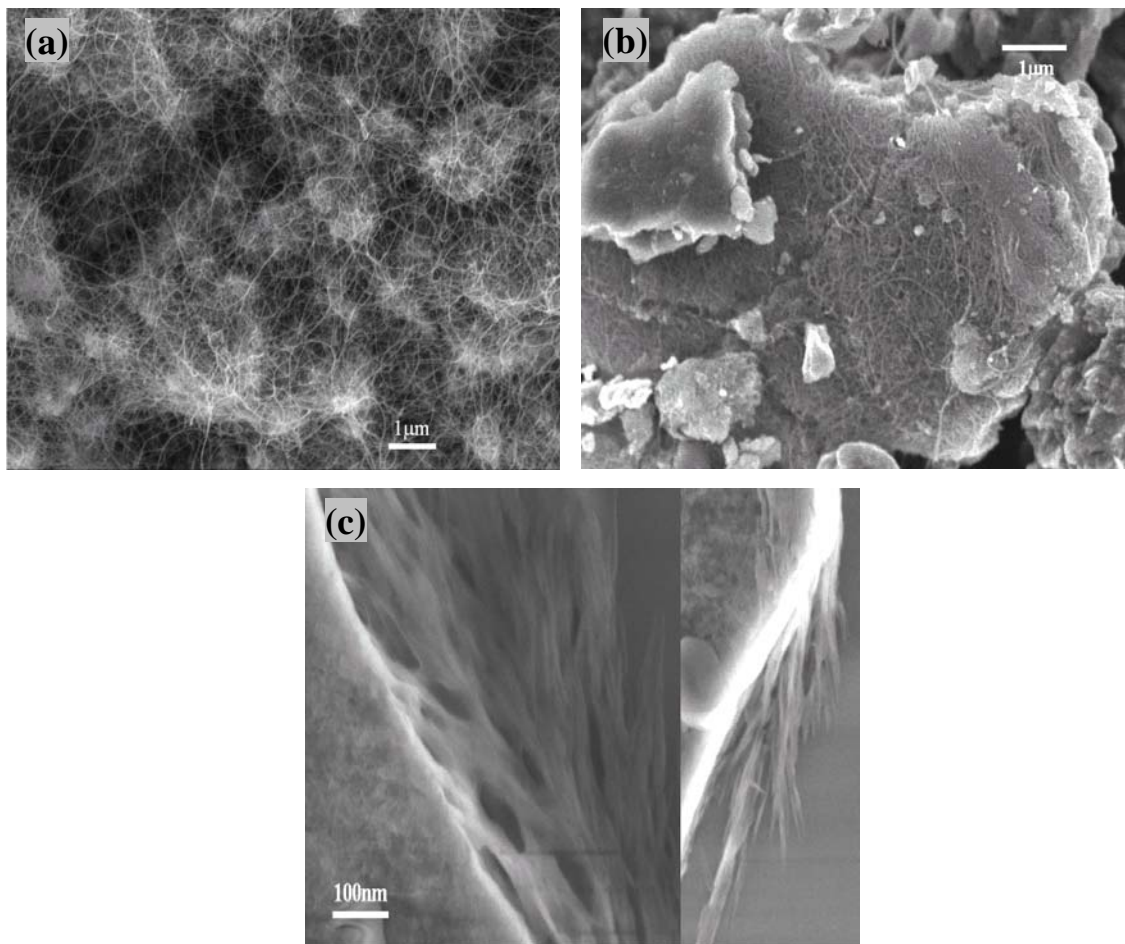


**Figure 9.1.** SEM images of (a) purified SWNT, (b) milled SWNT without KOH, and (c) functionalized SWNToh which was cast from a methanol suspension and bundles of tubes can be seen protruding from the clusters.

**9.1.2. Electron microscope analysis.**

Fig 9.1a shows the SEM image of the purified SWNT with a randomly entangled morphology. Pristine SWNT was also milled (without KOH) for 0.5 h to check the tubular integrity. As can be seen from Fig 9.1b, SWNTs were still observable after 0.5 h of milling without KOH. According to N. Pierard et al.<sup>7</sup>, a 0.5hr milling time is the optimal time to shorten SWNT. A methanol suspension of KOH-milled SWNTs was cast onto a Si substrate for SEM viewing (see Fig 9.1c). It can always be observed that bundles of SWNT protrude from the side of a cluster. Furthermore, the presence of KOH might act as a cushion for the SWNT during the milling process. The bundles of KOH-milled SWNT show considerable degree of alignment, in contrast to the entangled morphology of pristine SWNT, which can be attributed to the process of –OH functionalization.

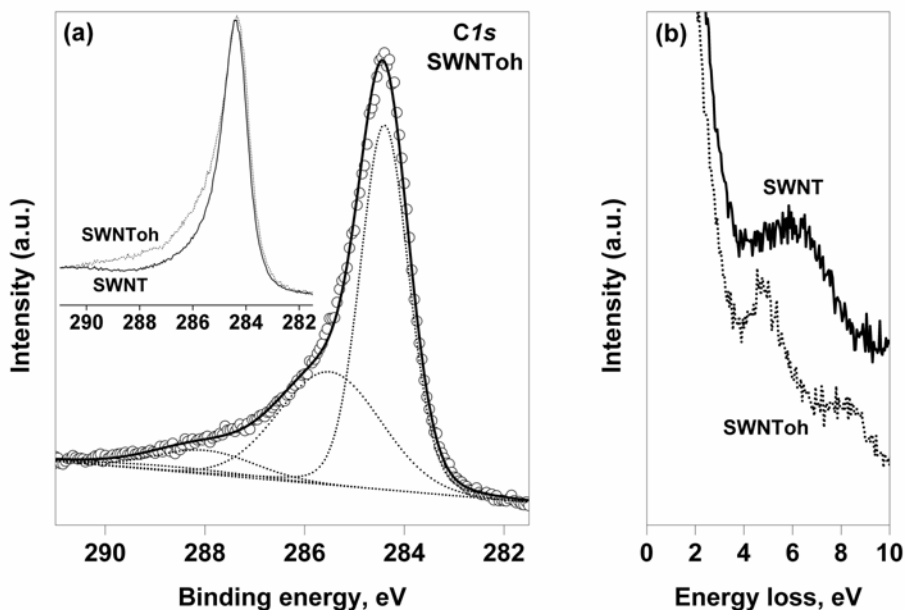


**Figure 9.2.** (a) Deconvoluted core-level XPS *C1s* spectrum of SWNToh. *Inset:* Normalized core-level *C1s* spectra of pristine SWNT and SWNToh. (b) The *C1s* photoelectron energy-loss spectra for SWNT (solid line) and SWNToh (dotted line). *Energy-loss spectra have been normalized to C 1s main peak and relocated with the loss energy of the main peaks all being zero.*

### 9.1.3. X-ray photoelectron spectroscopy core level analysis

Chemical species that were introduced onto the nanotubes could be determined from the high-resolution XPS spectra. Figure 9.2a shows the XPS  $C1s$  spectrum of SWNToh. The deconvoluted  $C1s$  spectrum of SWNToh showed evident shoulders at binding energies 286.2eV and 287.5eV which corresponded to C-OH and C=O species respectively (see also Fig 9.2a inset). However, the C-OH moieties were much more than the C=O, thus SWNToh is predominantly functionalized by the hydroxyl groups. The XPS  $C1s$  spectrum of SWNToh gave an estimated molar ratio of C: OH = 5: 1. The attachment of multiple -OH groups to the sidewalls of SWNT was also supported by FTIR result (see below).

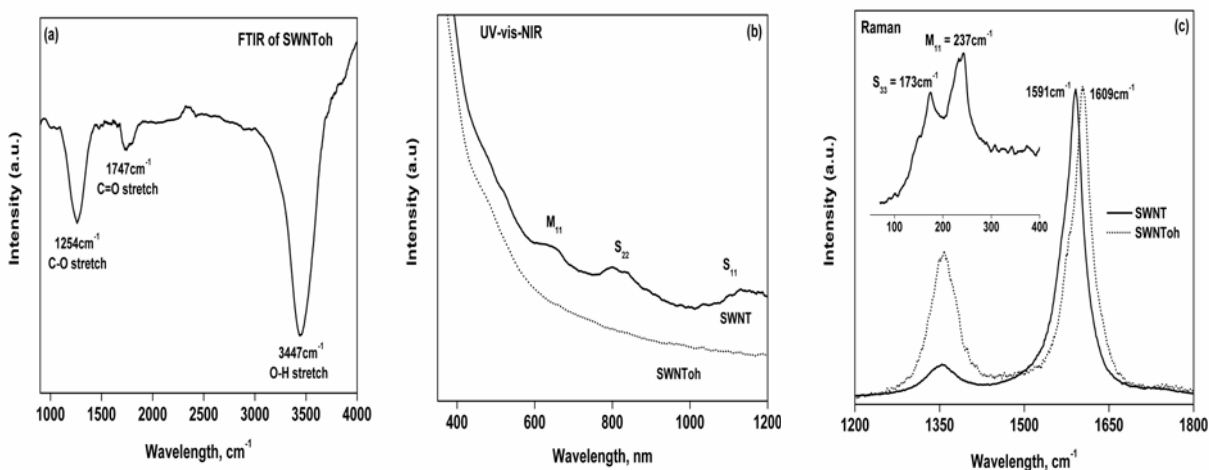


**Figure 9.3.** (a) FTIR of SWNToh functionalized with hydroxyl groups. (b) UV-vis-NIR spectra of pristine SWNT (solid line) and SWNToh (dotted line). (c) Raman scattering spectra of pristine SWNT (solid line) and SWNToh (dotted line). *Inset:* RBM signals of pristine SWNT. *The spectra have been scaled so that the strongest  $\omega^+_G$  peaks have the same intensity to elucidate the upshift of  $\omega^+_G$  peaks.*

### 9.1.4. Optical Spectroscopic characterizations.

The FTIR spectrum of SWNToh was displayed in Fig 9.3a. A very intense -OH band centered at  $\sim 3447\text{cm}^{-1}$ , C-O stretching mode at  $\sim 1254\text{cm}^{-1}$  and C=O groups at  $\sim 1747\text{cm}^{-1}$  were observed for SWNToh. These observed functional groups were consistent with XPS analysis.

The UV-vis-NIR absorption spectra of pristine SWNT and SWNT<sub>oh</sub> were presented in Fig 9.3b. Collective van Hove transitions are noted for pristine SWNT and the absorption bands at  $S_{11} \sim 1200\text{nm}$  and  $S_{22} \sim 800\text{nm}$  are assigned to the first and second van Hove (vH) singularities of semiconducting nanotubes respectively, and the  $M_{11} \sim 650\text{nm}$  band is due to the first vH transition in metallic nanotubes. –OH functionalization renders SWNT<sub>oh</sub> better solubility in polar solvents such as water, ethanol and DMF, in contrast to pristine SWNT. This is important to the application of SWNTs as reinforcers for the fabrication of polymer composites. The solubility of SWNT<sub>oh</sub> in water is estimated to be  $\sim 2.5\text{mg/ml}$  using a specific extinction coefficient of  $\epsilon = 2.86 \times 10^4 \text{ cm}^2/\text{g}$  at  $500\text{nm}$ <sup>16</sup>. However, the UV-vis-NIR absorption spectrum of SWNT<sub>oh</sub> is featureless, without any vH absorption bands, and this provide additional evidence for sidewalls functionalizaion of SWNT<sup>3</sup>. This loss of absorption features is a consequence of the conversion of significant numbers of  $sp^2$ -hybridized carbons to  $sp^3$ -hybridization. This was further elucidated by Raman spectroscopy.

Raman scattering at 514nm excitation laser energy was used to monitor the effects of –OH functionalization of the SWNT samples. The radial breathing modes (RBM) and the tangential modes (G band) are characteristic Raman peaks of SWNT (see Fig 3c). The RBM signals are particularly sensitive to the tube diameters,  $\nu \text{ (cm}^{-1}\text{)} = 224/d + 12 \text{ (nm)}$ ,<sup>17</sup> and its intensity is selectively enhanced when the photon energy matches a nanotube's van Hove transition. The RBMs of the pristine SWNTs (Shenzhen nanoport) under 514nm (2.41eV) laser excitation exhibit two prominent peaks at  $237\text{cm}^{-1}$  and  $173\text{cm}^{-1}$  (see Fig. 9.3c inset). The peaks at  $S_{33}=173\text{cm}^{-1}$  and  $M_{11}=237\text{cm}^{-1}$  were assigned to be semiconducting nanotubes with diameter 1.39nm and metallic nanotubes with diameter 1.05nm respectively<sup>17</sup>.

The D-band ( $\sim 1300\text{cm}^{-1}$ ) is related to the  $sp^3$  states of carbon and can be used to elucidate the disruption of the aromatic system of  $\pi$ -electrons on the nanotube sidewalls by the attached functional groups<sup>3,18</sup>. It could be seen that the D-band of SWNT<sub>oh</sub> is relatively increased which

indicates an increase in disordered structures due to the introduction of multiple –OH groups to the wall of SWNToh. This high degree of sidewall functionalization of SWNToh caused complete disappearance of the RBM signals. The disappearance of RBM signals had also been observed in fluorinated and doped SWNTs<sup>1-3,18-20</sup>. As shown in Figure 9.3c, the G-band of SWNToh was located at 1609 cm<sup>-1</sup> and upshifted by +18 cm<sup>-1</sup> as compared to that (1591 cm<sup>-1</sup>) of SWNTs. Similar upshifts  $\Delta\omega$  of the high frequency tangential mode had been reported as a good indicator of charge transfer in *p*-doped (e.g. HSO<sub>4</sub><sup>-</sup>, COOH<sup>-</sup>, Br<sub>2</sub>, O<sub>2</sub>-doped) SWNTs<sup>19,20</sup>. By using a parameter  $\Delta\omega/\Delta f = \sim 320\text{cm}^{-1}$  frequency upshift per hole per C-atom for *p*-doped SWNTs<sup>20</sup>, we can estimate 1/22 of an electron charge transfer, or one free hole per 22 C atoms in SWNToh.

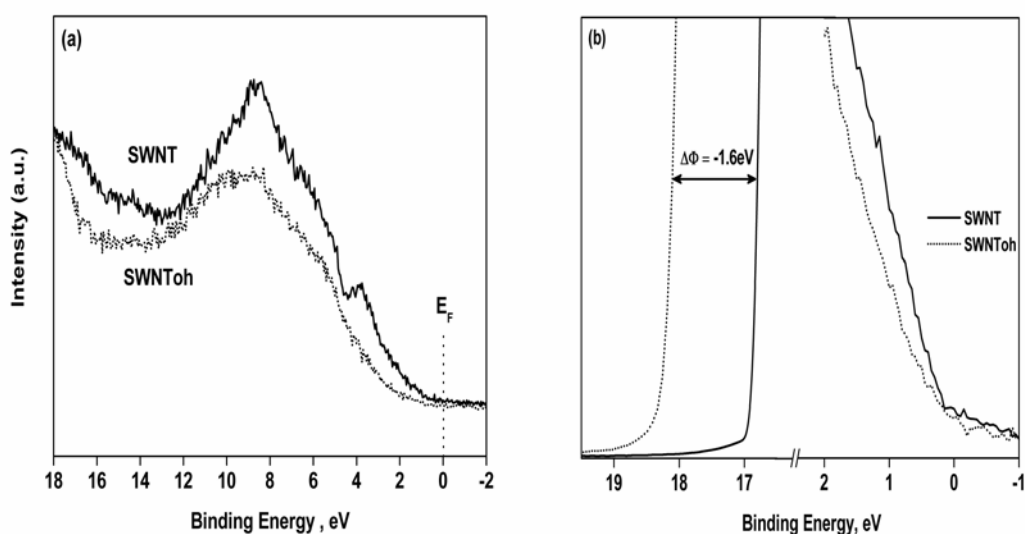


**Figure 9.4.** (a) UPS He II (40.8eV) valence band spectra of pristine SWNT (solid line) and SWNToh (dotted line). (b) UPS He I (21.2eV) secondary electron tail threshold and the Fermi level for pristine SWNT (solid line) and SWNToh (dotted line).

### 9.1.5. UPS valence band analysis

The charge transfer in the functionalized tubes was expected to result from the chemical bonding of -OH groups to the tubes, which could be verified by UPS and XPS studies. In Fig.

9.4a the UPS HeII spectra of pristine SWNT and OH-functionalized SWNToh were displayed. For pristine SWNTs (Shenzhen Nanoport), the valence band (VB) spectrum exhibits two bands located at binding energies at  $\sim 4$  and  $\sim 9$  eV, which are the  $\pi$  and  $\sigma$  bonds due to the  $C2p$  electrons and the measured VB spectrum is consistent with the previous VB study of carbon nanotubes (see Chapter 4, page 122). The decay of the  $2p\pi$  peak at  $\sim 4$  eV, and  $2p\sigma$  at  $\sim 9$  eV binding energies below  $E_f$  of the SWNToh were clear. The relative intensity enhancement at 6 eV below  $E_f$  was also observable in the SWNToh VB spectrum, which might correspond to the O  $2p$  orbital. These indicated that  $2p\pi$  as well as the  $2p\sigma$  orbital of the carbon nanotube were strongly involved in the overlapping and bonding with the corresponding molecular orbitals of the OH group. Since the oxygen  $p$  orbitals were either partially filled ( $2p$ ) or totally unoccupied ( $3p$ ), the C-OH bonding would result in the charge transfer from C to OH, leaving hole carriers in the valence band of functionalized SWNToh. The XPS  $CI_s$  energy loss spectra in Fig. 9.2b demonstrated that the loss peak corresponding to the  $2p\pi \rightarrow 2p\pi^*$  transition<sup>15</sup>, which was centered at about +6 eV apart from the main  $CI_s$  peak for the pristine SWNTs, was down-shifted by 1 eV due to the OH functionalization, while a new loss feature at +8 eV must be related to the unoccupied anti-bonding molecular orbital mainly contributed from oxygen  $3s$  and  $3p$  hybridized orbitals. SWNT's  $2p\pi^*$  is  $\sim 1-2$  eV above the Fermi level, as estimated based on the valence band data and the C  $1s$  electron energy loss spectrum. According to NIST atomic spectra database the energy gap is 9.1 eV between oxygen  $2s^22p^33s$  and  $2s^22p^4$ , and 10.7 eV between  $2s^22p^33p$  and  $2s^22p^4$ . If O  $2p$  was usually considered to be at 6 eV below the Fermi level, these would position the unoccupied  $3s$  and  $3p$  at  $\sim 3$  and 5 eV above the Fermi level respectively. By applying molecular orbital theory, the bonding of the unoccupied O  $3s/3p$  orbitals with carbon  $2p\pi$  and  $2p\pi^*$  orbitals can well explain the decay of the SWNT's  $2p\pi$  peak, the downshift of the  $2p\pi \rightarrow 2p\pi^*$  energy loss peak and the observation of new energy loss feature.

As the  $2p\pi$  state of the tube was dispersive, extending up to  $E_f$ , the C-O bonding must have influence in the density of state near  $E_f$ . UPS He I is a suitable tool for this study since the photoemission cross section of C 2p is higher at lower photon energies (21.2 eV of He I vs 40.8 eV of He II). Figure 9.4b highlights the Fermi edge of the SWNT and SWNToh samples, with their Fermi level both coincided at zero binding energy. Note that the density-of-states near the Fermi edge for SWNToh was not as steep as that for SWNTs, indicating the depletion of electron density at the top valence band. This is an evidence of the charge transfer from SWNT's HOMO to the OH group which acts like an electron-acceptor. The charge transfer from the SWNToh top valence band to the partially occupied oxygen orbitals would result in the depletion of the top valence band for SWNToh.

In Fig. 9.4b the secondary electron tail threshold of the functionalized SWNToh was drastically shifted towards higher binding energy by 1.6 eV, as compared to the pristine SWNT, which was an indication of a downshift of vacuum level (with respect to  $E_f$ ) and thus a significant decrease in the work function. Since the wall of SWNToh was heavily modified with the -OH groups, a dipole layer with protons on the surface would be responsible for the marked decrease in the work function. This phenomenon may result in a high contact potential when two different types of tubes join together, and may find useful thermal sensing and thermal power applications.

#### **9.1.6. Optical limiting (OL) properties of SWNToh**

Highly dispersed or solubilized SWNTs in solvents provide excellent opportunities to study their optical properties. Stable solutions of SWNT and SWNToh were prepared with 70% transmittance and their nonlinear optical properties towards 532nm 7ns laser pulses were studied (see Fig 9.5). A slight improvement of the OL properties of SWNToh was observed. At input fluence of less than  $0.1 \text{ Jcm}^{-2}$ , a plateau of energy transmittance was observed. But when the input fluence continued to increase the transmittance decreased; onset of optical limiting behavior. The



limiting threshold was defined as the input fluence whereby the transmittance decreased to half of the linear transmittance. The threshold of SWNToh and SWNT were around 1.0 and 1.2 Jcm<sup>-2</sup> respectively.

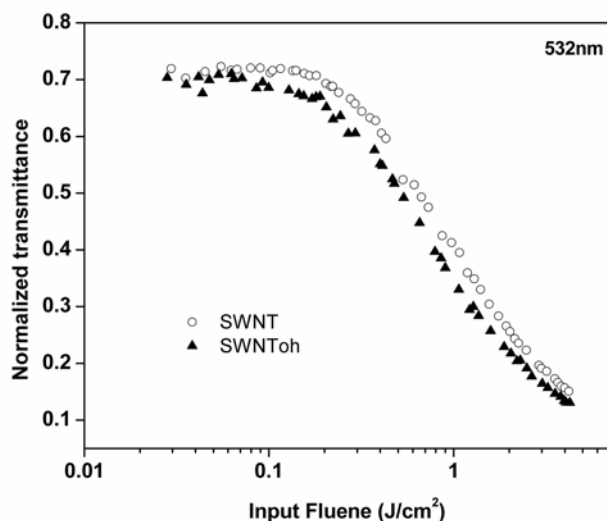


**Figure 9.5.** Optical limiting responses to 7ns, 532nm optical pulses of pristine SWNT (ooo) and SWNToh (▲▲▲) in aqueous medium.

### 9.1.7. Conclusions

OH-functionalized SWNTs (SWNToh) were prepared by ball-milling SWNTs with KOH. SEM observation reveals that these SWNToh exhibits well-aligned self-assembled structures. Detailed spectroscopic characterizations of SWNToh showed that the –OH functionalization leads to a charge transfer from C to OH, the depletion of top valence band density, the modification of energy band structure, and the significant reduction in the work function of SWNToh. The SWNToh dissolves easily in water and exhibits slightly enhanced OL properties.

## **9.2. Gravitation-dependent, thermally-induced self-diffraction of octadecylamine (ODA) modified carbon nanotube solution**

### *Introduction*

The dissolution of carbon nanotubes in solvents can be achieved by oxidation, wrapping, grafting and surfactant addition. However the preparation of uniform and ordered nanotubes assemblies remains a challenge. Somoza et al.<sup>21</sup> proposed that finite-size carbon nanotubes can be considered as variable-length rigid rods and can act as liquid crystals. In the presence of strong van der Waals interaction between the carbon nanotubes, a columnar phase dominates all other phases to very high temperatures, which explains the formation of nanotubes ropes at high temperature growth. In the absence of strong van der Waals interaction, such as well-dispersed carbon nanotubes in low-molecular-weight organic solvents which screen out van der Waals interactions, both nematic and smectic phases (i.e. liquid crystalline behaviors) are possible at relatively high packing fractions. Indeed, Song et al.<sup>22</sup> had observed nematic liquid crystallinity of modified multi-walled carbon nanotubes. It is known that liquid crystals exhibit a variety of nonlinear-optical effects<sup>23,24</sup>. For example, self diffraction is often observed in nematic liquid crystal which is commonly caused by laser-induced molecular reorientation<sup>25</sup>. Therefore it is of great interest to study the nonlinear-optical effects of solubilized carbon nanotubes in organic solvents. It is anticipated that such solubilized carbon nanotubes exhibit phenomena similar to liquid crystals. In addition, the observed nonlinear-effect can be used to estimate the molecular weights of the solubilized CNTs.

### **9.2.1. Experimental procedures**

The octadecylamine (ODA)-modified multi-walled carbon nanotubes (MWNTs) have an average length of a few microns, which were provided by the courtesy of Professor Guo Zhixin (Institute of Chemistry, Chinese Academy of Science). Briefly, MWNTs were refluxed in

concentrated nitric acid for 24hr. The surface-bound carboxylic acid ( $-\text{COOH}$ ) groups were converted into acyl chloride ( $-\text{COCl}$ ) groups using thionyl chloride at  $70^\circ\text{C}$ . The resulting MWNTs were mixed with excess ODA at  $80^\circ\text{C}$  for 96hr under  $\text{N}_2$  protection. The remaining ODA was extracted with ethanol in a Soxhlet extractor. After 24hr the ethanol was discarded and replaced by chloroform to extract the soluble ODA-MWNTs for another 24hr. Since ODA-MWNTs were not soluble in chloroform, the solvent was removed by rotary evaporator. A detailed preparation of ODA-MWNTs is given in ref [26]. Figure 9.6 gives the TEM image and Raman spectrum of the ODA-MWNT sample, which has diameters of  $\sim 20\text{-}30\text{nm}$  and average length of about  $1\mu\text{m}$ . The Raman spectrum of ODA-MWNT has a broad D-band which is a good indication of functionalization.

A continuous-wave laser beam from a double-frequency Nd:YAG ( $532\text{nm}$ ) and Ti:Sapphire ( $780\text{nm}$ ) laser were used in these experiments. The ODA-MWNTs were dissolved in toluene with concentrations between  $0.02$  to  $0.08\text{mg/ml}$ . The CNT solution was placed in a  $1\text{mm}$  quartz cell. The laser beam was focused onto the ODA-MWNT solution and the experiment was conducted at  $295\text{K}$ . On the basis of Figure 9.6, the quartz cell was placed either horizontally flat (setup I) or vertically upright (setup II). The CNT solution exhibits a gravitational dependent characteristic in experimental setup II.

A theoretical modeling of CNT solution was proposed to explain the self-diffraction behavior. The model simulations are credited to Professor Ji Wei (Physics department, National University of Singapore) and the detail of the work has been presented in ref [27]. I have adopted the model simulations in this section to explain the self-diffraction of CNT solution. The crux of the simulation rely on finding mathematical expressions for the temperature rise  $\Delta T$  due to laser heating and the electric field  $E(\rho)$  of the transmitted laser beam (Huygens principle). Hence I will only cite the final mathematical expressions for  $\Delta T$  and  $E(\rho)$  in this section.

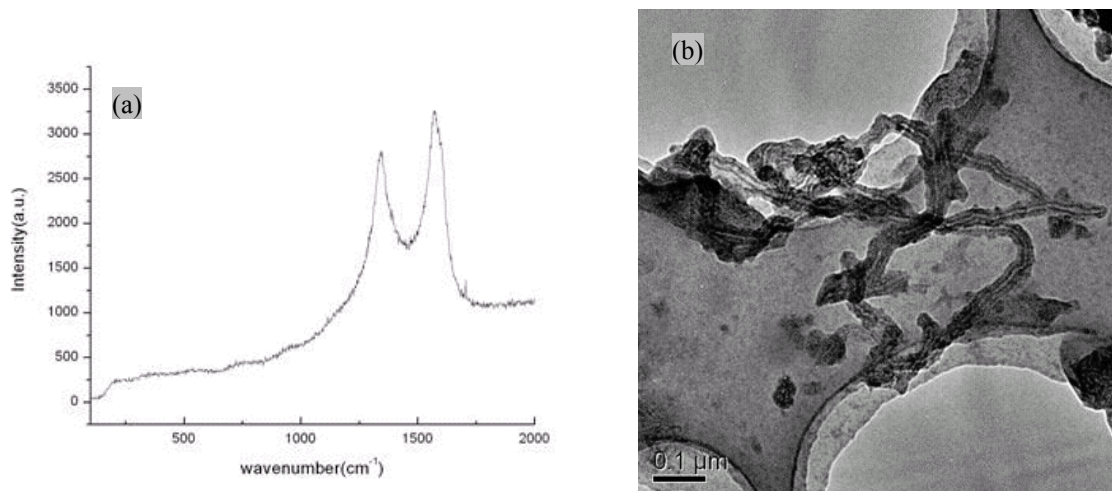


**Figure 9.6.** (a) Raman spectrum and (b) TEM images of ODA-MWNT sample.

### **9.2.2. Gravitational dependent, thermally-induced self-diffraction**

#### *Setup I – CNT solution in a horizontal position*

For experimental setup I, a spatial traverse variation of the transmitted irradiance at far-field was observed when the laser beam was normal incident onto the CNT solution. As shown in the left panel of Figure 9.7, at a low laser power (< 4mW), nearly Gaussian spatial profiles were observed. As the incident laser power was increased, the profile developed a diffraction pattern with concentric rings. Figure 9.7(c) and Fig. 9.7(e) show the diffraction pictures taken at 532nm and 780nm lasers, respectively, with 100mW power. This phenomenon is reminiscent of the self-diffraction due to thermal lensing of liquid crystals<sup>25</sup>. Likewise the observed diffraction pattern of CNT solution is attributed to thermally-induced self-diffraction (or self-defocusing) whereby the solublized MWNTs absorbed and dissipated the laser heat energy to toluene and gave rise to a temperature rise.

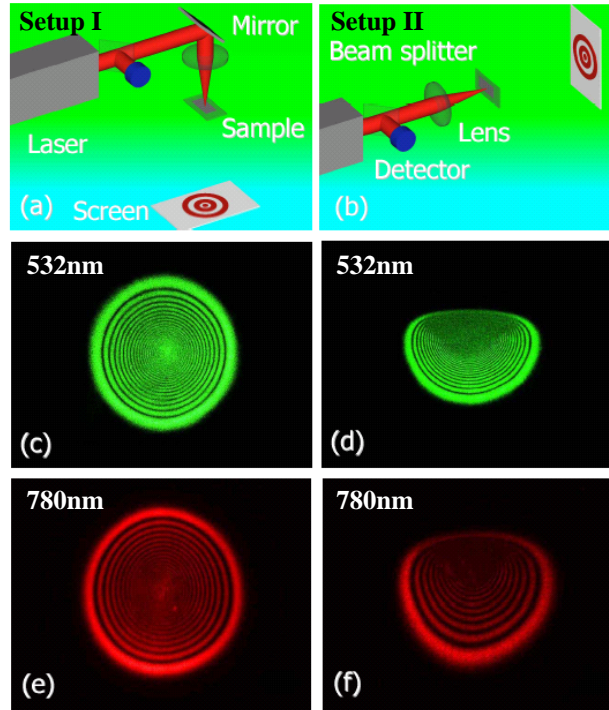


**Figure 9.7.** Gravitation-dependant, thermally-induced self-diffraction in carbon nanotubes solutions. (a) and (b) Schematic diagrams of two experimental set-ups. (c) and (d) Diffraction patterns recorded at 532nm with the set-ups shown in (a) and (b) respectively. (e) and (f) Diffraction patterns observed at 780nm with setups shown in (a) and (b) respectively. The input laser power used were  $\sim 100\text{mW}$ .

#### Setup I – numerical simulation

A theoretical model has been proposed to describe the thermally-induced self-diffraction pattern of CNT solution. The temperature rise,  $\Delta T$ , is determined by the heat flow equation under steady-state condition:

$$\Delta T(\rho) = \frac{0.25\alpha_0 P}{k} \left[ E_n\left(-\frac{2\rho^2}{\omega^2}\right) - E_n\left(-\frac{2a^2}{\omega^2}\right) - 2\ln\left(\frac{\rho}{a}\right) \right] \quad [9.1]$$

where  $P$  is the input laser power,  $\rho$  is the radial distance from the center of symmetry,  $\alpha_0$  is the absorption coefficient of the CNT solution,  $k$  is the thermal conductivity,  $\omega$  is the laser beam waist,  $a$  is the radial position at which the temperature rise,  $\Delta T(a)=0$ , and  $E_n(x) = -\int_{-x}^{\infty} e^{-t} dt/t$ .

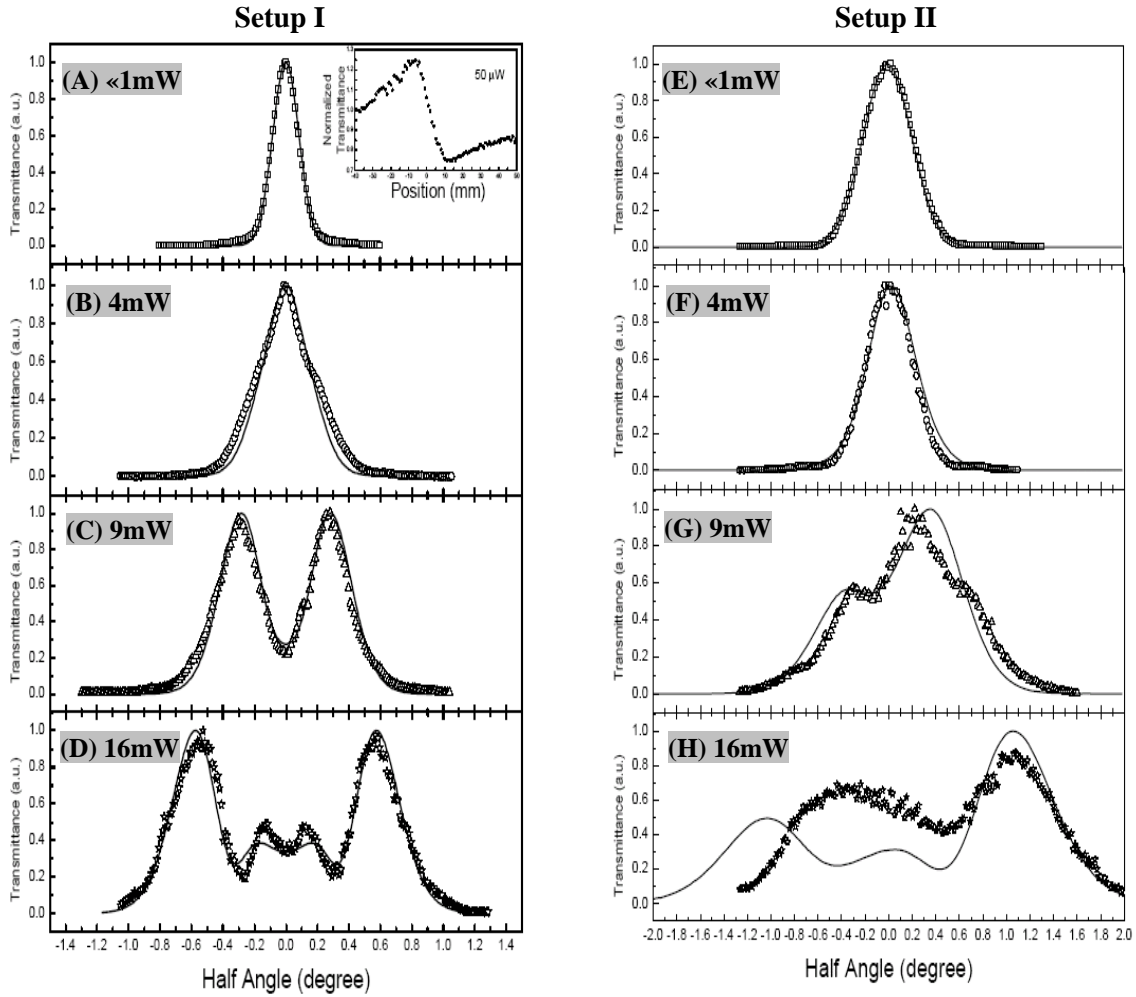


**Figure 9.8.** Far-field distribution of the transmitted irradiance measured at 780nm at different laser powers. The transmittance of the CNT solution is 85.2%. The half angle is defined as the ratio of the  $x'$ -coordinate on the observation screen to the distance of the  $z$ . The opened symbols denote experimental data. The results of left and right panels correspond to experimental setup I and II respectively. The solid lines of the left and right panels are the numerical simulations using Eqs [9.1 & 9.2] and Eqs [9.3 & 9.4] respectively.

The electric field of the transmitted beam can be calculated by the Huygens principle under cylindrical symmetry:

$$E(\rho') = E(0) \int_0^{\infty} \exp[-i \frac{2\pi}{\lambda} \Delta n(\rho) L - \frac{\rho^2}{w^2}] J_0(\frac{2\pi\rho\rho'}{\lambda z}) \rho d\rho \quad [9.2]$$

where  $\rho'$  is the radial distance on the observation screen which is at a distance of  $z$  from the focal point,  $E(0)$  is the field at  $\rho'=0$  and  $J_0(x)$  is the zeroth-order Bessel function. The irradiance distribution can be numerically simulated using Eqs [9.1] and [9.2].

The numerical simulation fits the experimental data well if  $k=0.18\text{Wm}^{-1}\text{K}^{-1}$ , which is slightly larger than the thermal conductivity of toluene ( $0.15\text{Wm}^{-1}\text{K}^{-1}$ ). The larger  $k$  value is attributed to the excellent thermal conductivity of carbon nanotubes. The  $Z$ -scan measurement (inset of Figure 9.8, left panel) showed a negative sign for nonlinear refraction, which was consistent with the thermo-optical property of solvent. Figure 9.9 also showed the linear dependence of the diffraction pattern with the CNT solution concentration, and no diffraction was observed for pure toluene solvent.

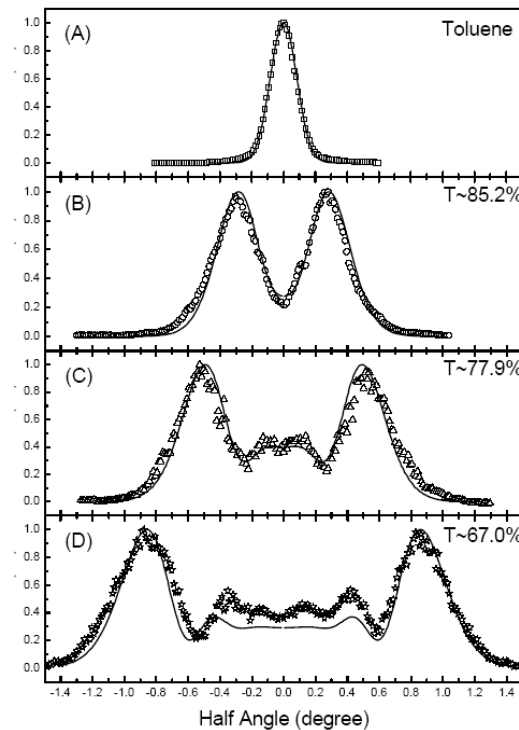


**Figure 9.9.** Far-field distribution of the transmitted irradiance recorded at 780nm and in incident power of 9mW with different CNT solution concentrations. The opened symbols denote experimental data and the solid lines are the numerical simulations using Eqs [9.1 & 9.2].

*Setup II – CNT solution in a vertical position*

When the ODA-MWNT solution was placed in a vertical position and the laser beam transverses across the sample in the horizontal direction, the observed diffraction rings were compressed in the upper half and stretched in the lower half of the rings (see Fig 9.7d, f). The non-symmetrical diffraction patterns of the ODA-MWNT solution in setup II is also displayed in right panel of Figure 9.8. MWNTs can be regarded as “supermolecules” with tens of million of carbon atoms in each nanotubes, and gravitational effect is not negligible. On the other hand, gravitational effect is negligible when the CNT solution lies horizontally and there is no variation in the nanotubes concentration along the laser transverse directions.

*Setup II – numerical simulation*

The numerical simulation of ODA-MWNT solution in setup II includes the influence of gravity. It is assumed that the solubilized MWNTs behave as Brownian particles and obey Maxwell-Boltzmann distribution of ideal gas molecules. The concentration of the CNT is postulated to vary exponentially on the vertical height as describe by Boltzmann distribution law,  $N = N_o \exp(-M_{tube}gx/k_B T)$ , where  $M_{tube}$  is the nanotubes mass,  $g$  is the gravitational constant,  $k_B$  is the boltzmann constant,  $N_o$  is the CNT concentration at  $x=0$ , and  $x$  denotes the vertical distance from the center of symmetry for the laser beam.

Using First-order approximation for small temperature rise ( $\Delta T < 5K$ ) or low laser power of a few mW, the expression for  $\Delta T$  has the following form:

$$\Delta T = \sum_i \frac{0.25q_i \sigma_i N_i(0)P}{k} \left[ E_n\left(-\frac{2\rho_i^2}{\omega^2}\right) - E_n\left(-\frac{2a^2}{\omega^2}\right) - 2\ln\left(\frac{\rho_i^2}{a}\right) \right] \quad [9.3]$$

with  $\rho_i = \sqrt{y^2 + \left(x + \frac{M_i g \omega^2}{2k_B T_o}\right)^2}$  and  $q_i = \exp\left(\frac{M_i^2 g^2 \omega^2}{8k_B^2 T_o^2}\right)$ .

And the Huygens principle for setup II is as followed:

$$E(x', y') = E(0,0) \int_{-\infty}^{\infty} \int_{-\infty}^{\infty} \exp\left(i \frac{2\pi}{\lambda} \frac{dn}{dT} \Delta TL - \frac{x^2 + y^2}{\omega^2}\right) \exp\left[i \frac{2\pi}{\lambda z} (xx' + yy')\right] dx dy \quad [9.4]$$



where  $x'$  and  $y'$  are the Cartesian coordinates on the observation screen.

To further simplify the numerical simulation of the transmitted beam along the  $x'$ -axis, the mass distribution of CNTs is very narrow and the mass of CNT can be represented as a single average mass  $M_{\text{tube}}$ . All the parameters of Eqs [9.3] and [9.4] are known constants or measurable values except for  $M_{\text{tube}}$ , which has been varied to give the best fit to the experimental data. As shown in the right panel of Figure 9.7, a good simulation fit is obtained for  $M_{\text{tube}} = 8 \times 10^{-15}$  g for input laser power  $< 10$  mW. However the numerical simulation deviates significantly from the experimental data at higher laser power ( $> 10$  mW), and this is expected because the First-order approximation for small temperature rise becomes invalid due to higher temperature rise.

### **9.2.3. Conclusions**

Solubilized MWNTs exhibit thermally-induced self-diffraction phenomenon which is similar to liquid crystals. Due to the heavy molecular weight of MWNT, the observed self-diffraction is influenced by gravitational effect. The solubilized MWNTs are modeled to distribute itself exponentially along the vertical height. For small temperature rise approximation and narrow mass distribution, the model gives good agreement with experimental observation at low laser powers. This gravitation-dependent characteristic might be applicable to study other giant molecular weights.

**References**

- [1] M. S. Strano, C. A. Dyke, M. L. Usrey, P. W. Barone, M. J. Allen, H. W. Shan, C. Kittrell, R. H. Hauge, J. M. Tour, R. E. Smalley, *Science* 301, 1519 (2003).
- [2] S. Niyogi, M. A. Hamon, H. Hu, B. Zhao, P. Bhowmik, R. Sen, E. Itkis, R. C. Haddon, *Acc. Chem. Res.* 35, 1105 (2002).
- [3] J. L. Bahr, J. M. Tour, *J. Mater. Chem.* 12, 1952 (2002).
- [4] H. Pan, L. Liu, Z. X. Guo, L. Dai, F. Zhang, D. Zhu, R. Czerw, D. L. Carroll, *Nano. Lett.* 3, 29 (2003).
- [5] Z. Konya, I. Vesselenyi, K. Niesz, A. Kukovecz, A. Demortier, A. Fonseca, J. Delhalle, Z. Mekhalif, J. B. Nagy, A. A. Koos, Z. Osvath, A. Kocsonya, L. P. Biro, I. Kiricsi, *Chem. Phys. Lett.* 360, 429 (2002).
- [6] A. Ikeda, K. Hayashi, J. Kikuchi, *Chem. Commun.* 11, 1334 (2004).
- [7] N. Pierard, A. Fonseca, J.-F. Colmer, C. Bossuot, J.-M. Benoit, G. van Tendeloo, J.-P. Pirard, J. B. Nagy, *Carbon* 42, 1691 (2004).
- [8] A. Kuznetsova, I. Popova, J. T. Yates, M. J. Bronikowski, C. B. Huffman, J. Liu, R. E. Smalley, *J. Am. Chem. Soc.* 123, 10699 (2001).
- [9] X. Lu, L. L. Zhang, X. Xu, N. Q. Wang, Q. N. Zhang, *J. Phys. Chem. B.* 106, 2136 (2002).
- [10] P. G. Collins, K. Bradley, M. Ishigami, A. Zettl, *Science* 287, 1801 (2000).
- [11] S. Jhi, S. G. Louie, M. L. Cohen, *Phys. Rev. Lett.* 85, 1710 (2000).
- [12] G. S. Duesberg, S. Roth, P. Downes, A. Minett, R. Grauper, L. Ley, N. Nicoloso, *Chem. Mater.* 15, 3314 (2003).
- [13] S. Banerjee, T. Hemraj-Benny, M. Balasubramanian, D. A. Fischer, J. A. Misewich, S. S. Wong, *Chem. Commun.* 7, 772 (2004).
- [14] <http://www.nanotubes.com.cn/>
- [15] P. Chen, X. Wu, X. Sun, J. Lin, W. Ji, K. L. Tan, *Phys. Rev. Lett.* 82, 2549 (1999).
- [16] J. L. Bahr, E. T. Mickelson, M. J. Bronikowski, R. E. Smalley, J. M. Tour, *Chem. Commun.* 2, 193 (2001).
- [17] Y. F. Wang, X. W. Cao, S. F. Hu, Y. Y. Liu, G. X. Lan, *Chem. Phys. Lett.* 47, 336 (2001).
- [18] V. N. Khabashesku, W. E. Billups, J. L. Margrave, *Acc. Chem. Res.* 35, 1087 (2002).
- [19] J. Kong, N. R. Franklin, C. W. Zhou, M. G. Chapline, S. Peng, K. J. Cho, H. J. Dai, *Science*, 287, 622 (2000).
- [20] G. U. Sumanasekera, J. L. Allen, S. L. Fang, A. L. Loper, A. M. Rao, P. C. Eklund, *J. Phys. Chem. B.* 103, 4292 (1999).
- [21] A.M. Somoza, C. Sagui, C. Roland, *Phys. Rev. B.* 63, 081403 (2001).

- [22] W.H. Song, I.A. Kinloch, A.H. Windle, *Science* 302, 1363 (2003).
- [23] P. G. de Gennes and J. Prost, *The Physics of Liquid Crystals* (2<sup>nd</sup> Edition, Oxford University Press, 1995).
- [24] I. C. Khoo and S. T. Wu, *Optics and Nonlinear Optics of Liquid Crystals* (World Scientific, Singapore 1993)
- [25] S. Brugioni, R. Meucci, *Appl. Opt.* 41, 7627 (2002).
- [26] Y. Qin, L. Liu, J. Shi, W. Wu, J. Zhang, Z. -X Guo, Y. Li, and D. Zhu, *Chem. Mater.* **15**, 3256-3260 (2003).
- [27] W. Ji, W. Chen, S. Lim, J. Lin, Z. Guo, *Opt. Express* 14, 8958 (2006).

## Chapter 10. Conclusions and future work

Experimental and theoretical studies of modified carbon nanotubes have been conducted in this thesis. A DFT study of ultrasmall 4Å SWNTs shows that the structural, electronic, and optical properties deviate from the predictions of Tight-binding theory, which ignores curvature effects and  $\sigma$ - $\pi$  hybridizations. The presence of Stone-Wales defects significantly alter the electronic density of states of ultrasmall 4Å SWNTs. The Stone-Wales defects were characterized by simulating its STM images under different bias polarity.

A comprehensive first-principles study of nitrogenated SWNTs was performed. The effects of different types of nitrogenation have been elucidated from the band structures, density of states (DOS), and molecular orbital. Our calculations indicate that the substitutional nitrogenation, -NH<sub>2</sub> functionalization as well as chemisorption will convert semiconducting nanotubes into metallic, while pyridine-like nitrogenation narrow the band gap. For metallic (5,5) nanotubes the N-doping is shown to significantly enhance the state density at the vicinity of Fermi level. Covalent sidewall -NH<sub>2</sub> functionalization is as effective as direct substitutional doping in lowering the ionization potential values, which are beneficial for field emission. Spin polarization calculations shows that the magnetic moment of chemisorbed N adatom ranges from 0.5-0.7 $\mu_B$ . The structural relaxation of SWNTs with two chemisorbed N adatoms in certain “perpendicular” configurations may result in the formation of N-N bond, mainly due to the breaking or elongating of the bridged C-C bonds. The coalescence of two neighboring N adatoms into a N<sub>2</sub> molecule needs to overcome an energy barrier in the range between 0.9 and 3.4eV, depending on the N-chemisorption configuration and tubular diameter.

A first-principles study of single-walled carbon nanotubes with bamboo-shape (BS) and pentagon-pentagon fusion defects was conducted. Sharp resonances occur on the BS-nanotubes as strong DOS localized at carbon atoms adjacent to the partitions, while at the partition the localized DOS was greatly depleted. The study of a (5,5) nanotube with pentagon-pentagon

fusion ring shows that the resonant states is attributed to the pentagon defects. The high chemical reactivity of the BS-nanotubes is correlated to the presence of localized resonant states.

A molecular mechanics and Monte Carlo simulations have been performed to study H<sub>2</sub> physisorption of SWNTs. Static calculations show that the adsorption energy is much higher (lower) for a H<sub>2</sub> physisorbed on the inside (outside) a (5,5) nanotube. Assembly of SWNTs in bundle array gives rise to addition stronger adsorption sites such as groove (~118meV) and interstitial channels (~170meV). Monte Carlo simulations estimated that the H<sub>2</sub> uptakes of SWNT bundles are very diluted (~0.5w% for (5,5) and (10,10) tubes) at 300K and the amount of H<sub>2</sub> stored can be enhanced to ~1-2wt% at low temperature of 80K. The H<sub>2</sub> density field of SWNT bundles reveals that the interstitial channel spacing must be at least ~5Å so that H<sub>2</sub> molecules can be intercalated in it.

Single-walled and multi-walled carbon nanotubes have been synthesized using a CVD method. Important spectroscopic techniques such as Raman and XPS-UPS have been employed to study its electronic property. Highly nitrogen-doped (~12at%) multi-walled carbon nanotube has been synthesized and characterized using synchrotron light source. The work function of N-doped carbon nanotubes is reduced by 0.5eV, the enhancement of electron density near the top of valence band, the rise of the valence band  $\pi$  peak and the decay of the valence band  $\sigma$  peak are all related to the N-substitution to the carbon network. The richer density of  $\pi$ -electrons in N-doped nanotube endows it with larger third-order susceptibility and better ultrafast saturable absorption.

The development of on-board H<sub>2</sub> storage via solid porous adsorbents is still a grand challenge. Nanomaterials hold a better promise to address the H<sub>2</sub> energy challenge, as evident by the comparative study of TiO<sub>2</sub> nanotube and BN nanotube, and its bulk form. Thus it is worthy to screen as many as possible candidates for H<sub>2</sub> storage, though the process can be time-consuming. Nonetheless theoretical considerations help to narrow down the search as follow: (i) Ti-doping of CNT, (ii) increasing the interlayer spacing of nanotubes via chemical intercalation, so that H<sub>2</sub>

molecules can be sandwiched between the layers. (iii) creation of defects. In other words, surface and pore modifications of carbon nanotubes are crucial to improve its H<sub>2</sub> storage.

Nanoparticle-CNT hybrid possesses interesting electrochemical properties, which can be applied as biosensors. The nanoparticles serve as anchoring points for bio-molecules, while CNTs act as the transducing platform. A glucose biosensor and a genosensor based on MWNT-palladium nanoparticle and MWNT-gold nanoparticle, respectively, have been successfully fabricated.

### ***Future work***

1. To apply theoretical methods as high-throughput screening of potential H<sub>2</sub> storage materials. Suppose a particular class of materials is deemed potential candidates of H<sub>2</sub> storage, and then in-depth theoretical calculations can be conducted to study its properties.
2. The synthesis of vertically aligned and nitrogen-doped single-walled carbon nanotubes has yet to be developed fully. The keys to obtained N-doped SWNT via a CVD process are to parameterize the catalyst Co/Mo ratio, and using diluted CH<sub>3</sub>CN flow rate. It is also worthy to explore other volatile nitrogen-containing precursors and other combination of catalysts such as iron and titanium, whereby solubility of nitrogen is high in these catalysts.
3. The study of H<sub>2</sub> uptake and preparation of alkali-doped or alkali-solvated and shortened SWNTs would be interesting candidates.
4. To investigate the conditions for co-electrodeposition of metals, such as gold, silver and platinum, and enzymes onto a CNT thin film.